Final Report

THE CHEMISTRY, DISPERSION, AND TRANSPORT OF AIR POLLUTANTS EMITTED FROM FOSSIL FUEL POWER PLANTS IN CALIFORNIA: DATA ANALYSIS AND EMISSION IMPACT MODEL

Contract No. ARB 4-258

EF76-18R

September 15, 1976

Prepared for

Air Resources Board
State of California
Sacramento, California 95814

by

Mei-Kao Liu
(Principal Investigator)
Dale Durran
Pravin Mundkur
Mark Yocke
Jody Ames

Systems Applications, Incorporated
950 Northgate Drive
San Rafael, California 94903

DISCLAIMER

The statements and conclusions in this report are those of the Contractor and not necessarily those of the State Air Resources Board. The mention of commercial products, their source or their use in connection with material reported herein is not to be construed as either an actual or implied endorsement of such products.

ABSTRACT

In 1974, the California Air Resources Board initiated a monitoring and analysis program to study the effects on air quality of using high-sulfur fuels in power plants. As a part of this effort, three mathematical models were developed in this study for simulating plume behavior. The Reactive Plume Model (RPM), adopting a trajectory approach, accommodates variations in wind speed, plume spread, and ambient concentrations. A modified Hecht-Seinfeld-Dodge kinetic mechanism was used to describe gas-phase reactions between NO_x, SO_x, and hydrocarbons. RPM predictions compare remarkably well with measurements. RPM generally predicts conversion of SO_2 to sulfate at a rate of 3 percent per hour.

The Buoyant Plume Model (BPM) predicts plume rise and effluent dispersion near the stack. It invokes the Navier-Stokes equation with the Boussinesq approximation, and allows for plume-generated turbulent diffusion. Predicted and measured plume rise and SO_2 distributions are in reasonable agreement with extensive airborne measurements.

The Plume Dispersion Model (PDM) simulates pollutant distributions far downwind. PDM solves the three-dimensional atmospheric diffusion equation, and incorporates variations in wind speeds,

ACKNOWLEDGMENTS

We would like to take this opportunity to express our appreciation to a number of individuals whose interest and kind assistance has been a constant source of encouragement during the course of this project: Mr. Charles L. Bennett, Jr. of the California Air Resources Board, Mr. Gary Palo of the California Energy Resources Conservation and Development Commission, Dr. L. Willard Richards of Air Monitoring Center - Rockwell International, Mr. Roger Sperling of Environmental Measurements, Inc., Dr. Bruce Appel of the Air and Industrial Hygiene Laboratory, Dr. Ted Smith of Meteorology Research, Inc., and Dr. Fred Shair of California Institute of Technology.

We would also like to thank many members of our staff for their assistance, in particular, Mr. Mark Meldgin for editing and Ms. Christine Smith for preparing this report.

CONTENTS

ABSTRACT iii

ACKNOWLEDGMENTS iv

LIST OF ILLUSTRATIONS vii

LIST OF TABLES xi

I INTRODUCTION 1

II DEVELOPMENT OF THE REACTIVE PLUME MODEL 5

A. Formulation of the Reactive Plume Model 6
B. Chemical Kinetic Mechanism 11
C. Numerical Solution Technique 16
D. Results of Validation Studies 20

III DEVELOPMENT OF THE BUOYANT PLUME MODEL 55

A. Review of the Literature 56
B. Formulation of the Buoyant Plume Model 67
C. Selection of the Numerical Method 77
D. Sensitivity of the Buoyant Plume Model 95
E. Model Application and Validation 100

IV DEVELOPMENT OF THE PLUME DISPERSION MODEL 121

A. Review of Mesoscale Air Pollution Modeling 121
B. Formulation of the Plume Dispersion Model. 130
C. Data Base for the Modeling Exercise. 145
D. Application of the Model 160

V SUMMARY AND CONCLUSIONS 163

APPENDICES

A A CRITICAL EXAMINATION OF THE GAUSSIAN DIFFUSION MODEL . . . A-1
B DESCRIPTION OF THE FIELD MEASUREMENT PROGRAM B-1
C A COMPARISON OF PLUME DISPERSION MODEL PREDICTIONS WITH MEASURED DATA C-1

REFERENCES. R-1

ILLUSTRATIONS

II-1	Sketch of the Coordinate System Used in the Reactive Plume Model	7
II-2	Some Major Geographic Features near the Moss Landing Power Plant and the Prevalent Directions of Plume Transport During the Measurement Program	20
II-3	Some Major Geographic Features near the Haynes and Los Alamitos Power Plants and the Prevalent Directions of Plume Transport During the Measurement Program	21
II-4	Predictions and Measurements--Moss Landing, 10 September 1974	26
II-5	Predictions and Measurements--Moss Landing, 11 September 1974	29
II-6	Predictions and Measurements--Haynes, 1 October 1974	32
II-7	Predictions and Measurements--Haynes, 11 October 1974	35
II-8	Predictions and Measurements--Haynes, 17 October 1974	38
II-9	Predictions and Measurements--Los Alamitos, 25 October 1974	41
II-10	Predictions and Measurements--Los Alamitos, 30 October 1974	44
II-11	Predictions and Measurements--Los Alamitos, 7 November 1974	47
III-1	Sketch of a Buoyant Plume	56
III-2	Comparison of Two Empirical Formulas for Plume Rise	61
III-3	The Effect of the Value of the Relaxation Parameter λ on the Convergence Characteristics of the Pressure Algorithm	92
III-4	The Variation of Ambient Diffusivity with Height	97
III-5	Plume Profile, Haynes Power Plant, 11 October 1974	103
III-6	Computed Flow Field at Haynes Power Plant on October 1, 1974	104

III-7	Predicted Plume Configuration at Haynes Power Plant on October 1, 1974	105
III-8	Observed Plume Profile, Haynes Power Plant - 1 October 1974	106
III-9	Computed Flow Field at Los Alamitos Power Plant on October 25, 1974	107
III-10	Predicted Plume Configuration at Los Alamitos Power Plant on October 25, 1974	108
III-11	Observed Plume Profile, Los Alamitos Power Plant - 25 October 1974	109
III-12	Computed Flow Field at Los Alamitos Power Plant on October 30, 1974	110
III-13	Predicted Plume Configuration at Los Alamitos Power Plant on October 30, 1974	111
III-14	Observed Plume Profile, Los Alamitos Power Plant - 30 October 1974	112
III-15	Computed Flow Field at Los Alamitos Power Plant on November 7, 1974	113
III-16	Predicted Plume Configuration at Los Alamitos Power Plant on November 7, 1974	114
III-17	Observed Plume Profile, Los Alamitos Power Plant - 7 November 1974	115
III-18	Computed Flow Field at Moss Landing Power Plant on September 10, 1974	116
III-19	Predicted Plume Configuration at Moss Landing Power Plant on September 10, 1974	117
III-20	Observed Plume Profile, Moss Landing Power Plant - 10 September 1974	118
IV-1	Modeling Region for the Haynes-Los Alamitos Study	131
IV-2	Modeling Region for Moss Landing	132
IV-3	The Calculated Vertical Diffusivity	138
IV-4	Surface Roughness in Centimeters by Grid Square for the Los Angeles Basin	153

IV-5 Mixing Depths at Moss Landing Versus Time 156

IV-6 Surface Roughness in Centimeters for Moss Landing 157

TABLES

II-1	The Kinetic Mechanism for an HC-NO_x-SO_x System	13
II-2	Field Experiments Used for Validating the Reactive Plume Model	25
II-3	Relative Humidity Variations in Los Angeles During the Period of the Field Study	51
II-4	Rate of SO_2--Sulfate Conversion as Estimated from the Predictions of the Reactive Plume Model	52
III-1	Coefficients for the Empirical Formulas	60
III-2	Exact Solutions and Model Predictions After 10 Time Steps	86
III-3	Exact Solutions and Model Predictions After 20 Time Steps	88
III-4	Summary of the Test Days	98
III-5	Summary of Stack Geometry	100
III-6	Summary of Plant Operating Conditions for Validation Study	101
IV-1	Pasquill Category and Stability Function	139
IV-2	Emissions of Oxides of Sulfur by Source	144
IV-3	24-Hour Traffic Count	145
IV-4	Los Angeles Power Plant Data--1974	147
IV-5	Major Chemical Plants and Refineries in the Los Angeles Basin	148
IV-6	APCD Wind Stations	150
IV-7	Mixing Depths for October 11, 1974	152
IV-8	SO_2 Sampling Stations	154
IV-9	Summary of Plume Dispersion Model Simulations	158

I INTRODUCTION

The search for energy sources for various industrial and domestic needs provides an interesting example of growing public awareness leading to a more rational approach to the management of the environment and resources. Prior to the late 1960s, the choice of fuels was probably dictated solely by economic factors, such as the price of the fuels; the impact of fuel usage on the environment and the availability of resources was considered only superficially, if at all. Since then concern about adverse effects on the environment has resulted in the enactment of federal, state, and local laws. Production, transport, and use of fuels are now regulated to protect the air, water, and land. As a result, pollution-free fuels, such as low-sulfur fuel oil and natural gas, are generally being used. But the increasing demand for energy and the dwindling supply of clean fuels has made it apparent that the availability of resources must also be carefully considered. For major users, such as the power generation industries, the implication is that serious thought must be given to the use high-sulfur fuel oil, which are relatively abundant, in a way that is environmentally acceptable.

With this general overall objective, in 1974 the California State Air Resources Board (ARB) initiated a comprehensive program to assess the effect on ambient air quality of the use of high-sulfur fuel oil by power plants. Specifically, the program was designed to:

- Investigate the role played by emissions of sulfur oxides in determining ambient pollutant concentrations under conditions typical of (1) a clean nonurban atmosphere and (2) a smoggy urban atmosphere.
- Study the chemical evolution of sulfur oxides in the air--in particular, the rate of conversion of sulfur dioxide to sulfate, a species that is known to have adverse effects.

> Establish a relationship between emissions and air quality so that alternative control strategies can be evaluated and the most cost-effective control of sulfur oxide emissions from the various sources can be achieved.

Under this program, five measurement teams were engaged in carrying out a coordinated field program to provide a comprehensive data base for characterizing the transport, diffusion, and chemical transformations of power plant emissions in the atmosphere. During the period September - November 1974, field studies were performed at two power plant sites in California; the Moss Landing site (representative of a rural environment), and the Los Alamitos and Haynes site (representative of an urban environment). The five measurement teams and their primary responsibilities in this field measurement program were:

Measurement Team	Primary Responsibility
Rockwell International Science Center	Ground-level pollutant measurement and analysis
Meteorology Research, Inc.	Airborne pollutant measurement and analysis
Environmental Measurements, Inc.	Mobile laboratory support for plume analysis
California Institute of Technology	Plume tracer (SF_6) measurement and analysis
California Department of Health, Air and Industrial Hygiene Laboratory	Chemical analysis of particulate samples for sulfate, nitrate, and trace element compositions

In addition to the measurement teams, the Air Resources Board retained Systems Applications, Incorporated (SAI) to develop computer-based models to characterize both the physical and chemical transformations of power plant plumes. The goal for the development of such models was to aid not only in the analysis of the field data collected in the project, but also to provide a tool for the assessment of the impact of power plant emissions on ambient air quality under a variety of conditions. This

report presents the results of this undertaking.

Chapter II of this report describes the development and validation of a reactive plume model for simulating the chemical reactions that take place in a plume. The justification, formulation, and validation of a buoyant plume model for predicting plume rise and pollutant concentrations in the vicinity of the stack are included in Chapter III. Chapter IV describes the development and validation of a plume dispersion model for the assessment of the impact of a plume at large distances from the power plant. The conclusions of this work are summarized in Chapter V.

II DEVELOPMENT OF THE REACTIVE PLUME MODEL

The Reactive Plume Model (RPM) is the first of the three component models that were developed to assess the impact of emissions from power plants. This model is designed to provide an overall description of the behavior of chemically reactive pollutants that are either emitted from the stack or entrained into the plume. By focusing only on the plume itself, and using simple assumptions that approximately characterize the complex transport and diffusion processes, the model permits a detailed examination of the plume chemistry. Despite its conceptual simplicity, this model has many useful and practical applications, such as:

> Prediction of the concentration variations of secondary pollutants, such as ozone.
> Estimation of the rate of production of sulfate and nitrate in the plume.
> Differentiation between decreases in pollutant concentrations due to chemical reactions and those due to plume dispersion.

Many of these applications will be discussed in this chapter.

The Reactive Plume Model is based on the equations of continuity (conservation of mass) for the various pollutant species. It follows the trajectory of an air parcel of varying size, and accounts, at least in principle, for the effects of transport, diffusion, and chemical reactions on pollutant concentrations within the air parcel. The model can also accommodate variations in wind speeds and inversion heights. The spread of the plume is determined either from actual measurements or by the classical Gaussian method. The interaction of the plume with pollutants in the ambient air is considered via a provision that allows for entrainment.

Finally, the model includes a chemical kinetic mechanism that describes gas-phase chemical reactions between NO_x, SO_x, and reactive hydrocarbons.

Sections A, B, and C of this chapter present detailed discussions of the various aspects of this model. Section D contains comparisons of the predictions and measurements using data collected in the field program.

A. FORMULATION OF THE REACTIVE PLUME MODEL

Because the physical and chemical processes within a plume are extremely complex, the model is based on assumptions that approximately characterize those processes. A quasi-one-dimensional trajectory approach is adopted for the treatment of transport and diffusion. Great emphasis, however, is placed upon a detailed description of the chemical transformations within the plume. This approach is supported by the following general observations:

- The physical configurations associated with a localized source are relatively simple (compared with an areal or diffusive source) and can be easily parameterized.
- The high pollutant concentrations in plumes from large point sources tend to accelerate the chemical reactions that take place in the plumes.

The assumptions used in the formulation of the Reactive Plume Model (RPM) simplify the equations that describe the physical transport of pollutants, reducing them to a set of ordinary differential equations, but retain much detail about the chemical transformations of pollutants.

The model equation is based on a simple mass balance for the pollutant species. As shown in Figure II-1, we assume that the shape of the plume can be described by two parameters:

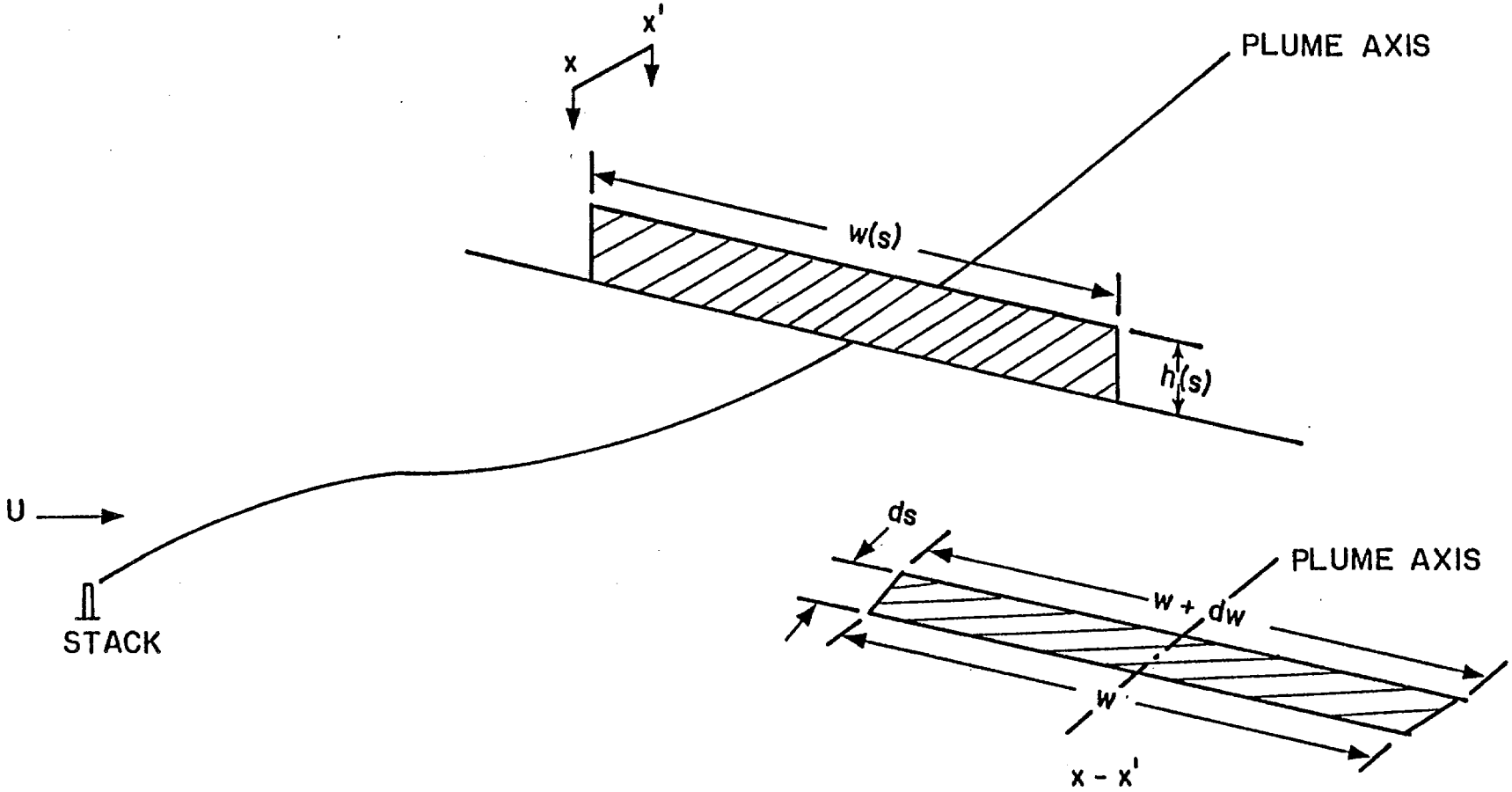

FIGURE II-1. SKETCH OF THE COORDINATE SYSTEM USED IN THE REACTIVE PLUME MODEL

$$w = w(s) \qquad \text{(II-1)}$$

$$h = h(s) \qquad \text{(II-2)}$$

where w denotes the width of the plume, h the height of the mixing layer, and s the distance downwind of a point source measured along the plume axis. As a crude approximation, we also assume that

> The wind speed is uniform but can be a function of time.
> The pollutant distribution is homogeneous at any cross section perpendicular to the plume axis.

These restrictive assumptions can be relaxed somewhat if warranted. For example, a Gaussian profile can be used to approximate the concentration profile across the plume, if it is deemed more realistic.

Two meteorological conditions are favorable to the validity of these assumptions:

> A moderate wind.
> An unstable or neutral layer near the earth's surface that is capped by a strong elevated temperature inversion.

These are also the conditions conducive to the occurrence of severe air pollution episodes, which are of particular interest in the study of plumes.

Under the above assumptions, a balance of mass flux for species i across two cross sections separated by a distance ds can be expressed by

$$C_i\Big|_s \cdot U \cdot w \cdot h = C_i\Big|_{s+ds} \cdot U \cdot (w + dw) \cdot (h + dh) - C_{Ai}\left(\frac{dV}{dt}\right)$$

$$- \left(\frac{dC_i}{dt}\right)_{Chem} \cdot \left(w + \frac{dw}{2}\right) \cdot \left(h + \frac{dh}{2}\right) \cdot ds \quad , \qquad \text{(II-3)}$$

where the rate of entrainment is given by

$$\frac{dV}{dt} = \frac{(w+dw)\cdot(h+dh)\cdot ds - w\cdot h\cdot ds}{dt}$$

and

t = time
C_i = concentration of pollutant species i within the plume
U = wind speed
w = plume spread in the horizontal direction
h = plume spread in the vertical direction
C_{Ai} = concentration of pollutant species i in ambient air.

Note that

$$C_i\Big|_{s+ds} = C_i + dC_i \quad . \qquad \text{(II-4)}$$

With knowledge of the windspeed at plume height, the travel time between cross sections can be computed by

$$ds = U\cdot dt \quad . \qquad \text{(II-5)}$$

Thus, the following modeling equation can be derived for a plume along a wind trajectory:

$$\frac{dC_i}{dt} = \left(\frac{dC_i}{dt}\right)_{Chem} + U\cdot(C_{Ai} - C_i)\cdot\left(\frac{1}{w}\frac{dw}{ds} + \frac{1}{h}\frac{dh}{ds}\right) \qquad \text{(II-6)}$$

The first term on the right-hand side is the rate of production of species i through chemical reactions; the second term accounts for the rate of dilution of pollutant species i within the plume due to horizontal spreading and the variation in mixing depth, and for the entrainment of pollutant species i from the ambient air.

The solution of Eq. II-6 for species i requires the following inputs:

> Plume width, w, as a function of downwind distance
> Plume height, h, as a function of downwind distance
> Wind speed, U
> A kinetic mechanism to describe the reaction(s) of species i
> Ambient pollutant concentrations for species i.

The first two inputs can be specified in either of two ways. From observed plume cross sections at selected downwind distances the plume height and width can be determined. If no observations of the plume are available, plume dispersion may be estimated by a predictive scheme. Both approaches have been included as options in the Reactive Plume Model. For the latter approach, the well-known Pasquill-Gifford dispersion coefficients, which are usually presented in graphical forms (Turner, 1969), are approximated by equations of the type

$$\sigma_y = ax^b \qquad \text{(II-7)}$$

where σ_y is horizontal dispersion coefficient (in meters), x is the downwind distance (in kilometers), and a and b are constants obtained by best fittings of Turner's empirical curves. The values for a and b under different atmospheric stabilities are tabulated below.

Atmospheric Stability	a	b
A	212	0.850
B	156	0.865
C	104	0.888
D	68	0.889
E	50	0.894
F	34	0.891

The application of the Turner's dispersion coefficients to either rough terrain or urban complexes has recently been questioned. A critical examination of this problem is presented in Appendix A.

B. CHEMICAL KINETIC MECHANISM

Extensive efforts have been made to develop a valid kinetic mechanism for photochemical smog, but most of these investigations focused on systems of hydrocarbons and oxides of nitrogen (Eschenroeder and Martinez, 1972; Hecht et al., 1974; Demerjian et al., 1974). As a consequence, only qualitative or semi-quantitative characterizations of the interaction of SO_2 with components of photochemical smog have resulted. The apparent lack of interest in including SO_2 in smog formation models is probably due to two main reasons: Until recently, sulfur oxide emissions have been relatively low; and reactions involving SO_2 are extremely complex. It is now generally agreed that oxidation of SO_2 in an urban atmosphere occurs through two principal mechanisms:

- Gas phase reactions with free radicals, such as OH, that are produced when organic compounds and oxides of nitrogen undergo photochemical reactions.
- Heterogeneous reactions with aerosols or particulates, particularly in the presence of heavy metal ions, which serve as catalysts.

These reactions primarily result in the transformation of sulfur dioxide to sulfuric acid or sulfate, although some investigators (Wilson and Levy, 1970; Davis et al., 1974) reported that the reactions may also affect the formation of ozone in a smoggy atmosphere.

In an attempt to provide more insight into the relative importance of the dilution of SO_2 due to transport and diffusion, as opposed to the loss of SO_2 through chemical reactions, we developed a provisional kinetic mechanism for the oxidation of SO_2 by homogeneous gas-phase reactions. Despite the fact that the individual reaction steps are based on the best

information available, we emphasize that the postulated mechanism is still incomplete and speculative. The development of a more complete and accurate mechanism must await the results of detailed kinetic studies of elementary reactions and controlled experiments in smog chambers.

The kinetic mechanism, shown in Table II-1, is based primarily upon a detailed mechanism for an HC-NO_x system developed by Hecht, Seinfeld, and Dodge (1974). To modify the Hecht-Seinfeld-Dodge mechanism, we augmented it with seven reaction steps involving SO_2. The first SO_2 reaction we consider is

$$HO_2\cdot + SO_2 \xrightarrow{k_{29}} OH\cdot + H_2SO_4 \quad . \qquad \text{(II-8)}$$

From his experimental data, Davis et al. (1974) estimated the rate constant of this reaction as 1.3 $ppm^{-1}min^{-1}$. The observed rate is sufficiently high to suggest that the $HO_2\cdot$-SO_2 reaction is important at about the time that the NO_2 concentration reaches its maximum value and O_3 begins to accumulate. Studies of SO_2 in smog simulation experiments have shown that this is the time at which the oxidation rate of SO_2 is greatest.

Wilson and Levy (1970, 1972) observed that SO_2 disappears rapidly in a system of NO_2, O_3, and SO_2. In separate experiments, they demonstrated that the NO_2-SO_2 and O_3-SO_2 reactions were very slow. Thus, they surmised that a product of the reaction between NO_2 and O_3--namely, NO_3 or N_2O_5--oxidized SO_2. However, Calvert and McQuigg (1975) determined that the rate constant for the reaction between SO_2 and N_2O_5 is 6×10^{-8} $ppm^{-1}min^{-1}$, a value so low that the reaction is of negligible importance. In addition, they set the upper bound for the rate constant for the reaction between SO_2 and NO_3 at 10^{-5} $ppm^{-1}min^{-1}$. Davis et al. (1974), however, estimated a limiting value of 14 $ppm^{-1}min^{-1}$. Although the rate of reaction of SO_2 with NO_3 is relatively uncertain, we include it as the second step involving SO_2. Thus,

$$SO_2 + NO_3 \xrightarrow{k_{30}} NO_2 + SO_3 \quad , \qquad \text{(II-9)}$$

Table II-1

THE KINETIC MECHANISM FOR AN HC-NO_x-SO_2 SYSTEM

Reaction	Rate Constant
$NO_2 + h\nu \xrightarrow{1} NO + O$	7.0×10^{-1} (variable)
$O + O_2 + M \xrightarrow{2} O_3 + M$	2.1×10^{-5}
$O_3 + NO \xrightarrow{3} NO_2 + O_2$	3.05×10
$O + NO_2 \xrightarrow{4} NO + O_2$	1.38×10^{4}
$O_3 + NO_2 \xrightarrow{5} NO_3 + O_2$	4.6×10^{-2}
$NO_3 + NO \xrightarrow{6} 2NO_2$	1.3×10^{4}
$NO_3 + NO_2 + H_2O \xrightarrow{7} 2HNO_3$	3.0×10^{-3}
$NO + NO_2 + H_2O \xrightarrow{8} 2HNO_2$	2.0×10^{-9}
$HNO_2 \xrightarrow{9} OH\cdot + NO$	4.9×10^{-2} (variable)
$OH\cdot + NO_2 \xrightarrow{10} HNO_3$	7.2×10^{3}
$OH\cdot + NO \xrightarrow{11} HNO_2$	9.0×10^{3}
$OH\cdot + CO \xrightarrow{12} CO_2 + HO_2\cdot$	2.06×10^{2}
$HO_2\cdot + NO \xrightarrow{13} OH\cdot + NO_2$	8.0×10^{2}
$2HO_2\cdot \xrightarrow{14} H_2O_2 + O_2$	8.3×10^{3}
$H_2O_2 + h\nu \xrightarrow{15} 2OH\cdot$	2.8×10^{-3} (variable)
2 Olefin + $2O\cdot \xrightarrow{16} 2RO_2\cdot + RCO_3\cdot + HO_2\cdot$	5.2×10^{3}
2 Olefin + $2O_3 \xrightarrow{17} RCO_3\cdot + HO_2\cdot$ + 2 Aldehyde + $2OH\cdot$	1.6×10^{-2}

Table II-1 (Concluded)

Reaction	Rate Constant
$2\ \text{Olefin} + OH\cdot \xrightarrow{18} RO_2\cdot + 2\ \text{Aldehyde} + HO_2\cdot$	2.5×10^4
$\text{Paraffin} + O \xrightarrow{19} RO_2\cdot + OH\cdot$	1.2×10^2
$\text{Paraffin} + OH\cdot \xrightarrow{20} RO_2\cdot + H_2O$	8.0×10^3
$2\ \text{Aldehyde} + h\nu \xrightarrow{21} RO_2\cdot + 3HO_2\cdot$	4.9×10^{-3} (variable)
$3\ \text{Aldehyde} + 3OH\cdot \xrightarrow{22} 2RCO_3\cdot + HO_2\cdot + 3H_2O$	2.1×10^4
$\text{Aromatic} + O \xrightarrow{23} RO_2\cdot + OH\cdot$	6.5×10
$\text{Aromatic} + OH\cdot \xrightarrow{24} RO_2\cdot + H_2O$	3.8×10^3
$4RO_2\cdot + 4NO \xrightarrow{25} 4\ \text{Aldehyde} + 4NO_2 + 3HO_2\cdot + RO_2\cdot$	9.1×10^2
$RCO_3\cdot + NO \xrightarrow{26} RO_2\cdot + HO_2 + CO_2$	9.1×10^2
$RCO_3\cdot + NO_2 \xrightarrow{27} \text{PAN}$	3.0×10^2
$\text{PAN} \xrightarrow{28} RCO_3\cdot + NO_3$	1.7×10^{-2}
$SO_2 + HO_2\cdot \xrightarrow{29} H_2SO_4 + OH\cdot$	1.3
$SO_2 + NO_3 \xrightarrow{30} H_2SO_4 + NO_2$	1.0×10
$4SO_2 + 4RO_2\cdot \xrightarrow{31} 4H_2SO_4 + 4\ \text{Aldehyde} + 3HO_2\cdot + RO_2\cdot$	1.5
$SO_2 + RCO_3\cdot \xrightarrow{32} H_2SO_4 + RO_2\cdot + CO_2$	1.5
$SO_2 + OH\cdot \xrightarrow{33} HSO_5\cdot$	9.0×10^2
$HSO_5\cdot + NO \xrightarrow{34} HSO_4\cdot + NO_2$	8.0×10^2
$HSO_4\cdot + HO_2\cdot \xrightarrow{35} H_2SO_4 + O_2$	2.5×10^3

where we assume k_{30} = 10.0 $ppm^{-1}min^{-1}$.

Because of the functional similarity of peroxyalkyl and peroxyacyl radicals to $HO_2\cdot$, it does not seem unreasonable to presume that these three species undergo similar chemical reactions with a given reductant. Although the rate constants for these reactions are not yet known, the reactions are thought to proceed more rapidly than the $HO_2\cdot$-NO reaction. We feel that, because of the analogies between the structure and behavior of $HO_2\cdot$, $RO_2\cdot$, and $RCO_3\cdot$, the last two species oxidize SO_2 at a rate somewhat faster than that for $HO_2\cdot$. The third and fourth reactions involving SO_2 are

$$RO_2\cdot + SO_2 \xrightarrow{k_{31}} RO\cdot + SO_3 \qquad \text{(II-10)}$$

$$RCO_3\cdot + SO_2 + (O_2) \xrightarrow{k_{32}} RO_2\cdot + SO_3 + CO_2 \quad . \qquad \text{(II-11)}$$

Rate constants for these reactions are estimated as $k_{31} = k_{32}$ = 1.5 ppm^{-1} min^{-1}. For the above reactions, we assume that SO_3 is immediately transformed into H_2SO_4, and $RO\cdot$ into aldehyde, 0.75 $HO_2\cdot$, and 0.25 $RO_2\cdot$.

Recent measurements of the $OH\cdot$-SO_2 rate constant suggest that the reaction

$$OH\cdot + SO_2 \longrightarrow HOSO_2\cdot \qquad \text{(II-12)}$$

may be an important loss mechanism for SO_2 in photochemical smog. Cox (1974) obtained a rate constant for this reaction of 850 $ppm^{-1}min^{-1}$ under atmospheric conditions, and Castlemen et al. (1974) found the value to be 600 $ppm^{-1}min^{-1}$. One can only speculate as to the fate of $HOSO_2\cdot$. However, in the kinetic mechanism we postulate that it immediately combines with atmospheric oxygen to form $HSO_5\cdot$. Therefore, the fifth reaction is

$$OH\cdot + SO_2 \xrightarrow{k_{33}} \left[HSO_3\cdot\right] \xrightarrow{O_2} HSO_5\cdot \qquad \text{(II-13)}$$

where k_{33} is estimated to be 900 $ppm^{-1}min^{-1}$. Furthermore, it has been postulated that $HSO_5^{\cdot}$ can combine with NO as follows

$$HSO_5^{\cdot} + NO \xrightarrow{k_{34}} HSO_4^{\cdot} + NO_2 \qquad \text{(II-14)}$$

where k_{34} is estimated to be 800 $ppm^{-1}min^{-1}$. In addition to these reactions, a simple termination reaction,

$$HO_2^{\cdot} + HSO_4^{\cdot} \xrightarrow{k_{35}} H_2SO_4 + O_2 \quad , \qquad \text{(II-15)}$$

with k_{35} = 2500 $ppm^{-1}min^{-1}$, has been included as the seventh reaction involving SO_2 chemistry in our modified Hecht-Seinfeld-Dodge mechanism.

In light of the current effort to elucidate the very complex reactions involving oxides of sulfur, the mechanism proposed above must be regarded as tentative. Nevertheless, it represents the best information currently available.

C. NUMERICAL SOLUTION TECHNIQUE

It has been shown in the previous sections that the equations that govern the concentration variations in an air parcel following the plume trajectory can be reduced to a system of first-order, coupled, nonlinear ordinary differential equations (Eq. II-6). A large number of techniques are available for the numerical solution of differential equations such as Eq. II-6. Selection of an appropriate technique depends to a large extent on the nature of the system that is represented by the differential equations. Chemically reacting systems often consist of individual reaction steps having very different time constants, particularly when fast free radical reactions and much slower initiation and termination reactions are occurring simultaneously (Hecht, Liu and Whitney, 1974). For example, characteristic reaction times for the reactions listed in Table II-1 vary from 10^{-3} seconds to 10^{3} seconds. In addition, there is a disparity in time scales between the diffusion term and the chemical reaction terms.

Mathematically, when such a situation exists, the associated system of ordinary differential equations is characterized by eigenvalues that vary greatly in magnitude. Such a system of equations, termed a "stiff" system, often presents substantial difficulties in the selection of a numerical integration technique.

The conditions for stability of most numerical integration procedures take the form

$$|\lambda_{max}\ \Delta t| \leq \alpha \qquad \text{(II-16)}$$

where λ_{max} is the largest eigenvalue and α, a constant that depends upon the numerical scheme selected, is usually of the order 1 to 10. If, for example, we use the fourth order Runge-Kutta method (for which $\alpha = 2.785$) and assume that $\lambda_{max} = 10^3\ sec^{-1}$ for the system of Equations II-6, a necessary condition for ensuring stability is

$$|1000\Delta t| \leq 2.785 \quad . \qquad \text{(II-17)}$$

The maximum allowable Δt, therefore, is 2.785×10^{-3}, which corresponds to nearly 2000 integration steps for a five-second time interval. Thus, although the component of the solution associated with the largest eigenvalue disappears early in the integration, we are constrained to use an unacceptably small time step to preserve stability, with the result that computation time is far too large.

A number of techniques for integrating stiff systems of ordinary differential equations have recently been proposed, and these methods are summarized by Lapidus and Seinfeld (1971). The objective of each is to permit the use of a time step that is sufficiently large to ensure economical integration times, while simultaneously maintaining stability. One of the most recent, and most promising, of these methods was proposed by Gear (1969, 1971). Its basic procedure is of the predictor-corrector type, in which one proceeds from the value of c(t) at $t = (n-1)h$ (where $h = \Delta t$) to the value of c(t) at $t = nh$ by computing a first approximation of c_n

$$c_n^{(0)} = c_{n-1} + h\beta_1 c'_{n-1} + \ldots + h\beta_p c'_{n-p} \qquad \text{(II-18)}$$

where p = number of prior values of concentration used to compute c_n. One then iteratively corrects $c_n^{(0)}$ by applying the formula

$$c_n^{(m+1)} = c_{n-1} + h\beta_0^* f[c_n^{(m)}, t_n] + h\beta_1^* c'_{n-1} + \ldots + h\beta_{p-1}^* c'_{n-p+1} \qquad \text{(II-19)}$$

for m = 0, 1, 2, ... until the computed sequence converges. (The notation c_n corresponds to $c(t_n)$, with $t_n = nh$. $c_n^{(0)}$ is termed the predicted value of c, $c_n^{(m+1)}$ the corrected value.) The β_i and β_i^*, which vary for different methods, also assume various values depending on the order of the method used, the order being equal to the number of terms included in the Taylor series approximation of the function c(t) at any point t_n. It is thus necessary that values of these parameters be taken from tables.

The computer program we employed to integrate Eqs. II-6 is a slightly modified version of that reported by Gear (1971). Gear's method is based on this predictor-corrector format. The coefficients β_i and β_i^* are chosen so that values of h can be used which are compatible with the non-stiff components of the solution, i.e., those associated with the smaller eigenvalues. Both step size h and order are selected automatically, with the order chosen so as to maximize step size while maintaining stability. The method and program have proven extremely efficient for the solutions attempted thus far.

D. RESULTS OF VALIDATION STUDIES

The validity of the Reactive Plume Model depends upon comparisons of the model predictions and actual measurements (see Appendix B) under a variety of atmospheric conditions. Ideally, these comparisons would be made using data for an air parcel over its entire trajectory, but this goal is difficult to achieve. Although the data collected in the present study are among the most comprehensive ever collected, certain compromises still have to be made because measurements were made at different locations and times, from different platforms, using different measurement principles. These measurements are not always comparable, and thus it is imperative that a critical examination of the data base collected by each measurement team

be undertaken. As described below, the objective of this tedious task is to construct a composite picture of the plume configuration.

1. Analysis of the Data

During the field measurement phase of this program, several groups collected data that can be used to validate the Reactive Plume Model. Plume measurements were made downwind of the Moss Landing power plant near Monterey, California (Figure II-2) and the Haynes and Los Alamitos power plants in the Los Angeles Basin (Figure II-3). Meterology Research, Inc. (MRI) used an instrumented aircraft flying spirals and traverses through the plume at various distances from the plant (Smith et al., 1975). These flights provided us with measurements of the plume widths and depths and concentration distributions of various pollutants within the plume at those distances. Concentrations measured while the aircraft was outside the plume provided an indication of background conditions. Furthermore, observations of pibals released by the MRI ground team were used to determine the wind speeds at plume height for our simulations.

A mobile van operated by Environmental Measurements, Inc. (EMI) was driven beneath the plume at various distances downwind of the plants. It carried a correlation spectrometer that provided supplementary information about plume geometry and the concentrations of SO_2 and NO_2 within the plume. The width of the plume can easily be determined from this data but estimates of the plume depth and wind speed are required to compute the plume concentrations from the measured total pollutant burden in the air column above the measurement point (see EMI, 1975). We estimated the plume depths for these computations by using information collected during the spirals and traverses of MRI's aircraft through the plume. Wind speed information was derived from the pibal data supplied by MRI. The ambient concentrations of SO_2 and NO_2 directly above and below the plume were assumed to be negligible for the purposes of these computations.

Syringe-loaded SF_6 samples and Gelman filter samples collected aboard the MRI aircraft were later analyzed by the California Institute of

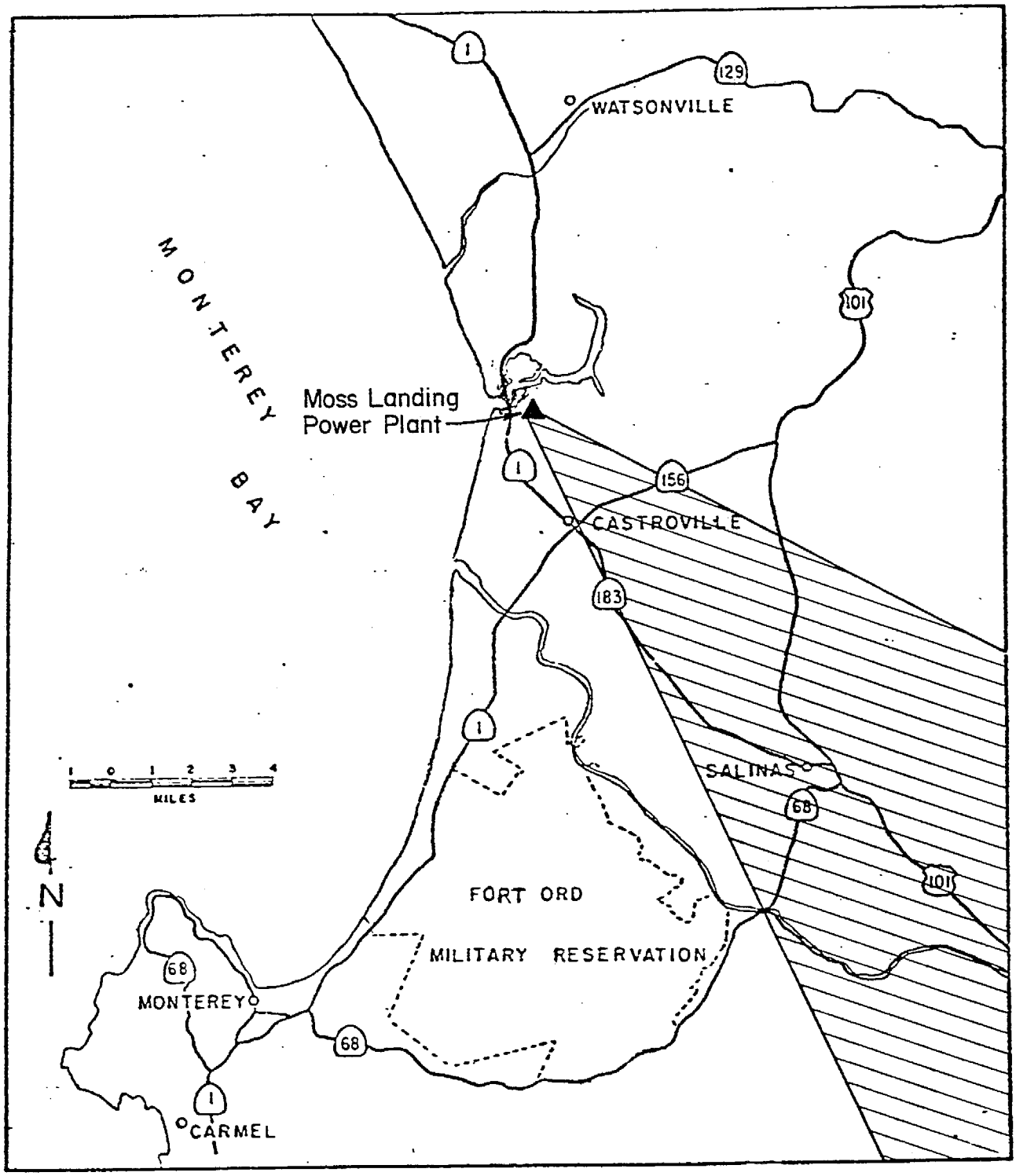

FIGURE II-2. SOME MAJOR GEOGRAPHIC FEATURES NEAR THE MOSS LANDING POWER PLANT AND THE PREVALENT DIRECTIONS OF PLUME TRANSPORT DURING THE MEASUREMENT PROGRAM

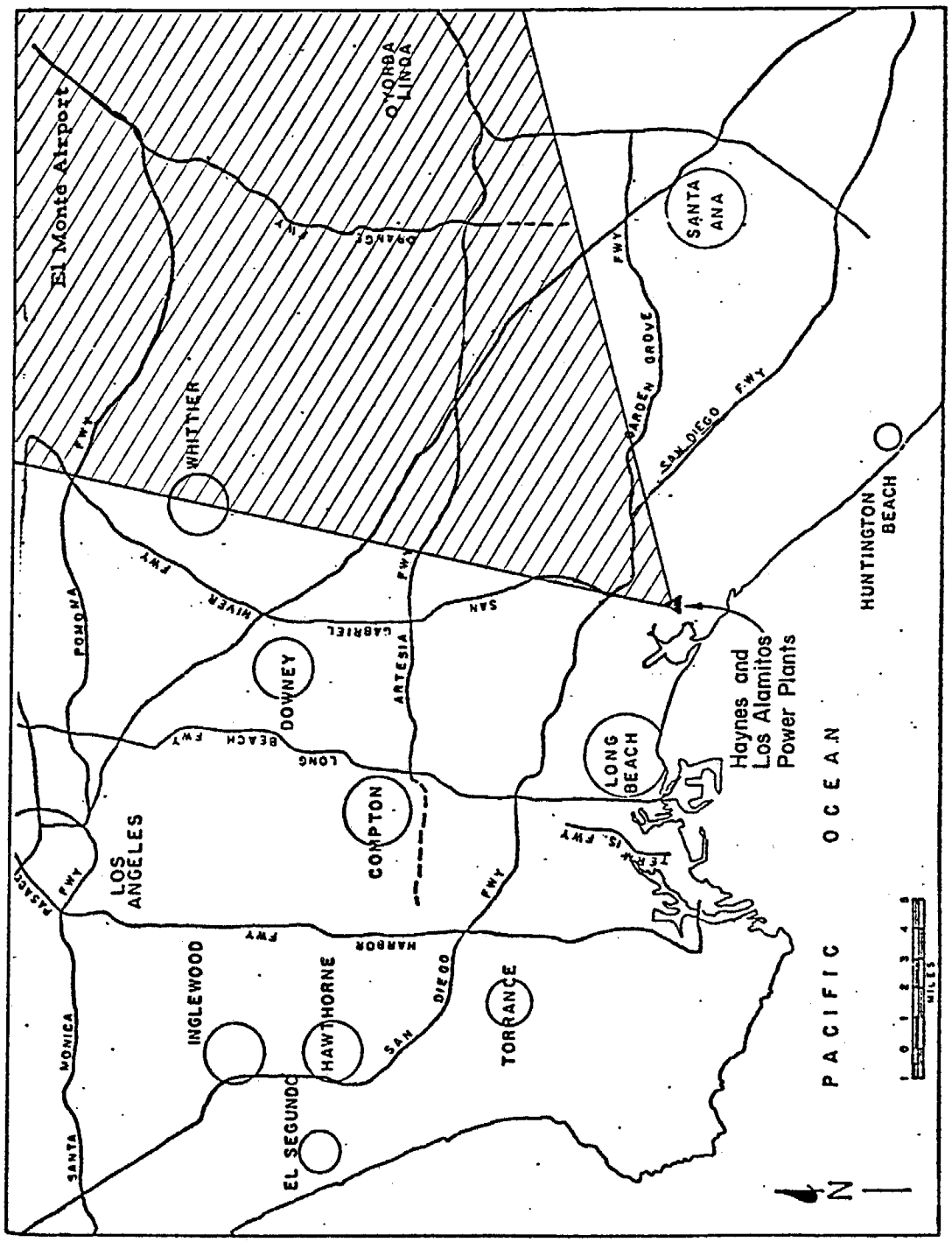

FIGURE II-3. SOME MAJOR GEOGRAPHIC FEATURES NEAR THE HAYNES AND LOS ALAMITOS POWER PLANTS AND THE PREVALENT DIRECTIONS OF PLUME TRANSPORT DURING THE MEASUREMENT PROGRAM

Technology and the Air and Industrial Hygiene Laboratory (AIHL), respectively. These analyses provided SF_6 and sulfate (SO_3 or $SO_4^=$) concentrations within the plume. The filter samples were "grab" type samples, representing average concentrations of the air parcels sampled. Only portions of these air parcels were within the plume; consequently, to obtain the plume concentrations, we used the correction formula (Appel, 1976)

$$C_{Plume} = [(C_{Average} \times T_T) - (C_{Ambient} \times T_A)]/T_P \qquad \text{(II-20)}$$

where

C_{Plume} = pollutant concentration in plume
$C_{Average}$ = average (sample) pollutant concentration
$C_{Ambient}$ = ambient pollutant concentration
T_T = total sampling time
T_P = sampling time in plume
T_A = sampling time out of plume (in ambient air).

In using this formula, we estimated T_P and T_A from the MRI data, and assumed that $C_{Ambient}$ is zero. However, this assumption introduces uncertainties into the measured sulfate concentrations in the plume, because although the true ambient sulfate concentrations are not known they are rarely close to zero.

On several occasions in the field programs, different measurement teams obtained different measurements of the same plume parameters at approximately the same time and location. The resolution of these apparent discrepancies in the data base caused some difficulty during the data reduction. Considering the variability and complexity of the system the differences were not unreasonably large, but they do contribute to further uncertainties in the preparation of the data base. However, we observed some systematic discrepancies in the data that could be traced to the measurement techniques employed by a particular group. For example, the plume widths measured by EMI were consistently larger than those measured by MRI, perhaps because the EMI data are representative of larger spatial and temporal averages

than the MRI data. The width of a plume determined by integrating over its entire depth will most frequently be larger than its width at any single traverse. In the case of discrepancies, we generally favored EMI's measured plume widths because they represent larger spatial and temporal averages and are therefore more compatible with the scale of the Reactive Plume Model.

In addition to the data discussed above, measurements made by the Los Angeles Air Pollution Control District were used to estimate the total ambient reactive hydrocarbon concentrations in Los Angeles. We estimated the percentages of olefins, paraffins, aldehydes, and aromatics in the hydrocarbon mixture from data collected in Los Angeles in 1969 (Scott Labs, 1970); the reactive hydrocarbons are split as 7.7% olefins, 46% paraffins, 7.7% aldehydes, and 38.6% aromatics. No ambient hydrocarbon concentration data were available for the Moss Landing area, so we assumed that the following concentration levels prevailed, based upon rural concentrations reported by Davis et al. (1975) and Bandy (1975): olefins = 0.01 ppm, paraffins = 0.06 ppm, aldehydes = 0.01 ppm, and aromatics = 0.05 ppm. Furthermore, no information about solar radiation was collected on any of the days during the measurement program. Therefore, we estimated radiation values from the work of Jeffries, Fox, and Kamens (1974) and Peterson and Flowers (1974), and corrected for the latitude of the plant site and for the day of the year. From these estimates, we were able to derive corresponding photolysis rate factors.

Finally, it is well known that the atmospheric concentrations of NO, NO_2, and O_3 are approximately related by the photostationary relationship (Stephens, 1969):

$$(O_3)(NO)/(NO_2) = k_1/k_3 \quad ,$$

where

(O_3) = O_3 concentration
(NO) = NO concentration
(NO_2) = NO_2 concentration
k_1 and k_3 = reaction rate constants (see Table II-1).

During initial testing of the model we found that, if NO, NO_2, and O_3 concentrations deviated significantly from this photostationary relationship, the model produced unreasonable results because the predictions reflected large perturbations in the system of reaction equations. We used this relationship as a check of the ambient concentrations input to the model. When gross inconsistencies were observed, adjustments were made to one or more of the three concentrations for those values which appeared to be the least reliable.

2. Comparisons of Predictions and Measurements

After careful examination of the data base, eight field experiments were deemed to contain information sufficient for validating the Reactive Plume Model. The locations, dates, and times of these eight experiments are listed in Table II-2. For each of these experiments, the Reactive Plume Model was exercised. The results of these simulations are plotted in Figures II-4 through Figures II-11 along with the pertinent measurements. As the series of figures designated by "a" shows, the match between the predictions and the measured SF_6 concentration ratios is extremely good. The only possible exceptions are those of 25 October 1974 and 30 October 1974, and only for downwind distances greater than 5 kilometers. This result is rather surprising in view of the uncertainties we discussed in the data reduction section. It is also most encouraging, because it provides both confidence and justification for the use of the Reactive Plume Model to explore the reactive species. The series of curves designated by "b", "c", and "d" show that the comparisons between predicted and measured concentrations for NO, NO_2, and O_3 are reasonably good. The large scatter in the NO_2 measurements in Los Angeles is probably traceable to the interaction with the urban plume. As shown in the e-series figures, the predicted SO_2 concentrations also compare very favorably with the measurements, despite the large scatter present in the measured values.

The comparison of predictions and measurements for sulfate is, for obvious reasons, more complicated. In the f-series of figures, the symbols "M" and "C" denote uncorrected and corrected measurements respectively, as

Table II-2

FIELD EXPERIMENTS USED FOR VALIDATING
THE REACTIVE PLUME MODEL

Power Plant	Date	Time of Day
Moss Landing	10 September 1974	1210-1500
" "	11 September 1974	1235-1354
Haynes	1 October 1974	1415-1600
"	11 October 1974	1350-1540
"	17 October 1974	1500-1730
Los Alamitos	25 October 1974	1340-1530
" "	30 October 1974	1300-1430
" "	7 November 1974	1300-1430

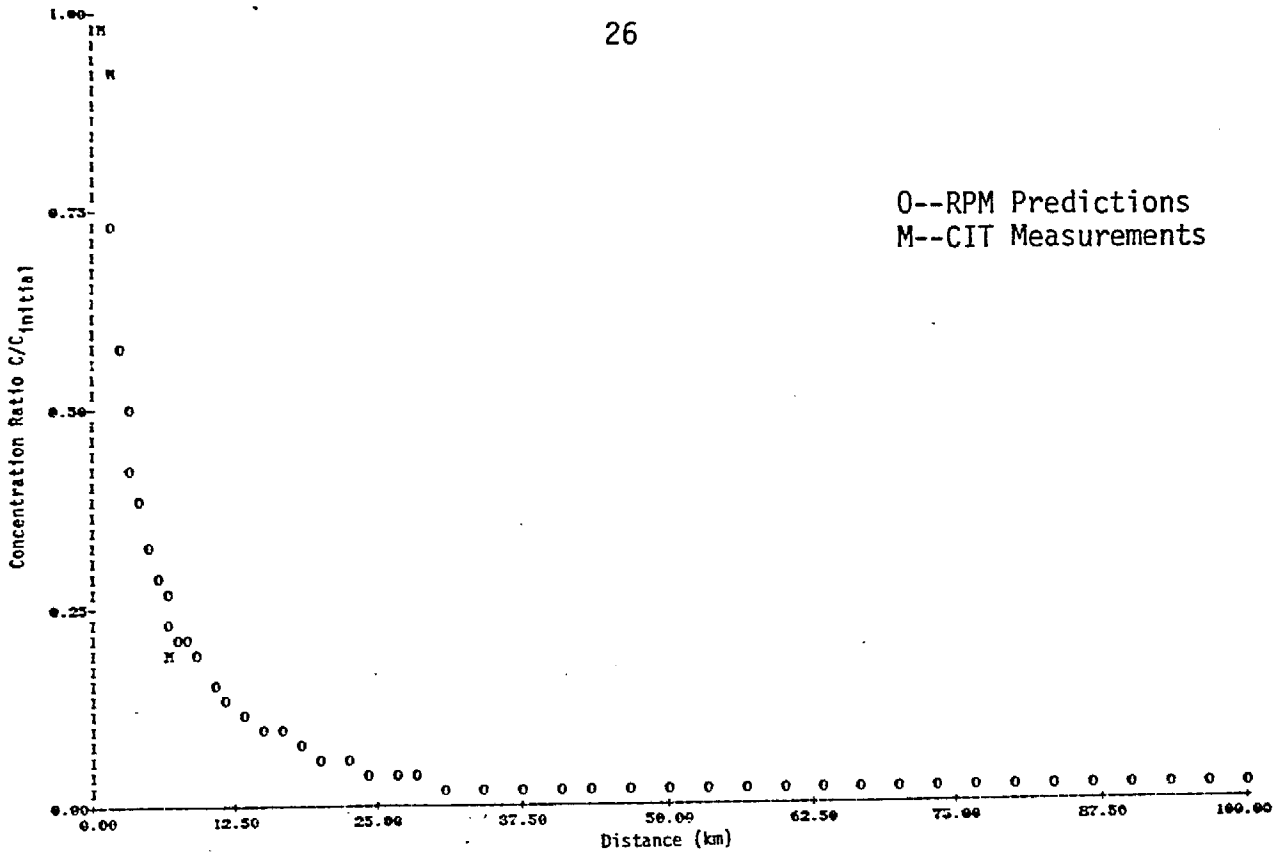

FIGURE II-4a. COMPARISON OF PREDICTED AND MEASURED SF_6 CONCENTRATION RATIOS AT MOSS LANDING ON SEPTEMBER 10, 1974 (1210-1500 HRS) VERSUS DISTANCE FROM THE STACKS.

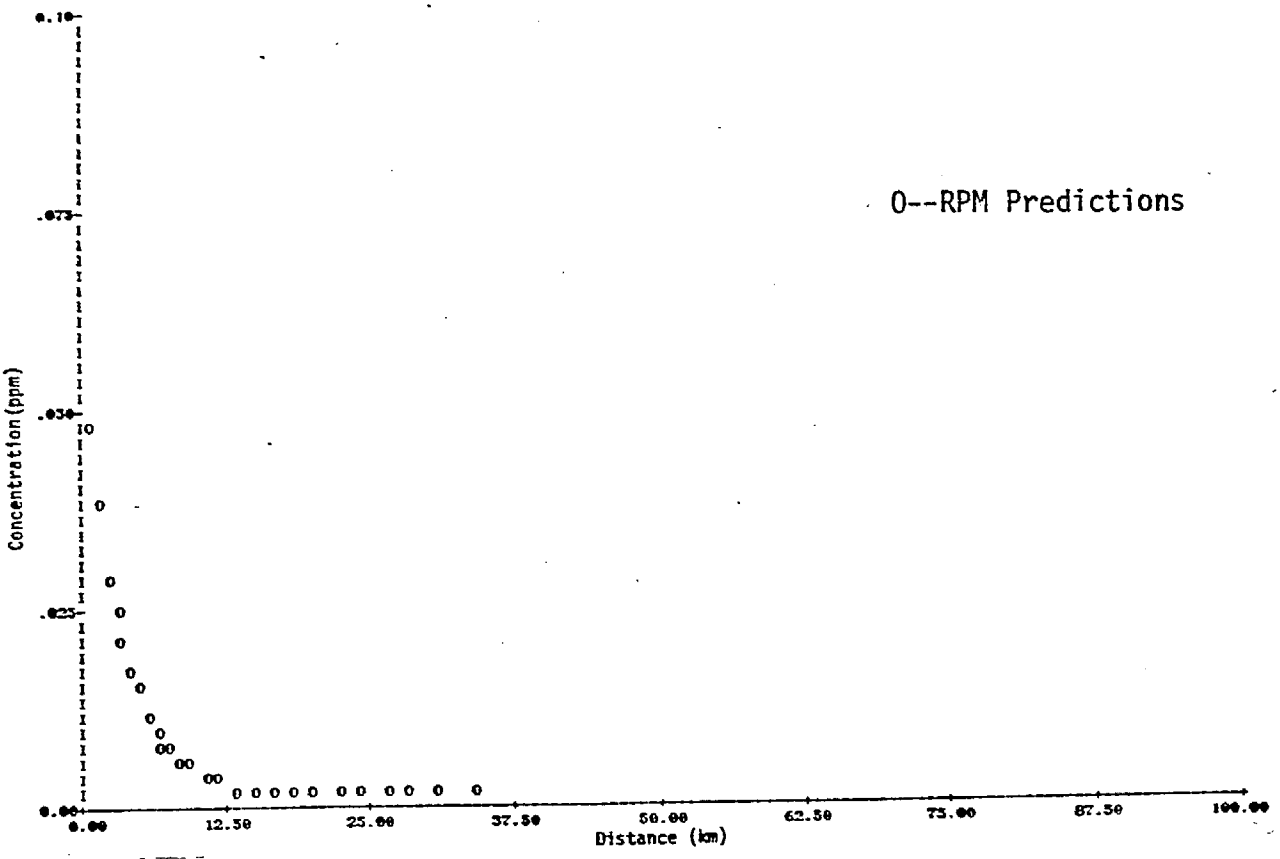

FIGURE II-4b. PREDICTED NO CONCENTRATIONS AT MOSS LANDING ON SEPTEMBER 10, 1974 (1210-1500 HRS) VERSUS DISTANCE FROM THE STACKS.

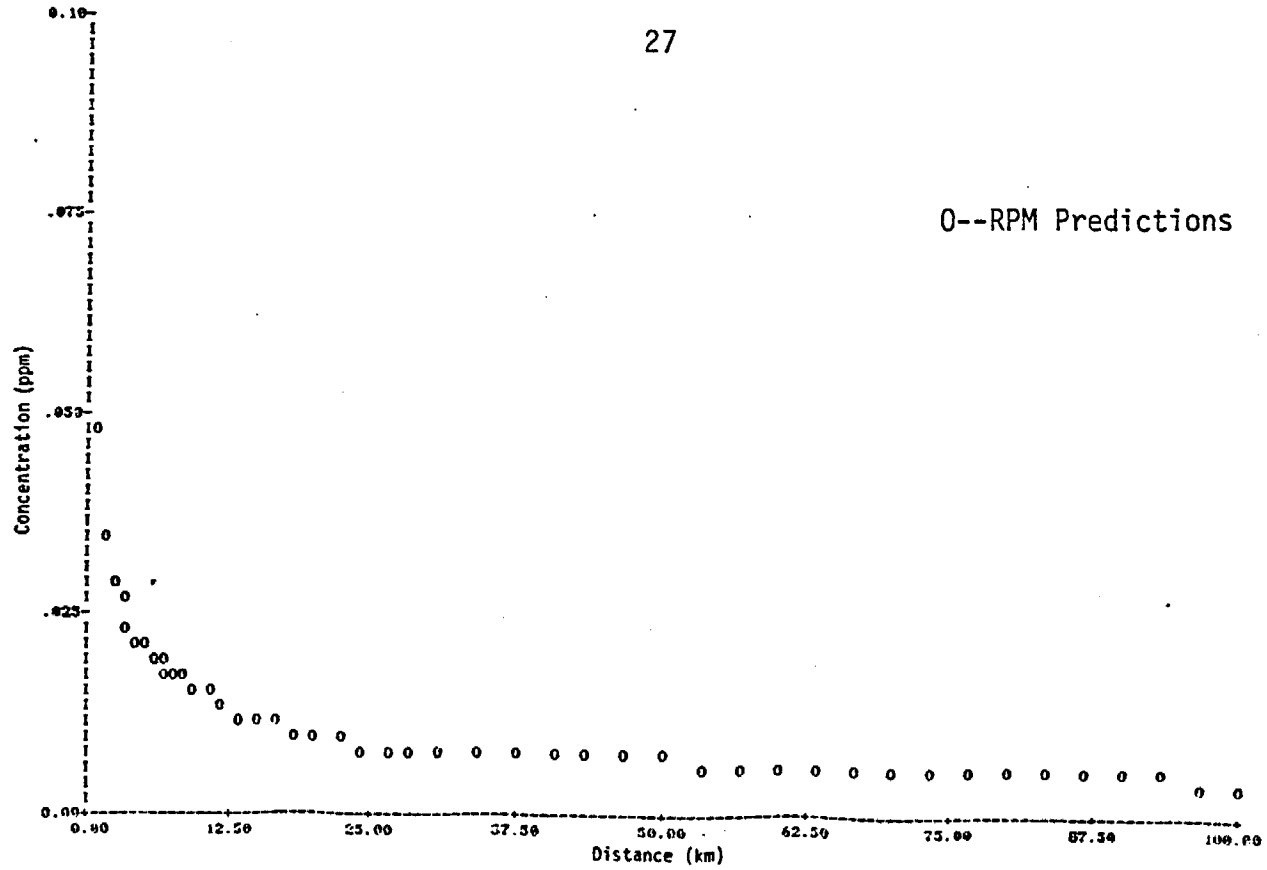

FIGURE II-4c. PREDICTED NO_2 CONCENTRATIONS AT MOSS LANDING ON SEPTEMBER 10, 1974 (1210-1500 HRS) VERSUS DISTANCE FROM THE STACKS.

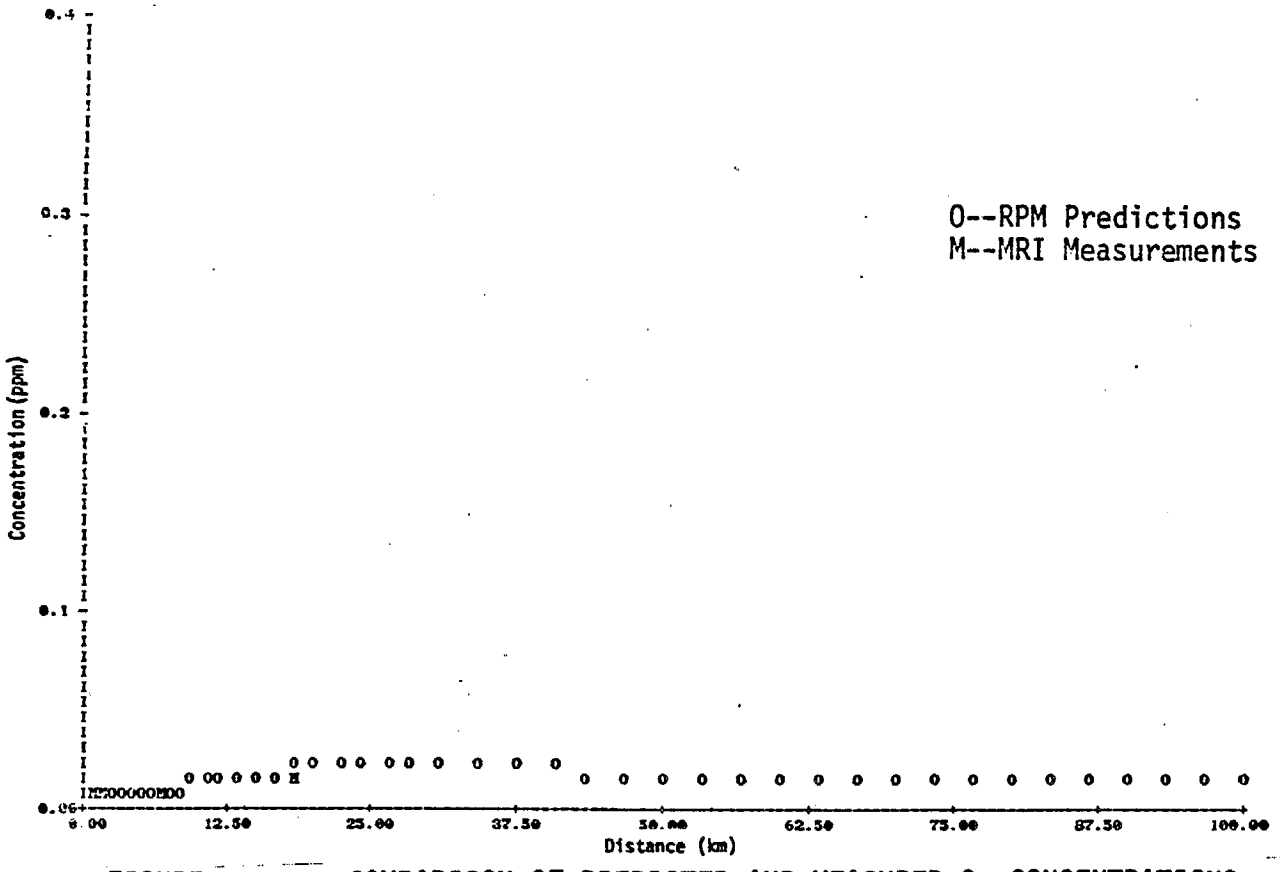

FIGURE II-4d. COMPARISON OF PREDICTED AND MEASURED O_3 CONCENTRATIONS AT MOSS LANDING ON SEPTEMBER 10, 1974 (1210-1500 HRS) VERSUS DISTANCE FROM THE STACKS.

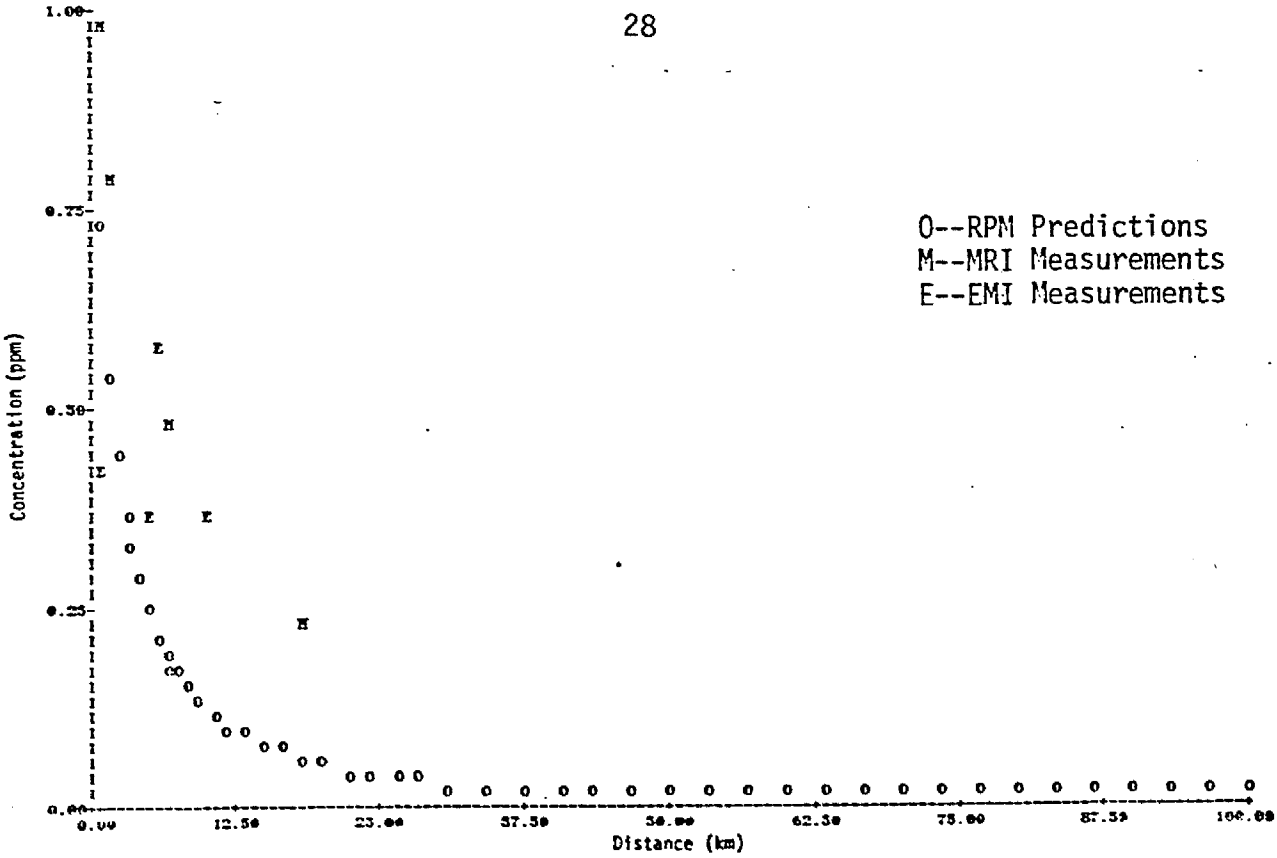

FIGURE II-4e. COMPARISON OF PREDICTED AND MEASURED SO_2 CONCENTRATIONS AT MOSS LANDING ON SEPTEMBER 10, 1974 (1210-1500 HRS) VERSUS DISTANCE FROM THE STACKS.

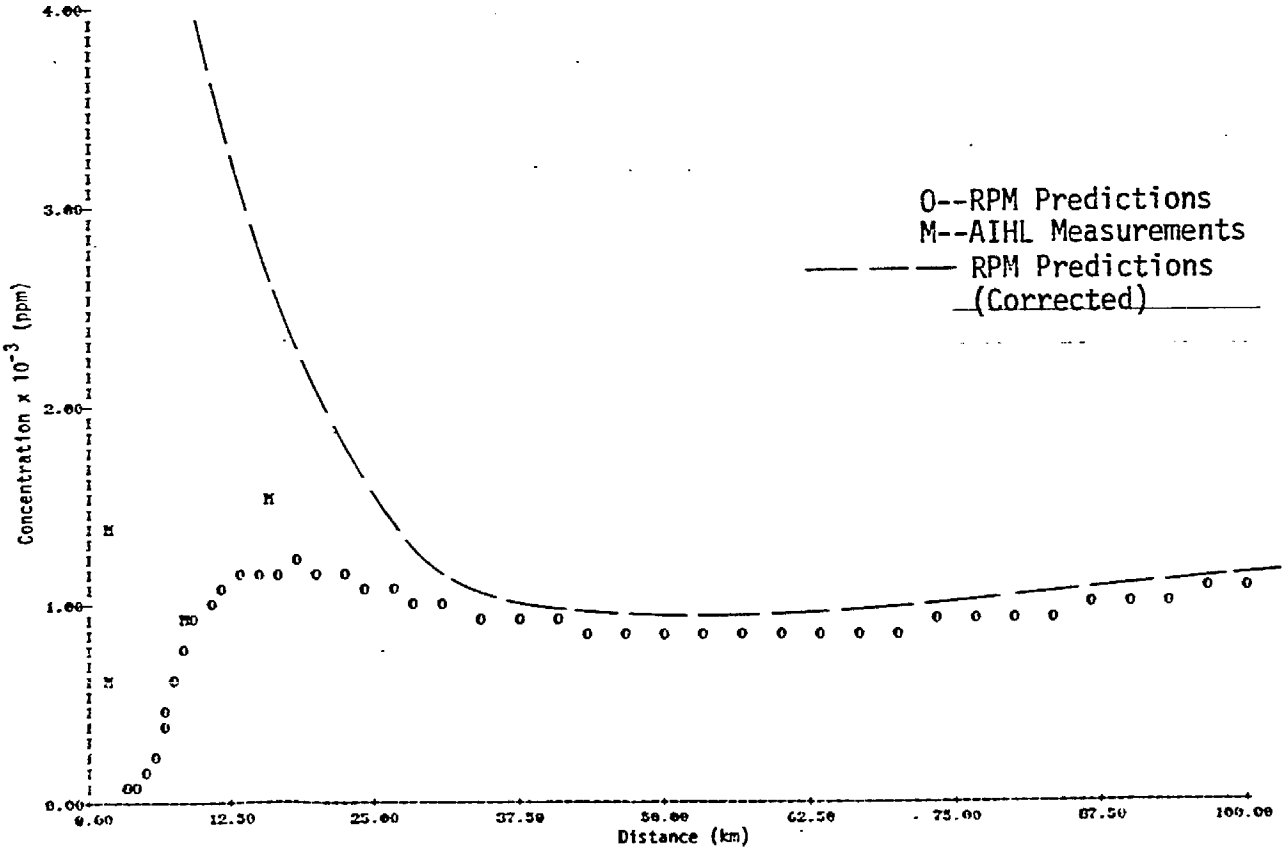

FIGURE II-4f. COMPARISON OF PREDICTED AND MEASURED SO_3 CONCENTRATIONS AT MOSS LANDING ON SEPTEMBER 10, 1974 (1210-1500 HRS) VERSUS DISTANCE FROM THE STACKS.

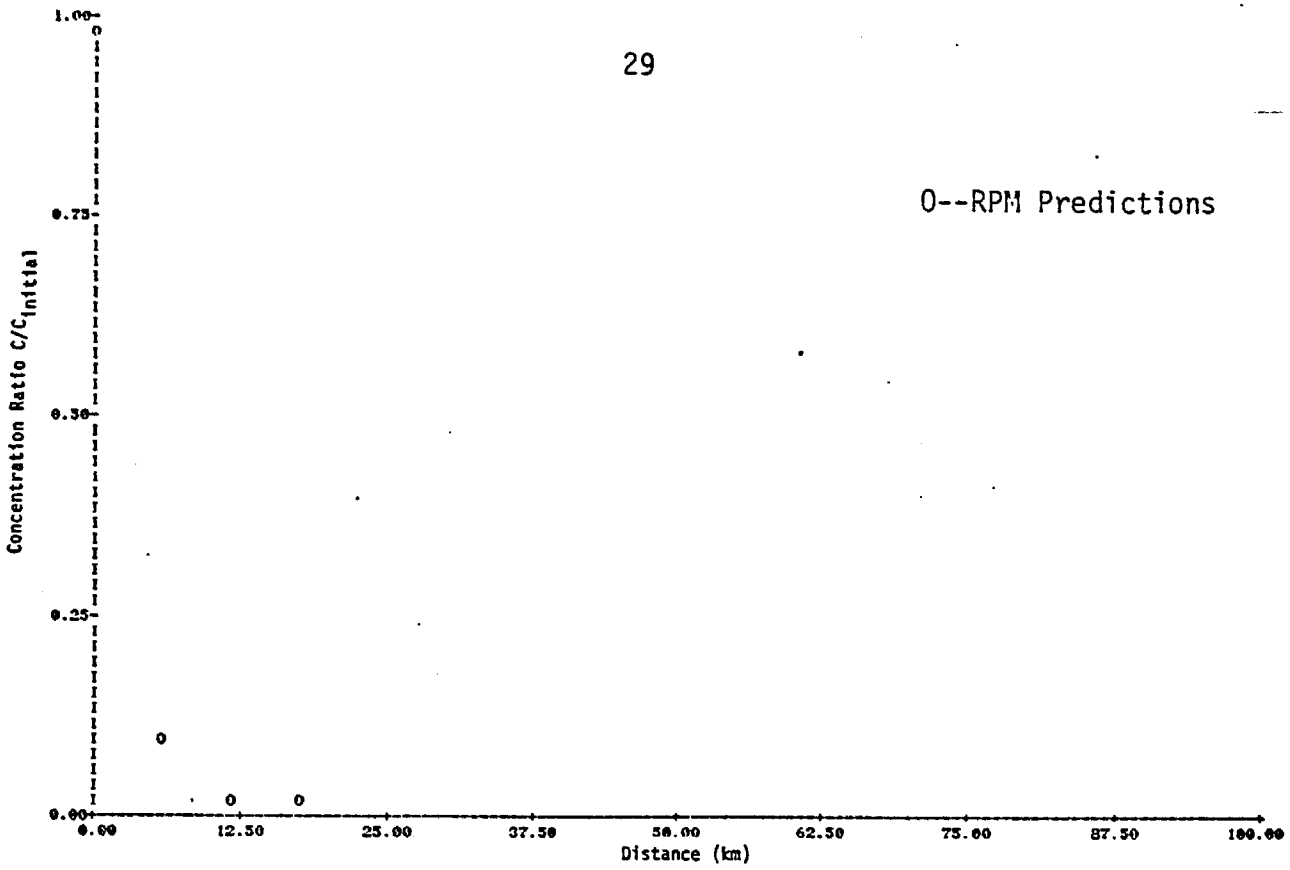

FIGURE II-5a. PREDICTED SF_6 CONCENTRATION RATIOS AT MOSS LANDING ON SEPTEMBER 11, 1974 (1235-1354 HRS) VERSUS DISTANCE FROM THE STACKS.

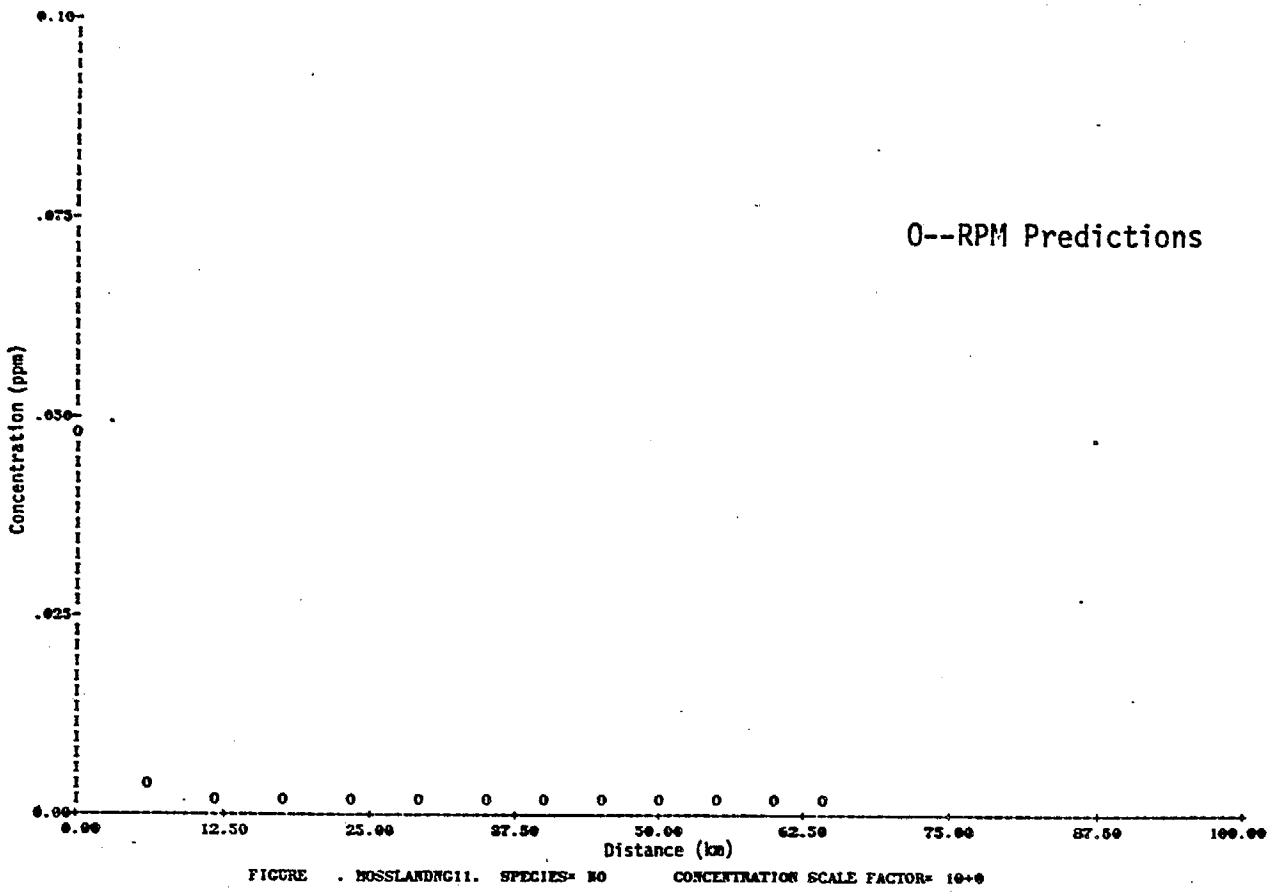

FIGURE II-5b. PREDICTED NO CONCENTRATIONS AT MOSS LANDING ON SEPTEMBER 11, 1974 (1235-1354 HRS) VERSUS DISTANCE FROM THE STACKS

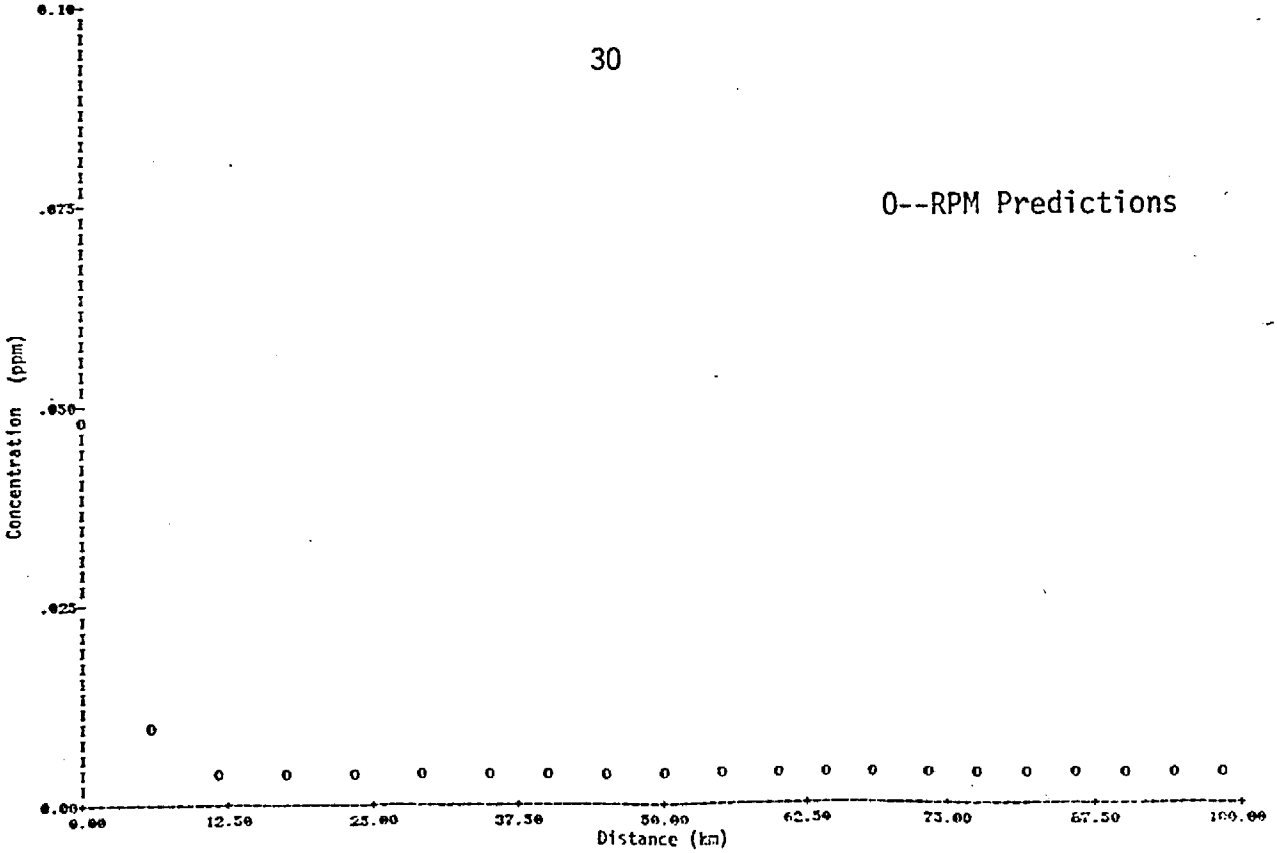

FIGURE II-5c. PREDICTED NO_2 CONCENTRATIONS AT MOSS LANDING ON SEPTEMBER 11, 1974 (1235-1354 HRS) VERSUS DISTANCE FROM THE STACKS.

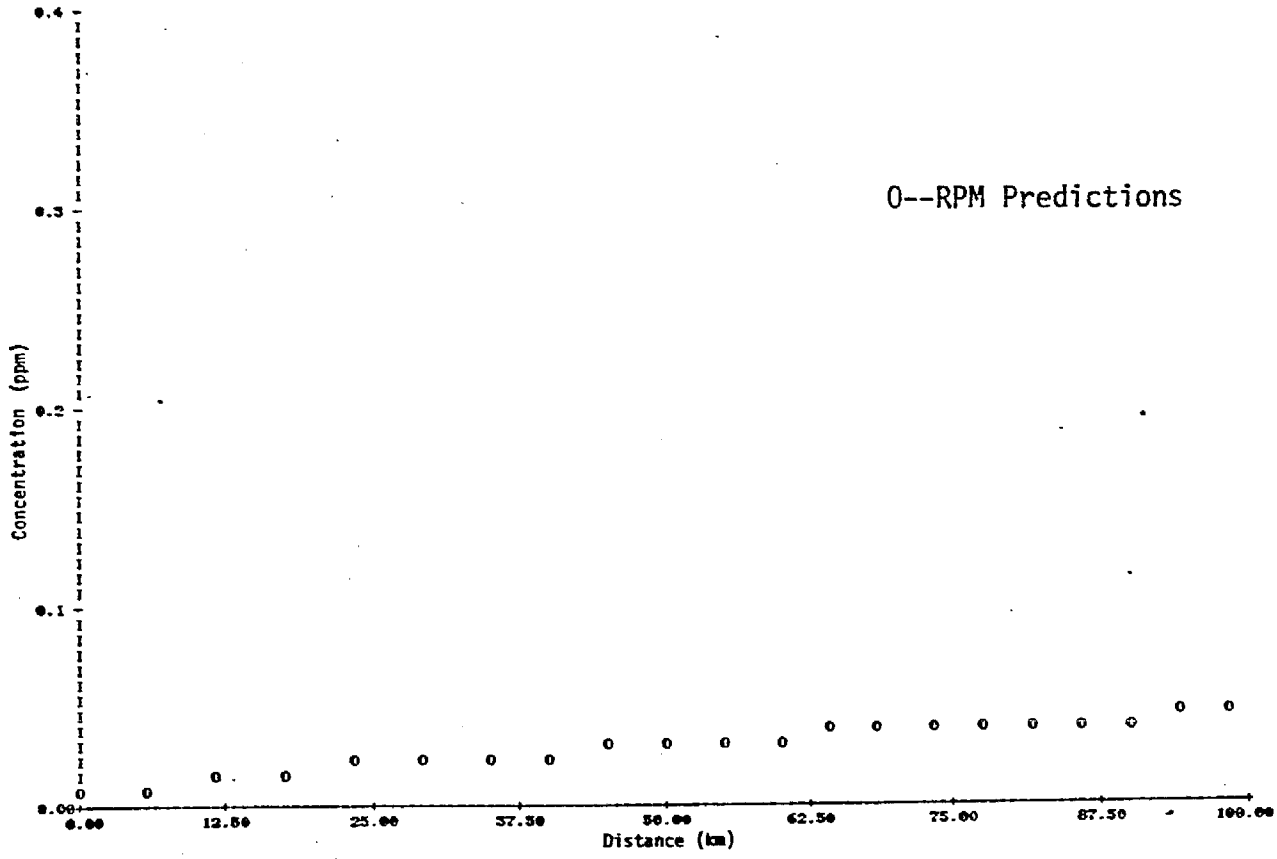

FIGURE II-5d. PREDICTED O_3 CONCENTRATIONS AT MOSS LANDING ON SEPTEMBER 11, 1974 (1235-1354 HRS) VERSUS DISTANCE FROM THE STACKS.

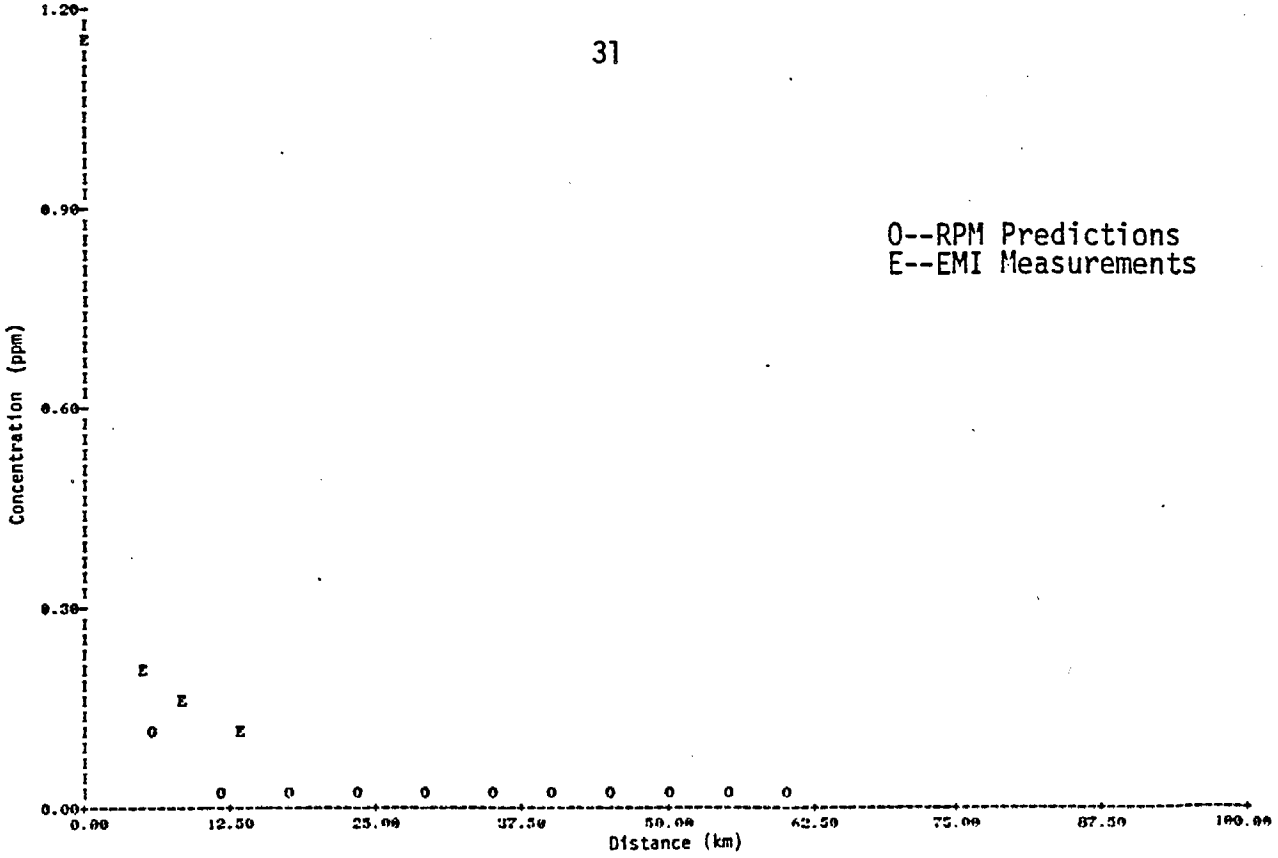

FIGURE II-5e. COMPARISON OF PREDICTED AND MEASURED SO_2 CONCENTRATIONS AT MOSS LANDING ON SEPTEMBER 11, 1974 (1235-1354 HRS) VERSUS DISTANCE FROM THE STACKS.

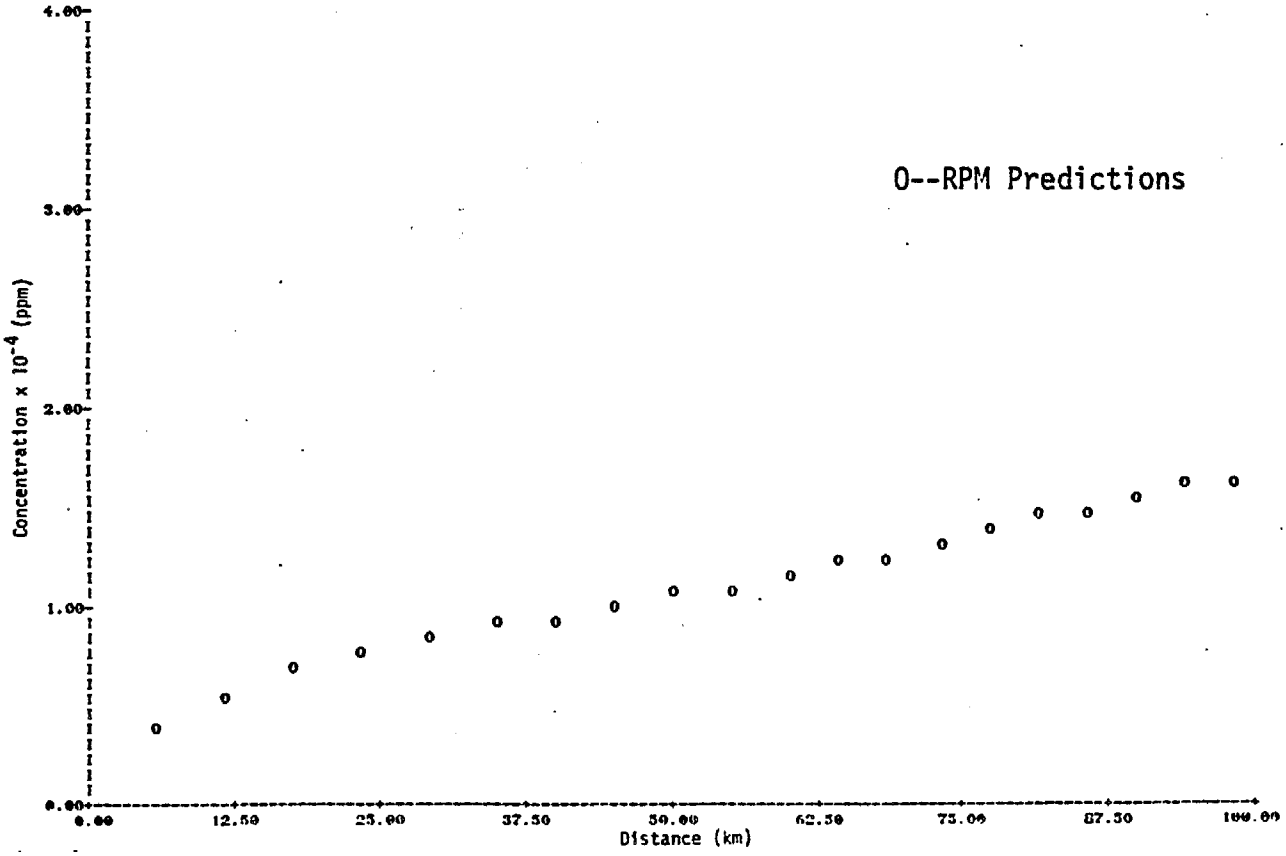

FIGURE II-5f. PREDICTED SO_3 CONCENTRATIONS AT MOSS LANDING ON SEPTEMBER 11, 1974 (1235-1354 HRS) VERSUS DISTANCE FROM THE STACKS.

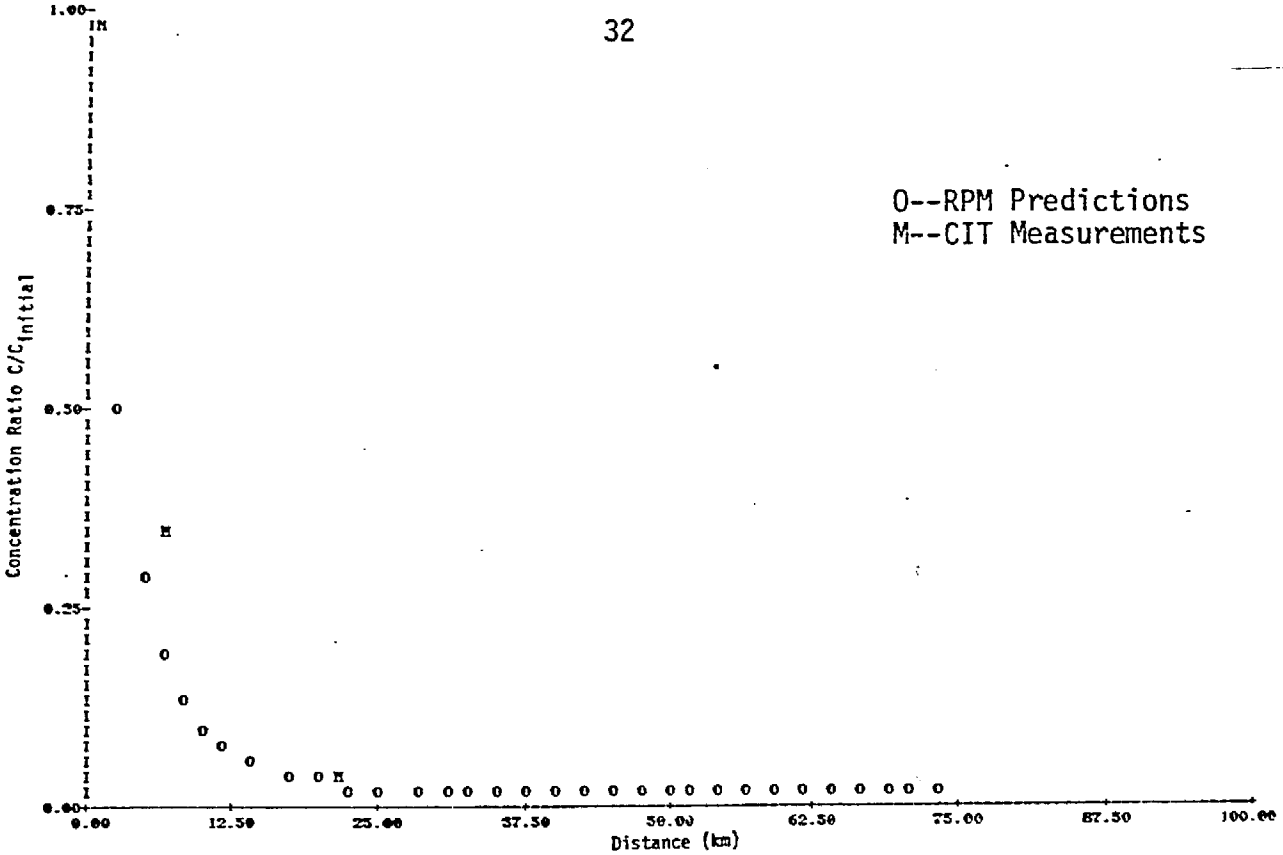

FIGURE II-6a. COMPARISON OF PREDICTED AND MEASURED SF_6 CONCENTRATION RATIOS AT HAYNES ON OCTOBER 1, 1974 (1415-1600 HRS) VERSUS DISTANCE FROM THE STACKS.

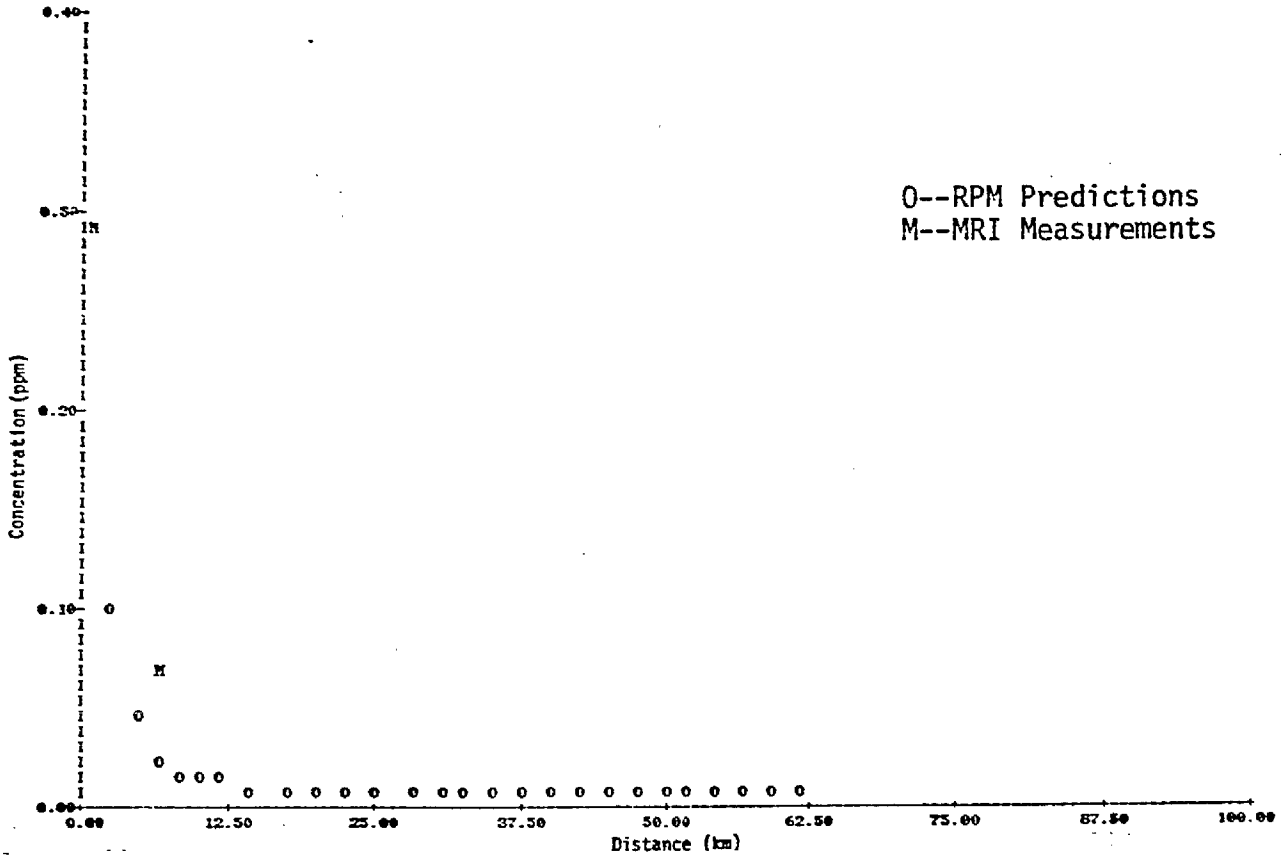

FIGURE II-6b. COMPARISON OF PREDICTED AND MEASURED NO CONCENTRATIONS AT HAYNES ON OCTOBER 1, 1974 (1415-1600 HRS) VERSUS DISTANCE FROM THE STACKS.

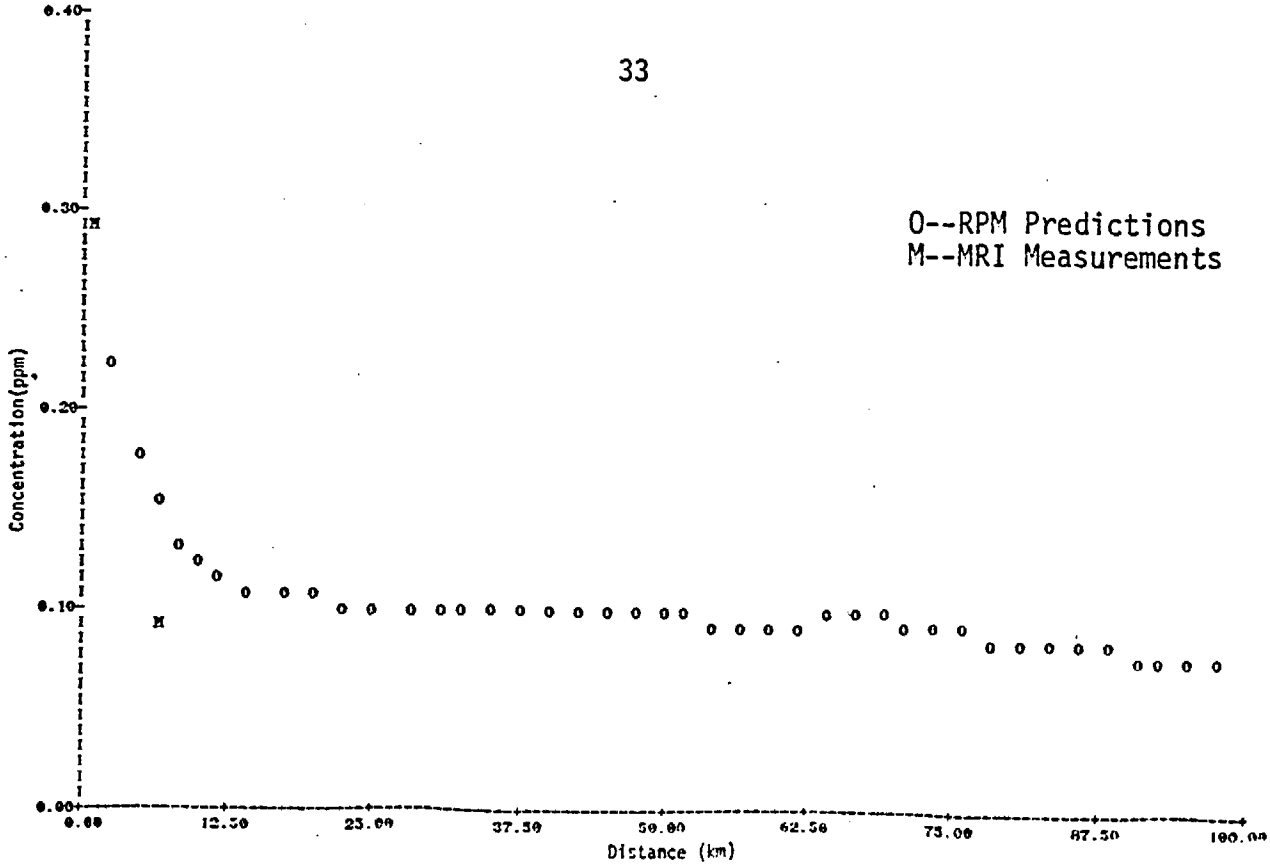

FIGURE II-6c. COMPARISON OF PREDICTED AND MEASURED NO_2 CONCENTRATIONS AT HAYNES ON OCTOBER 1, 1974 (1415-1600 HRS) VERSUS DISTANCE FROM THE STACKS.

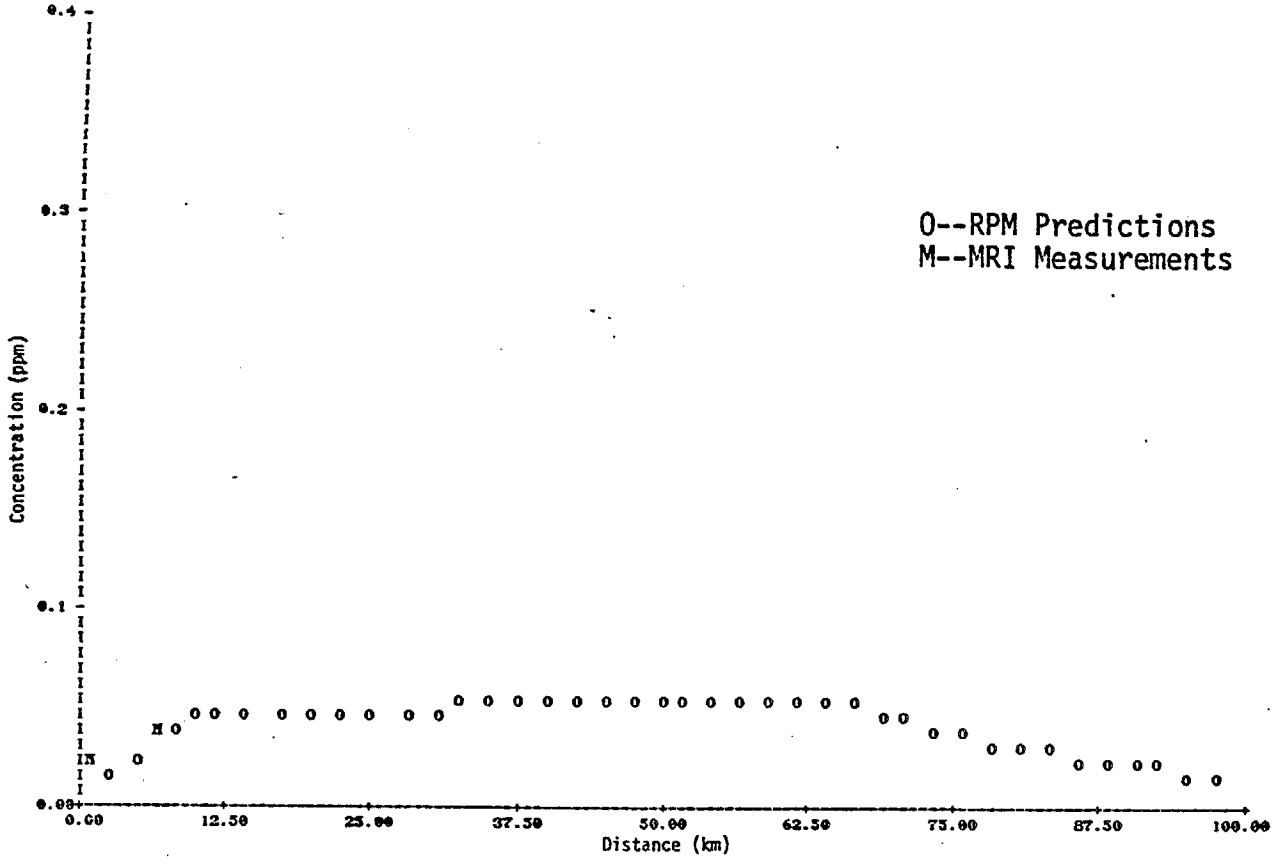

FIGURE II-6d. COMPARISON OF PREDICTED AND MEASURED O_3 CONCENTRATIONS AT HAYNES ON OCTOBER 1, 1974 (1415-1600 HRS) VERSUS DISTANCE FROM THE STACKS.

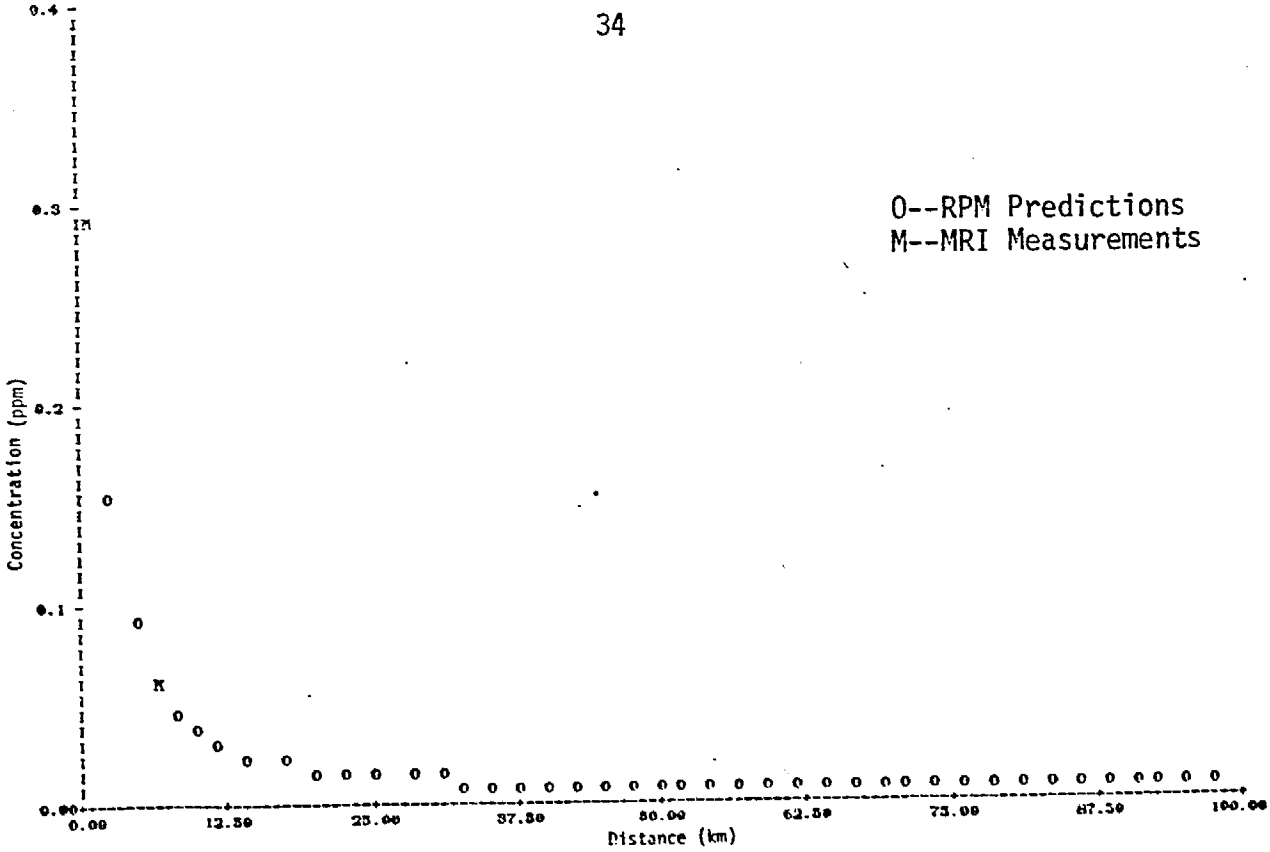

FIGURE II-6e. COMPARISON OF PREDICTED AND MEASURED SO_2 CONCENTRATIONS AT HAYNES ON OCTOBER 1, 1974 (1415-1600 HRS) VERSUS DISTANCE FROM THE STACKS.

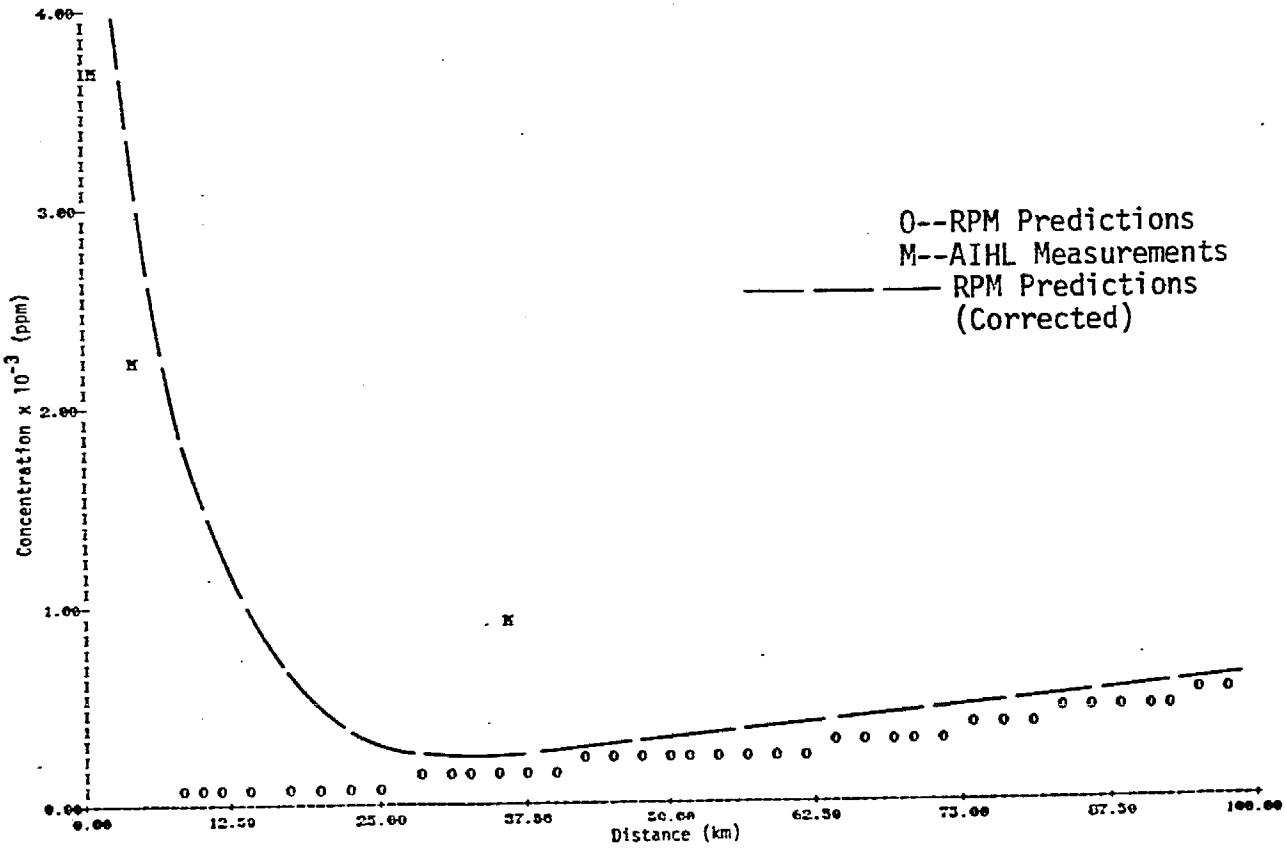

FIGURE II-6f. COMPARISON OF PREDICTED AND MEASURED SO_3 CONCENTRATIONS AT HAYNES ON OCTOBER 1, 1974 (1415-1600 HRS) VERSUS DISTANCE FROM THE STACKS.

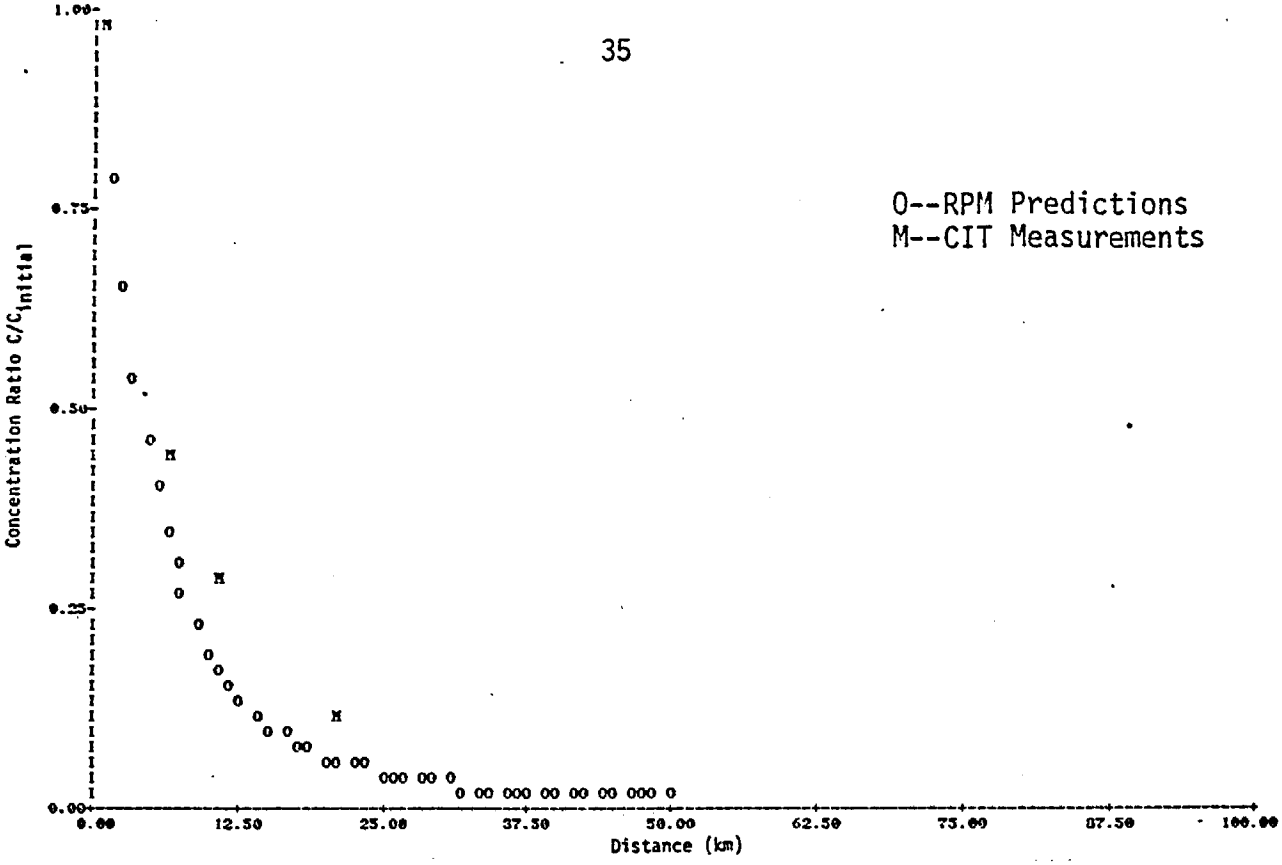

FIGURE II-7a. COMPARISON OF PREDICTED AND MEASURED SF_6 CONCENTRATION RATIOS AT HAYNES ON OCTOBER 11, 1974 (1350-1540 HRS) VERSUS DISTANCE FROM THE STACKS.

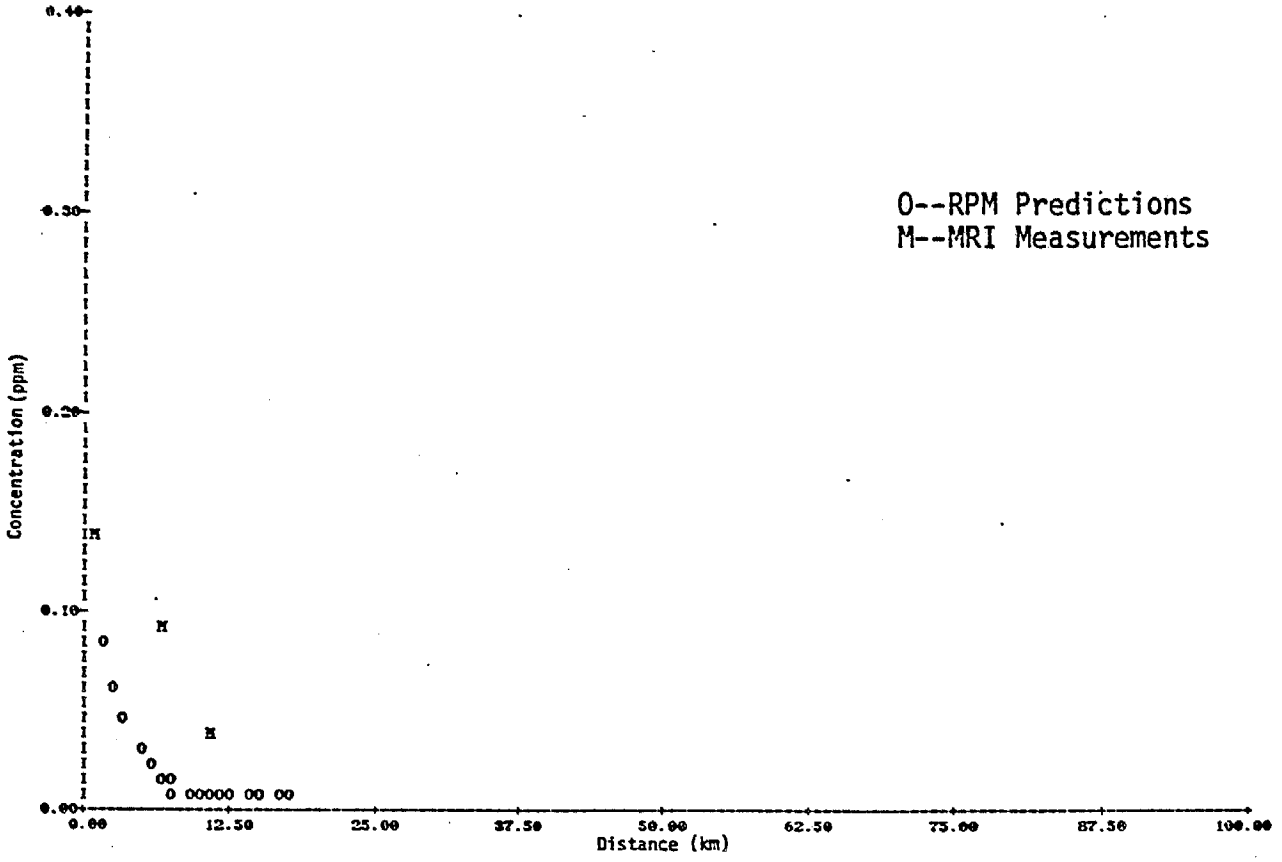

FIGURE II-7b. COMPARISON OF PREDICTED AND MEASURED NO CONCENTRATIONS AT HAYNES ON OCTOBER 11, 1974 (1350-1540 HRS) VERSUS DISTANCE FROM THE STACKS.

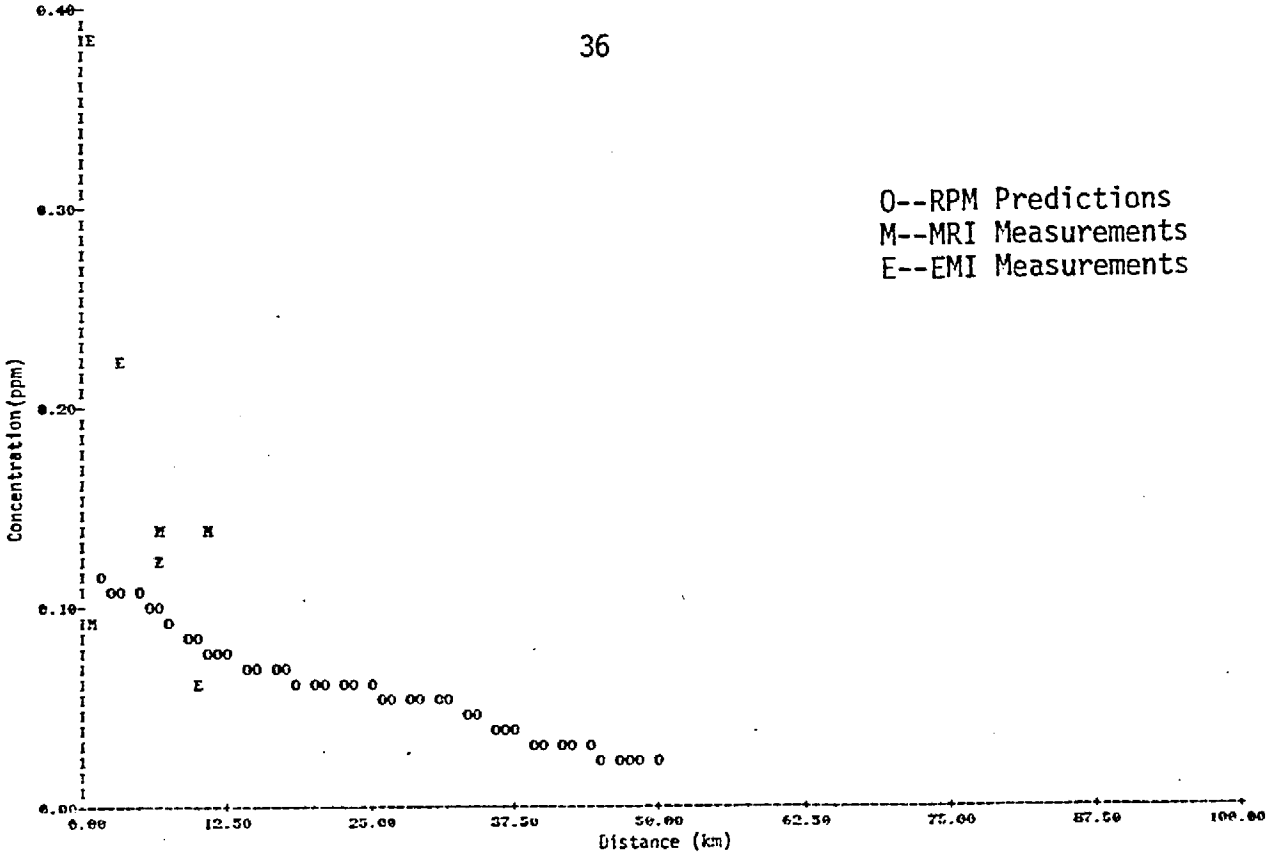

FIGURE II-7c. COMPARISON OF PREDICTED AND MEASURED NO_2 CONCENTRATIONS AT HAYNES ON OCTOBER 11, 1974 (1350-1540 HRS) VERSUS DISTANCE FROM THE STACKS.

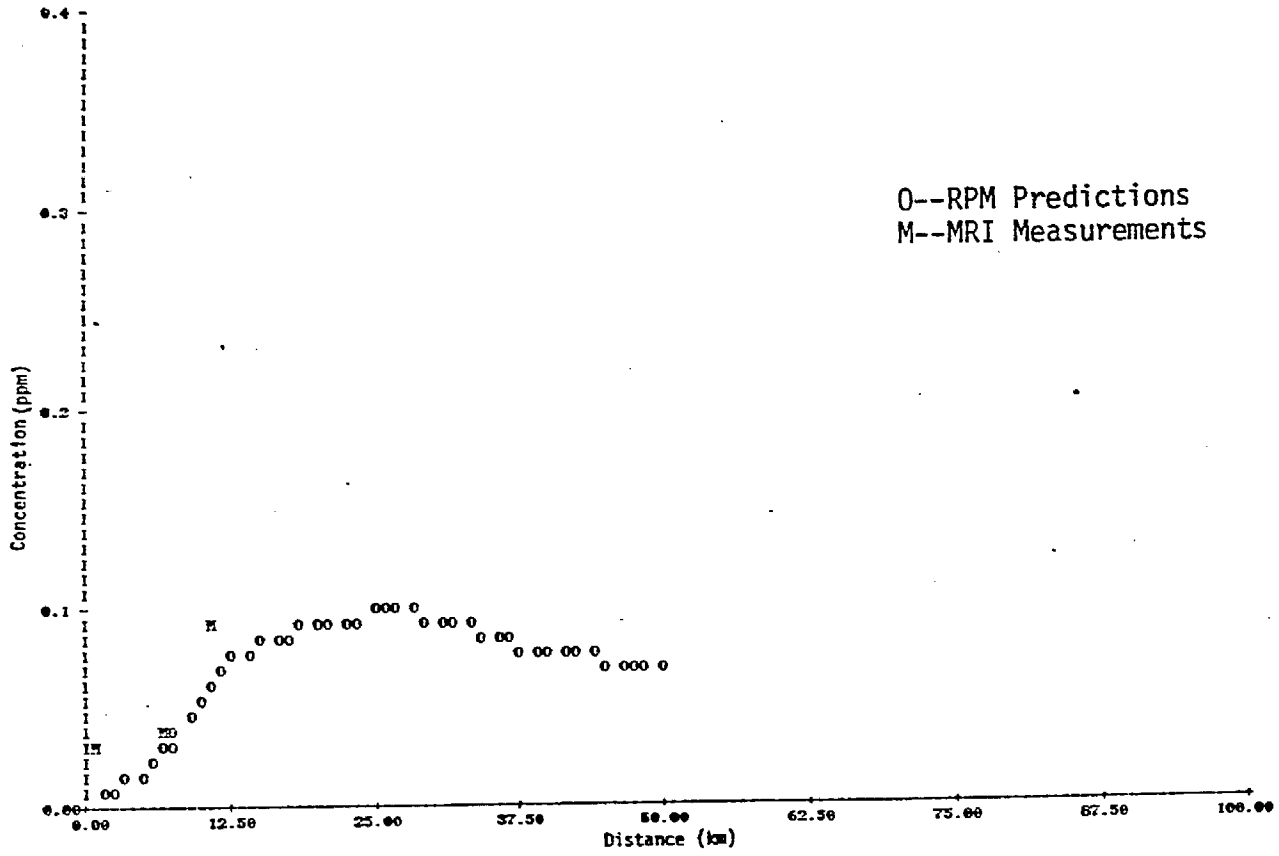

FIGURE II-7d. COMPARISON OF PREDICTED AND MEASURED O_3 CONCENTRATIONS AT HAYNES ON OCTOBER 11, 1974 (1350-1540 HRS) VERSUS DISTANCE FROM THE STACKS.

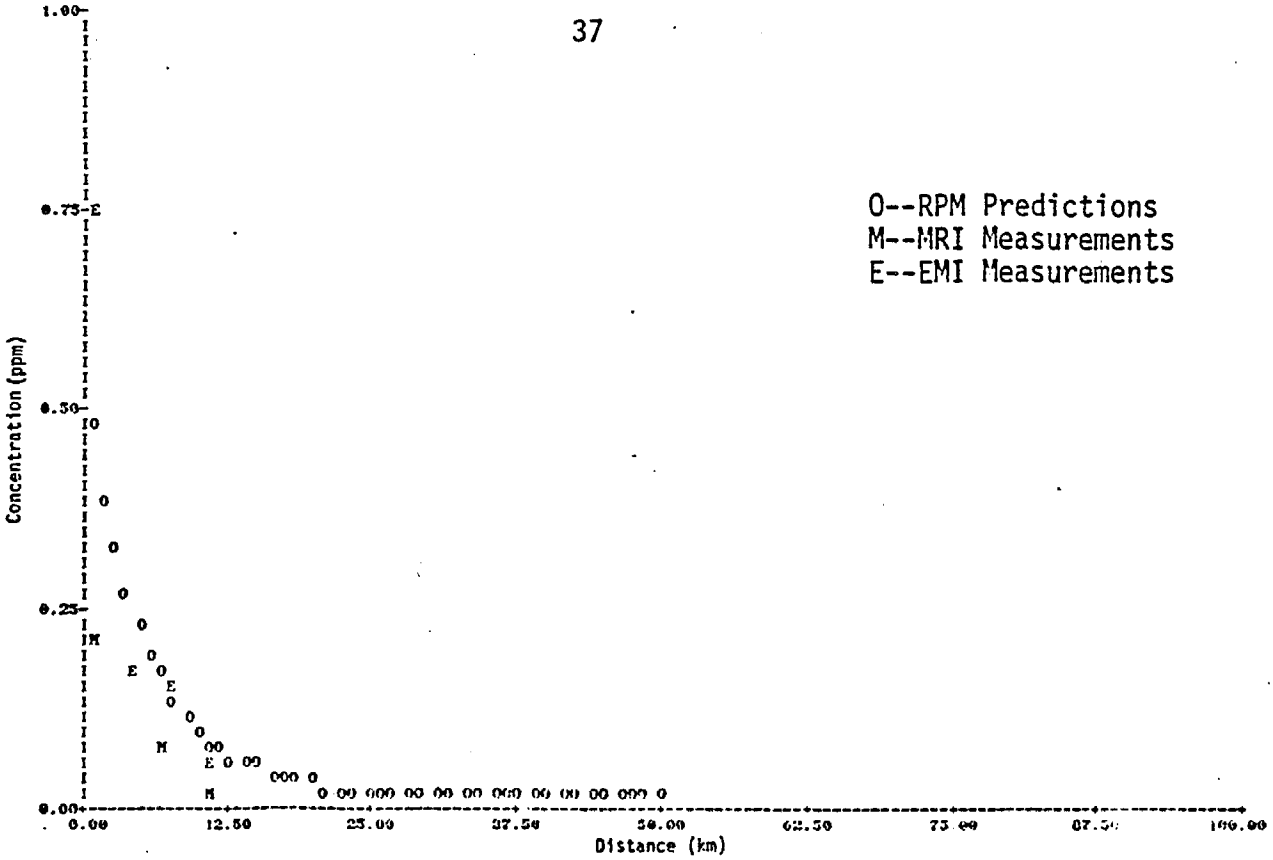

FIGURE II-7e. COMPARISON OF PREDICTED AND MEASURED SO_2 CONCENTRATIONS AT HAYNES ON OCTOBER 11, 1974 (1350-1540 HRS) VERSUS DISTANCE FROM THE STACKS.

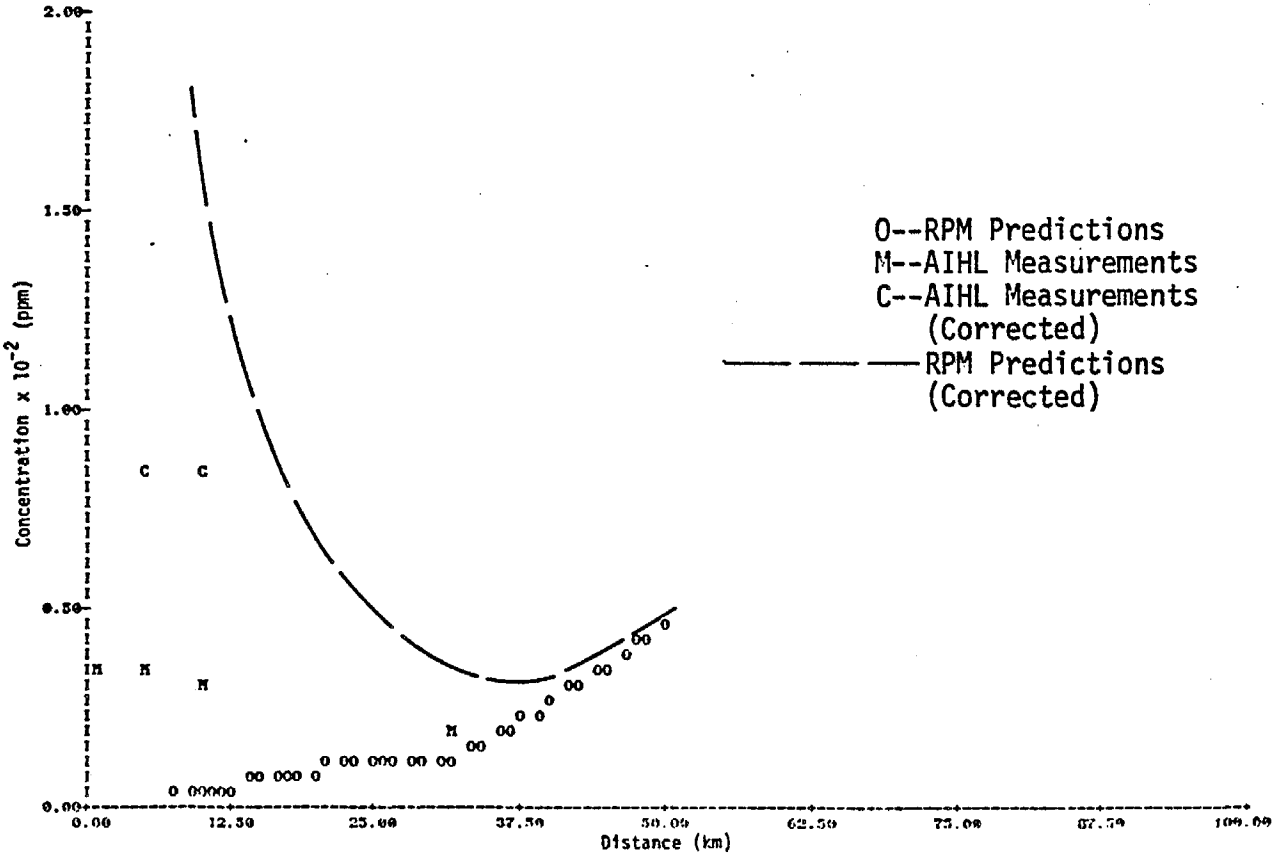

FIGURE II-7f. COMPARISON OF PREDICTED AND MEASURED SO_3 CONCENTRATIONS AT HAYNES ON OCTOBER 11, 1974 (1350-1540 HRS) VERSUS DISTANCE FROM THE STACKS.

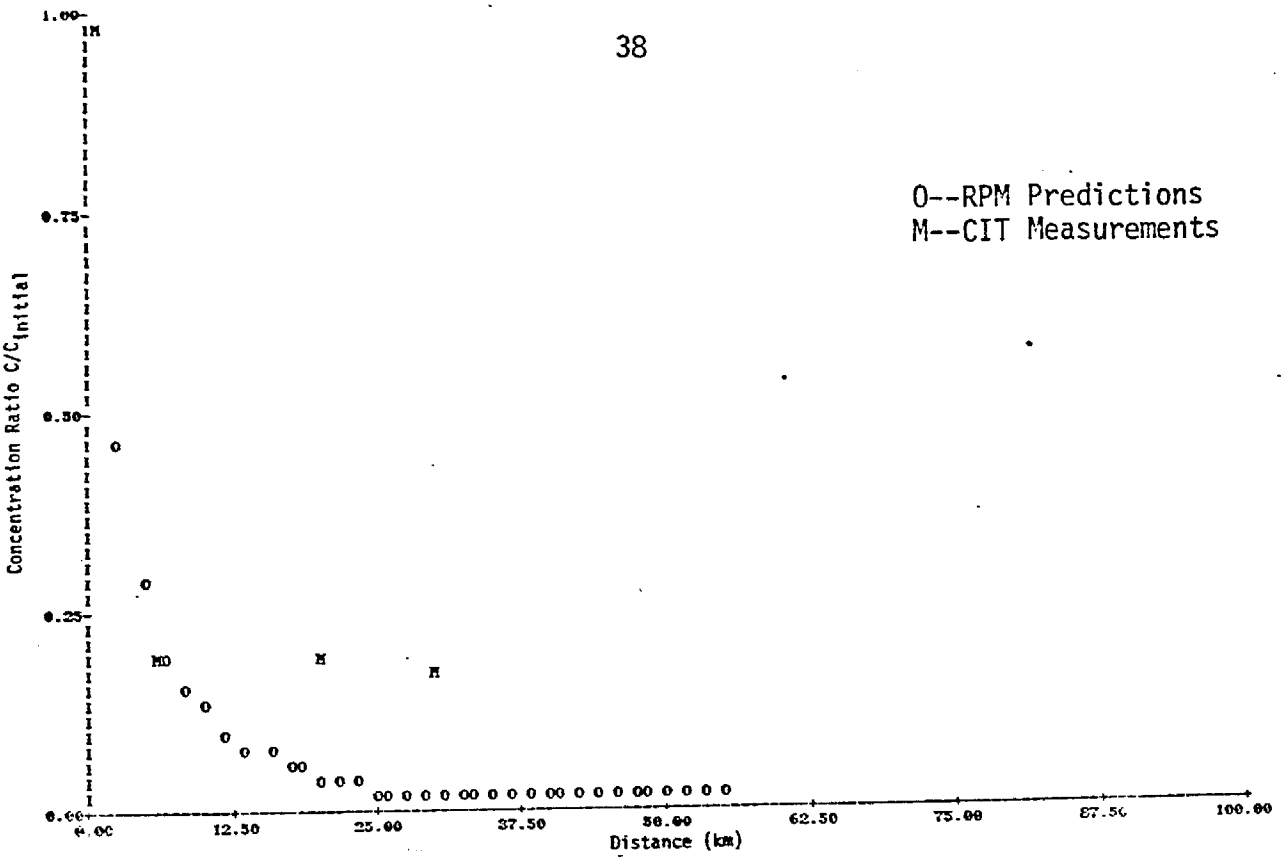

FIGURE II-8a. COMPARISON OF PREDICTED AND MEASURED SF_6 CONCENTRATION RATIOS AT HAYNES ON OCTOBER 17, 1974 (1500-1730 HRS) VERSUS DISTANCE FROM THE STACKS

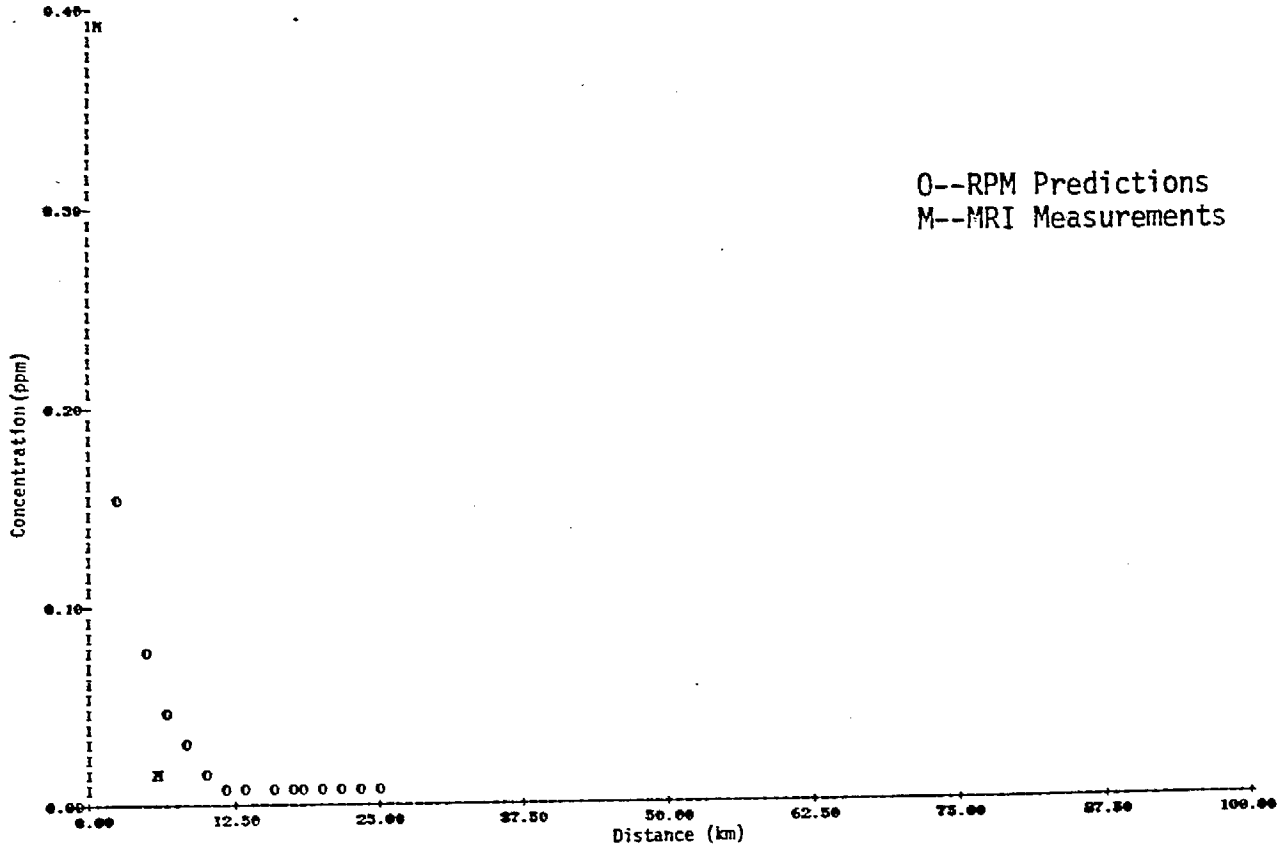

FIGURE II-8b. COMPARISON OF PREDICTED AND MEASURED NO CONCENTRATIONS AT HAYNES ON OCTOBER 17, 1974 (1500-1730 HRS) VERSUS DISTANCE FROM THE STACKS.

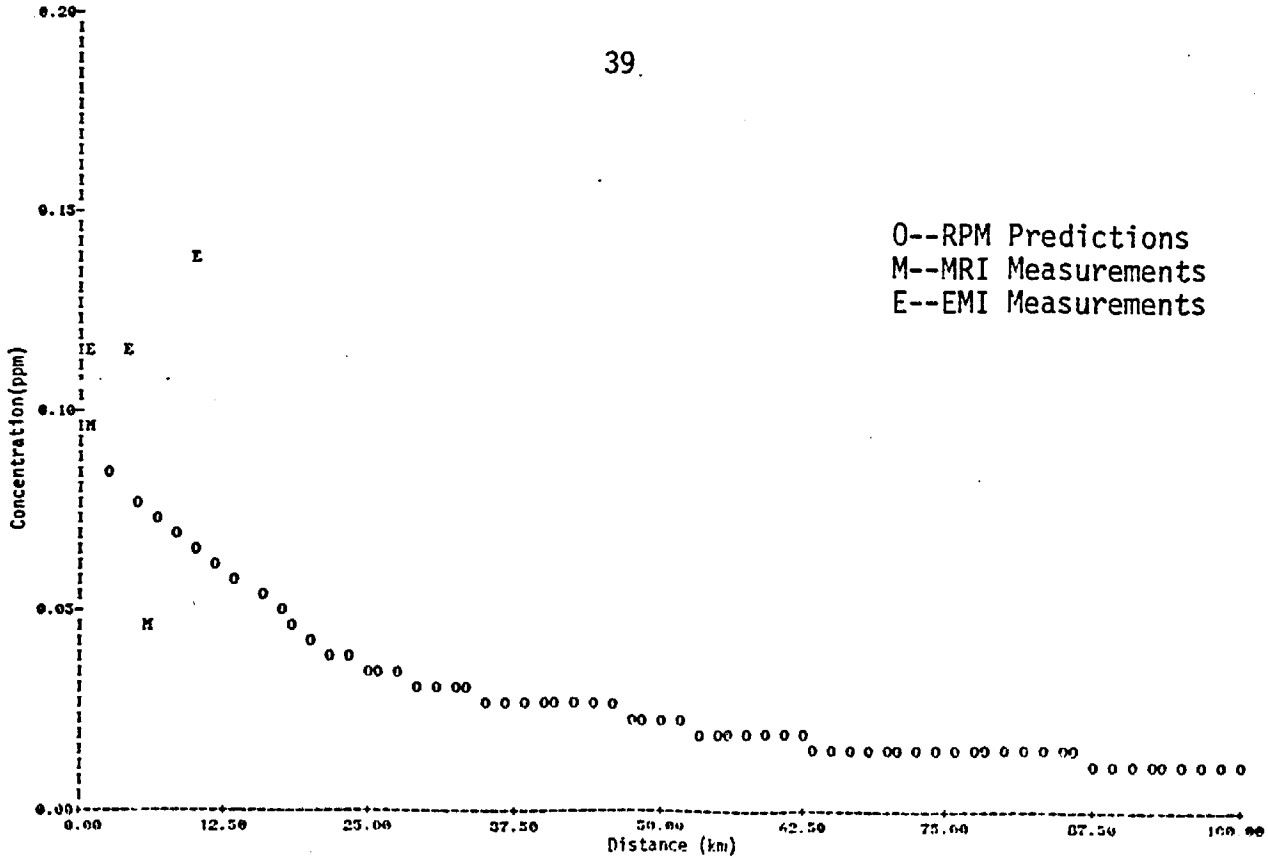

FIGURE II-8c. COMPARISON OF PREDICTED AND MEASURED NO_2 CONCENTRATIONS AT HAYNES ON OCTOBER 17, 1974 (1500-1730 HRS) VERSUS DISTANCE FROM THE STACKS.

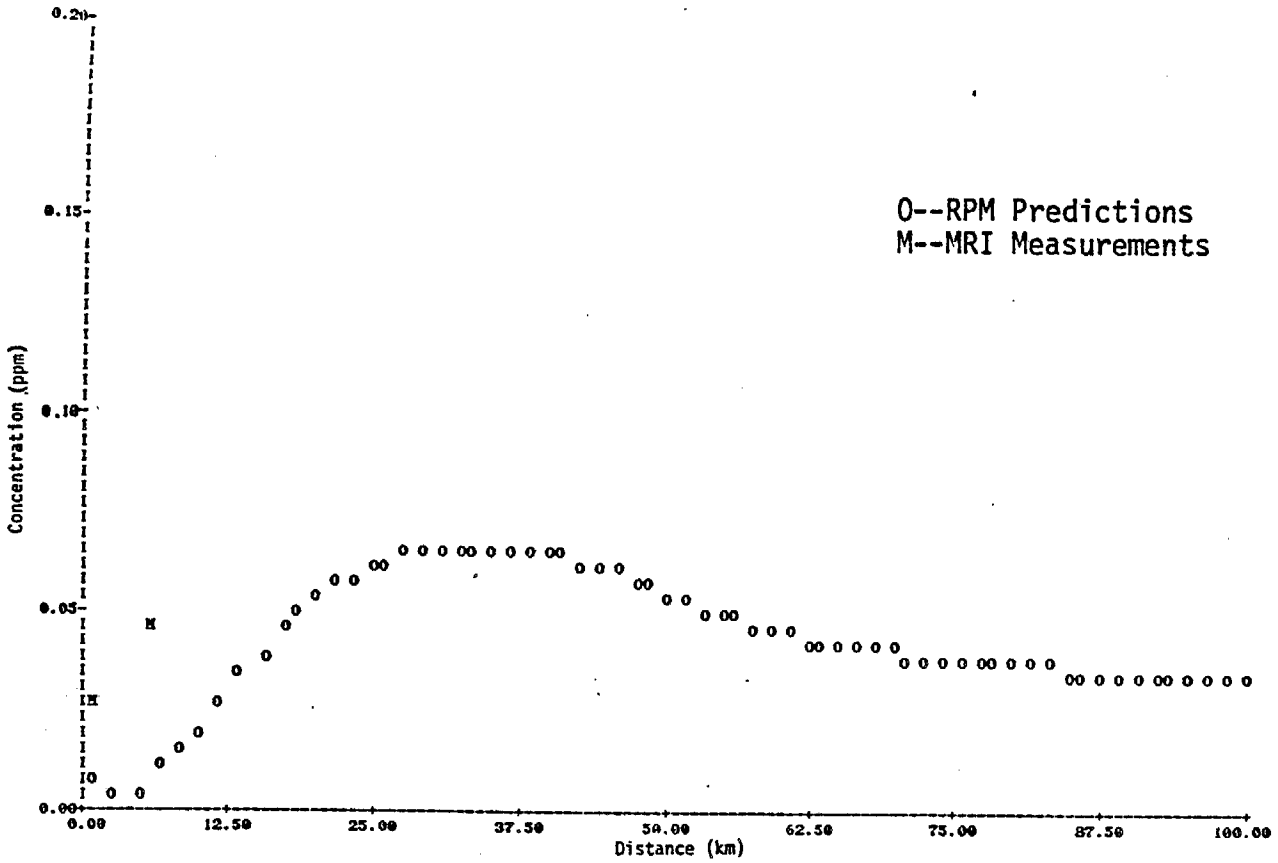

FIGURE II-8d. COMPARISON OF PREDICTED AND MEASURED O_3 CONCENTRATIONS AT HAYNES ON OCTOBER 17, 1974 (1500-1730 HRS) VERSUS DISTANCE FROM THE STACKS.

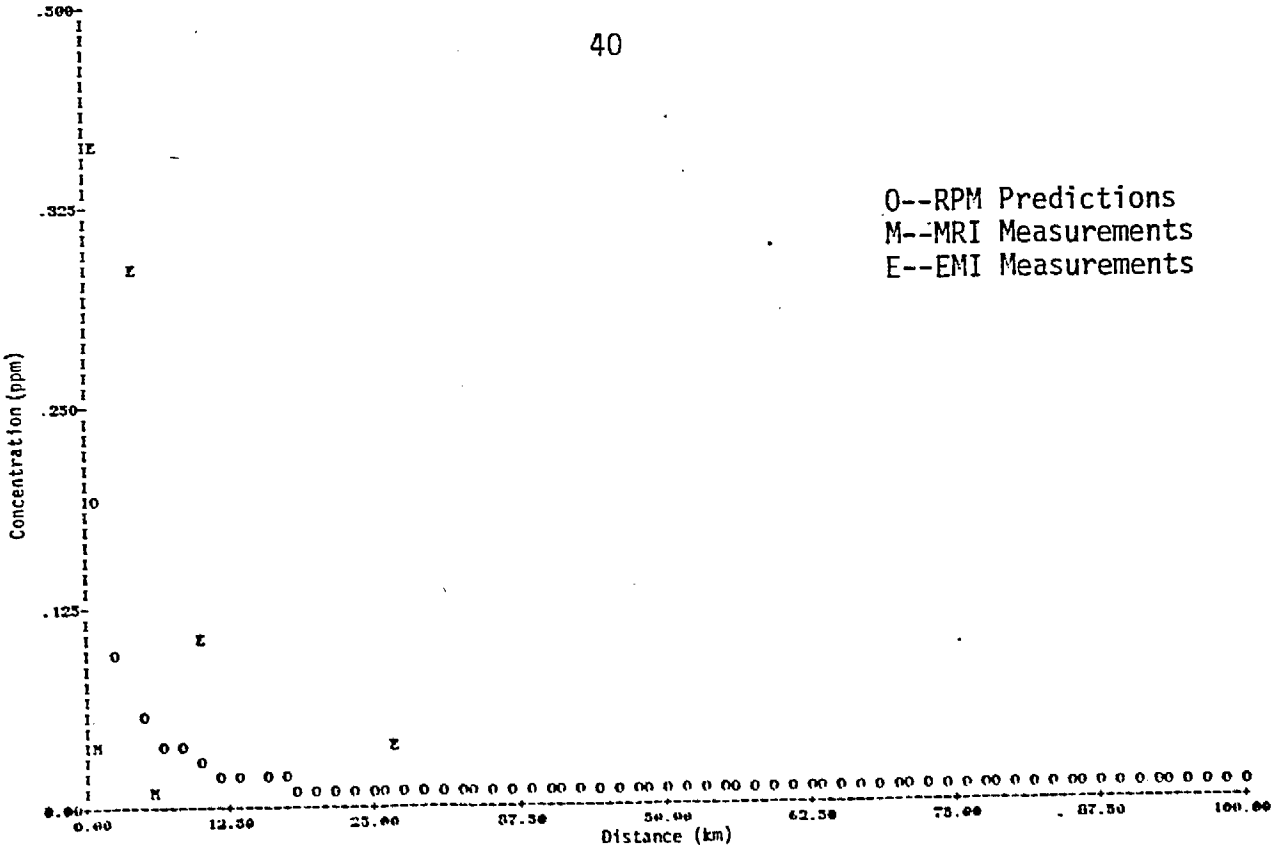

FIGURE II-8e. COMPARISON OF PREDICTED AND MEASURED SO_2 CONCENTRATIONS AT HAYNES ON OCTOBER 17, 1974 (1500-1730 HRS) VERSUS DISTANCE FROM THE STACKS.

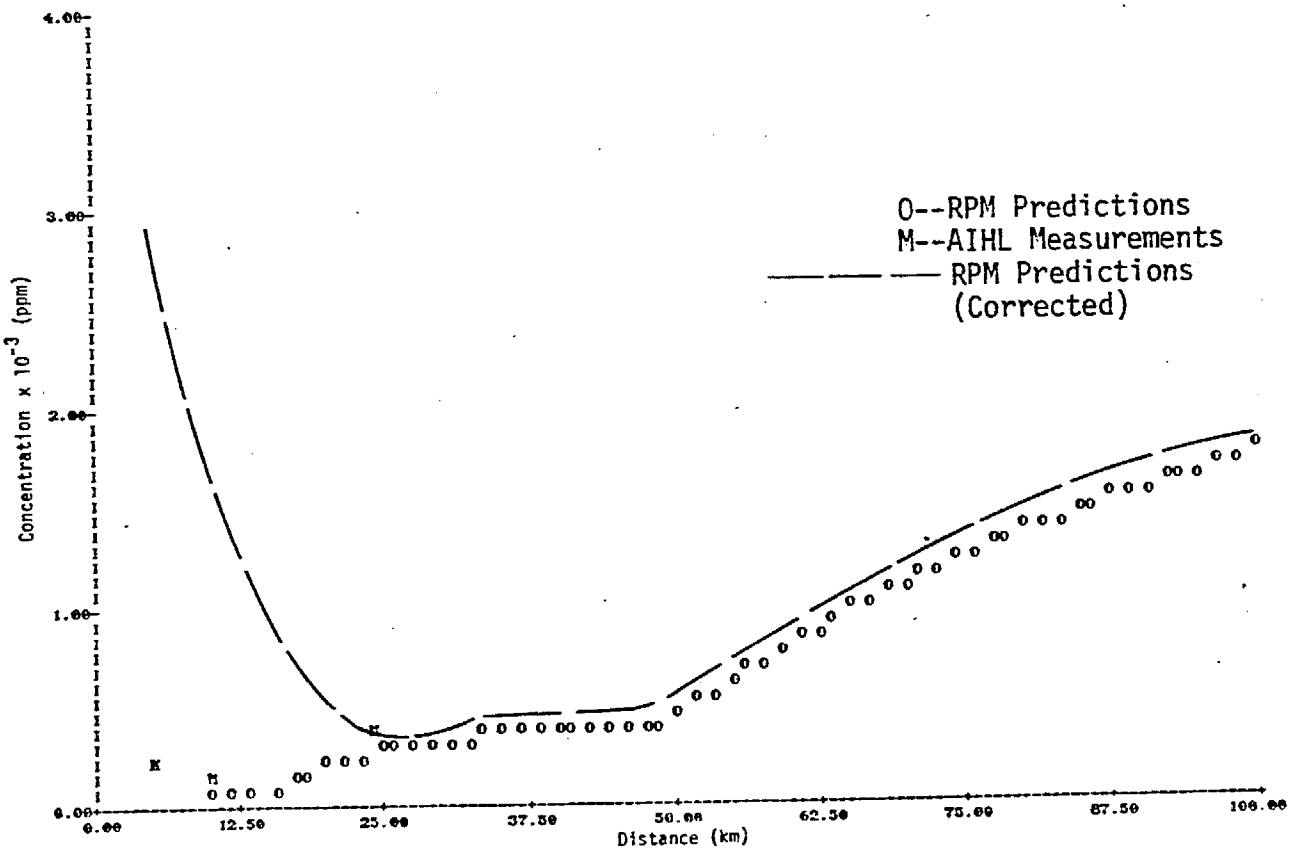

FIGURE II-8f. COMPARISON OF PREDICTED AND MEASURED SO_3 CONCENTRATIONS AT HAYNES ON OCTOBER 17, 1974 (1500-1730 HRS) VERSUS DISTANCE FROM THE STACKS.

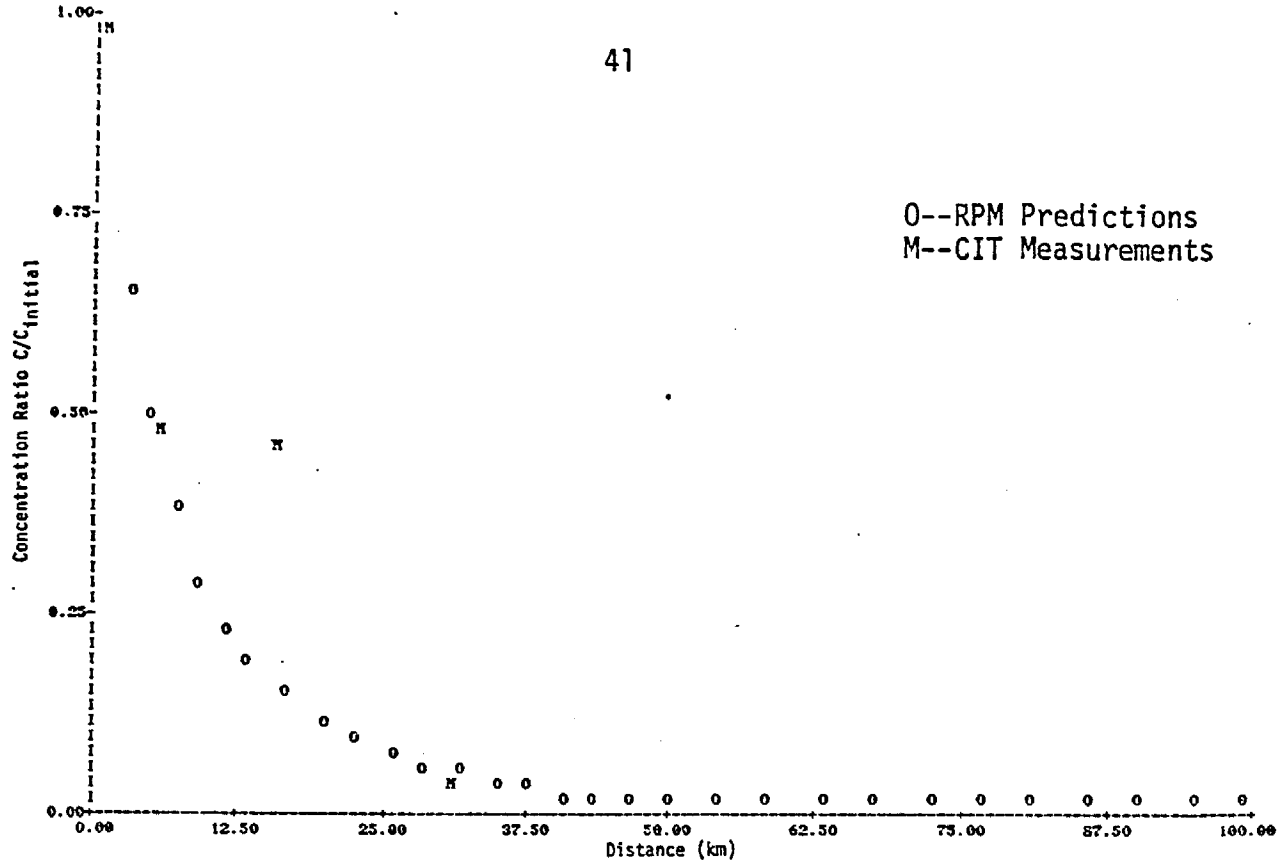

FIGURE II-9a. COMPARISON OF PREDICTED AND MEASURED SF_6 CONCENTRATION RATIOS AT LOS ALAMITOS ON OCTOBER 25, 1974 (1340-1530 HRS) VERSUS DISTANCE FROM THE STACKS.

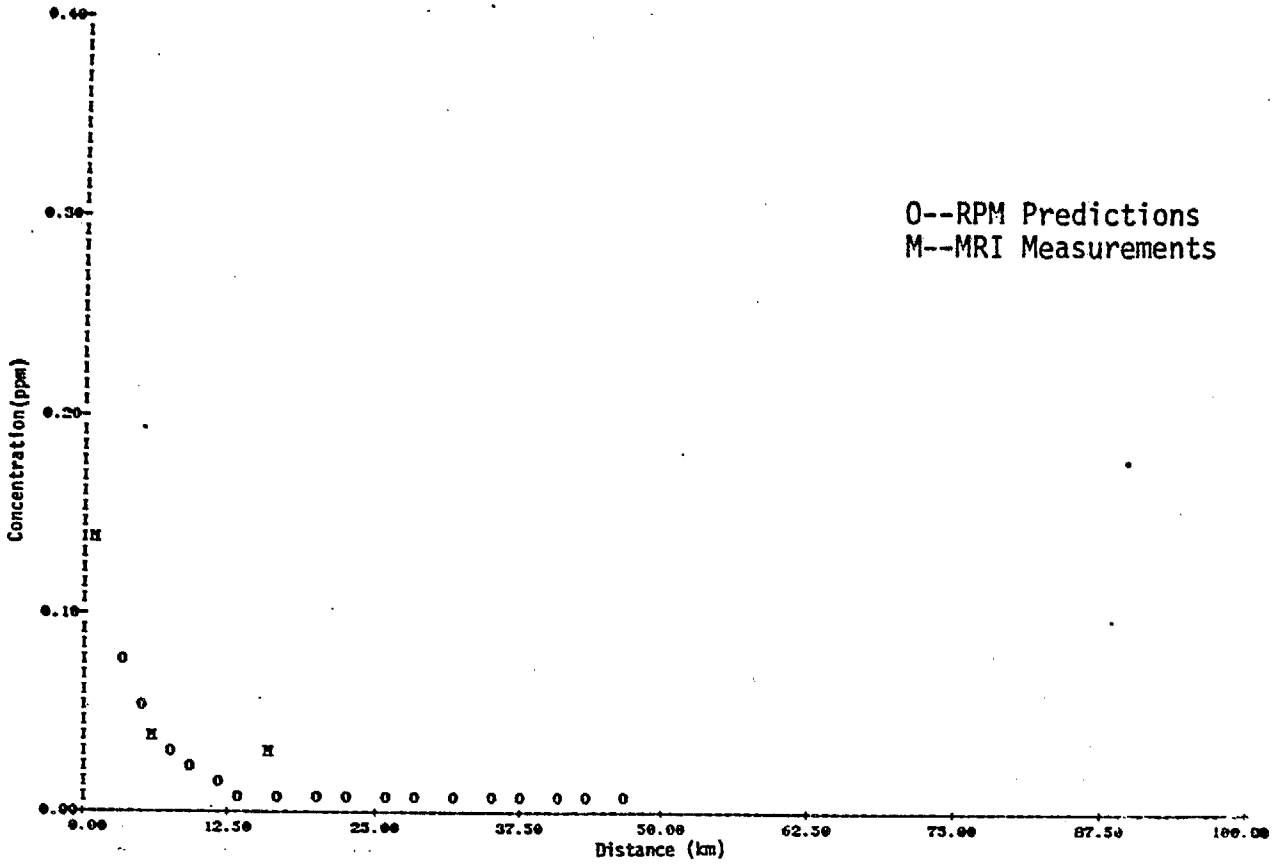

FIGURE II-9b. COMPARISON OF PREDICTED AND MEASURED NO CONCENTRATIONS AT LOS ALAMITOS ON OCTOBER 25, 1974 (1340-1530 HRS) VERSUS DISTANCE FROM THE STACKS.

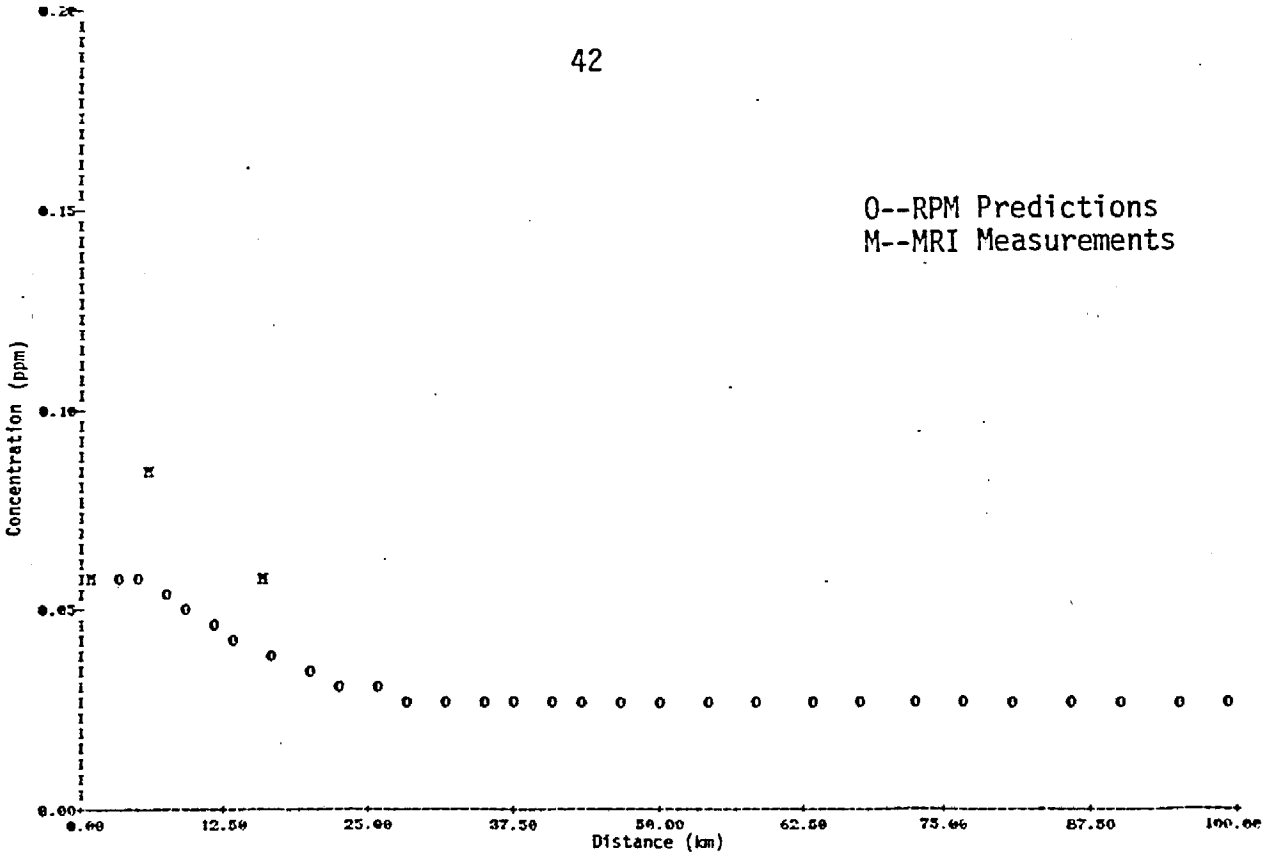

FIGURE II-9c. COMPARISON OF PREDICTED AND MEASURED NO_2 CONCENTRATIONS AT LOS ALAMITOS ON OCTOBER 25, 1974 (1340-1530 HRS) VERSUS DISTANCE FROM THE STACKS.

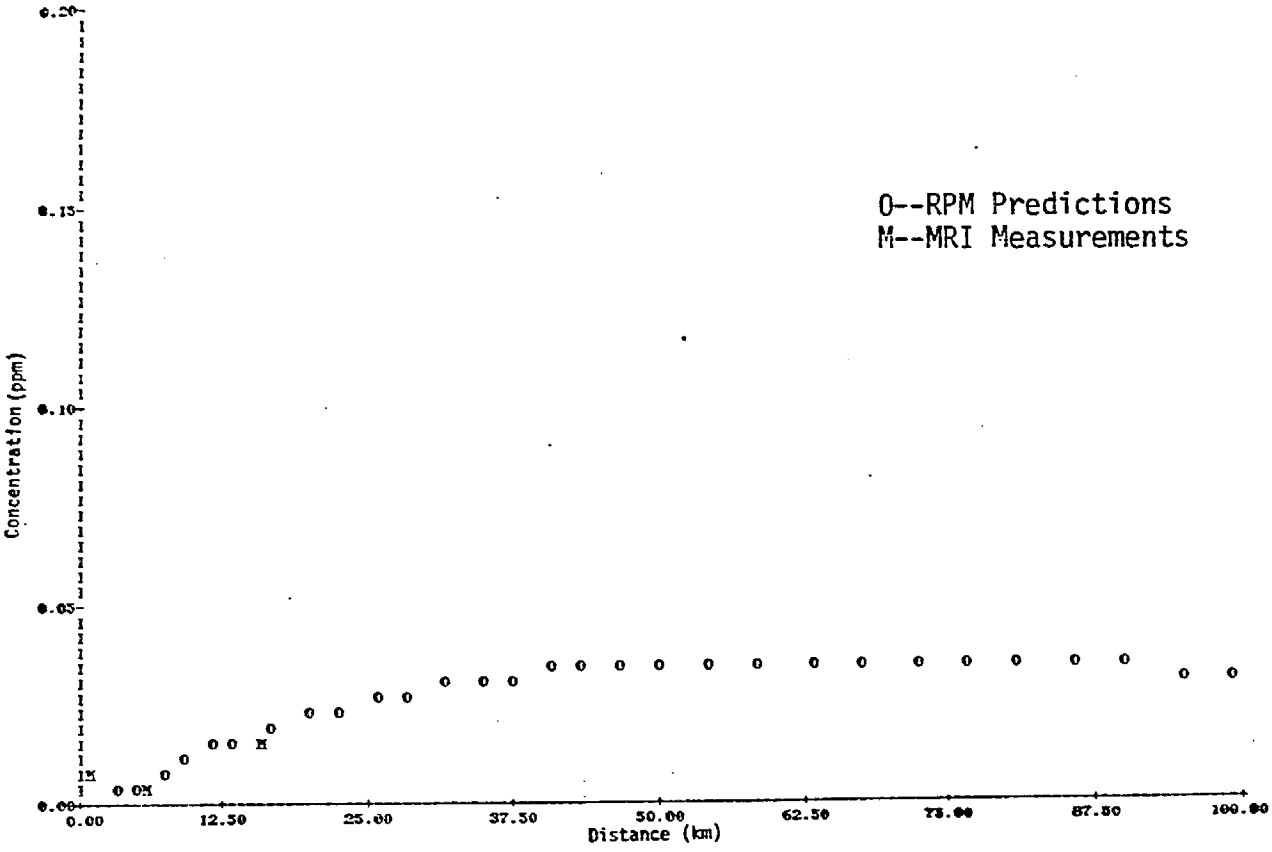

FIGURE II-9d. COMPARISON OF PREDICTED AND MEASURED O_3 CONCENTRATIONS AT LOS ALAMITOS ON OCTOBER 25, 1974 (1340-1530 HRS) VERSUS DISTANCE FROM THE STACKS.

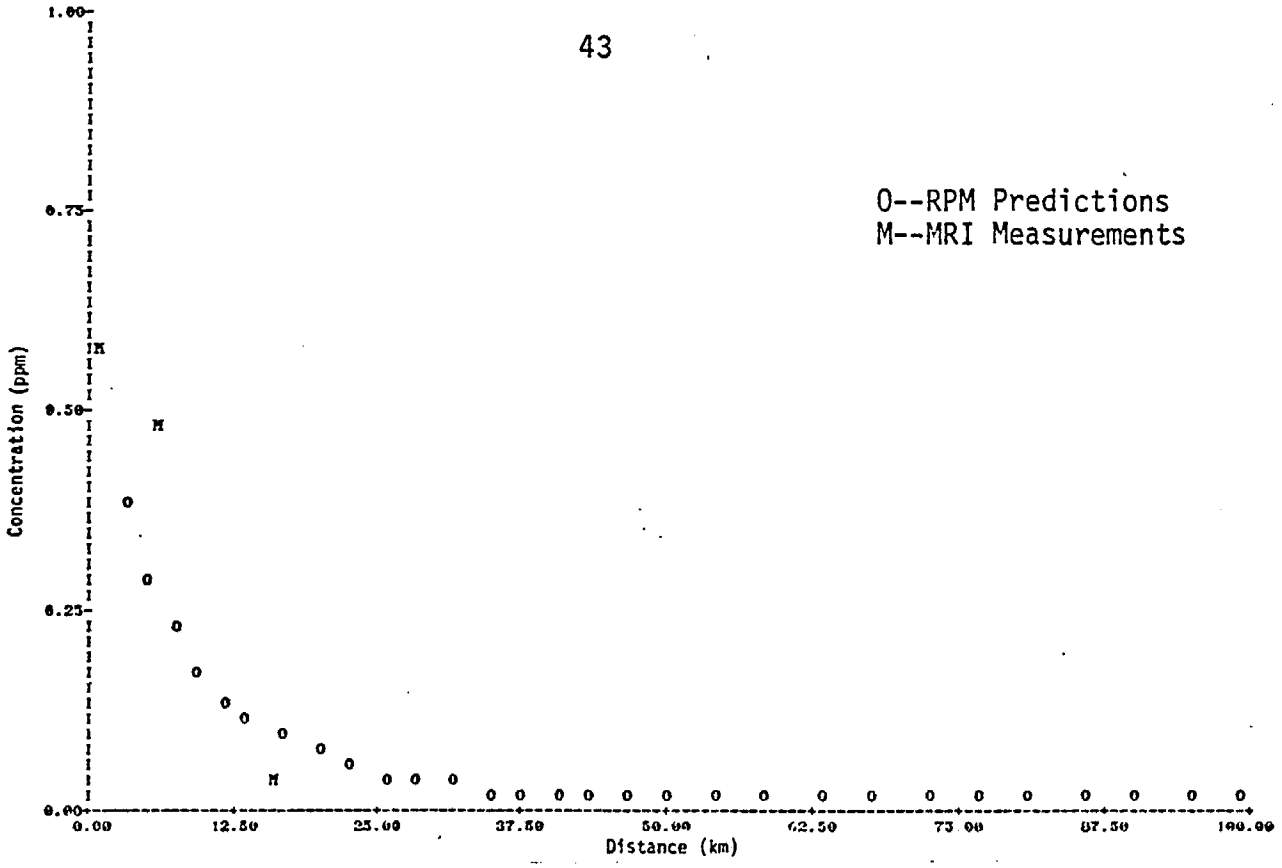

FIGURE II-9e. COMPARISON OF PREDICTED AND MEASURED SO_2 CONCENTRATIONS AT LOS ALAMITOS ON OCTOBER 25, 1974 (1340-1530 HRS) VERSUS DISTANCE FROM THE STACKS.

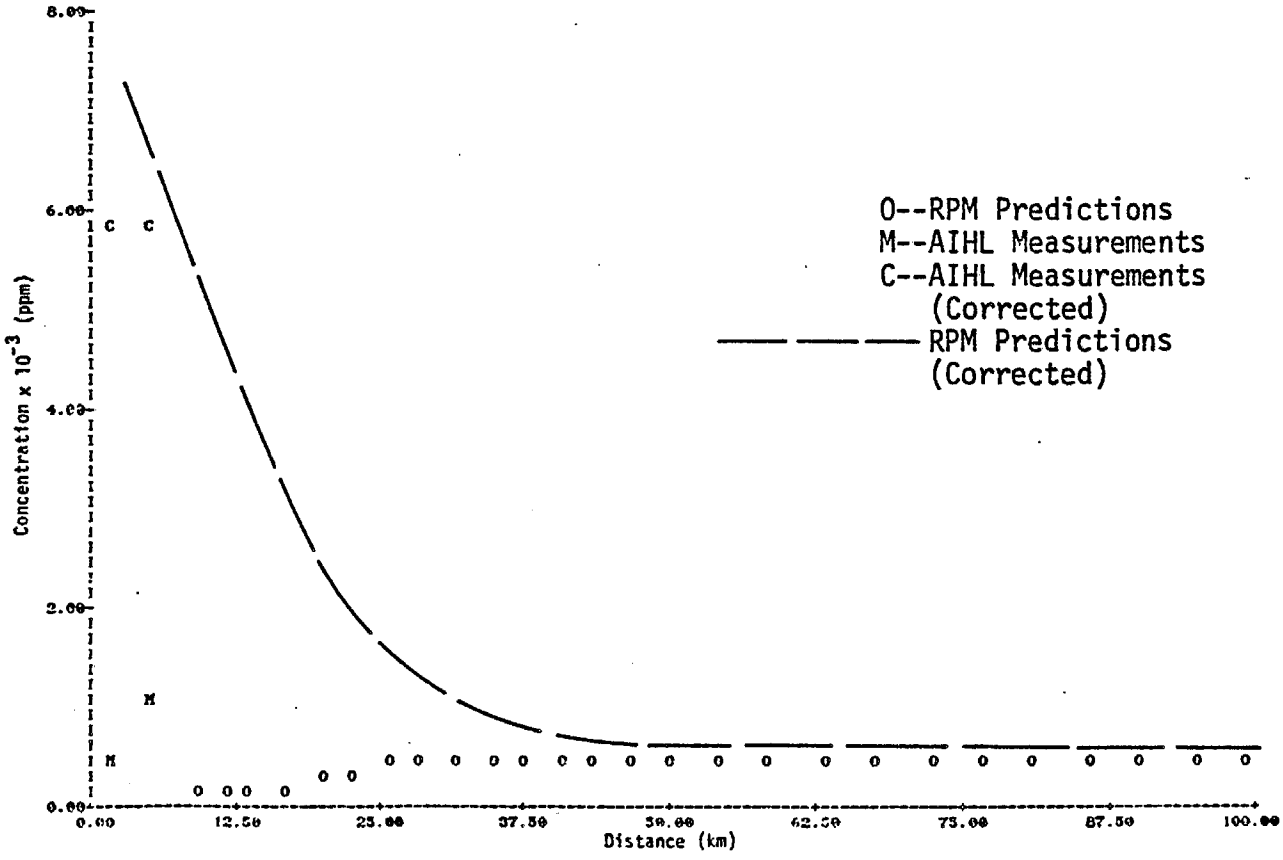

FIGURE II-9f. COMPARISON OF PREDICTED AND MEASURED SO_3 CONCENTRATIONS AT LOS ALAMITOS ON OCTOBER 25, 1974 (1340-1530 HRS) VERSUS DISTANCE FROM THE STACKS.

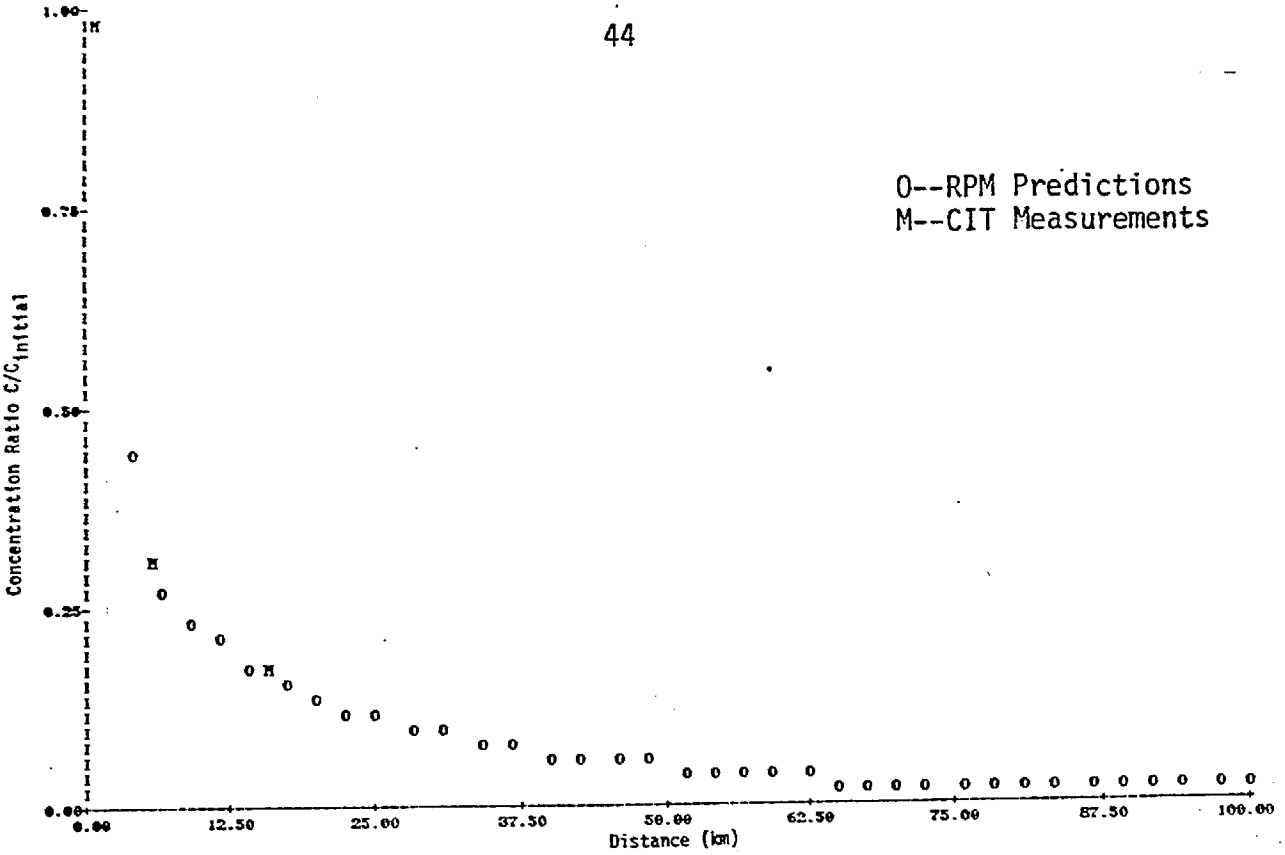

FIGURE II-10a. COMPARISON OF PREDICTED AND MEASURED SF_6 CONCENTRATION RATIOS AT LOS ALAMITOS ON OCTOBER 30, 1974 (1300-1430 HRS) VERSUS DISTANCE FROM THE STACKS

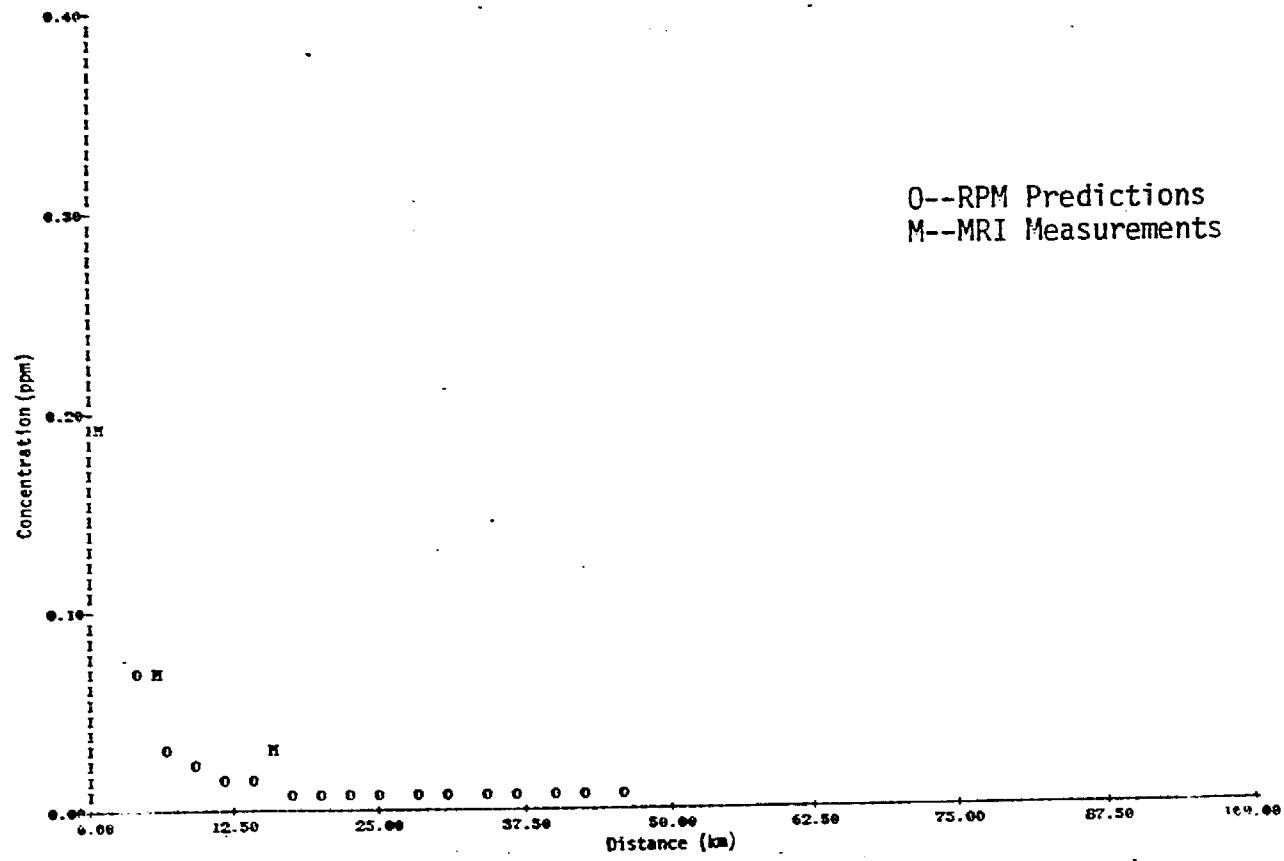

FIGURE II-10b. COMPARISON OF PREDICTED AND MEASURED NO CONCENTRATIONS AT LOS ALAMITOS ON OCTOBER 30, 1974 (1300-1430 HRS) VERSUS DISTANCE FROM THE STACKS

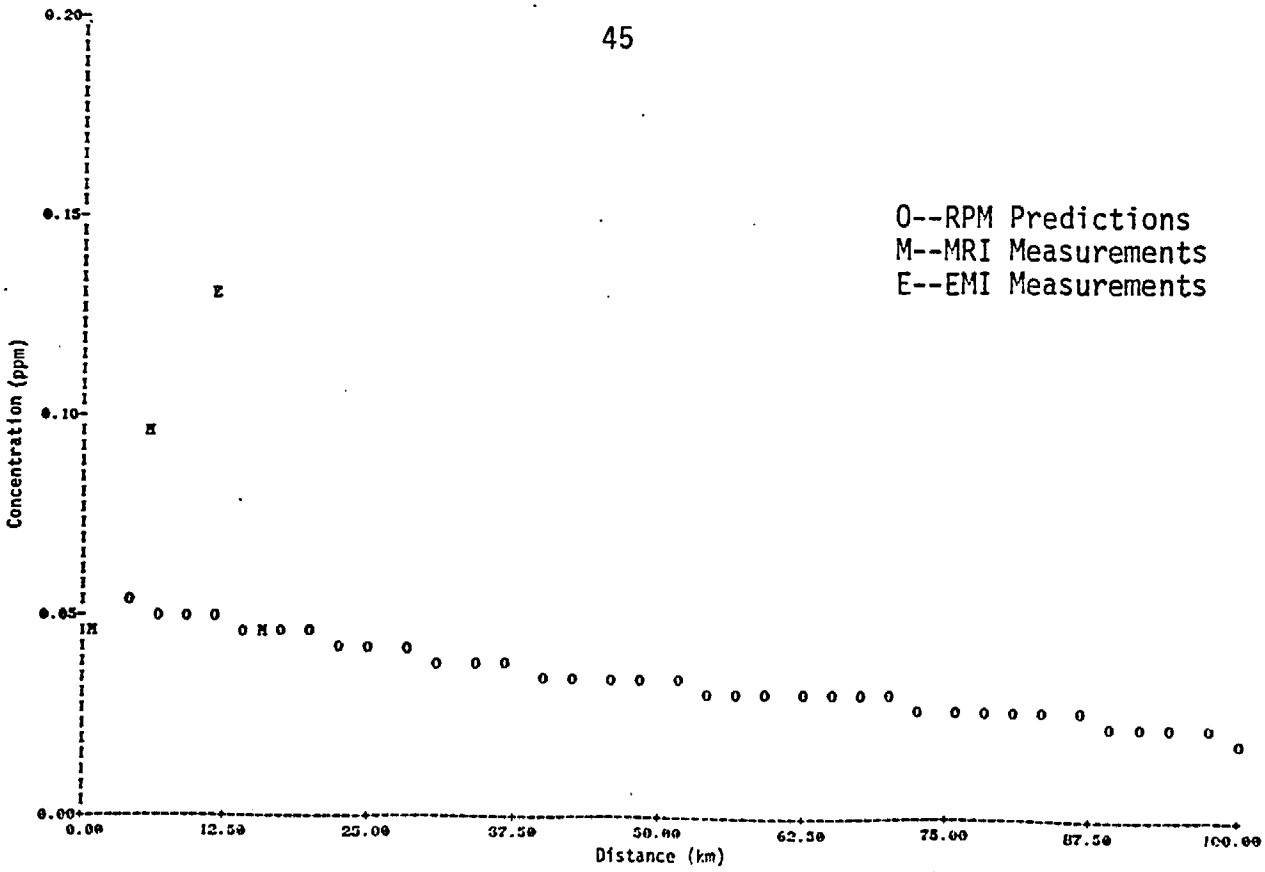

FIGURE II-10c. COMPARISON OF PREDICTED AND MEASURED NO_2 CONCENTRATIONS AT LOS ALAMITOS ON OCTOBER 30, 1974 (1300-1430 HRS) VERSUS DISTANCE FROM THE STACKS.

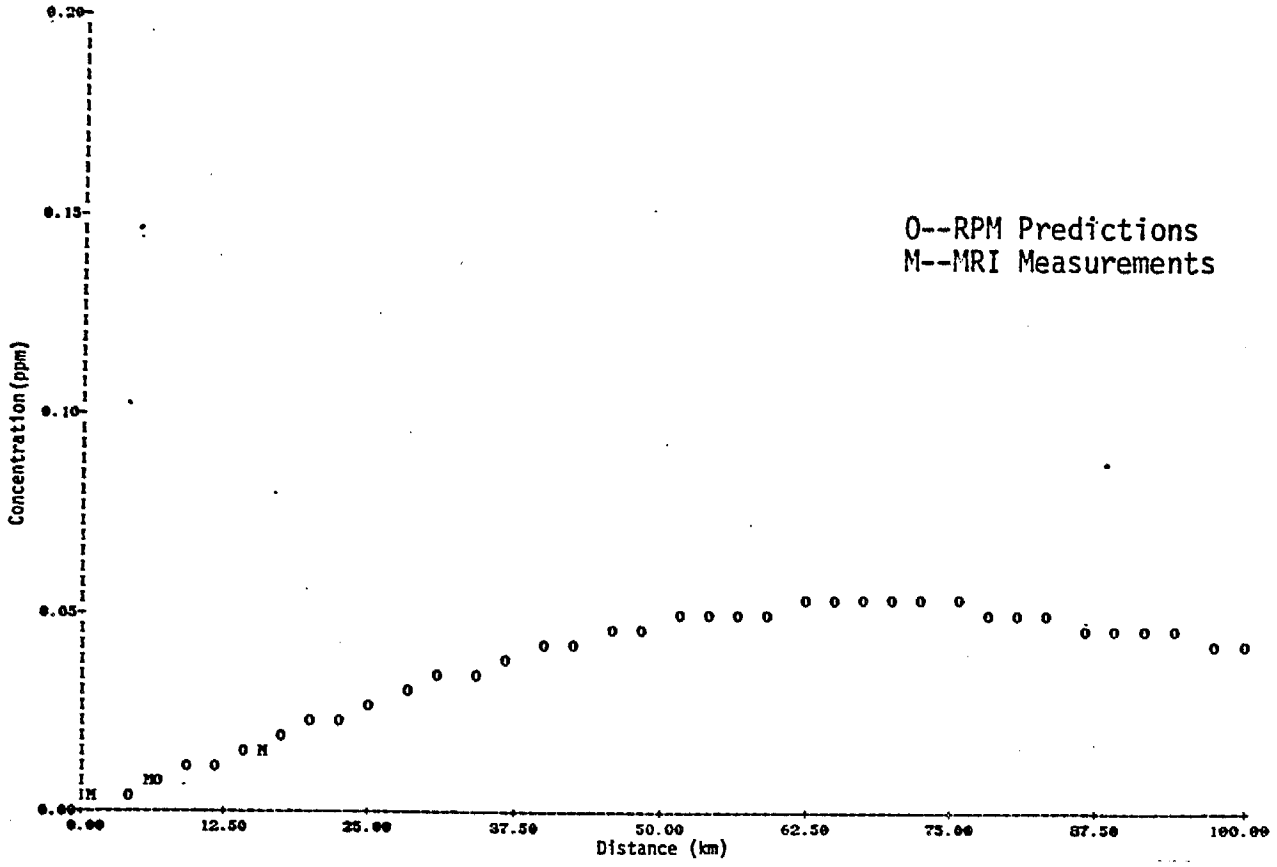

FIGURE II-10d. COMPARISON OF PREDICTED AND MEASURED O_3 CONCENTRATIONS AT LOS ALAMITOS ON OCTOBER 30, 1974 (1300-1430 HRS) VERSUS DISTANCE FROM THE STACKS.

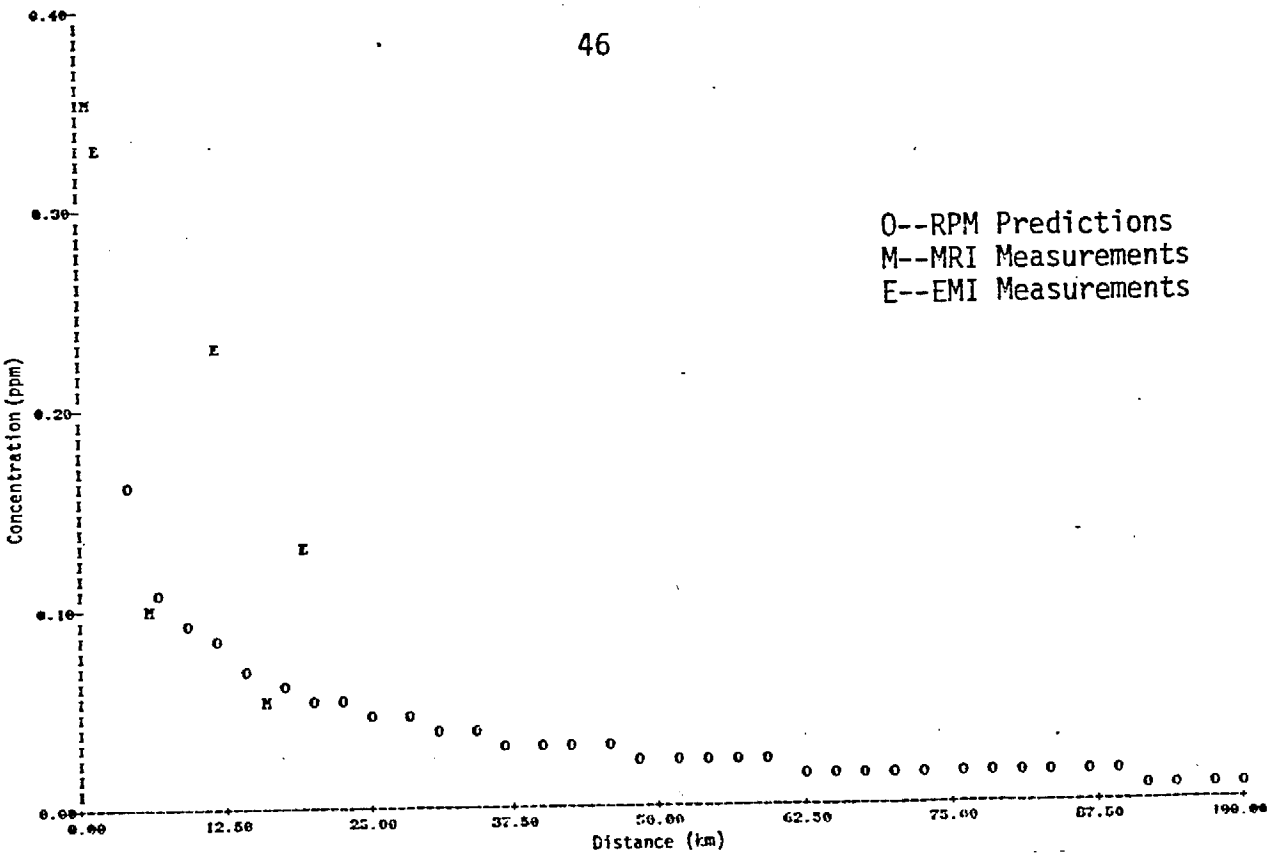

FIGURE II-10e. COMPARISON OF PREDICTED AND MEASURED SO_2 CONCENTRATIONS AT LOS ALAMITOS ON OCTOBER 30, 1974 (1300-1430 HRS) VERSUS DISTANCE FROM THE STACKS.

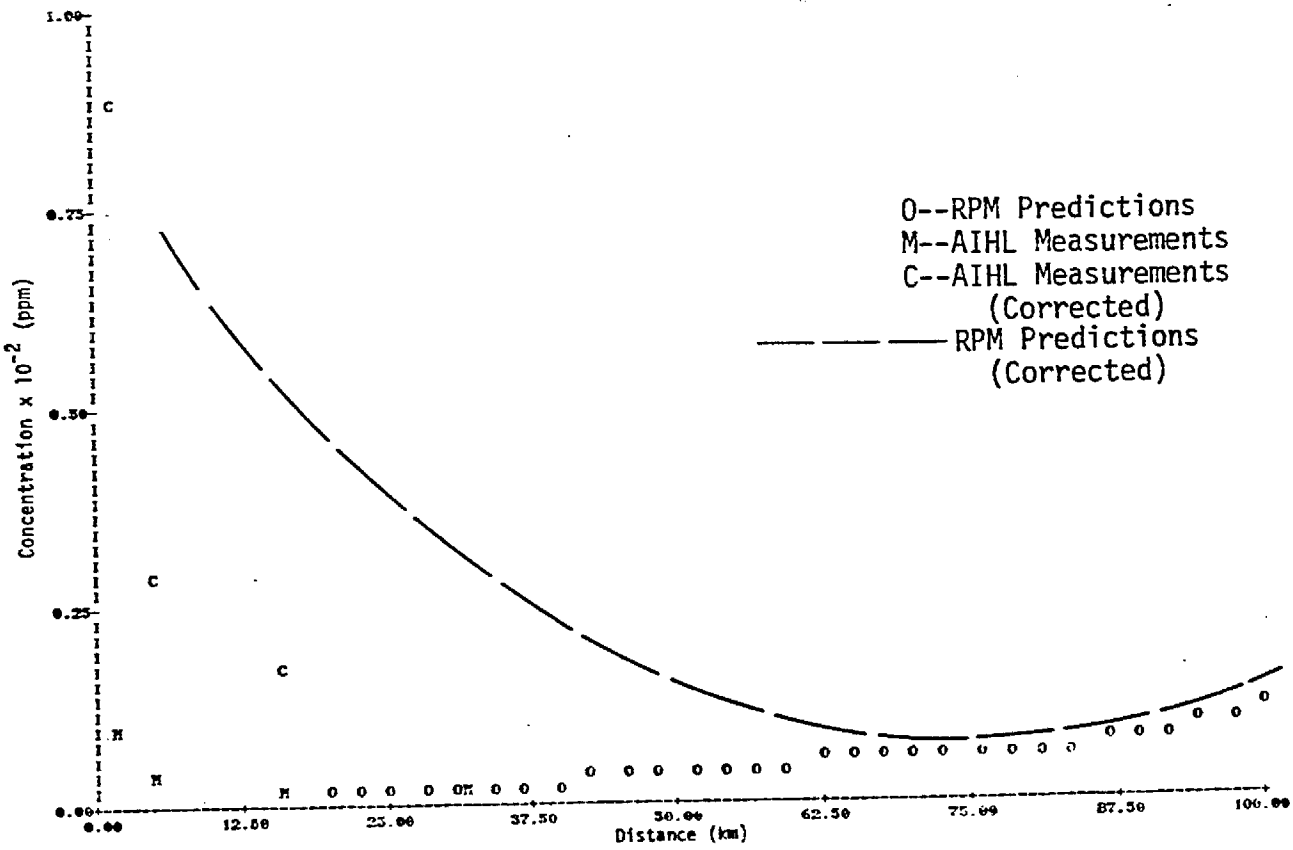

FIGURE II-10f. COMPARISON OF PREDICTED AND MEASURED SO_3 CONCENTRATIONS AT LOS ALAMITOS ON OCTOBER 30, 1974 (1300-1430 HRS) VERSUS DISTANCE FROM THE STACKS.

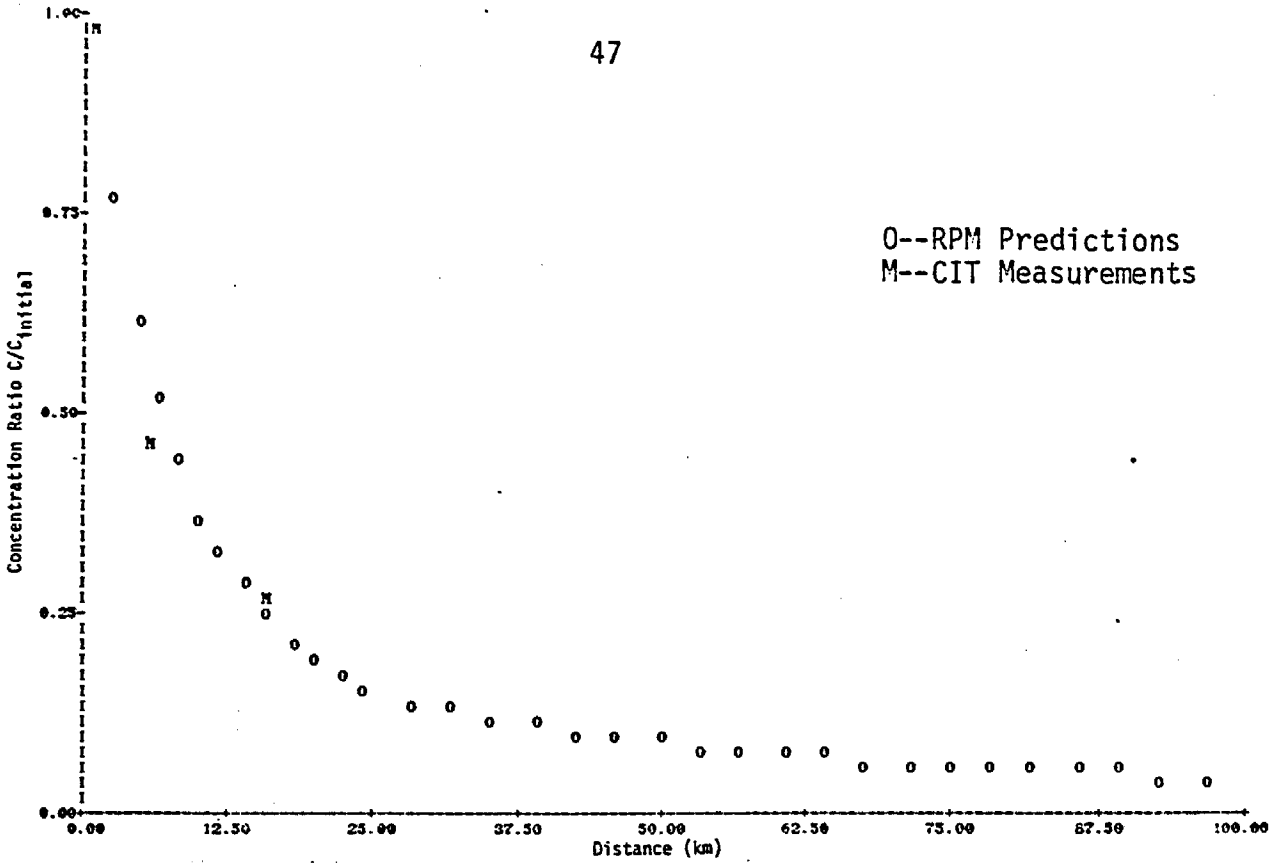

FIGURE II-11a. COMPARISON OF PREDICTED AND MEASURED SF_6 CONCENTRATION RATIOS AT LOS ALAMITOS ON NOVEMBER 7, 1974 (1300-1430 HRS) VERSUS DISTANCE FROM THE STACKS

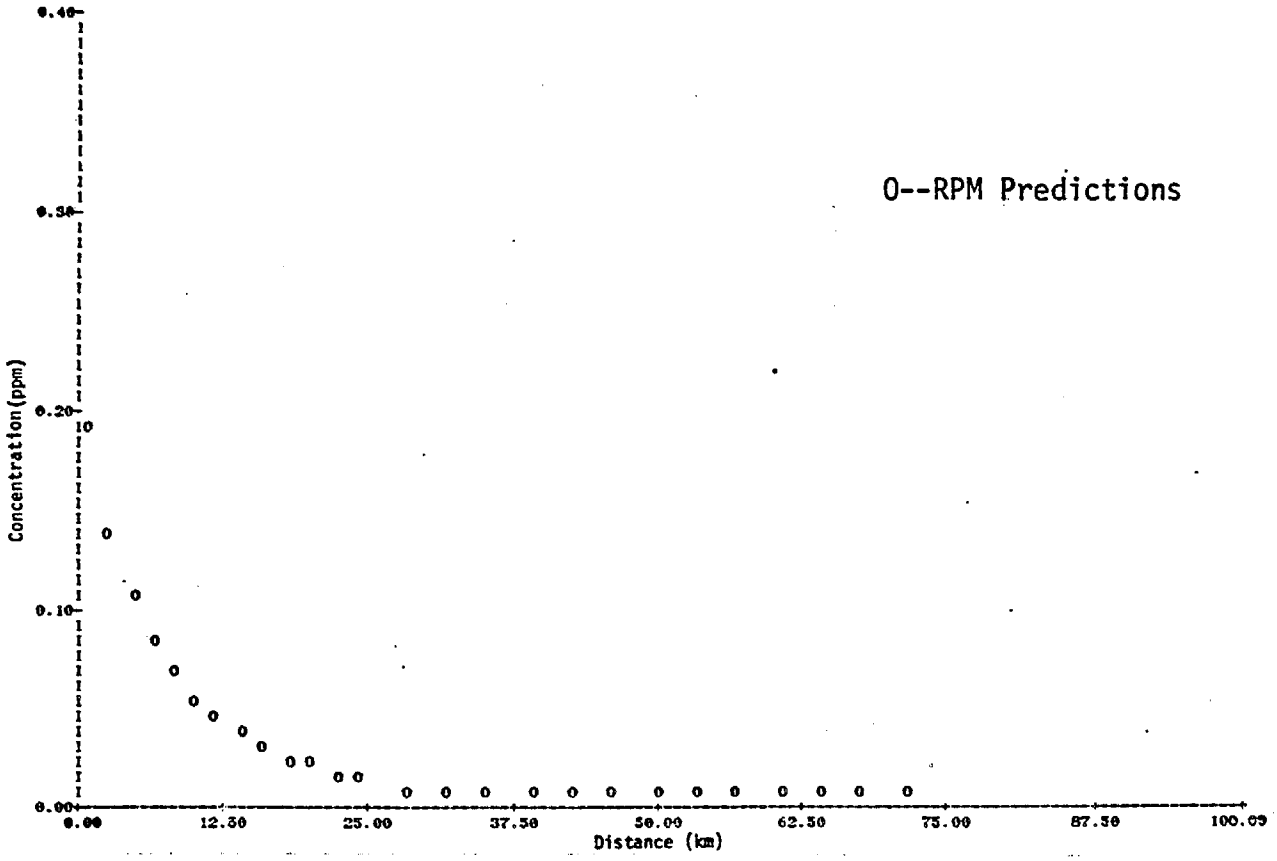

FIGURE II-11b. PREDICTED NO CONCENTRATIONS AT LOS ALAMITOS ON NOVEMBER 7, 1974 (1300-1430 HRS) VERSUS DISTANCE FROM THE STACKS.

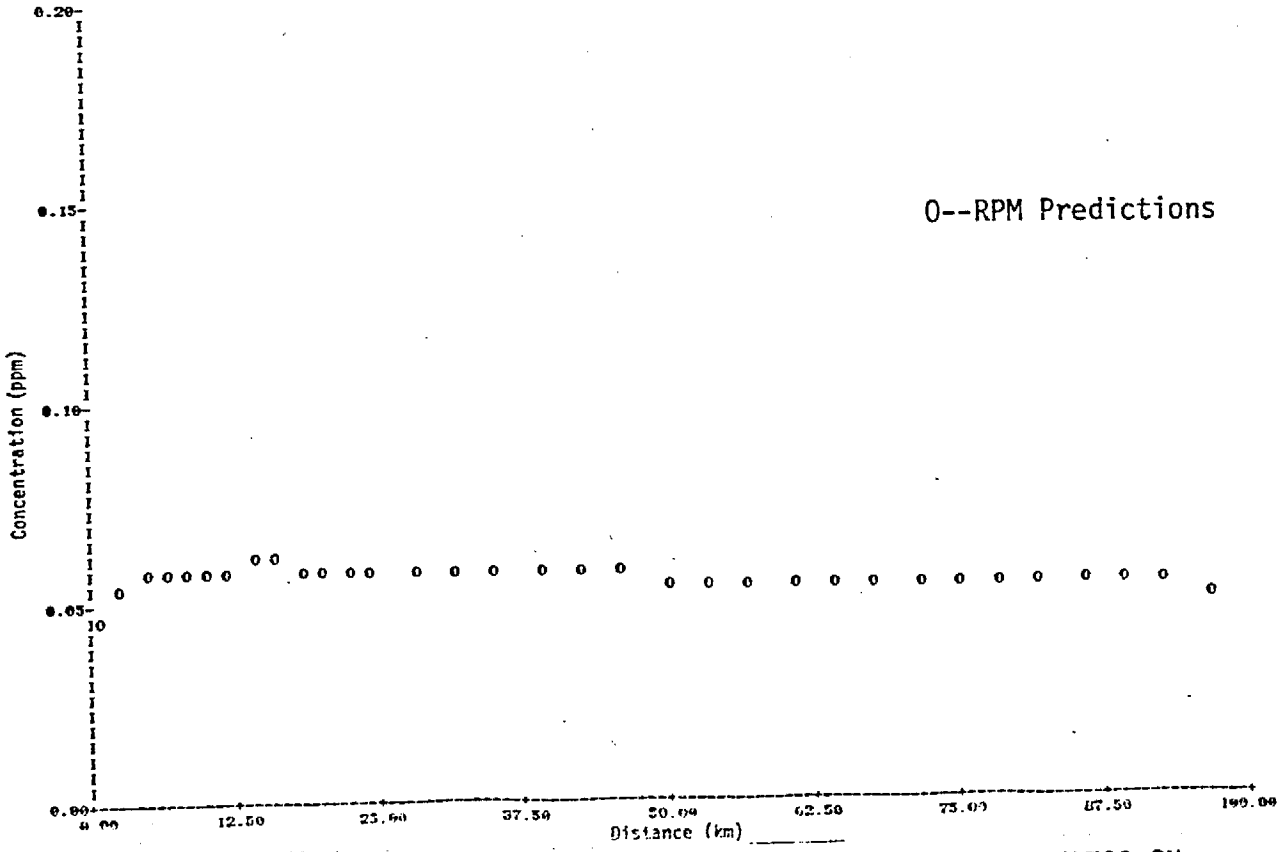

FIGURE II-11c. PREDICTED NO_2 CONCENTRATIONS AT LOS ALAMITOS ON NOVEMBER 7, 1974 (1300-1430 HRS) VERSUS DISTANCE FROM THE STACKS.

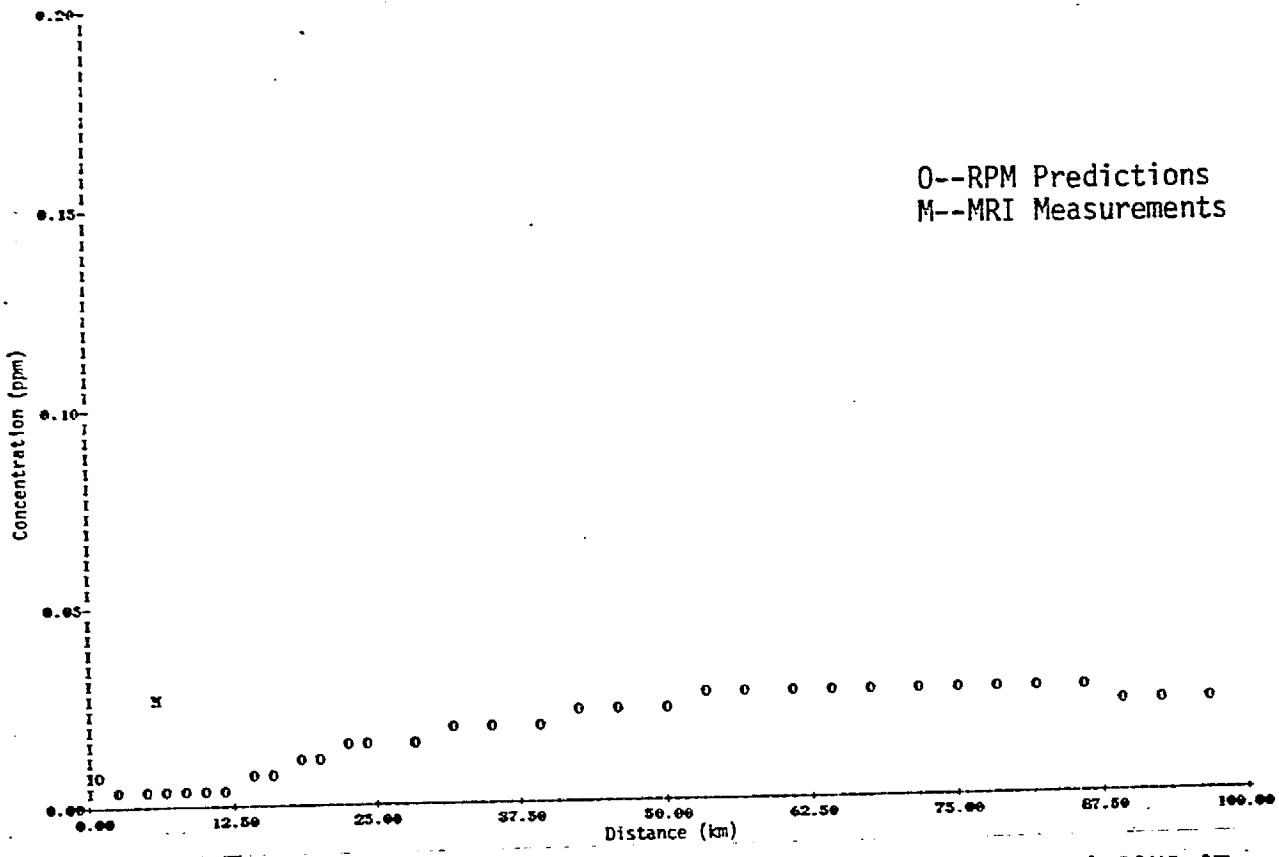

FIGURE II-11d. COMPARISON OF PREDICTED AND MEASURED O_3 CONCENTRATIONS AT LOS ALAMITOS ON NOVEMBER 7, 1974 (1300-1430 HRS) VERSUS DISTANCE FROM THE STACKS.

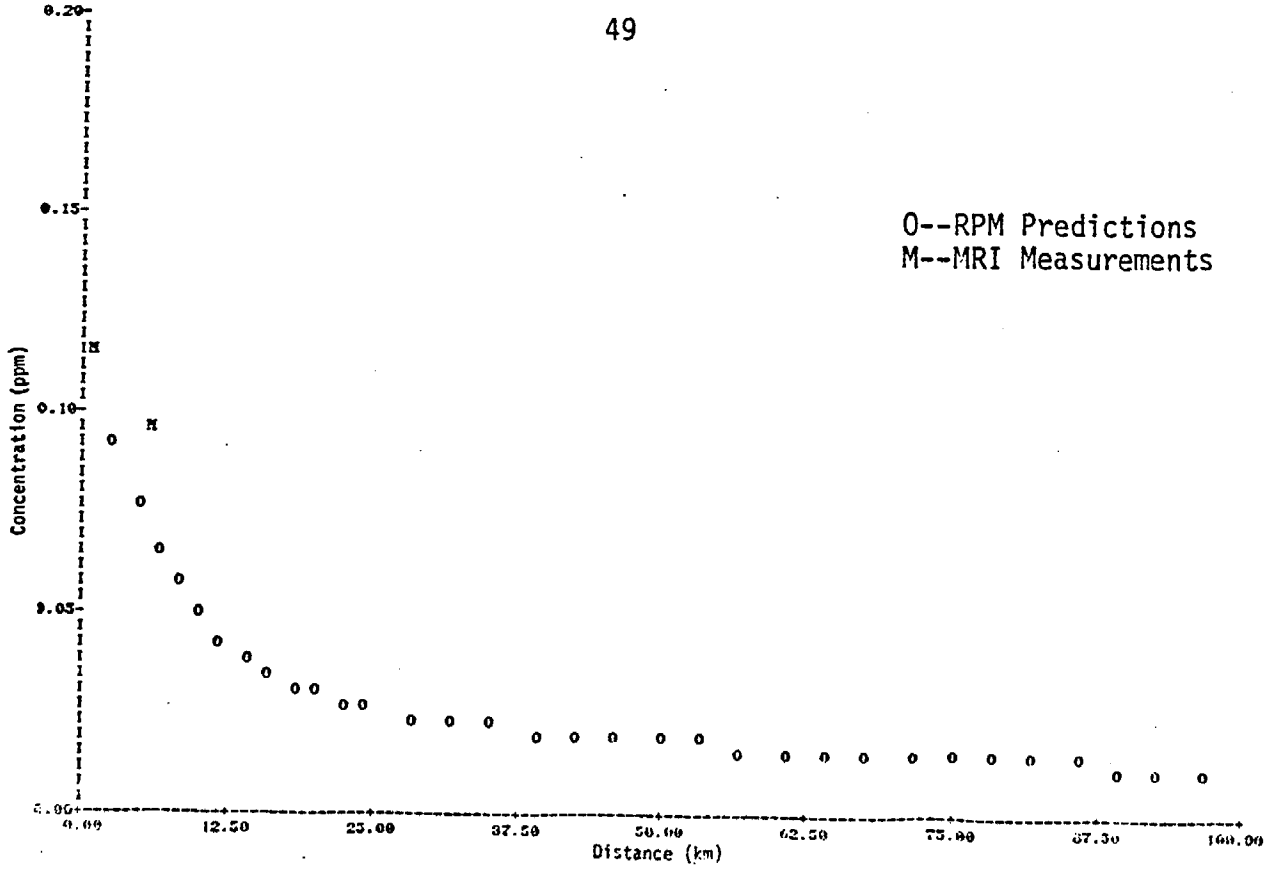

FIGURE II-11e. COMPARISON OF PREDICTED AND MEASURED SO_2 CONCENTRATIONS AT LOS ALAMITOS ON NOVEMBER 7, 1974 (1300-1430 HRS) VERSUS DISTANCE FROM THE STACKS.

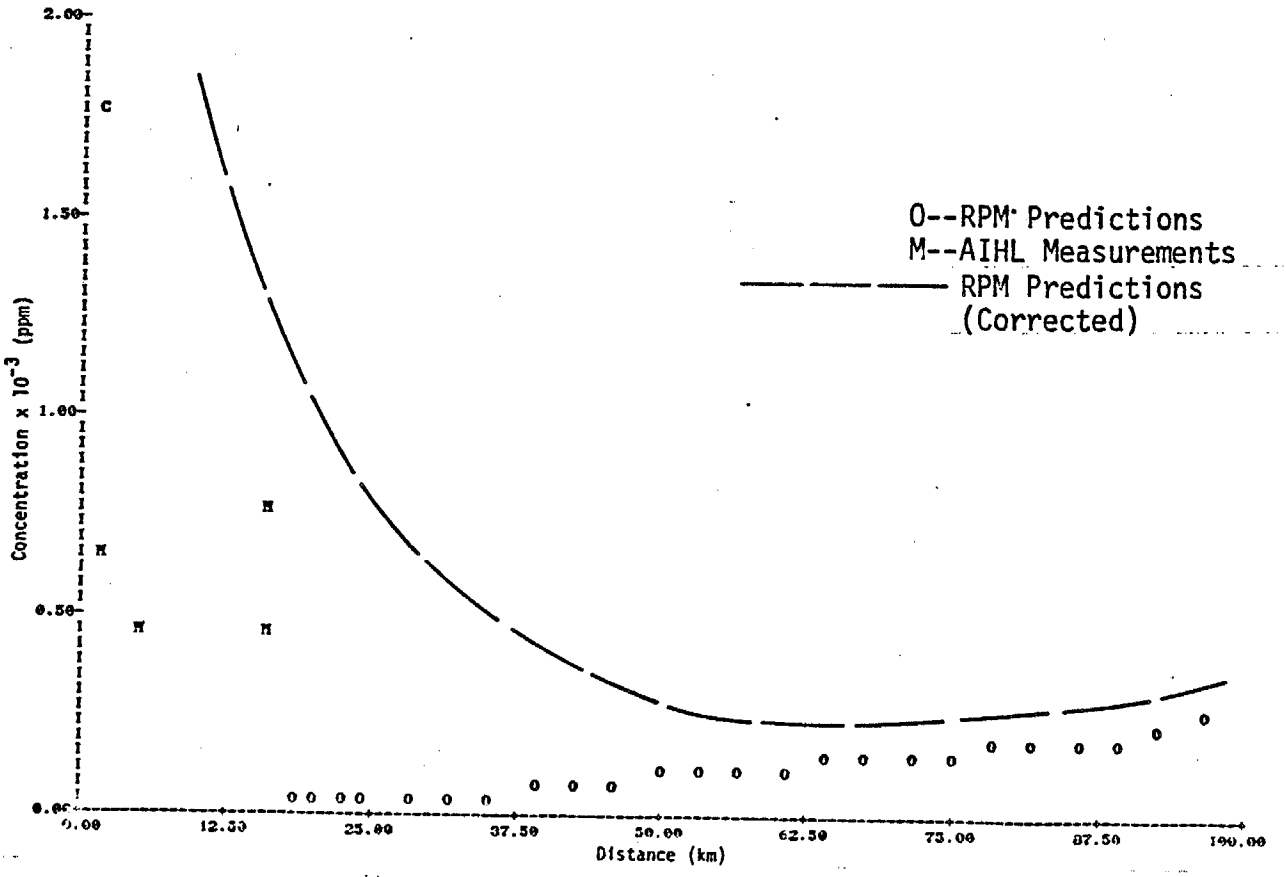

FIGURE II-11f. COMPARISON OF PREDICTED AND MEASURED SO_3 CONCENTRATIONS AT LOS ALAMITOS ON NOVEMBER 7, 1974 (1300-1430 HRS) VERSUS DISTANCE FROM THE STACKS.

discussed in the previous section. The predicted sulfate, without considering sulfate emissions from the stack, are represented by the symbol "0", and the Reactive Plume Model predictions, with the stack sulfate emissions included, are plotted as dotted lines. It can be seen that the predicted concentrations are only marginally acceptable. There are a number of possible causes for the discrepancy between predicted and measured concentrations:

- Uncertainties involved in estimating the sulfate emissions from the stack.
- Inaccuracies present in other input parameters, notably in the ambient sulfate concentrations.
- Errors introduced in the sampling and averaging of the sulfate data.
- Inadequacies intrinsic to the kinetic mechanism that leads to sulfate formation. In particular, in view of the significant variations in relative humidity from day to day (see Table II-3 for example), the exclusion of heterogeneous processes may be important.

Based upon the present results, however, it can be stated that near the stack (for distances typically less than 10 kilometers), the contribution of the stack sulfate emissions appears to be dominant. This conclusion seems to be consistent with that reached by Rockwell International (Richards, 1976). On the other hand, the production of sulfate from SO_2 in the plume becomes important further downwind. The rate of conversion of SO_2 to sulfate was estimated from the Reactive Plume Model predictions for each of the eight days. The results are tabulated in Table II-4. The relatively slow conversion in the early stage may be attributable to the depression of the ozone concentrations near the stack.

In conclusion, based upon an overall appraisal of the results of the present validation exercise, the Reactive Plume Model predictions compare remarkably well with the measured values for all pollutant species except

Table II-3

RELATIVE HUMIDITY VARIATIONS IN LOS ANGELES
DURING THE PERIOD OF FIELD STUDY

Date	Time	Location	Temperature (°C)	Humidity (%)
10/1/74	14:02	Upwind of Plant	17	73
	15:29	Los Alamitos Airport	19	72
	16:37	Fullerton Airport	20	70
	16:56	Santa Ana Canyon	18	68
10/11/74	14:18	Los Alamitos Airport	17	72
	17:02	Santa Ana Canyon	19	75
	17:18	Fullerton Airport	19	78
	18:02	Riverside Airport	17	67
10/17/74	15:38	Los Alamitos Airport	27	28
	16:58	Fullerton Airport	30	30
	17:14	Shepherd Strip	30	34
	17:24	El Monte Airport	30	31
	17:58	Chino Airport	29	28
	18:21	Los Alamitos Airport	19	35
10/25/74	13:16	Los Alamitos Airport	19	72
	16:58	Fullerton Airport	18	80
	17:50	Santa Ana Canyon	16	86
10/30/74	12:43	Los Alamitos Airport	16	72
	15:54	Fullerton Airport	17	56
	16:41	Santa Ana Canyon	13	74
11/7/74	13:45	Los Alamitos Airport	23	30
	15:57	Fullerton Airport	23	34

Table II-4

RATE OF SO_2-SULFATE CONVERSION AS ESTIMATED FROM THE PREDICTIONS OF THE REACTIVE PLUME MODEL

September 10, 1974 (Moss Landing)	
<10 km from stack	0.6%/hr
>10 km	4.0%/hr
September 11, 1974 (Moss Landing)	
<10 km	0.46%/hr
>10 km	4.0 %/hr
October 1, 1974 (Haynes)	
<10 km	0.20%/hr
>10 km	6.0 %/hr
October 11, 1974 (Haynes)	
<10 km	0.3%/hr
>10 km	6.0%/hr
October 17, 1974 (Haynes)	
<10 km	0.3%/hr
>10 km	22.0%/hr
October 25, 1974 (Los Alamitos)	
<10 km	0.1%/hr
>10 km	3.0%/hr
October 30, 1974 (Los Alamitos)	
<10 km	0.05%/hr
>10 km	3.0 %/hr
November 7, 1974 (Los Alamitos)	
<10 km	0.02%/hr
>10 km	1.0 %/hr

sulfate. The comparison of the predicted and measured sulfate is only qualitative because of larger uncertainties in the stack emissions data and possibly because of intrinsic inadequacies in the kinetic mechanism that leads to sulfate formation as well as uncertainties associated with the measurement and reduction of the data.

III DEVELOPMENT OF THE BUOYANT PLUME MODEL

Effluents from power plant stacks are generally accompanied by emissions of heat. Thus, power plant plumes are usually buoyant. In describing the typical behavior of a buoyant plume in the atmospheric boundary layer, it is useful to divide plume development into two stages. The first stage is characterized by the dominance of the buoyant force. The plume rises under the influence of buoyancy, and, along with this induced vertical motion, dispersion due to the entrainment of ambient air results in the dilution of the plume. Although this first stage generally takes place within a kilometer or so from the stack, its effect on the eventual distribution of pollutant concentrations is significant. In the second stage of plume development, which generally spans a distance from one kilometer to a few tens of kilometers downwind of the stack, buoyancy is no longer important. The plume is essentially dynamically passive; and its behavior is dictated by the ambient flow and atmospheric turbulence.

Most methodologies used to predict the dispersion of pollutants in power plant plumes were developed with a recognition of the fundamental differences between the two stages of plume development. In general, these methodologies are based on a two-step calculation procedure. In the first step, simple empirical formulas are used to estimate the final height to which the hot stack gases will rise. In the second step, Gaussian formulas are used to estimate the dispersion of pollutants from a "virtual" height that is the sum of the stack height and the computed plume rise. In Section A of this chapter we review some of the more well-known formulas for plume rise, and discuss their advantages and disadvantages.

As we shall see in Section A, one of the major drawbacks of the conventional methods is that no single formula can provide reasonable predic-

tions under the wide range of atmospheric conditions that are encountered. Plume rise predictions of different formulas commonly vary by as much as 50 to 100%, and for complex situations the differences can be even larger. Chiefly for this reason, we have developed a numerical model that simulates the rise of buoyant plumes. We hope that this model will permit accurate simulation of the development of a plume under a wide range of conditions. The feasibility of the numerical modeling approach has been enhanced by the increasing availability of high speed digital computers. In Section B of this chapter we present the formulation of this mathematical model, and discuss in detail the assumptions underlying the equations of the model. In Section C we review numerical methods useful for solving the equations of the model, and present the numerical method we chose as the most appropriate. In this section we also outline the procedure used for testing the numerical method and the computer codes. A number of physical variables enter into the model equations; the sensitivity of the model results to the major physical variables is discussed in Section D. Finally, in Section E we present the results of applying the model to several field studies of this project, and compare the model predictions with observational data.

A. REVIEW OF THE LITERATURE

As stated above, most plumes of interest to air pollution studies are buoyant. Following Csanady (1965), we can conveniently divide the dynamic behavior of a buoyant plume into three phases:

- Initial phase. The upward motion caused by buoyancy induces turbulence, which provides the dominant mixing process in this phase. As more and more ambient air is entrained, the plume loses much of its buoyancy and its rate of upward motion decreases.
- Intermediate phase. As the buoyant force is further weakened by entrainment, atmospheric turbulence becomes important; the dominant turbulent eddies are in the inertial subrange.

Under the combined influence of the wind and buoyancy-induced upward motion, the plume bends over.

> Final phase. The plume begins to level off, and atmospheric turbulence is primarily responsible for the spreading of the plume.

The first two phases, which constitute the "near-stack" problem, are unique to the study of buoyant plumes. The third phase, the "far-field" problem, is quite similar to the ordinary dispersion of pollutants in the atmosphere. In fact, the conventional approach to the "far-field" problem once the plume rise is known is to calculate a virtual stack height, as illustrated in Figure III-1, and then to compute the concentration distribution using a Gaussian formula.

To provide adequate background for the present study, we reviewed various approaches to the study of plume development in the vicinity of a stack. In summarizing this effort, our intent is not to present a comprehensive review of the approaches, but rather to illustrate the salient aspects of the basic approaches so that their advantages and drawbacks can be assessed.

We note that, of the two important physical features of the buoyant plume (plume rise and the enhanced initial dispersion), only the former was explicitly addressed in most of the studies surveyed. Although these two features are intimately connected, there is observational evidence that the rate of dispersion is significantly higher in plumes from larger power plants (Start et al., 1973). It is very likely that a part of this increase is attributable to buoyancy-induced turbulence (McElroy, 1969). Thus, consideration of the plume rise alone is not sufficient in studying the fate of a buoyant plume.

1. Empirical Approaches for Calculating Plume Rise

One of the simplest approaches to describing the behavior of a buoyant plume is to establish a relationship between plume rise and other parameters

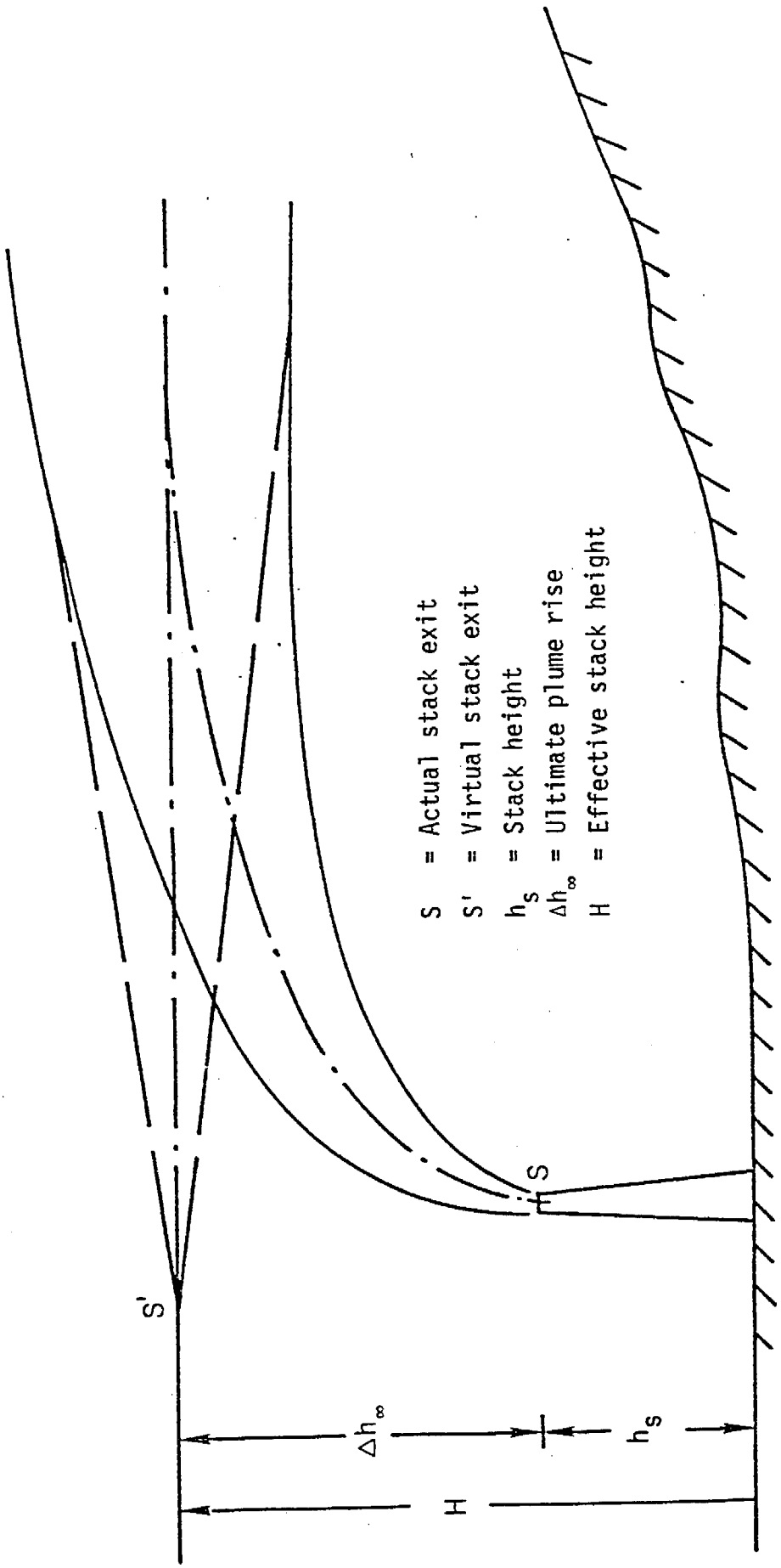

FIGURE III-1. SKETCH OF A BUOYANT PLUME

from observational data. The physical parameters that most investigators have used are the heat emission from the stack, the prevailing wind, and the atmospheric stability.

There is no lack of plume rise formulas in the literature. Briggs (1969) observed that there were over 30 documented formulas as of 1969, and he estimated that two more would be added each year. Although extensive efforts have been made both to assess and to reconcile the differences between these formulas (Carson and Moses, 1969; Briggs, 1969, 1971), no agreement has been reached. Apparently, the reason for these differences is the lack of an adequate definition for plume rise, as well as the lack of rigorous experimental techniques to measure it.* A more fundamental reason for the proliferation of different plume rise formulas, however, relates to the variety of conditions under which data were collected. For example, the effects of heat emissions of the large power plants on plume rise differ significantly from those of the smaller ones, and meteorological conditions characteristic of each plant site differ. Thus, a set of formulas developed from data collected at one site can rarely be extrapolated to another site.

To illustrate the wide variety of empirical formulas that one can find in the literature, we selected five classical formulas for predicting plume rise. We chose them because they are relatively well known. To facilitate comparison, we have attempted to recast the original formulas

---

* This point is succinctly expressed in the following quote from Slawson and Csanady (1967):

> With an ostrich-like philosophy, the effective stack height is often defined to be the point where the smoke plume is just lost sight of. It is then not very surprising to find that the observed thermal rise of the plume depends, for example, on a power of the heat flux ranging from 1/4 to 1.0, influenced by a number of factors including, presumably, the observer's eyesight.

on a uniform basis. Thus, in the formulas presented below, the definitions and units of the parameters are the same, and minor corrections, such as the effect of finite stack diameter, are neglected. In their simplest form, these formulas can be written as follows:

> The Holland formula* (Holland, 1953)

$$\Delta h_\infty = 9.6 \frac{Q}{U} \quad . \tag{III-1}$$

> The Lucas-Moore-Spurr formula* (Brummage, 1968)

$$\Delta h_\infty = 475 \frac{Q^{1/4}}{U} \quad . \tag{III-2}$$

> The CONCAWE† formula (Brummage, 1968)

$$\Delta h_\infty = 86 \frac{Q^{1/2}}{U^{3/4}} \quad . \tag{III-3}$$

> The Moses-Carson formula (Moses and Carson, 1968)

$$\Delta h_\infty = 82.7 \frac{Q^{1/2}}{U} \quad . \tag{III-4}$$

> The Briggs formula* (Briggs, 1971)

$$\Delta h_\infty = \left(15.3\ h_s^{2/3}\right) \frac{Q^{1/3}}{U} \quad . \tag{III-5}$$

---

*For a neutral atmosphere.

†Conservation of Clean Air and Water, Western Europe.

In all of these formulas, the definitions of the variables are as follows:

Δh_∞ = final height of the plume rise (in m),
Q = rate of heat emission (in MW),
U = average wind speed (in m/s),
h_s = stack height (in m).

As a comparison of these formulas immediately reveals, the only consensus among them is that they are of the following general form:

$$\Delta h_\infty = C \frac{Q^A}{U^B} \quad . \tag{III-6}$$

The values chosen for A, B, and C by each investigator are all different, as shown in Table III-1. In particular, the exponent for heat emission, A, varies from 1/3 to 1. To demonstrate the significance of these differences, we plotted the predicted plume rise from the CONCAWE formula and the Lucas-Moore-Spurr formula as a function of wind speed for typical heat emissions from large power plants. Figure III-2 shows that the predicted values can easily differ by a factor of 2 between the two formulas. Therefore, these empirical formulas can be used to provide only a rule-of-thumb estimate of plume rise.

2. Theoretical Approaches for Calculating Plume Rise

One of the earliest theories describing plume rise was presented by Batchelor (1954), who based his formulation on dimensional analysis. He considered the case of an axisymmetric buoyant plume in a calm, stratified atmosphere. By first identifying the pertinent physical variables, such as the buoyancy flux, the plume radius, and the height, and then invoking the π-theorem, he obtained the following equations for a neutral atmosphere:

$$R = \text{Constant} \cdot z \quad , \tag{III-7}$$

Table III-1

COEFFICIENTS FOR THE EMPIRICAL FORMULAS

Formula	C	A	B
Holland	9.6	1	1
Lucas-Moore-Spurr	475	1/4	1
CONCAWE	86	1/2	3/4
Moses-Carson	82.7	1/2	1
Briggs	15.3 $h_s^{2/3}$	1/3	1

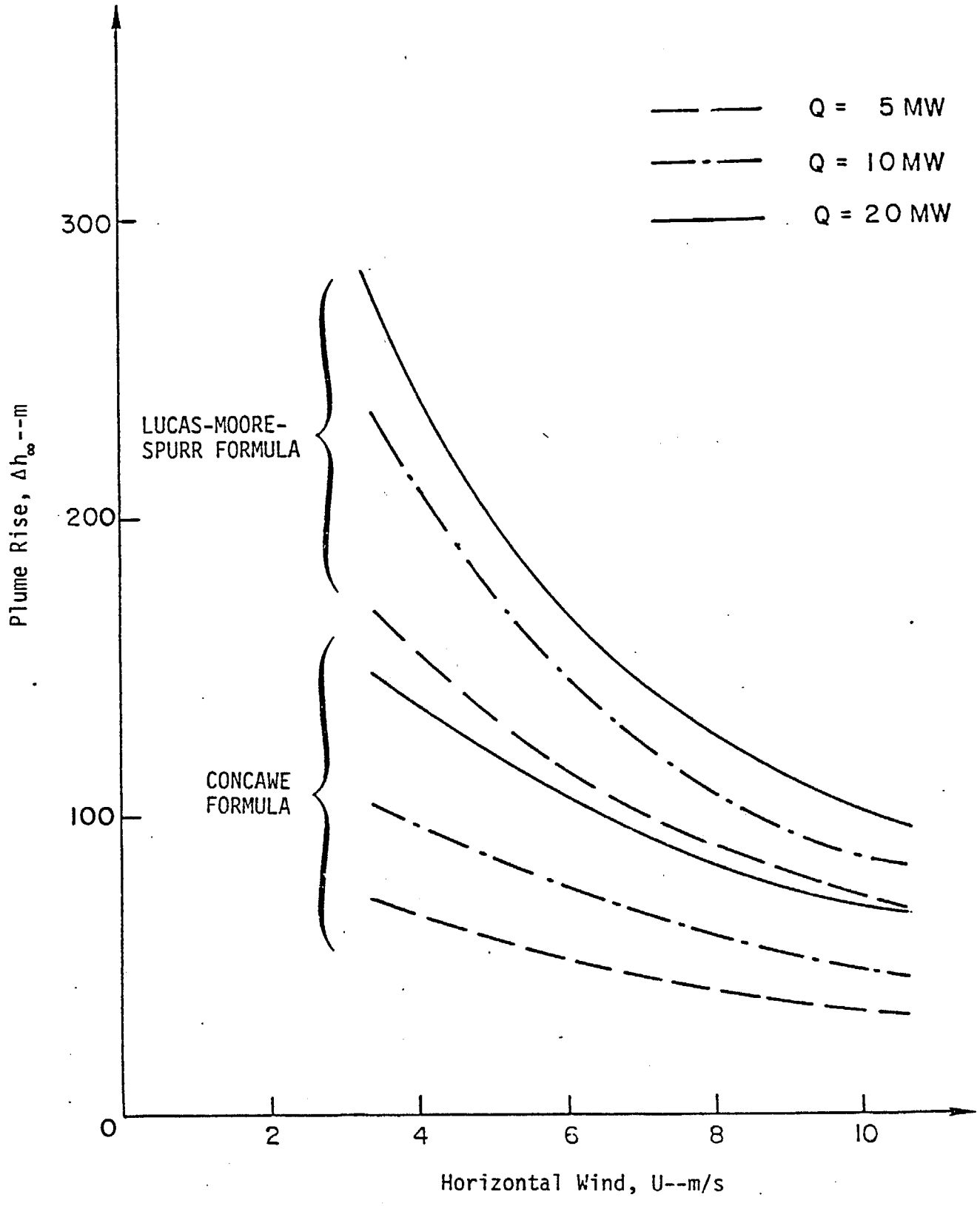

FIGURE III-2. COMPARISON OF TWO EMPIRICAL FORMULAS FOR PLUME RISE

$$w = F^{1/3} \cdot z^{-1/3} \cdot \text{Function}\left(\frac{r}{R}\right) \quad , \qquad \text{(III-8)}$$

$$g \cdot \left(\frac{T - T_r}{T_r}\right) = F^{2/3} \cdot z^{-5/3} \cdot \text{Function}\left(\frac{r}{R}\right) \quad , \qquad \text{(III-9)}$$

where

R = plume radius
w = vertical velocity of the plume
F = buoyancy flux (= $gQ/\pi\rho C_p T$)
T = plume temperature
T_r = reference temperature (a constant)
r = distance from the plume axis.

For an unstably stratified atmosphere with the ambient temperature T_a, characterized by

$$-\frac{g}{T_R}\frac{dT_a}{dz} = kz^p \quad , \qquad \text{(III-10)}$$

where T_a is the ambient temperature, which may be a function of height, and p is an exponent that characterizes the vertical temperature profile, Batchelor also derived the following equations:

$$R = \text{Constant} \cdot z \quad , \qquad \text{(III-11)}$$

$$w = (kz^p)^{1/2} \cdot z \cdot \text{Function}\left(\frac{r}{R}\right) \quad , \qquad \text{(III-12)}$$

$$g \cdot \left(\frac{T - T_a}{T_r}\right) = (kz^p) \cdot z \cdot \text{Function}\left(\frac{r}{R}\right) \quad . \qquad \text{(III-13)}$$

However, these results can also be obtained, as a limiting case, from a more sophisticated approach based upon the so-called entrainment theory.

In its simplest form, the entrainment theory, as invoked by Morton, Taylor, and Turner (1956), entails the use of the equations for conservation of mass, momentum, and heat along the cross-wind direction. For a neutral atmosphere with a uniform horizontal wind, these equations can be written as

Mass

$$U \frac{dR^2}{dx} = 2\alpha w R \quad , \qquad \text{(III-14)}$$

Momentum

$$U \frac{d}{dx}(R^2 w) = R^2 \cdot g \cdot \left(\frac{\rho_a - \rho}{\rho}\right) \quad , \qquad \text{(III-15)}$$

Heat

$$R^2 \cdot U \cdot g\left(\frac{\rho_a - \rho}{\rho}\right) = F \quad . \qquad \text{(III-16)}$$

where

α = entrainment constant
ρ_a = density of ambient air
ρ = density of plume
F = buoyancy flux.

Equation (III-14) specifies that ambient air with a mass proportional to the vertical movement is entrained into the plume at the plume's edge. The proportionality constant, α, must be determined from experimental data. Furthermore, a flat-top profile has also been assumed for the temperature and vertical velocity across the plume. For the simple case in which the effect of the initial plume radius and effluent exit velocity can be neglected, the integration of Eq. (III-10) yields the following expression for the plume rise:

$$\Delta h = \int_0^x \left(\frac{w}{U}\right) \, dx \quad ,$$

$$= \left(\frac{3}{2\alpha^2}\right)^{1/3} \frac{F^{1/3} \, x^{2/3}}{U} \quad . \qquad \text{(III-17)}$$

This is the well-known two-thirds power law for plume rise as a function of downwind distance. Note also that Eq. (III-17) is similar to the Briggs' formula, Eq. (III-5), except for the experimentally determined constant.

Like their empirical counterparts, analytical approaches based on simple theories are somewhat controversial. Many relationships have been derived that are similar to Eq. (III-17) but that have different functional dependences. For example, if one assumes that the entrainment is due to environmental turbulence and that it is proportional to the wind speed--an assumption made in an analysis by Bosanquet (1957)--then the modified Eq. (III-14) will yield a linear growth of plume radius that leads to the following expression for plume rise:

$$\Delta h \sim \frac{F \cdot \ell n \, x}{U^3} \quad . \qquad \text{(III-18)}$$

Obviously, this equation is not applicable in the initial phase, and it will tend to underestimate the plume rise at large distances downwind.

Using a different approach, Priestly (1956) chose as governing equations those for the conservation of momentum, heat, and kinetic energy. Furthermore, instead of assuming that mass is being entrained into the plume as we discussed earlier, he postulated that kinetic energy is being entrained into the plume. This theory predicts a linear rate of growth for the plume radius as a function of height. Consequently, the following relationship for plume rise can be deduced:

$$\Delta h \sim \frac{F^{1/4} \, x^{3/4}}{U} \quad . \qquad \text{(III-19)}$$

This equation is similar to the Lucas-Moore-Spurr formula, Eq. (III-2). In fact, Moore (1968) pointed out that buoyant plumes tend to break up into discrete puffs and that the problem is three-dimensional. He showed that a three-dimensional model similar to Eq. (III-19) can indeed be derived if one assumes that the heat content of the surviving lumps increases linearly with distance downwind. He thus stated that the basic difference between the two-dimensional and three-dimensional models is that the former gives a two-thirds power law dependence on downwind distance for plume rise, whereas the latter specifies a three-fourths power law dependence. In a more recent paper, Moore (1974) further maintained that a three-dimensional "lumpy" model of the plume gives marginally better agreement with observations than a two-dimensional "continuous" model, such as Eq. (III-17). This finding apparently contradicts the conclusions of Briggs (1969, 1971), who showed that Eq. (III-2), when compared with data, overpredicts plume rise by 30 percent, whereas Eq. (III-5) does so by only 9 percent (Briggs, 1969).

As is evident from this cursory review, neither the empirical approaches nor the theoretical ones based on the simple entrainment concept are sufficient to describe the behavior of buoyant plumes. The main difficulty is that both approaches are too simple to account adequately for the complex physical processes undergone by the plume in the atmosphere. Stack parameters (such as the rate of heat emission and the stack height) and ambient conditions (such as atmospheric stability, surface roughness, and wind shear) are all known to affect plume behavior. These parameters and their variations must therefore be incorporated in a realistic model.

B. FORMULATION OF THE BUOYANT PLUME MODEL

Before embarking on a full discussion of a three-dimensional numerical model for simulating a buoyant plume, we first summarize the arguments in favor of such an endeavor.

> As emphasized previously, the parameters affecting the behavior of buoyant plumes are numerous and the processes

involved are complex. Therefore, to provide a realistic description of plume development, a model must at least be able to accommodate these complexities.

> As suggested by Moore (1968), dispersion of the plume in the atmosphere is not one-dimensional in nature. This points out not only the weakness in the conventional entrainment theory, but also the need for a multi-dimensional approach.

> As indicated by Turner (1972), there is a discrepancy between the effects of buoyancy and the kinetic motion of the mean flows in the formulation of the entrainment theory. Depending upon the velocity profile assumed, only one-third to three-fifths of the potential energy can be accounted for in a neutral atmosphere. Thus, a more sophisticated formulation is warranted to further the understanding of the various processes.

> And finally, because of the availability of large, high-speed digital computers in the last few years, the three-dimensional approach has become feasible.

Having made these comments, we now proceed to delineate the formulation of a three-dimensional model based on the numerical solution of the simplified Navier-Stokes equations. In Subsection 1, we briefly describe the derivation of the model equations. Because of their importance, turbulent diffusivities for a buoyant plume provide the focus of the second subsection.

1. Derivation of the Model Equations

The model equations for buoyant plume simulation can be derived in three steps. In the first step, we establish the equations for the reference state, corresponding to conditions in the absence of the plume or upwind of the stack. In the second, we derive the equations describing per-

turbations to the reference state due to the presence of the plume. In the last step, we obtain the final form of the model equations by performing time averages over the field equations to account for turbulent motion.

The general equations governing the temperature, velocity, pressure, and density variations in the atmosphere pertinent to the buoyant plume can be written as follows:

The equation of continuity

$$\left(\frac{\partial}{\partial t} + \mathbf{v} \cdot \nabla\right) \rho + \rho \nabla \cdot \mathbf{v} = 0 \quad , \tag{III-20}$$

The momentum equation

$$\left(\frac{\partial}{\partial t} + \mathbf{v} \cdot \nabla\right) \mathbf{v} = \frac{1}{\rho} \nabla p - g\mathbf{k} + \nu \left[\nabla^2 \mathbf{v} + \frac{1}{3} \nabla (\nabla \cdot \mathbf{v})\right] \quad , \tag{III-21}$$

The energy equation

$$\rho c_v \left(\frac{\partial}{\partial t} + \mathbf{v} \cdot \nabla\right) T + p \nabla \cdot \mathbf{v} = K \nabla^2 T \quad , \tag{III-22}$$

The species equation

$$\left(\frac{\partial}{\partial t} + \mathbf{v} \cdot \nabla\right) \chi + \chi \nabla \cdot \mathbf{v} = D \nabla^2 \chi \quad , \tag{III-23}$$

The equation of state

$$p = \rho R T \quad , \tag{III-24}$$

where

$\mathbf{v}$ = velocity vector,
T = temperature,
p = pressure,
ρ = density,
χ = concentration,
g = gravitational constant,
ν = kinematic viscosity,
K = heat conductivity,
D = molecular diffusivity,
c_v = constant-volume specific heat.

We should note that the Coriolis force is neglected in the momentum equation because the horizontal scale involved is rather small. To accommodate an arbitrary prescription of temperature stratification and wind shear in the undisturbed atmosphere, we describe the reference state by

$$T_r = T_r(z) \quad , \tag{III-25}$$

$$\mathbf{v}_r = \begin{bmatrix} u_r(z) \\ v_r(z) \\ 0 \end{bmatrix} \quad . \tag{III-26}$$

Substitution of Eq. (III-26) into Eq. (III-21) immediately yields the following equation for p_r:

$$\frac{dp_r}{dz} = -\rho_r g \quad . \tag{III-27}$$

Thus, the reference state is in hydrostatic equilibrium. By integrating Eq. (III-27) with the aid of Eq. (III-24), we obtain

$$p_r(z) = p_r\,(0)\,\exp\left[-\frac{g}{R}\int_0^z \frac{dz}{T_r(z)}\right] \qquad \text{(III-28)}$$

$$\rho_r(z) = \frac{p_r(z)}{RT_r(z)} \quad . \qquad \text{(III-29)}$$

Equations (III-25) through (III-29) give the complete description of the reference state.

The next step is to derive a set of equations describing the effects due to the plume. These effects are considered to be perturbations to the reference state. Thus, we decompose the variables as follows:

$$p = p_r(z) + \tilde{p} \quad ,$$

$$\rho = \rho_r(z) + \tilde{\rho} \quad ,$$

$$T = T_r(z) + \tilde{T} \quad .$$

By assuming that $\tilde{p}$, $\tilde{\rho}$, and $\tilde{T}$ are small deviations from p_r, ρ_r, and T_r, and assuming that the density variation in the reference state is small, we can simplify Eqs. (III-20) through (III-24) by using the Boussinesq approximation. As a result, we can derive the following set of equations (Spiegel and Veronis, 1960; Dutton and Fichtl, 1969):

$$\nabla \cdot \mathbf{v} = 0 \quad , \qquad \text{(III-30)}$$

$$\frac{\partial \mathbf{v}}{\partial t} + \mathbf{v} \cdot \nabla\, \mathbf{v} = -\frac{\nabla \tilde{p}}{\rho_m} + g\,\frac{\tilde{T}}{T_m}\,\mathbf{k} + \nu\,\nabla^2\,\mathbf{v} \quad , \qquad \text{(III-31)}$$

$$\frac{\partial \tilde{T}}{\partial t} + \mathbf{v} \cdot \nabla\, \tilde{T} = -w\left(\frac{\partial T_r}{\partial z} + \frac{g}{c_p}\right) + K\,\nabla^2\,\tilde{T} \quad , \qquad \text{(III-32)}$$

$$\frac{\partial \chi}{\partial t} + \mathbf{v} \cdot \nabla \chi = D \nabla^2 \chi \quad , \tag{III-33}$$

where c_p is the constant-pressure specific heat and ρ_m and T_m denote constant mean values for density and temperature, respectively.

It is important to note that when Boussinesq used a similar set of equations in 1903, he did so for an incompressible fluid with density fluctuations due to variations in specific weights. As later shown by Spiegel and Veronis (1960), the restriction of incompressibility can be removed for a shallow layer of fluid. Finally, Dutton and Fichtl (1969) showed that the Boussinesq approximation is valid if deviations from a reference state are small and, therefore, that it is not necessarily limited to shallow layers. It is in this sense we invoked the Boussinesq approximation to deduce the above system of equations.

To derive the appropriate equations for a turbulent flow, we decomposed the velocity, pressure, and temperature into time-average mean values and fluctuating components:

$$\mathbf{v} = \overline{\mathbf{v}} + \mathbf{v}' \quad ,$$

$$\tilde{p} = \overline{p} + p' \quad ,$$

$$\tilde{T} = \overline{T} + T' \quad ,$$

$$\chi = \overline{\chi} + \chi' \quad ,$$

Substituting these expressions into Eqs. (III-30) through (III-33), which govern the instantaneous values of the field variables, and taking time averages, we can readily show that the following system of equations for the mean variables can be derived (Monin and Yaglom, 1971):

$$\nabla \cdot \bar{v} = 0 \quad , \tag{III-34}$$

$$\frac{\partial \bar{v}}{\partial t} + \bar{v} \cdot \nabla \bar{v} = - \frac{\nabla \bar{p}}{\rho_m} + g \cdot \frac{\bar{T}}{T_m} k + \nabla \cdot (K_M \nabla \bar{v}) \quad , \tag{III-35}$$

$$\frac{\partial \bar{T}}{\partial t} + \bar{v} \cdot \nabla \bar{T} = -\bar{w} \cdot \left[\frac{\partial T_r}{\partial z}\right] + \nabla \cdot (K_H \nabla \bar{T}) \quad , \tag{III-36}$$

$$\frac{\partial \bar{\chi}}{\partial t} + \bar{v} \cdot \nabla \bar{\chi} = \nabla \cdot (K_\chi \nabla \bar{\chi}) \quad . \tag{III-37}$$

In deriving this final form of the model equation, we neglected the molecular diffusion of heat, mass, and momentum, since they are typically small compared with their turbulent counterparts. More importantly, however, in the derivation of these equations is the assumption of turbulent eddy diffusivities, as defined by

$$K_M \nabla \bar{v} = - \overline{v'v'} \quad , \tag{III-38}$$

$$K_H \nabla \bar{T} = - \overline{T'v'} \quad , \tag{III-39}$$

$$K_\chi \nabla \bar{c} = - \overline{c'v'} \quad , \tag{III-40}$$

That is, the model equations are based on the so-called K-theory. Because of the important role played by the eddy diffusivities, particularly in the dispersion of a buoyant plume, we devote the next section to a discussion of these diffusivities, as well as to a description of a scheme for prescribing them.

2. Approximating Turbulent Diffusion of a Buoyant Plume by Eddy Diffusivities

As in many other related studies of the atmosphere, the most difficult, and also the most crucial, factor in the simulation of plumes is the specification of a reasonable scheme to represent turbulent processes. This is

particularly true for the dispersion of a buoyant plume because the fate of a buoyant plume is controlled not only by the ambient atmospheric turbulence, but also by the turbulence generated by its own buoyancy. Both of these are extremely complicated and still defy accurate analytic description. Although theoretical studies based on higher closure schemes for hierarchies of turbulence moment equations have recently been carried out (Deardorff, 1970, 1972), they have been restricted to certain special cases. Furthermore, the computational effort required for this approach is beyond the limits of a practically oriented problem. Thus, our model is based on a simple alternative--the concept of turbulent eddy diffusivities, or K-theory.

The limitations of models based on the K-theory or the gradient transport theory are numerous and well known. They can be generally grouped into the following two categories:

> Length- and time-scale constraints
> Directional constraints.

The first type is related to the spatial and temporal homogeneities of the mean field. Corrsin (1974) summarized the conditions necessary for satisfying such constraints:

> The transport mechanism length scale must be much smaller than the distance over which the curvature of the mean transported field gradient changes appreciably.
> The transport mechanism time scale must be much smaller than the time during which the mean transported field gradient changes appreciably.
> The transport mechanism length scale must be essentially constant over a distance of a length scale and over a distance for which the mean transported field changes appreciably.
> The transport mechanism velocity must be appreciably more uniform than the length scale.

The second constraint arises when, for example, the Reynolds stress, a second-order tensor, has been replaced by an inner product of a second rank tensor and a vector. The conditions for satisfying this constraint are, however, more difficult to delineate. Although qualitative estimates for the validity of both constraints can be made, we assume for the present that the gradient transport approach is plausible.

The gradient transport approach we have adopted here entails a parameterization of turbulent eddy diffusivities, which are determined by a self-regulating procedure. Because of the special nature of buoyant plumes, our relationships for the eddy diffusivities consist of two parts:

$$K = f_p K_p + f_a K_a \quad , \qquad \text{(III-41)}$$

where K denotes the total eddy diffusivity for momentum, heat, or mass, and K_p and K_a, respectively, represent the contributions from turbulence generated by the buoyancy of the plume and the ambient atmospheric turbulence. To account for their relative importance adequately in the initial and final phases of plume development, we have made f_p and f_a weighting factors that depend on the distance from the stack. Let s be the distance from the stack and let L represent a scale length. Note that near the stack we must have

$$f_a(s) \approx 0 \quad , \quad f_p(s) \approx 1 \quad , \quad \frac{s}{L} << 1 \quad ,$$

and at a distance far downwind of the stack,

$$f_p(s) \approx 0 \quad , \quad f_a(s) \approx 1 \quad , \quad \frac{s}{L} >> 1 \quad ,$$

expressing the relative dominance of the buoyancy-generated turbulence and ambient atmospheric turbulence in the respective regions.

The specifications for K_p and K_a are, of course, very difficult. Following Slawson and Csanady (1967), we propose to use the following

simple formula for characterizing the turbulent diffusion in the vicinity of the stack:

$$K_p = c\, w\, R \quad , \tag{III-42}$$

where c is a constant of the order of 10^{-1}, w is the vertical velocity, and R is a measure of the plume radius that can be taken to be the standard deviation of the plume dispersion. Equation (III-42) appears to be realistic because it assumes that turbulent eddy diffusivity is proportional to the vertical movement, which is, in turn, generated by the buoyancy. As a matter of fact, Slawson and Csanady (1967) actually established the equivalence between Eq. (III-42) and the commonly used entrainment theory.

At large distances from the stack, where the plume loses its buoyancy, the ambient turbulence in the atmosphere becomes the dominant mechanism for for dispersing the plume. There are many established formulas for the turbulent eddy diffusivities in the atmospheric surface layer (Businger, 1973; Pandolfo, 1969). For example Pandolfo proposed a scheme which has been successfully applied in the simulation of land and sea breezes by Liu, Mundkur, and Yocke (1974).

In this scheme, the eddy diffusivities for the momentum fluxes are given by

$$(k_m)_a = \begin{cases} k^2 \cdot (z + z_0)^2 \cdot S \cdot (1 + \alpha R_i)^2 \quad , & R_i \geq 0 \quad , \\ k^2 \cdot (z + z_0)^2 \cdot S \cdot (1 - \alpha R_i)^{-2} \quad , & 0 > R_i > -0.048 \quad , \\ (hk)^{\frac{2}{3}} (z + z_0)^2 \cdot \left| \frac{g}{t} \left(\frac{\partial \bar{T}}{\partial z} + \Gamma \right) \right|^{\frac{1}{2}} \cdot |R_i|^{-\frac{1}{6}} \quad , & -0.048 \geq R_i \quad , \end{cases} \tag{III-43}$$

where

k = the von Kármán constant,
h = the Priestley constant,
α = the Monin-Obukhov constant,
z_0 = the roughness parameter,
$S = \partial|\overline{v}|/\partial z$, the wind shear,
$R_i = (g/T_m)\{(\partial\overline{T}/\partial z) + \Gamma\}/S^2$, the Richardson number,
$\Gamma = g/c_p$, the adiabatic lapse rate.

The eddy diffusivities for the heat fluxes are given by

$$(k_e)_a = \begin{cases} k^2 \cdot (z + z_0)^2 \cdot S \cdot (1 + \alpha R_i)^2 & , \quad R_i \geq 0 \\ k^2 \cdot (z + z_0)^2 \cdot S \cdot (1 - \alpha R_i)^{-3} & , \quad 0 > R_i > -0.048 \\ h \cdot (z + z_0)^2 \cdot \left| \frac{g}{T_m} \left(\frac{\partial \overline{T}}{\partial z} + \Gamma \right) \right|^{\frac{1}{2}} & , \quad -0.048 \geq R_i \end{cases} \qquad \text{(III-44)}$$

To prevent the values of these eddy diffusivities from becoming unrealistically small or large, Pandolfo (1969) imposed the following limits:

$$10^7 \text{ cm}^2/\text{sec} \geq K_m, K_e \geq 10^4 \text{ cm}^2/\text{sec} \quad , \quad z \geq 100 \text{ m} \quad ,$$

$$10^7 \text{ cm}^2/\text{sec} \geq K_m, K_e \geq 10^2 \text{ cm}^2/\text{sec} \quad , \quad z < 100 \text{ m} \quad .$$

C. SELECTION OF THE NUMERICAL METHOD

Numerical methods for solving the set of equations described in Section B are not lacking. A variety of methodologies have been developed to compute the flow fields from fluid dynamic equations, and many new ones

are being proposed. These methods can be generally classified in the following two categories:

> The functional approach
  - Finite element methods (Tong, 1970)
  - Galerkin methods (Finalayson and Scriven, 1966)
  - Spectral or quasi-spectral methods (Orszag and Israeli, 1972, 1974).

> The finite difference approach
  - Conventional finite difference schemes
  - Unconventional finite difference schemes
    - Particle-in-cell technique (Harlow, 1963, 1964)
    - The second-moment method (Egan and Mahoney, 1972)
    - SHASTA* method (Boris and Book, 1973)
    - Other methods.

In the functional approach, the solutions to the governing equations are generally obtained by expanding them into known functions (base functions). A variety of functions, such as piecewise linear functions and harmonic functions, can be chosen as the base functions. The application of this approach to any particular problem is, however, critically dependent on the selection of these base functions, which in turn depends on the nature of the problem. Although this approach has been extensively applied to problems in solid mechanics (Zienkiewicz and Cheung, 1967), its use in fluid dynamics is restricted to problems that have either (1) complex boundaries or (2) spherical or cylindrical geometries.

In the finite difference approach, the domain of interest is first divided into an array of cells. A set of finite difference equations is then then derived based on an approximation to the governing equations in

*Sharp and Smooth Transport Algorithm.

differential form. The solutions are then obtained by solving the resultant finite difference equations. A number of classical (or conventional) finite difference schemes have been developed and are widely used; they differ, in general, only in the order of approximation for the space and time derivatives. The drawback of the conventional finite difference schemes is also well known. Artificial smoothing and phase shift, introduced in the process of discretization, tend to degrade the accuracy of the numerical solutions. The unconventional schemes are thus designed to reduce these errors. Unfortunately, none of these has yet proved to be universally applicable. Furthermore, like the functional approach, the unconventional finite difference schemes are often rather cumbersome to use. Thus, on the basis of a preliminary assessment, we ruled out both the unconventional finite difference schemes and the functional approach as possible candidates for the means of solving the model equations for buoyant plumes.

In selecting a finite difference method, one must consider the following characteristics of each possible candidate:

> Stability, convergence, and consistency of the solution procedure.
> Accuracy of the numerical scheme.
> Computing time required to perform the calculations.
> Computer storage required to carry out the computations.
> Ease of implementation of the numerical algorithm.
> Adaptability of the numerical method.

The first four criteria are of particular importance in the long-period simulation of three-dimensional flow fields. They have therefore played the dominant roles in the selection of a finite difference scheme for solving the buoyant plume problem.

A review of previous applications of finite difference techniques to solve transient fluid flow problems reveals that most investigations have been carried out for only one or two spatial dimensions (e.g., Harlow and

Welch, 1965)*. The extension of these techniques to the more practical and thereby more interesting case of three-dimensional space has probably been lacking for two reasons. The first and most obvious one is the requirement for a large amount of computation associated with the finite difference solution of a three-dimensional problem. The amount of computing effort required could not be accommodated until the latest generation of high-speed computers emerged. The second reason for the late appearance of the three-dimensional application is intimately connected with the special role played by one of the dependent variables--the pressure. The equations of motion, which govern both the velocities and pressure, do not involve the time derivative of the pressure. Difficulties are thus encountered in the explicit numerical solution of a time-dependent problem.

In two-dimensional problems, this difficulty is resolved through an approach based on the vorticity formulation. By introducing a vorticity and a stream function (Harlow and Welch, 1965), one can replace the momentum equation by a single vorticity transport equation. Furthermore, the pressure, which is explicitly eliminated from the momentum equation, is now governed by a Poisson equation. Although problems still exist regarding the treatment of boundary conditions (Chorin, 1967), this approach becomes at least numerically tractable. However, this approach cannot be extended to three dimensions, since a simple Poisson equation for the pressure is difficult to obtain for that case.

The method of fractional steps, also known as the method of splitting, offers a powerful means for solving complicated partial differential equations containing several variables. This method, first developed by Yanenko in Russia, divides the integration step into a series of intermediate steps, one in each spatial coordinate (Yanenko, 1971). Consistency with the original equations and stability criterion at each stage is thus

---

*Numerical techniques for solving special three-dimensional flow problems have been developed [for example, see Pandolfo and Jacobs (1973)]. However, these problems invoke the hydrostatic assumption and are not three-dimensional in the most general sense.

assured. As a result, the method allows for the construction of an accurate and efficient numerical scheme. Although most of the applications to date have been to potential flow problems, this method appears to be ideally suited for the buoyant plume problem.

In a series of publications, Chorin (1967, 1968, 1970) described a numerical scheme, which is basically an application of the method of fractional steps, for solving the three-dimensional time-dependent Navier-Stokes equations. In this scheme, the computation of the pressure field is handled via an iterative process, which Chorin (1968) reported led to the successful simulation of three-dimensional thermal convection. We adopted this scheme in the present project as the general approach to solving the equations governing the behavior of buoyant plumes.

1. Description of the Numerical Method

The system of equations governing the behavior of a buoyant plume in a turbulent, stratified atmosphere was derived in Section B. To facilitate the description of the solution procedure, we repeat this set of equations here:

$$\nabla \cdot \bar{v} = 0 \quad , \tag{III-34}$$

$$\frac{\partial \bar{v}}{\partial t} + \bar{v} \cdot \nabla \bar{v} = - \frac{\nabla \bar{p}}{\rho_m} + g \cdot \frac{\bar{T}}{T_m} k + \nabla \cdot (K_M \nabla \bar{v}) \quad , \tag{III-35}$$

$$\frac{\partial \bar{T}}{\partial t} + \bar{v} \cdot \nabla \bar{T} = -\bar{w} \cdot \left[\frac{\partial T_r}{\partial z}\right] + \nabla \cdot (K_H \nabla \bar{T}) \quad , \tag{III-36}$$

$$\frac{\partial \bar{\chi}}{\partial t} + \bar{v} \cdot \nabla \bar{\chi} = \nabla \cdot (K_\chi \nabla \bar{\chi}) \quad . \tag{III-37}$$

In our treatment, the method of fractional steps is applied to Eqs. (III-35) through (III-37). Essentially, this method entails splitting any single time step into three intermediate steps, one for each space coordinate. For example, the equation governing the χ component velocity in Eq. (III-35) is replaced by the following three equations:

$$u^{*} = u^{n} + \Delta t \left[-u^{n} \frac{\partial u^{*}}{\partial x} + \frac{\partial}{\partial x} \left(K_{MH} \frac{\partial u^{*}}{\partial x} \right) \right] \quad , \qquad \text{(III-45)}$$

$$u^{**} = u^{*} + \Delta t \left[-v^{*} \frac{\partial u^{**}}{\partial y} + \frac{\partial}{\partial y} \left(K_{MH} \frac{\partial u^{**}}{\partial y} \right) \right] \quad , \qquad \text{(III-46)}$$

$$u^{aux} = u^{**} + \Delta t \left[-w^{**} \frac{\partial u^{aux}}{\partial z} + \frac{\partial}{\partial z} \left(K_{MH} \frac{\partial u^{aux}}{\partial z} \right) \right] \quad , \qquad \text{(III-47)}$$

where the superscripts "*," "**," and "aux (auxiliary field)" denote the three intermediate steps, Δt is the time increment, and n denotes the given x-direction velocity at time level n. Similar expressions for the y- and z-direction velocities, temperature, and pollutant concentration can also be written. The spatial derivatives appearing in these equations must be further discretized by adopting appropriate difference schemes. However, for simplicity, these schemes are not given here.

The solution procedure is then completed by relating the auxiliary velocity fields to the desired solutions at time level n + 1 through the following equations:

$$u^{n+1} = u^{aux} - \Delta t \frac{\partial p^{n+1}}{\partial x} \quad , \qquad \text{(III-48)}$$

$$v^{n+1} = v^{aux} - \Delta t \frac{\partial p^{n+1}}{\partial y} \quad , \qquad \text{(III-49)}$$

$$w^{n+1} = w^{aux} - \Delta t \frac{\partial p^{n+1}}{\partial z} \quad , \qquad \text{(III-50)}$$

which are subject to the constraint expressed by Eq. (III-34):

$$\frac{\partial u^{n+1}}{\partial x} + \frac{\partial v^{n+1}}{\partial y} + \frac{\partial w^{n+1}}{\partial z} = 0. \quad . \qquad \text{(III-51)}$$

Chorin (1968) proposed an iterative scheme to solve Eqs. (III-48) through (III-50), subject to the constraint given by Eq. (III-51). His scheme can be symbolically expressed as follows:

$$p^{n+1,m+1} - p^{n+1,m} = -\lambda \, \mathbf{D} \cdot \mathbf{v}^{n+1,m+1} \quad , \tag{III-52}$$

$$\mathbf{v}^{n+1,m+1} = \mathbf{v}^{aux} - \Delta t \mathbf{G}^{m}p \quad , \tag{III-53}$$

where the second superscript m is the iterative index, $\mathbf{D}$ and $\mathbf{G}$ are finite difference versions of the divergence and gradient vectors, respectively, and λ is an adjustable parameter for optimizing the iterative procedure. The initial value for p can be taken, for example, as

$$p^{n+1,1} = p^{n} \quad . \tag{III-54}$$

The iteration is considered to be successful when the difference between two succeeding iterations is less than a prescribed criterion, ε:

$$\left| p^{n+1,m+1} - p^{n+1,m} \right| < \varepsilon \quad . \tag{III-55}$$

A discussion of the technique used to determine an optimum value for the relaxation parameter, λ, is discussed in the following

An alternative approach for obtaining the pressure field is the following. By taking the appropriate derivatives of Eqs. (III-48) through (III-50), and with the use of Eq. (III-51), one can derive the following Poisson equation:

$$\nabla^2 p^{n+1} = \frac{1}{\Delta t} \mathbf{D} \cdot \mathbf{v}^{aux} \quad . \tag{III-56}$$

This will, of course, require a fast and accurate Poisson solver, which does indeed exist. As part of this search for the most efficient numerical method, we also assessed this Poisson solver. However, in the first version of the computer codes that we developed for the present study, we used the Chorin approach.

To summarize the algorithm just described and to indicate the final form of the difference equations that were used to compute the velocity and pressure field, we present below the equations for the x-direction velocity:

$$u^{*}_{q+1}\left[\left(\frac{\Delta t}{2\Delta x}\right)\left(u_R + u^{n}_{q}\right) - \left(\frac{\Delta t}{\Delta x^2}\right) K^{n}_{MH,q} - \left(\frac{\Delta t}{4\Delta x^2}\right)\left(K^{n}_{MH,q+1} - K^{n}_{MH,q-1}\right)\right]$$

$$+ u^{*}_{q}\left[1 + \left(\frac{2\Delta t}{\Delta x^2}\right) K^{n}_{MH,q}\right] + u^{*}_{q-1}\left[-\left(\frac{\Delta t}{2\Delta x}\right)\left(u_R + u^{n}_{q}\right)\right.$$

$$\left. - \left(\frac{\Delta t}{\Delta x^2}\right) K^{n}_{MH,q} + \left(\frac{\Delta t}{4\Delta x^2}\right)\left(K^{n}_{MH,q+1} - K^{n}_{MH,q-1}\right)\right] = u^{n}_{q} \quad . \tag{III-57}$$

$$u^{**}_{r+1}\left[\left(\frac{\Delta t}{2\Delta y}\right)\left(V_R + V^{*}_{r}\right) - \left(\frac{\Delta t}{\Delta y^2}\right) K^{n}_{MH,r} - \left(\frac{\Delta t}{4\Delta y^2}\right)\left(K^{n}_{MH,r+1} - K^{n}_{MH,r-1}\right)\right]$$

$$+ u^{**}_{r}\left[1 + \left(\frac{2\Delta t}{\Delta y^2}\right) K^{n}_{MH,r}\right] + u^{**}_{r-1}\left[-\left(\frac{\Delta t}{2\Delta y}\right)\left(V_R + V^{*}_{r}\right)\right.$$

$$\left. - \left(\frac{\Delta t}{\Delta y^2}\right) K^{n}_{MH,r} + \left(\frac{\Delta t}{4\Delta y^2}\right)\left(K^{n}_{MH,r+1} - K^{n}_{MH,r-1}\right)\right] = u^{*}_{r} \quad . \tag{III-58}$$

$$u_{s+1}^{aux}\left[\left(\frac{\Delta t}{2\Delta z}\right) w_s^{**} - \left(\frac{\Delta t}{\Delta z^2}\right) K_{MV,s}^n - \left(\frac{\Delta t}{4\Delta z^2}\right)\left(K_{MV,s+1}^n - K_{MV,s-1}^n\right)\right]$$

$$+ u_s^{aux}\left[1 + \left(\frac{2\Delta t}{\Delta z^2}\right) K_{MV,s}^n\right] + u_{s-1}^{aux}\left[-\left(\frac{\Delta t}{2\Delta z}\right) w_s^{**}\right.$$

$$\left. - \left(\frac{\Delta t}{\Delta z^2}\right) K_{MV,s}^n + \left(\frac{\Delta t}{4\Delta z^2}\right)\left(K_{MV,s+1}^n - K_{MV,s-1}^n\right)\right]$$

$$= u_s^{**} - \Delta t w_s^{**}\left(\frac{\partial u_R}{\partial z}\right)_S \quad . \tag{III-59}$$

In these equations, the subscripts q, r, and s denote the nodes in the discretization of x, y, and z coordinates, respectively. Furthermore, we also have

$$P_{q,r,s} = (1 + \alpha_x + \alpha_y + \alpha_z)^{-1}\left\{\left[1 - \alpha_x - \alpha_y - \alpha_z\right] P_{q,r,s}^{n+1,m}\right.$$

$$+ \alpha_x\left[P_{q+2,r,s}^{n+1,m} + P_{q-2,r,s}^{n+1,m}\right] + \alpha_y\left[P_{q,r+2,s}^{n+1,m} + P_{q,r-2,s}^{n+1,m}\right]$$

$$\left. + \alpha_z\left[P_{q,r,s+2}^{n+1,m} + P_{q,r,s-2}^{n+1,m}\right] - \lambda D u^{aux}\right\} \quad , \tag{III-60}$$

where the subscript r denotes the reference state and,

$$\alpha_x = \frac{\lambda \Delta t}{4\Delta x^2} \quad ,$$

$$\alpha_y = \frac{\lambda \Delta t}{4\Delta y^2} \quad ,$$

$$\alpha_z = \frac{\lambda \Delta t}{4\Delta z^2} \quad .$$

The equations for v_r and w_r are similar to Eqs. (III-57) through (III-59). Equation (III-60) must be slightly modified at the boundaries depending on the type of boundary conditions used. Again, to avoid repetition, we do not present the full forms of these equations here.

2. Testing of the Computer Codes and the Numerical Algorithm

In order to obtain a more comprehensive understanding of the numerical algorithm, we tested a few of its aspects in some depth. A brief summary and a review of the most important results are provided in the following paragraphs.

To test both the methodologies we selected and the computer codes we developed, we applied the model to a simple but hypothetical case. The test case utilized a two-dimensional modeling region bounded by

$$0 \leq x \leq \frac{\pi}{4} \quad ,$$

$$0 \leq y \leq \frac{\pi}{2} \quad ,$$

with the following expressions at the boundaries

$$u = - \cos x \sin y \, e^{-2t} \quad , \tag{III-61}$$

$$v = \sin x \cos y \, e^{-2t} \quad , \tag{III-62}$$

and initial conditions

$$u = - \cos x \sin y \quad , \tag{III-63}$$

$$v = \sin x \cos y \quad . \tag{III-64}$$

The exact solutions of this problem, through direct substitution into the governing equation, are (Chorin, 1968)

$$u = - \cos x \sin y \, e^{-2t} \quad , \tag{III-65}$$

$$v = \sin x \cos y \, e^{-2t} \quad . \tag{III-66}$$

The exact solutions for 10 and 20 time steps are tabulated in Tables III-2a and III-3a, respectively. The differences between these exact solutions and corresponding model predictions are listed in Tables III-2b and III-3b for 10 and 20 time steps, respectively. It is clear from a perusal of these tables that the predicted velocities are accurate to within 1 percent of the exact solutions.

3. Optimization of the Computing Algorithm

As mentioned above, the numerical algorithm incorporates an iterative procedure for computation of the pressure field at every time step. Given the pressure field (p^n) at any time step n and the auxilliary velocity ($\underset{\sim}{v}^{aux}$) corresponding to time step n, the iterative procedure enables the pressure field (p^{n+1}) and velocity field (K^{n+1}) at time step n+1 to be estimated by the following symbolic scheme:

$$p^{n+1,m+1} - p^{n+1,m} = -\lambda(\underset{\sim}{D} \cdot \underset{\sim}{v}^{n+1,m+1}) \tag{III-67}$$

and

$$\underset{\sim}{v}^{n+1,m+1} = \underset{\sim}{v}^{aux} - \Delta t \underset{\sim}{G}^{m} p \tag{III-68}$$

As before, the subscript m is an iterative index and D and G are finite difference representations of the divergence and gradient vectors, respectively. The initial value of p is taken as

$$p^{n+1,1} = p^n \quad . \tag{III-69}$$

Table III-2a

EXACT SOLUTIONS AFTER 10 TIME STEPS

U-VELOCITY (ANALYTIC)

-0.	-0.	-0.	-0.	-0.	-0.	-0.	-0.	-0.	-0.
-6.43088E-02	-6.40641E-02	-6.33318E-02	-6.21175E-02	-6.04305E-02	-5.82836E-02	-5.56931E-02	-5.26787E-02	-4.92634E-02	-4.54732E-02
-1.28128E-01	-1.27641E-01	-1.26182E-01	-1.23762E-01	-1.20401E-01	-1.16124E-01	-1.10962E-01	-1.04956E-01	-9.81519E-02	-9.06003E-02
-1.90972E-01	-1.90246E-01	-1.88071E-01	-1.84465E-01	-1.79455E-01	-1.73080E-01	-1.65387E-01	-1.56435E-01	-1.46293E-01	-1.35038E-01
-2.52363E-01	-2.51403E-01	-2.48529E-01	-2.43764E-01	-2.37144E-01	-2.28719E-01	-2.18553E-01	-2.06724E-01	-1.93321E-01	-1.78448E-01
-3.11833E-01	-3.10647E-01	-3.07096E-01	-3.01208E-01	-2.93028E-01	-2.82617E-01	-2.70056E-01	-2.55439E-01	-2.38878E-01	-2.20500E-01
-3.68930E-01	-3.67527E-01	-3.63326E-01	-3.56359E-01	-3.46681E-01	-3.34365E-01	-3.19503E-01	-3.02210E-01	-2.82617E-01	-2.60873E-01
-4.23220E-01	-4.21609E-01	-4.16790E-01	-4.08799E-01	-3.97696E-01	-3.83567E-01	-3.66519E-01	-3.46681E-01	-3.24205E-01	-2.99261E-01
-4.74288E-01	-4.72483E-01	-4.67082E-01	-4.58127E-01	-4.45685E-01	-4.29851E-01	-4.10745E-01	-3.88514E-01	-3.63326E-01	-3.35372E-01
-5.21746E-01	-5.19761E-01	-5.13820E-01	-5.03968E-01	-4.90281E-01	-4.72863E-01	-4.51846E-01	-4.27390E-01	-3.99681E-01	-3.68930E-01

V-VELOCITY (ANALYTIC)

0.	6.43088E-02	1.28128E-01	1.90972E-01	2.52363E-01	3.11833E-01	3.68930E-01	4.23220E-01	4.74288E-01	5.21746E-01
0.	6.40641E-02	1.27641E-01	1.90246E-01	2.51403E-01	3.10647E-01	3.67527E-01	4.21609E-01	4.72483E-01	5.19761E-01
0.	6.33318E-02	1.26182E-01	1.88071E-01	2.48529E-01	3.07096E-01	3.63326E-01	4.16790E-01	4.67082E-01	5.13820E-01
0.	6.21175E-02	1.23762E-01	1.84465E-01	2.43764E-01	3.01208E-01	3.56359E-01	4.08799E-01	4.58127E-01	5.03968E-01
0.	6.04305E-02	1.20401E-01	1.79455E-01	2.37144E-01	2.93028E-01	3.46681E-01	3.97696E-01	4.45685E-01	4.90281E-01
0.	5.82836E-02	1.16124E-01	1.73080E-01	2.28719E-01	2.82617E-01	3.34365E-01	3.83567E-01	4.29851E-01	4.72863E-01
0.	5.56931E-02	1.10962E-01	1.65387E-01	2.18553E-01	2.70056E-01	3.19503E-01	3.66519E-01	4.10745E-01	4.51846E-01
0.	5.26787E-02	1.04956E-01	1.56435E-01	2.06724E-01	2.55439E-01	3.02210E-01	3.46681E-01	3.88514E-01	4.27390E-01
0.	4.92634E-02	9.81519E-02	1.46293E-01	1.93321E-01	2.38878E-01	2.82617E-01	3.24205E-01	3.63326E-01	3.99681E-01
0.	4.54732E-02	9.06003E-02	1.35038E-01	1.78448E-01	2.20500E-01	2.60873E-01	2.99261E-01	3.35372E-01	3.68930E-01

Table III-2b

DIFFERENCES BETWEEN EXACT SOLUTIONT
AND MODEL PREDICTIONS AFTER 10 TIME STEPS

U-ERROR (ANALYTIC - MODEL)

0.	0.	0.	0.	0.	0.	0.	0.	0.	0.
0.	-1.55723E-05	-1.01777E-04	-1.12911E-04	-1.09434E-04	-1.18689E-04	-7.32238E-05	-5.09410E-05	-2.31837E-05	0.
0.	-1.10922E-05	-3.82617E-05	-7.26889E-05	-3.06646E-05	-1.02201E-04	-6.07487E-05	-7.49346E-05	-7.39278E-06	0.
0.	1.23288E-05	4.86331E-05	1.37105E-05	2.94170E-05	-3.37527E-05	-2.84038E-05	-6.77192E-05	-3.35313E-05	0.
0.	1.93426E-05	8.93612E-05	3.35743E-05	5.92178E-05	4.03921E-06	2.08030E-05	-5.21479E-05	-4.35046E-05	0.
0.	3.02860E-05	1.04057E-04	5.61082E-05	9.84807E-05	4.97722E-05	4.57671E-05	-1.79523E-05	-3.48914E-05	0.
0.	2.12352E-05	7.86069E-05	6.87314E-05	1.09385E-04	6.52291E-05	4.41565E-05	1.28087E-05	-2.20670E-05	0.
0.	-4.13809E-06	3.75054E-05	3.34958E-05	8.95526E-05	5.39080E-05	8.20304E-05	8.77612E-05	-1.06185E-05	0.
0.	-5.58368E-06	-3.29699E-05	-3.05919E-05	-9.61332E-06	1.01623E-05	3.64074E-05	9.03959E-05	-2.93336E-05	0.
0.	0.	0.	0.	0.	0.	0.	0.	0.	0.

V-ERROR (ANALYTIC - MODEL)

0.	0.	0.	0.	0.	0.	0.	0.	0.	0.
0.	4.28379E-05	2.26907E-05	-9.51906E-07	5.90660E-06	-9.04190E-07	-1.38215E-05	-4.07801E-05	-4.65038E-06	0.
0.	1.33683E-04	1.10152E-04	2.81071E-05	3.93382E-05	-1.59049E-05	-4.22922E-05	-5.25991E-05	-1.64749E-05	0.
0.	8.15639E-05	6.75389E-05	2.70530E-05	1.54594E-05	-4.18126E-05	-3.50191E-05	-8.28804E-05	-7.82755E-05	0.
0.	1.06838E-04	1.37393E-04	7.92417E-05	8.28465E-05	3.05272E-05	3.10483E-05	-4.09911E-05	-6.30299E-05	0.
0.	2.06924E-05	3.28438E-05	2.85608E-05	4.51962E-05	1.95816E-05	1.25627E-05	-1.04035E-04	-1.20079E-04	0.
0.	2.53857E-05	6.90563E-05	7.61700E-05	1.08897E-04	8.73337E-05	8.65262E-05	-7.26055E-06	-5.81170E-05	0.
0.	-5.22078E-05	-1.89238E-05	2.65930E-05	3.68930E-05	3.99103E-05	7.69094E-05	-3.04151E-05	-1.01753E-04	0.
0.	-9.30941E-06	2.76740E-05	3.07404E-05	3.72394E-05	5.13945E-05	6.74778E-05	5.36989E-05	2.40035E-05	0.
0.	0.	0.	0.	0.	0.	0.	0.	0.	0.

Table III-3a

EXACT SOLUTIONS AFTER 20 TIME STEPS

U-VELOCITY (ANALYTIC)

-0.	-0.	-0.	-0.	-0.	-0.	-0.	-0.	-0.	-0.
-4.74510E-02	-4.72704E-02	-4.67301E-02	-4.58341E-02	-4.45893E-02	-4.30052E-02	-4.10937E-02	-3.88695E-02	-3.63495E-02	-3.35529E-02
-9.45408E-02	-9.41810E-02	-9.31045E-02	-9.13194E-02	-8.88393E-02	-8.56830E-02	-8.18747E-02	-7.74433E-02	-7.24224E-02	-6.68504E-02
-1.40911E-01	-1.40375E-01	-1.38770E-01	-1.36110E-01	-1.32413E-01	-1.27709E-01	-1.22033E-01	-1.15428E-01	-1.07944E-01	-9.96392E-02
-1.86209E-01	-1.85500E-01	-1.83380E-01	-1.79864E-01	-1.74979E-01	-1.68763E-01	-1.61262E-01	-1.52533E-01	-1.42644E-01	-1.31670E-01
-2.30090E-01	-2.29214E-01	-2.26594E-01	-2.22250E-01	-2.16214E-01	-2.08532E-01	-1.99264E-01	-1.88478E-01	-1.76259E-01	-1.62698E-01
-2.72219E-01	-2.71183E-01	-2.68084E-01	-2.62944E-01	-2.55802E-01	-2.46714E-01	-2.35749E-01	-2.22989E-01	-2.08532E-01	-1.92488E-01
-3.12277E-01	-3.11089E-01	-3.07533E-01	-3.01637E-01	-2.93445E-01	-2.83019E-01	-2.70440E-01	-2.55802E-01	-2.39218E-01	-2.20813E-01
-3.49958E-01	-3.48627E-01	-3.44642E-01	-3.38034E-01	-3.28853E-01	-3.17170E-01	-3.03073E-01	-2.86669E-01	-2.68084E-01	-2.47458E-01
-3.84976E-01	-3.83511E-01	-3.79128E-01	-3.71859E-01	-3.61759E-01	-3.48907E-01	-3.33399E-01	-3.15354E-01	-2.94909E-01	-2.72219E-01

V-VELOCITY (ANALYTIC)

0.	4.74510E-02	9.45408E-02	1.40911E-01	1.86209E-01	2.30090E-01	2.72219E-01	3.12277E-01	3.49958E-01	3.84976E-01
0.	4.72704E-02	9.41810E-02	1.40375E-01	1.85500E-01	2.29214E-01	2.71183E-01	3.11089E-01	3.48627E-01	3.83511E-01
0.	4.67301E-02	9.31045E-02	1.38770E-01	1.83380E-01	2.26594E-01	2.68084E-01	3.07533E-01	3.44642E-01	3.79128E-01
0.	4.58341E-02	9.13194E-02	1.36110E-01	1.79864E-01	2.22250E-01	2.62944E-01	3.01637E-01	3.38034E-01	3.71859E-01
0.	4.45893E-02	8.88393E-02	1.32413E-01	1.74979E-01	2.16214E-01	2.55802E-01	2.93445E-01	3.28853E-01	3.61759E-01
0.	4.30052E-02	8.56830E-02	1.27709E-01	1.68763E-01	2.08532E-01	2.46714E-01	2.83019E-01	3.17170E-01	3.48907E-01
0.	4.10937E-02	8.18747E-02	1.22033E-01	1.61262E-01	1.99264E-01	2.35749E-01	2.70440E-01	3.03073E-01	3.33399E-01
0.	3.88695E-02	7.74433E-02	1.15428E-01	1.52533E-01	1.88478E-01	2.22989E-01	2.55802E-01	2.86669E-01	3.15354E-01
0.	3.63495E-02	7.24224E-02	1.07944E-01	1.42644E-01	1.76259E-01	2.08532E-01	2.39218E-01	2.68084E-01	2.94909E-01
0.	3.35529E-02	6.68504E-02	9.96392E-02	1.31670E-01	1.62698E-01	1.92488E-01	2.20813E-01	2.47458E-01	2.72219E-01

Table III-3b

DIFFERENCES BETWEEN EXACT SOLUTIONS
AND MODEL PREDICTIONS AFTER 20 TIME STEPS

U-ERROR (ANALYTIC - MODEL)

0.	0.	0.	0.	0.	0.	0.	0.	0.	0.
0.	-2.01158E-05	-1.10134E-04	-9.72970E-05	-9.83005E-05	-8.62341E-05	-5.12226E-05	-4.05616E-05	-1.76561E-05	0.
0.	-1.41290E-05	-6.28194E-05	-8.23623E-05	-4.02388E-05	-9.17909E-05	-5.57289E-05	-6.72387E-05	-3.08616E-06	0.
0.	1.01275E-05	4.19891E-05	-1.42468E-06	1.75172E-05	-4.97118E-05	-2.86172E-05	-6.61370E-05	-2.80194E-05	0.
0.	2.18929E-05	1.08540E-04	3.80660E-05	6.09746E-05	-8.73537E-06	2.12144E-05	-4.97480E-05	-3.64344E-05	0.
0.	3.45593E-05	1.25285E-04	5.80070E-05	9.89019E-05	3.40192E-05	4.42012E-05	-1.89183E-05	-2.60894E-05	0.
0.	2.54819E-05	8.84927E-05	6.17148E-05	1.05776E-04	5.46661E-05	5.15186E-05	2.38490E-05	-9.83104E-06	0.
0.	-5.69454E-06	2.48858E-05	2.72425E-05	8.01825E-05	5.15406E-05	7.92297E-05	8.21184E-05	-2.54796E-06	0.
0.	-7.83992E-06	-3.71086E-05	-1.50228E-05	5.64530E-07	2.77369E-05	3.54499E-05	7.40177E-05	-2.06546E-05	0.
0.	0.	0.	0.	0.	0.	0.	0.	0.	0.

V-ERROR (ANALYTIC - MODEL)

0.	0.	0.	0.	0.	0.	0.	0.	0.	0.
0.	4.28965E-05	2.00245E-05	-5.75918E-06	-2.04831E-06	-1.93337E-06	-7.86446E-06	-3.68686E-05	-4.63863E-06	0.
0.	1.36822E-04	8.58448E-05	5.05287E-06	1.46823E-05	-2.13236E-05	-2.60384E-05	-4.70731E-05	-1.31568E-05	0.
0.	1.06766E-04	6.25678E-05	4.45903E-06	-1.66654E-06	-5.08039E-05	-3.48178E-05	-7.72102E-05	-6.95362E-05	0.
0.	1.13720E-04	1.18996E-04	5.58045E-05	5.82281E-05	1.50097E-05	2.17052E-05	-4.43855E-05	-6.26202E-05	0.
0.	2.50689E-05	3.88236E-05	2.75265E-05	3.74843E-05	1.13915E-05	3.62906E-06	-9.73165E-05	-1.13567E-04	0.
0.	8.14147E-06	5.90856E-05	7.63953E-05	9.82052E-05	7.17419E-05	6.37417E-05	-1.30360E-05	-6.25911E-05	0.
0.	-5.63616E-05	-6.68627E-06	3.83169E-05	4.08533E-05	2.68789E-05	4.09824E-05	-2.59759E-05	-8.33221E-05	0.
0.	-1.20786E-05	2.48962E-05	2.67402E-05	2.98888E-05	3.84825E-05	4.69532E-05	3.92611E-05	1.47603E-05	0.
0.	0.	0.	0.	0.	0.	0.	0.	0.	0.

The iteration is considered to be successful when the difference between successive iterations is less than a specified criterion, ε_p:

$$\left| p^{n+1,m+1} - p^{n+1,m} \right| < \varepsilon_p \quad . \tag{III-70}$$

This criterion ensures that the computed velocity field at time n+1 satisfies the divergence theorem to a certain accuracy at all points. Hence, from Eqs. (III-67) and (III-70):

$$\left| \underset{\sim}{D} \cdot \underset{\sim}{v}^{n+1,m+1} \right| \leq \varepsilon_p / \lambda \quad . \tag{III-71}$$

Since, in actuality it is the velocity field that is of primary interest, it is more meaningful to specify the desired accuracy in the computed velocity field. This may be done by specifying

$$\varepsilon_v = \varepsilon_p / \lambda \tag{III-72}$$

If the value of the relaxation parameter λ is known, the required convergence criterion, ε_p, for the iterative pressure computation is then easily estimated.

As pointed out by Chorin (1968), the iterative scheme may be expected to be convergent for a large range of values of λ, but will converge most rapidly for a certain value λ_{opt}. To determine the value of λ_{opt}, we examined the convergence characteristics of the algorithm for a number of different values of $\lambda_p (>0)$ and for a few simple test cases. Our results thus far indicate the following:

- For values of λ greater than a critical value λ_{crit}, the algorithm is oscillatory and divergent.
- For values of $\lambda = \lambda_{crit}$, the algorithm is oscillatory and neither divergent nor convergent.
- For values of λ very much less than λ_{crit} (but greater than zero) the algorithm is non-oscillatory and convergent, but convergence is slow.

> The algorithm is non-oscillatory and converges most rapidly for values of λ just slightly less than the critical value λ_{crit}.

The above conclusions are presented graphically in Figure III-3. In all the simulations executed thus far, we have found that a value of λ given by

$$\lambda_{opt} \approx (0.95 \text{ to } 0.98)\lambda_{crit} \tag{III-73}$$

gave the most rapid and satisfactory convergence. There was no appreciable change in the rate of convergence over the small range of λ values expressed by Eq. (III-73). In passing, we note that the above expression for λ_{opt} does not appear to hold when the grid lengths in the different directions differ by more than a factor of about three or four. This was not found to be a problem in our case since the grid lengths used in the simulations differed at most by a factor of about 1.5.

In order to obtain a stable solution with the numerical algorithm it is necessary to determine appropriate values for the time-step length (Δt) and the grid spacing ($\Delta x, \Delta y, \Delta z$).

An estimate of the appropriateness of the values chosen may be obtained by computing the following ratios.

$$R_t = \max\left(\frac{u\Delta t}{\Delta x}, \frac{v\Delta t}{\Delta y}, \frac{w\Delta t}{\Delta z}\right) \tag{III-74}$$

$$R_D = \max\left(\frac{K\Delta t}{\Delta x^2}, \frac{K\Delta t}{\Delta y^2}, \frac{K\Delta t}{\Delta z^2}\right) \tag{III-75}$$

where K is the value of diffusivity, and u,v, and w are the velocity components.

In order to obtain a stable solution it is necessary that $\Delta t, \Delta x, \Delta y$, and Δz be so chosen that $R_t < 1$ and $R_D < \frac{1}{2}$. For the solution of the problem of concern here, it was found that values of Δt substantially less than those dictated by the above constraints were required.

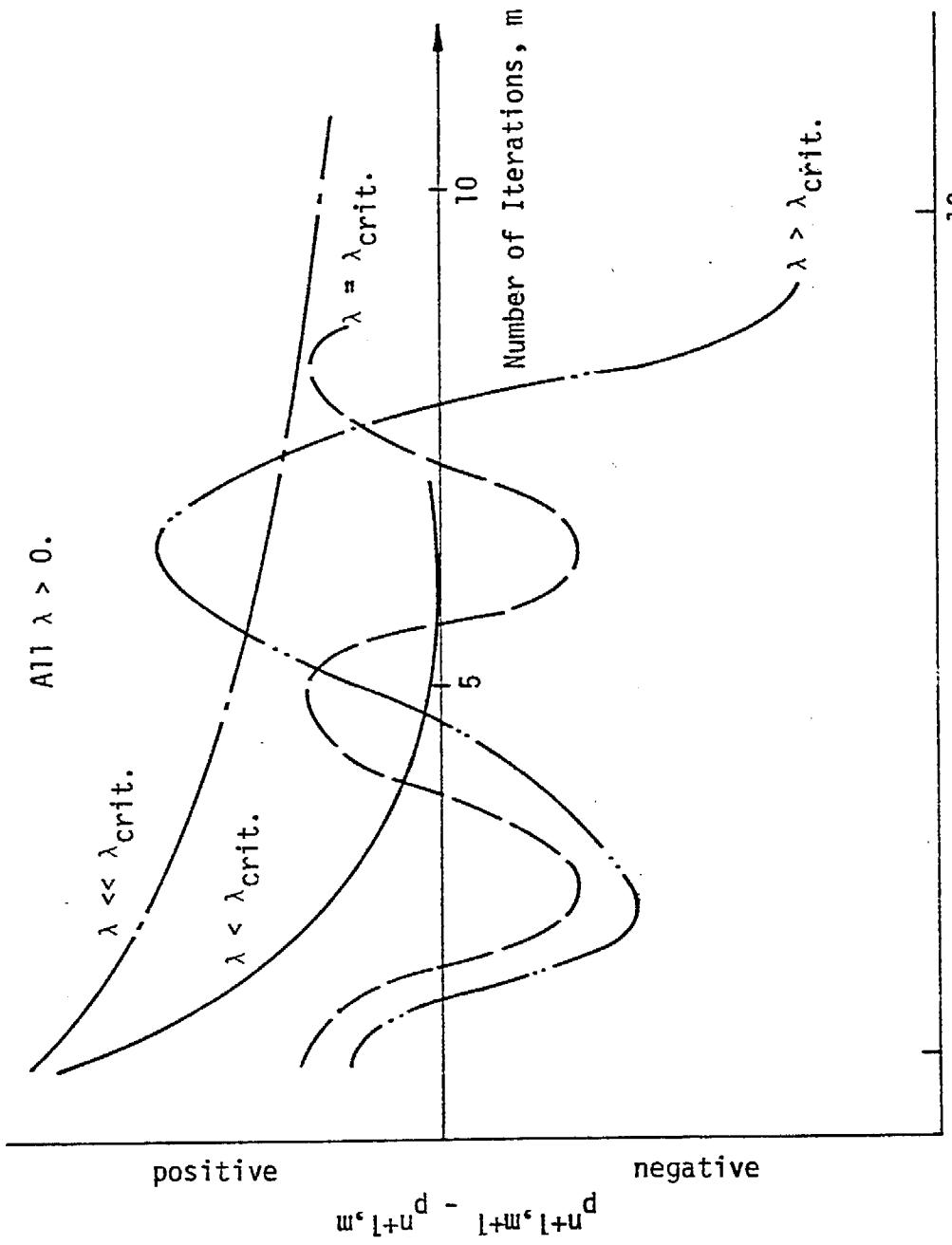

FIGURE III-3. THE EFFECT OF THE VALUE OF THE RELAXATION PARAMETER λ ON THE CONVERGENCE CHARACTERISTICS OF THE PRESSURE ALGORITHM

D. SENSITIVITY OF THE BUOYANT PLUME MODEL

Before the buoyant plume model is applied to simulate realistic situations, it is desirable to first examine the sensitivity of the numerical solution to the numerous variables and input parameters. In order to accomplish this we adopted a systematic approach in which the model was applied to progressively more complex and realistic conditions. By comparison of the simulations it was possible to identify the effects of each succeeding complication and hence to pinpoint those variables and parameters that had the most significant effect on the final solution. Furthermore, as the situations studied became more realistic, it was possible to evaluate the reasonableness of the model predictions. A large number of computer runs were made in this phase of the model development, and it is not possible to list here the details regarding each computer run. In the following paragraphs we summarize the most significant results we obtained.

As we expected, the ultimate plume rise was greatly influenced by the temperature of the hot gases from the stack, the volumetric flow rate of these gases, and the ejection velocity. As was also expected, the model predicts that a moderate crosswind greatly reduces the ultimate computed plume rise. The magnitudes and rates of variation of the diffusivities of momentum, heat, and concentration were found to have a considerable effect on the shape of the thermal plume. The lapse rate of the ambient temperature was also found to influence the ultimate plume rise to some extent but not quite as strongly as the other parameters.

1. Effects of Stack Gas Parameters

The volumetric flow rate, the temperature, and the velocity are the primary input to the buoyant plume model. In order to determine the relative importance of these variables, we made several computer runs using different values for the variables. For example, we first varied the total flow rate of gases over about two orders of magnitude while keeping the temperature of the stack gases at the ambient temperature. This was then repeated with gases at various elevated temperatures. These simulations enabled us to

determine that both the total volumetric flow rate and the temperature of exhaust gases greatly influence the predicted plume rise. Plume rise increased with both increasing volumetric flow rate and increasing temperature. As expected, the greatest plume rise was obtained for high volumetric flow rates of hot gases. Plume rise was also affected by the ejection velocity of the gases, but to a far smaller extent than by the former two variables. The specification of the rate of emission of pollutant at the stack affects the concentration distribution of pollutant downwind of the stack, but does not affect the shape of the plume because the concentration of pollutant in the effluent is relatively small.

All of the above major effects are to be expected, both on the basis of field experience and from the standpoint of simple physical reasoning. The rise of the plume is primarily due to the buoyancy force acting on it, which in turn is a consequence of the elevated temperature of these gases with respect to the ambient atmosphere. Hence, the high temperature of the effluent gases is one of the key factors determining the ultimate plume rise. As the total volume of hot gases ejected increases, the surface area of the plume per unit volume decreases. Consequently, the relative rate of mixing of the hot gases with the ambient air is decreased, the hot gases tend to disperse and cool more slowly, and hence the plume rises to a greater altitude. Finally, we note that the momentum of the stack gases can be dissipated without actual mixing of the gases with ambient air. The heat content of the gases, on the other hand, is primarily dissipated by actual mixing of the gases with ambient air. Hence the rate of dissipation of the vertical momentum of the stack gases is much greater than the rate of dissipation of their heat content. This indicates that the plume rise will be only moderately affected by the vertical velocity with which these gases are ejected from the stack.

2. Effect of Crosswinds

In order to examine how crosswinds affect the predictions of the model, we simulated the development of the plume both under calm conditions (zero crosswind) and with a moderate crosswind (about 3 to 4 m/sec at the stack

height). These simulations were repeated for several different conditions of effluent flow rate, stack gas temperature, and atmospheric temperature. In all cases, the model indicated that a crosswind resulted in substantial reduction in the predicted plume rise. In addition, the shape of the plume was greatly altered, with the solution indicating the downwind drift of the hot gases from the stack, hence giving rise to a "bent-over" plume. As in the case of the sensitivity of the model to the stack effluent conditions, the above results are in qualitative agreement with the observed behavior of thermal plumes. At a given flow rate of stack gases, the volume of ambient air flowing past the stack exit increases as the cross-wind velocity increases. Hence the rate of dilution of the stack gases increases as the crosswind velocity increases, and the ultimate plume rise is consequently reduced. To simulate the crosswind, we also tested both a uniform velocity profile and realistic velocity profiles (with significant wind shear close to the ground). In all cases we found that the plume is only affected by the average wind speed at the stack height and at higher elevations.

3. Effect of Diffusivity

In our test simulations, we used a relatively wide range of values (0.1 m^2/s to 30 m^2/s) to represent the diffusivities of momentum, heat, and concentration. Assumptions regarding the magnitudes and the variation of the diffusivities have been found to affect the predictions very significantly.

In general, we found that the assumed values for the diffusivities of momentum, heat, and concentration must be reasonably close to each other in order to obtain a consistent solution. Use of large diffusivities tends to produce a smooth flow pattern with a relatively diffuse plume and a small plume rise. If a very small diffusivity is used, the solutions appear to be erratic and sometimes even become unstable. Hence, it is clear that the specification of the diffusivities is extremely important, especially in the vicinity of the stack.

Unfortunately, it is usually difficult to make quantitative estimates of the spatial variation of diffusivity near the stack, due to the paucity of experimental data. Considering this scarcity of information, we have

made only the crudest of approximations regarding the spatial variation of the diffusivity. We have assumed that the diffusivity may be expressed mathematically as the sum of two independent components, as follows:

$$K_{total} = K_{stack} + K_{ambient} \tag{III-76}$$

The first component, K_{stack}, accounts for the turbulence generated by buoyancy, and the second component, $K_{ambient}$, accounts for the turbulence inherent in the atmosphere. We further assumed that since vertical movement is caused only by the effluent gas from the stack, the vertical velocity at any point is indicative of the proximity of the stack and of the intensity of plume-generated turbulence. Hence, as a first approximation we assumed the following functional form for K_{stack}:

$$K_{stack} = \alpha|\omega| \tag{III-77}$$

where α is a proportionality constant. Due to a lack of data, the value of this constant was determined empirically in the model development. The constant α may be expected to be dependent primarily on the rate of flow of gases from the stack and secondarily on the crosswind speed, because the crosswind speed influences the nature of mixing even very close to the stack. We varied α over a range of values and determined the interval that produces the most reasonable simulations for effluent flow rates on the order of about 1000 kg/sec. A value of α approximately in the midpoint of this interval was then used for all the remaining simulations.

The second component of diffusivity, $K_{ambient}$, is dependent on the atmospheric stability, prevailing windspeed, elevation above ground surface and surface roughness. We found that the predictions are only moderately sensitive to the shape of diffusivity profile. Hence, in the validation runs we simplified the calculations by assuming the ambient diffusivity varies with height in the following fashion:

$$K_{ambient} = \begin{cases} a & z < h \\ a + bz & h < z < H \\ a + bH & z > H \end{cases}, \tag{III-78}$$

where constants a, b, h, and H depend upon atmospheric stability as illustrated in Figure III-4.

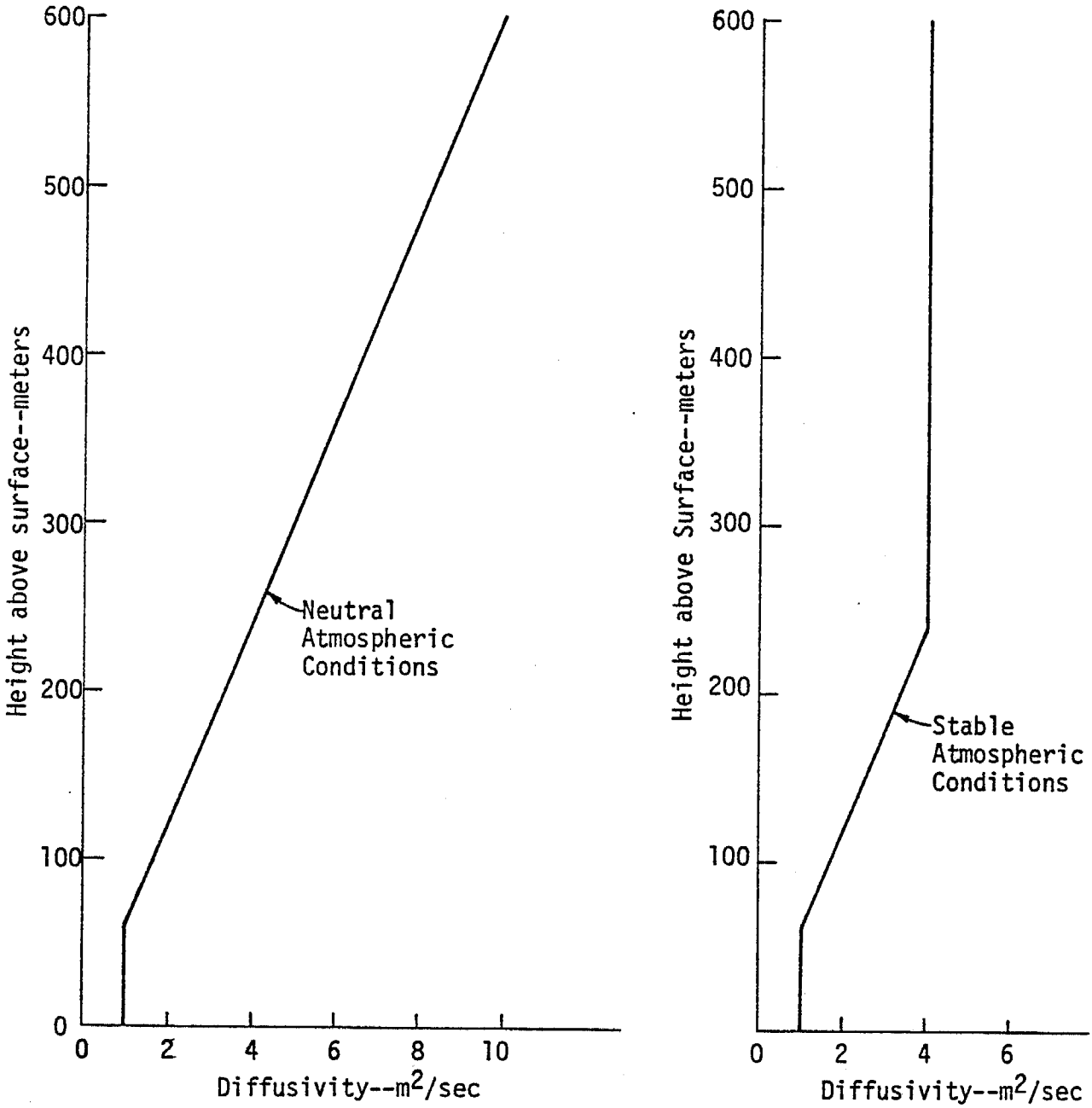

FIGURE III-4.. THE VARIATION OF AMBIENT DIFFUSIVITY WITH HEIGHT

E. MODEL APPLICATION AND VALIDATION

In the final phase of this effort, the Buoyant Plume Model described in the previous sections was applied to all cases where pertinent information was sufficient for the exercise and comparison of the model. In the field study of this program, meteorological data, which consist primarily of the wind profiles, temperature soundings, and SO_2 concentration distributions in the vicinity of the power plants of interest, were collected by Meteorology Research, Inc. The days for which data were available are tabulated below. The measurements for all of the days, taken from the Meteorology Research, Inc. report (Smith et al., 1976), are included in Figures III-5, 8, 11, 14, 17, and 20 at the end of this chapter. Of the six days, it was noted that on October 11, 1974 at Haynes, there was a reversal of the horizontal component of the wind above 300 meters. Interestingly enough, as shown in Figure III-5, the observed SO_2 concentration profiles appear to indicate that the plume bifurcated vertically into two branches. Since the exact nature of this occurrence is not clear, it was decided that this day was not suitable for testing the present model.

Table III-4

SUMMARY OF THE TEST DAYS

Plant	Date	Approximate Time Period
Haynes	October 1, 1974	1400 PDT - 1512 PDT
Haynes	October 11, 1974	1400 PDT - 1523 PDT
Los Alamitos	October 25, 1974	1400 PDT - 1441 PDT
Los Alamitos	October 30, 1974	1300 PST - 1420 PST
Los Alamitos	November 7, 1974	1248 PST - 1400 PST
Moss Landing	September 10, 1974	1400 PDT - 1530 PDT

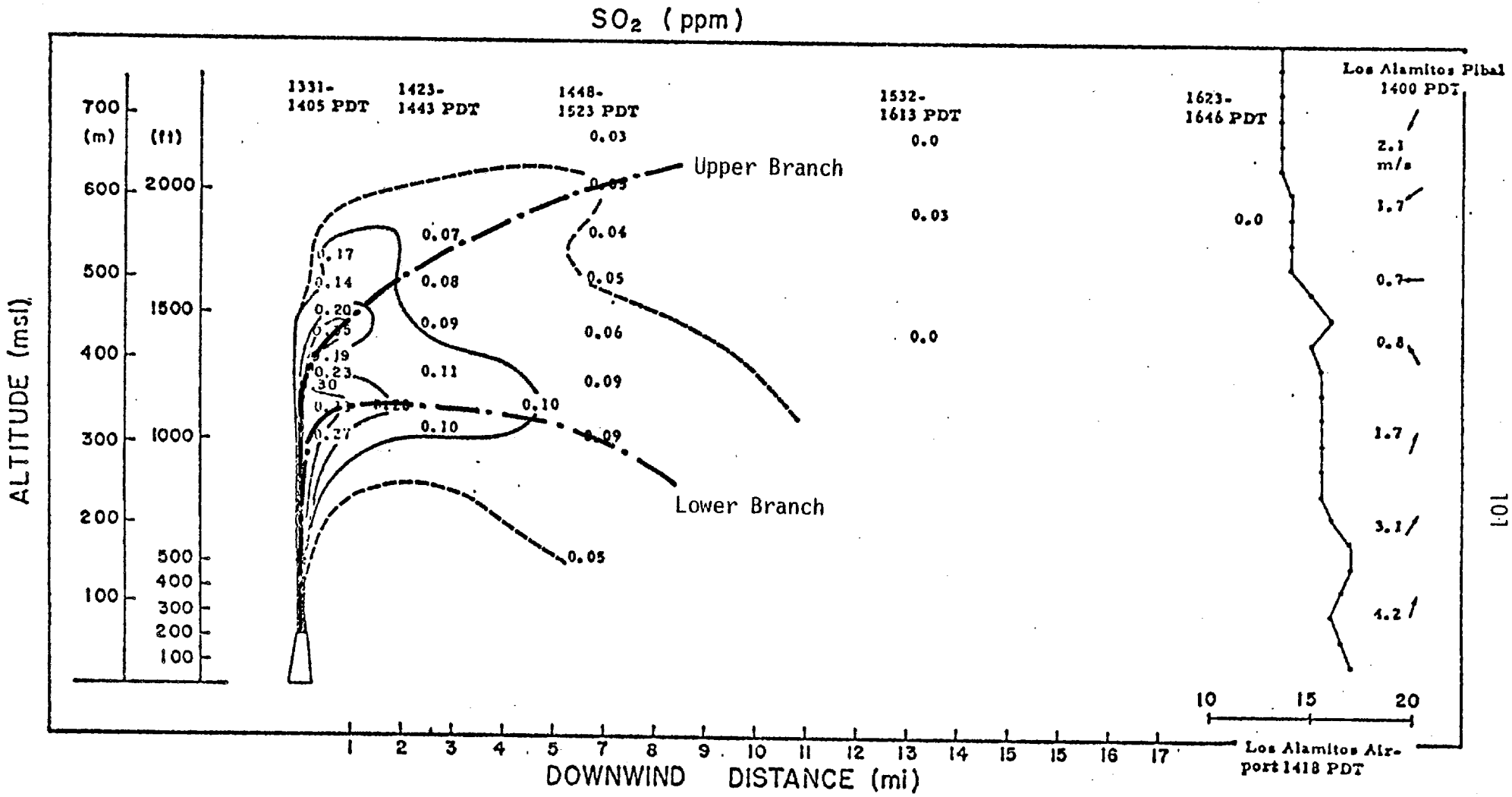

FIGURE III-5. OBSERVED PLUME PROFILE, HAYNES POWER PLANT - 11 OCTOBER 1974
(Source: Meteorology Research, Inc.)

In addition to the meteorological information, data regarding the plant operating conditions are also required for the exercise of the Buoyant Plume Model. Table III-5 summarizes the physical stack heights and diameters of all units at the three power plants for the five days selected. The effluent velocities, temperatures, and concentrations were derived from the plant operating conditions listed in Table III-6.

For each of the five days, the required inputs to the model were prepared based upon the data base described above, and the model was exercised. The computed flow field on October 1, 1974, at Haynes is shown in Figure III-6.† A perusal of this result indicates that there is an induced convergent flow in the vicinity of the stack. The influence of this convergence extends about 300 meters above the stack and several hundred meters both upwind and downwind of the plant. This feature was present in all five cases tested. The computed SO_2 concentration distributions are plotted in Figure III-7, and the observed values in Figure III-8. It should be emphasized, however, that the spatial scales of these two plots are not comparable. Although the measurements span a distance of a few kilometers downwind of the stack, the model predictions only cover a distance of a few hundred meters. In principle, the coverage of the model predictions can be extended by continuing the calculation, but a maximum distance of a few hundred meters was imposed in the present model simulation because of computational considerations--both time and accuracy. Thus, the comparison is qualitative. Nevertheless, it can be shown by comparing these two figures that the shape of the plume is similar to the observed one. Furthermore, by extrapolating the center line of the plume, we estimated that the predicted plume rise is approximately 270 meters* while the observed initial and final plume rises are 330 and 300 meters respectively (Figure III-8). It thus appears that the model tends to underpredict the

†For all figures of computed flow fields and plume configurations, the ordinate denotes height in meters above mean sea level, and the abscissa denotes the horizontal distance in meters from the upwind edge of the modeling region.

*For all discussions in this chapter, we use the height above mean sea level.

Table III-5

SUMMARY OF STACK GEOMETRY

Power Plant	Unit	Stack Height (m)	Stack Diameter (m)
Haynes	1	73.2	4.02
	2	73.2	4.02
	3	73.2*	4.2§
	4	73.2	3.2
	5	73.2*	4.2§
	6	73.2	5.63
Los Alamitos	1	60*	3.66†
	2	60.98	3.66
	3	60*	4.27†
	4	60.98	4.27
	5	62.50	5.18
	6	62.50	5.18
Moss Landing	6-1	152.4	5.39
	7-1	152.4	5.39

*Stack heights assumed to be approximately the same as for the other units.

†Since air flow rates from Units 1 and 2 are similar, the diameters were assumed to be approximately equal, and similarly for Units 3 and 4.

§Diameters assumed equal to average value of diameters for other units.

Table III-6

SUMMARY OF PLANT OPERATING CONDITIONS FOR VALIDATION STUDY

Plant	Date (1974)	Unit	Oil Flow (10^3 lb/hr)	Air Flow (m^3/s at S.T.P.)	Effluent Temperature (°K)	Flow of SO_2* (lb/hr)	Flow of SO_2* (kg/s)
Haynes	Oct. 1	1	67	132	394	670	0.085
		2	10	170	394	100	0.013
		5	145	212	394	1450	0.183
		6	145	212	394	1450	0.183
Los Alamitos	Oct. 25	2	55	113	406	550	0.069
		4	89	203	406	890	0.112
		5	235	448	400	2107	0.266
		6	247	486	411	2210	0.279
	Oct. 30	2	71	137	406	710	0.090
		4	106	233	406	1060	0.134
		5	233	458	400	2330	0.294
		6	242	467	411	2420	0.306
	Nov. 7	1	79	151	406	790	0.100
		2	70	137	406	700	0.088
		3	70	189	406	700	0.088
		5	236	453	400	2360	0.298
		6	241	500	411	2410	0.304
Moss Landing	Sept. 10	6-1	---	620	426	2388	0.30
		7-1	---	665	423	2410	0.31

*Where measurements of the flow of SO_2 were not available, the flow was computed assuming the use of fuel oil containing 0.5 percent sulfur (Grade 1 fuel oil), and assuming that all of the sulfur exits in the flue gases.

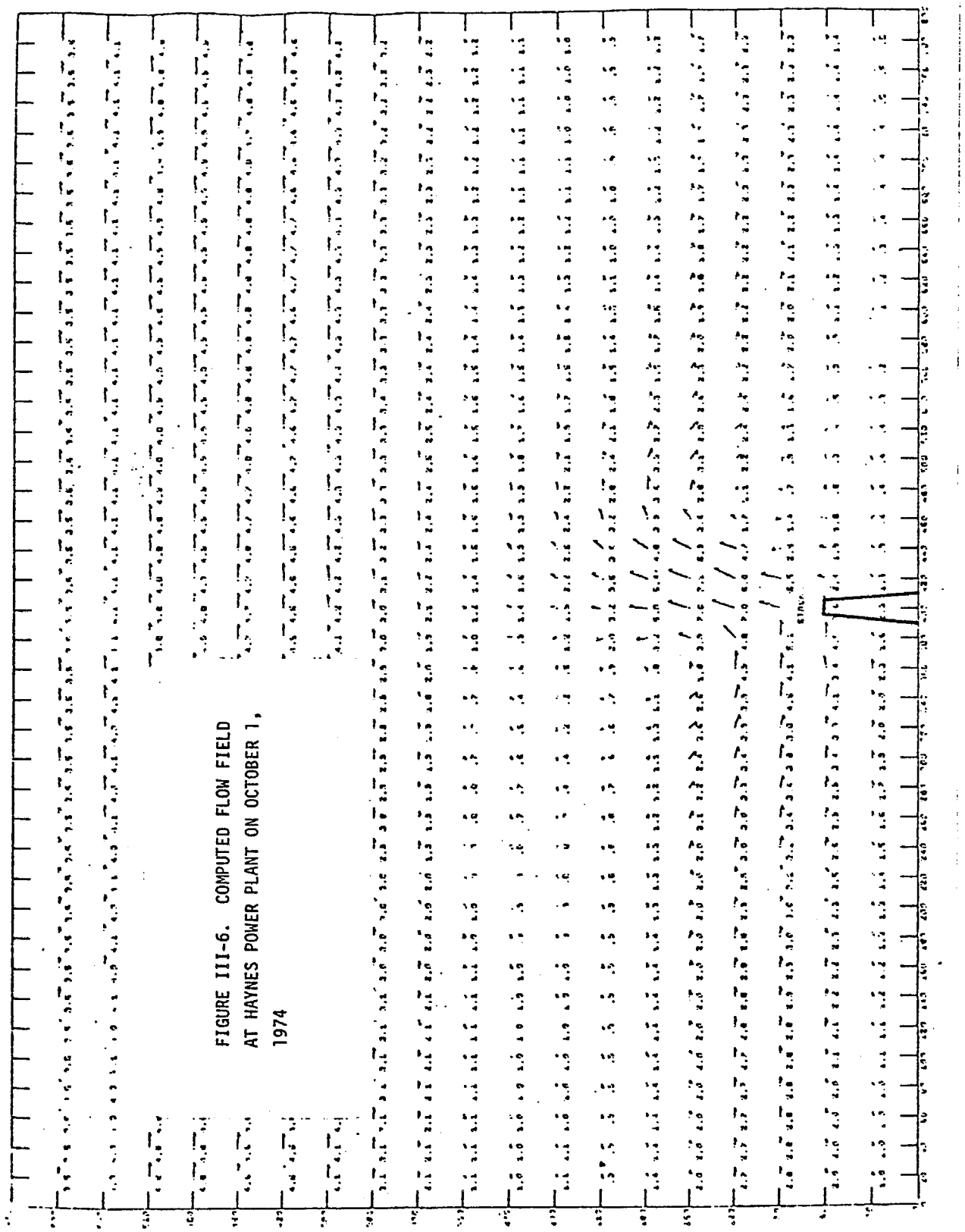

FIGURE III-6. COMPUTED FLOW FIELD AT HAYNES POWER PLANT ON OCTOBER 1, 1974

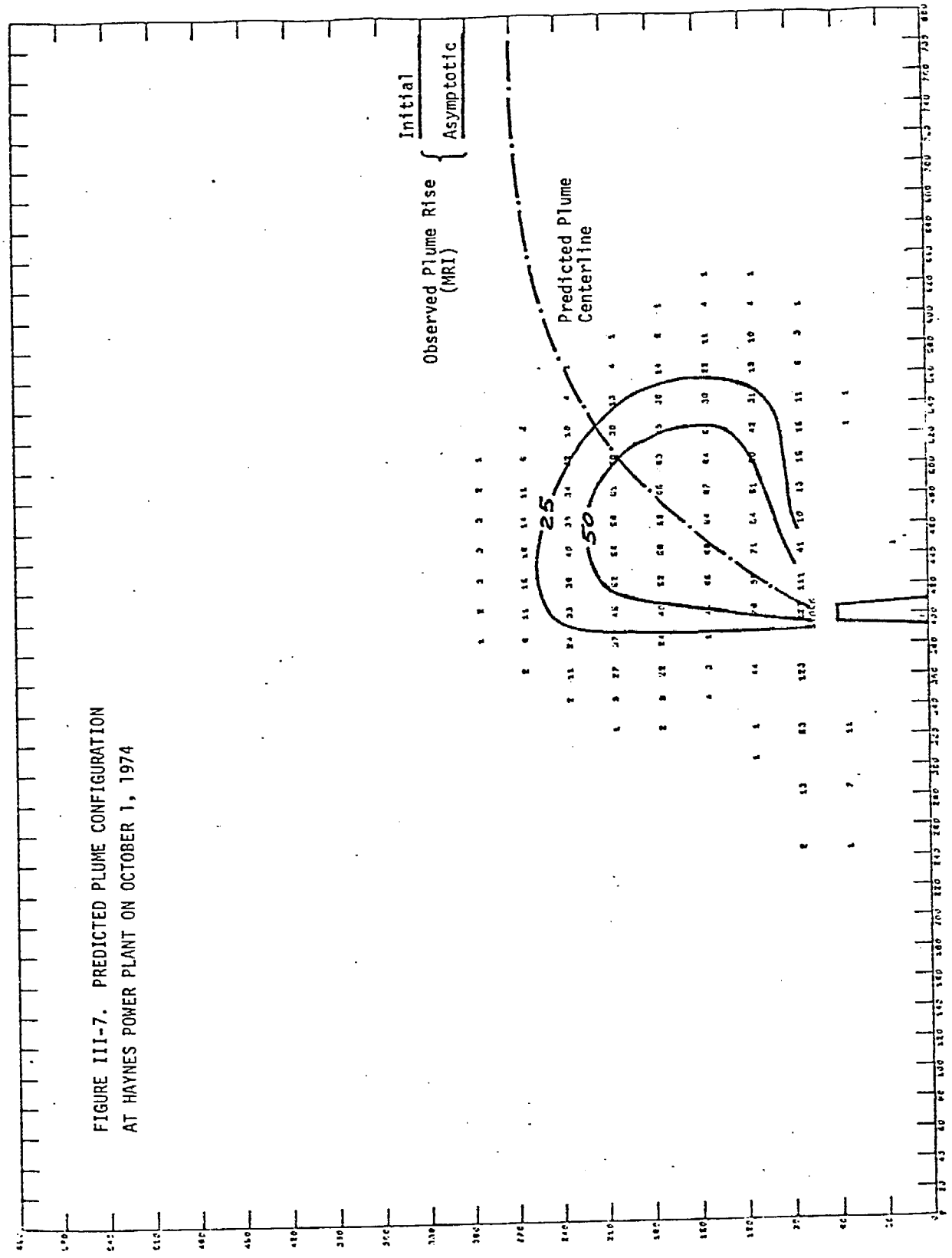

FIGURE III-7. PREDICTED PLUME CONFIGURATION
AT HAYNES POWER PLANT ON OCTOBER 1, 1974

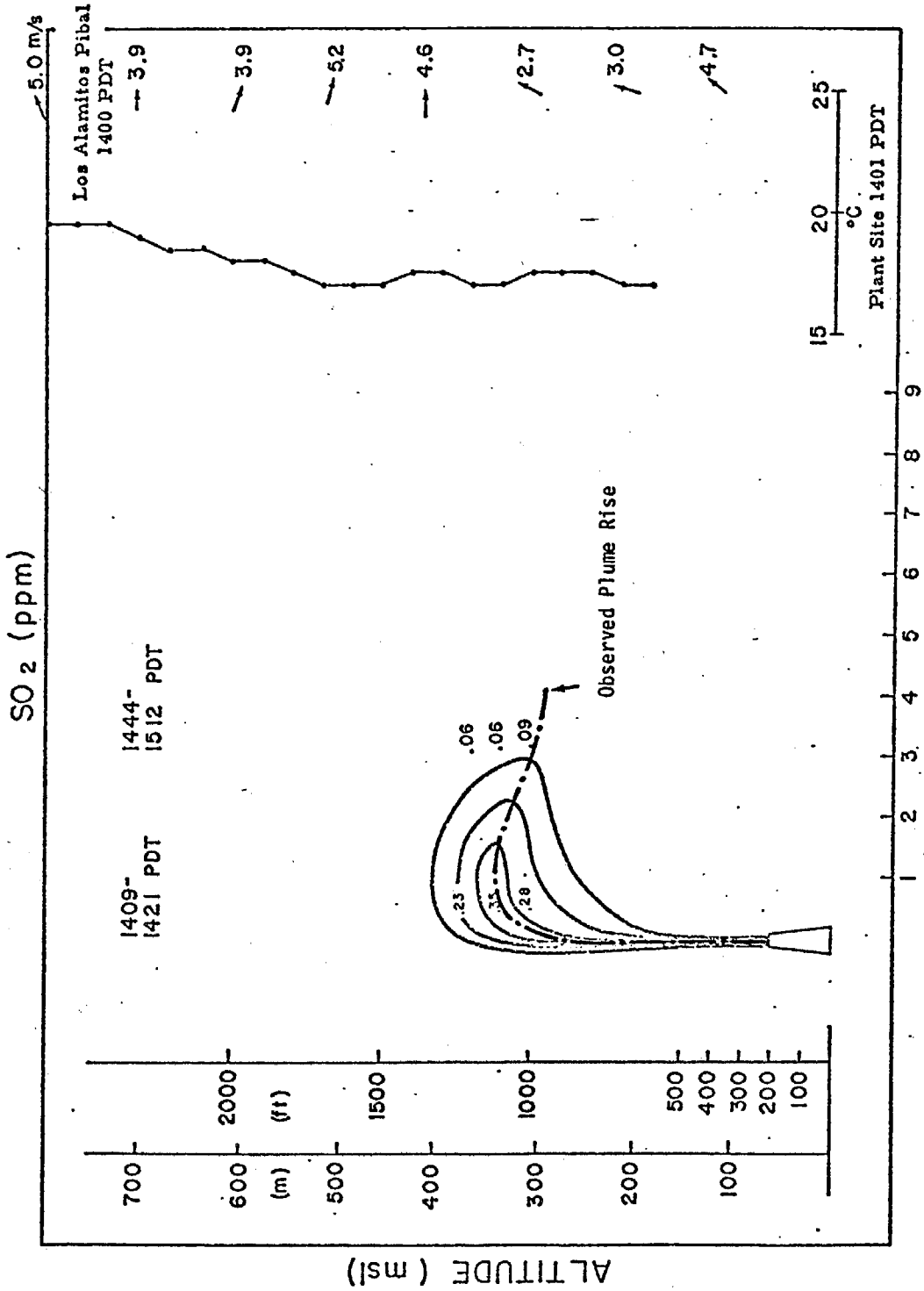

FIGURE III-8. OBSERVED PLUME PROFILE, HAYNES POWER PLANT - 1 OCTOBER 1974
(Source: Meteorology, Inc.)

observed plume rise. This trend is observed in all the days tested. Part of this underpredicting characteristic can be attributed to the presence of a strong convergence in the ambient flow, a phenomenon that is not included in the model. The computed flow field and SO_2 distribution for October 25, 1974 at Los Alamitos are plotted in Figures III-9 and III-10, and the observations in Figure III-11. The comparisons are generally similar to the first case. The predicted plume rise* is about 250 meters and the observed initial and final plume rises are 300 meters and 270 meters. Note that the convergence is relatively weak on this day. The predictions and measurements for October 30, 1974 at Los Alamitos are presented in Figures III-12, III-13, and III-14. Vertical bifurcation of the plume and a strong convergence in the ambient flow are both present on this day. The predicted plume rise is 275 meters and the measured ones are 275 meters for the lower branch and 420 meters for the upper branch. Results for the third test day in Los Alamitos are included in Figures III-15, III-16, and III-17. The predicted and measured plume rises are 270 meters and 280 meters, respectively. Note that the convergence in the ambient flow is very weak on this day. Finally, the model was applied to Moss Landing power plant for September 10, 1974. The results are shown in Figures III-18, III-19, and III-20. The predicted plume rise is 340 meters as compared to the measured value of 350 meters. In this case no significant convergence was present.

*All predicted plume rises mentioned are extrapolated values.

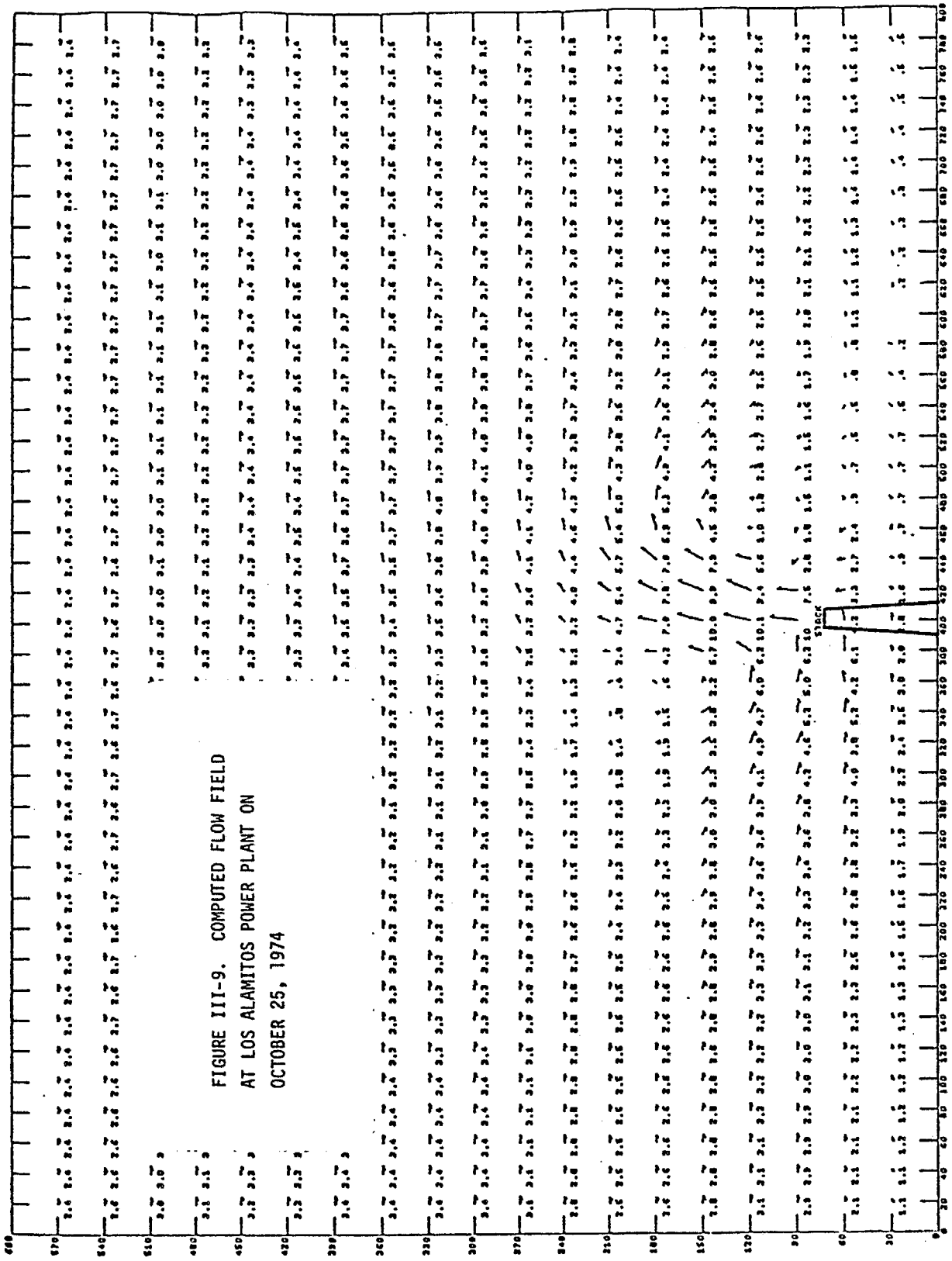

FIGURE III-9. COMPUTED FLOW FIELD AT LOS ALAMITOS POWER PLANT ON OCTOBER 25, 1974

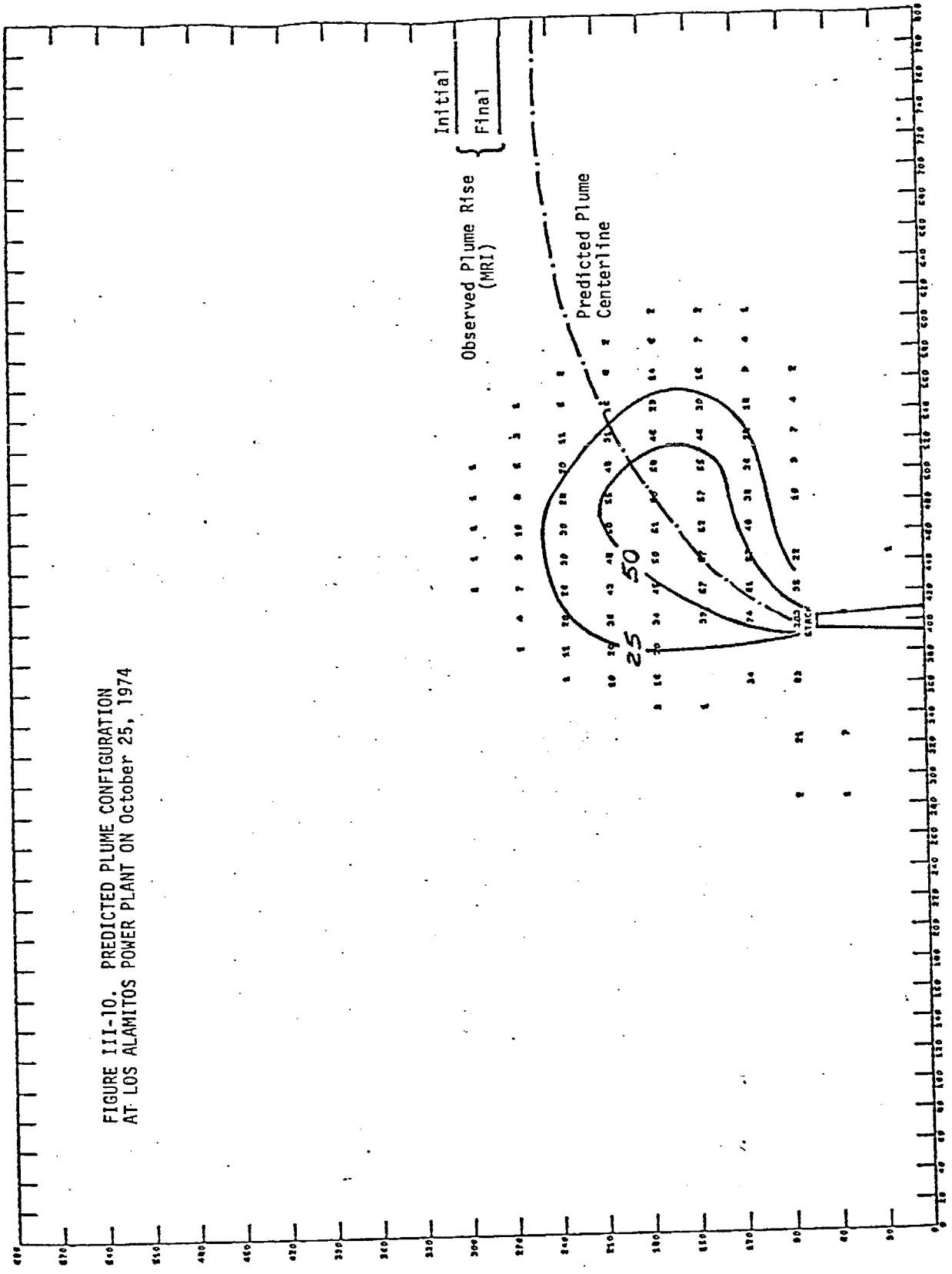

FIGURE III-10. PREDICTED PLUME CONFIGURATION
AT LOS ALAMITOS POWER PLANT ON October 25, 1974

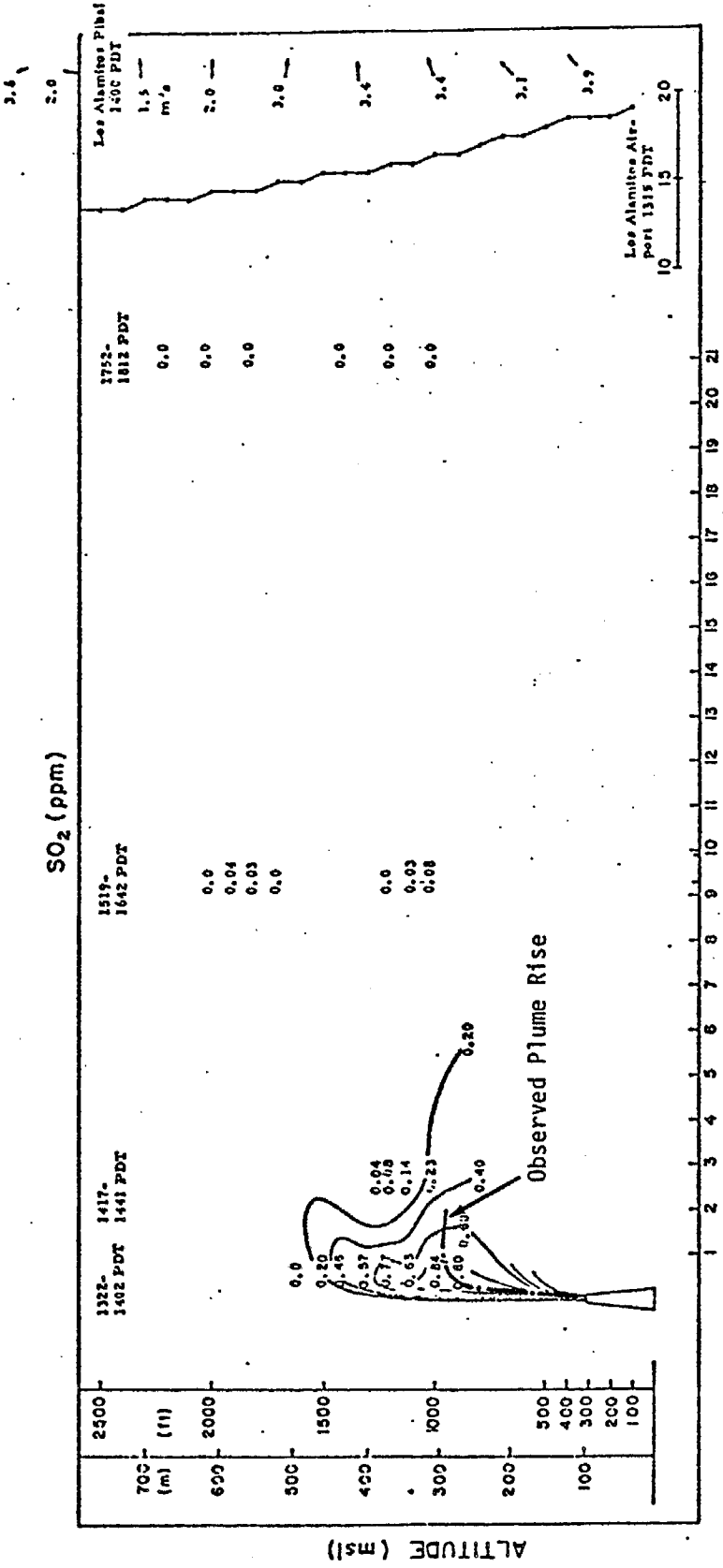

FIGURE III-11. OBSERVED PLUME PROFILE, LOS ALAMITOS POWER PLANT - 25 OCTOBER 1974
(Source: Meteorology Research, Inc.)

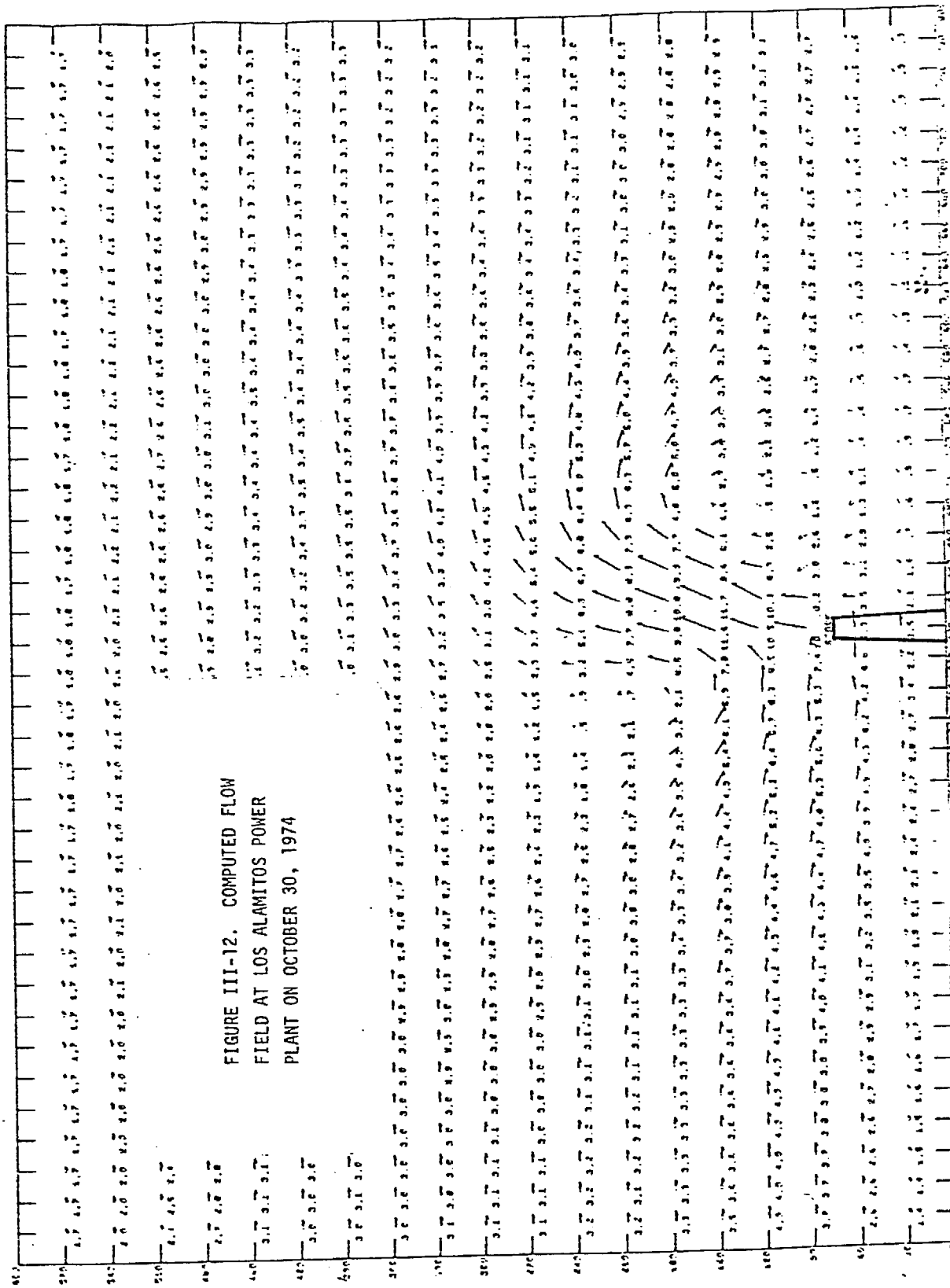

FIGURE III-12. COMPUTED FLOW
FIELD AT LOS ALAMITOS POWER
PLANT ON OCTOBER 30, 1974

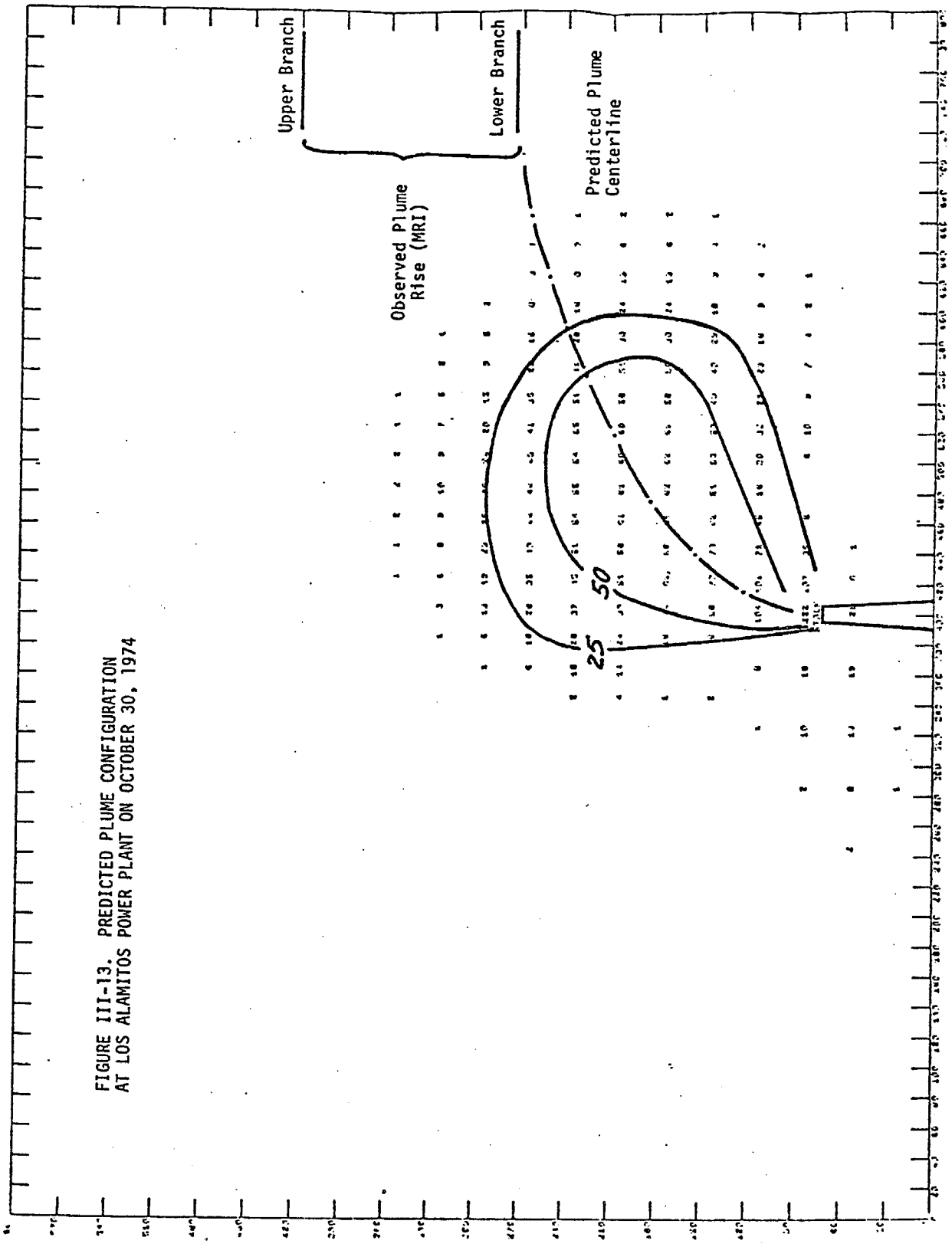

FIGURE III-13. PREDICTED PLUME CONFIGURATION AT LOS ALAMITOS POWER PLANT ON OCTOBER 30, 1974

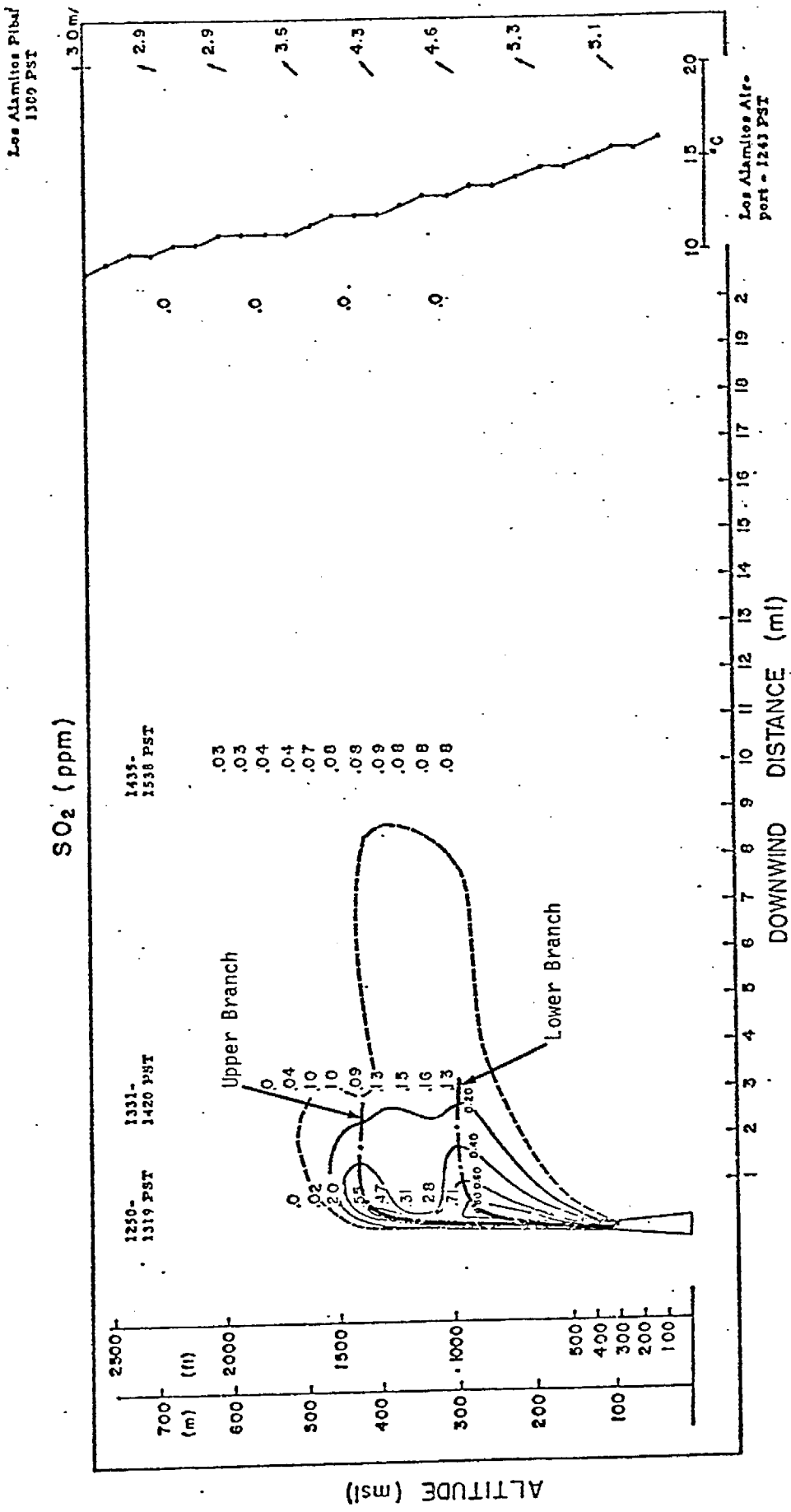

FIGURE III-14. OBSERVED PLUME PROFILE, LOS ALAMITOS POWER PLANT - 30 OCTOBER 1974
(Source: Meteorology Research, Inc.)

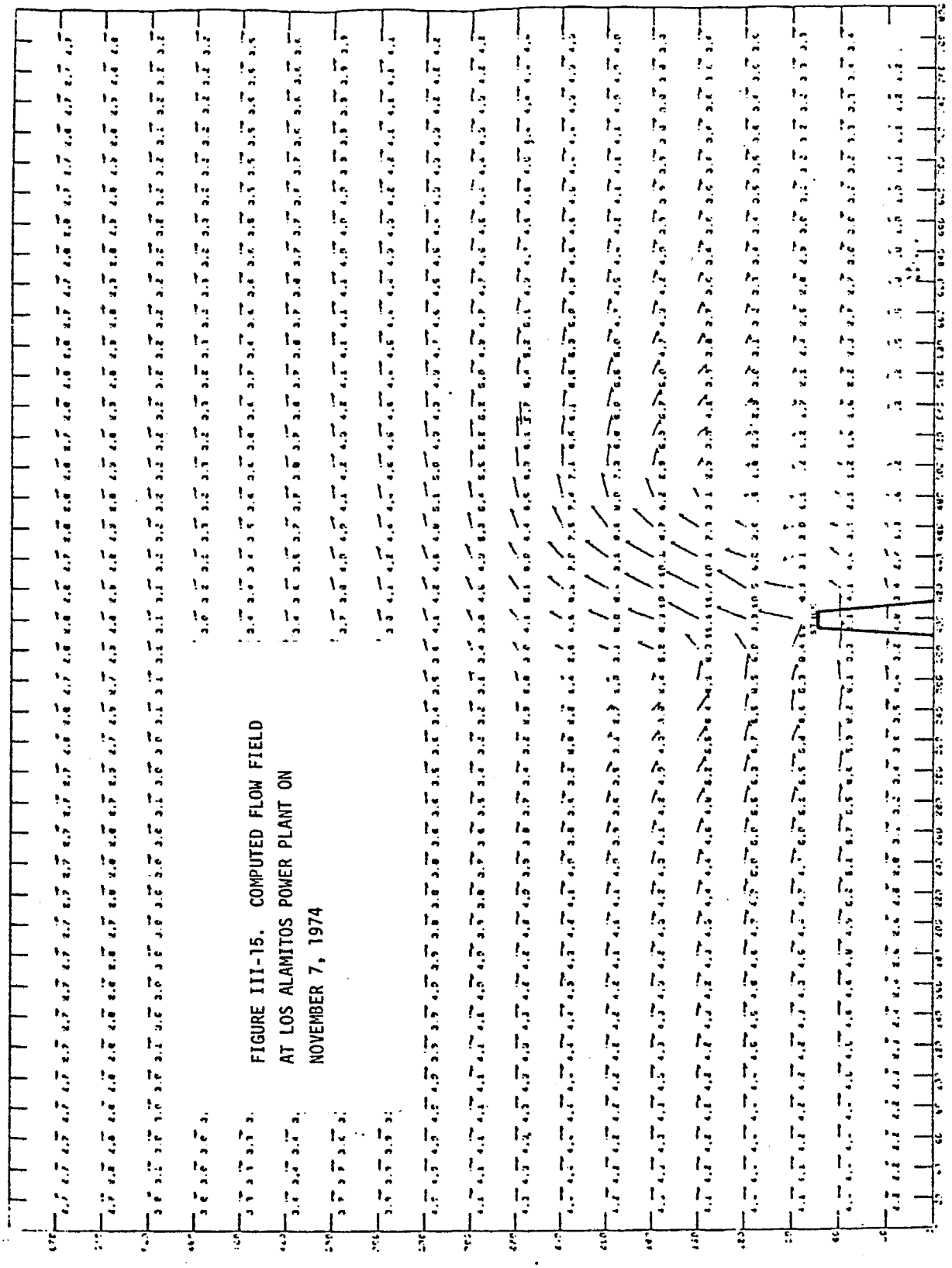

FIGURE III-15. COMPUTED FLOW FIELD AT LOS ALAMITOS POWER PLANT ON NOVEMBER 7, 1974

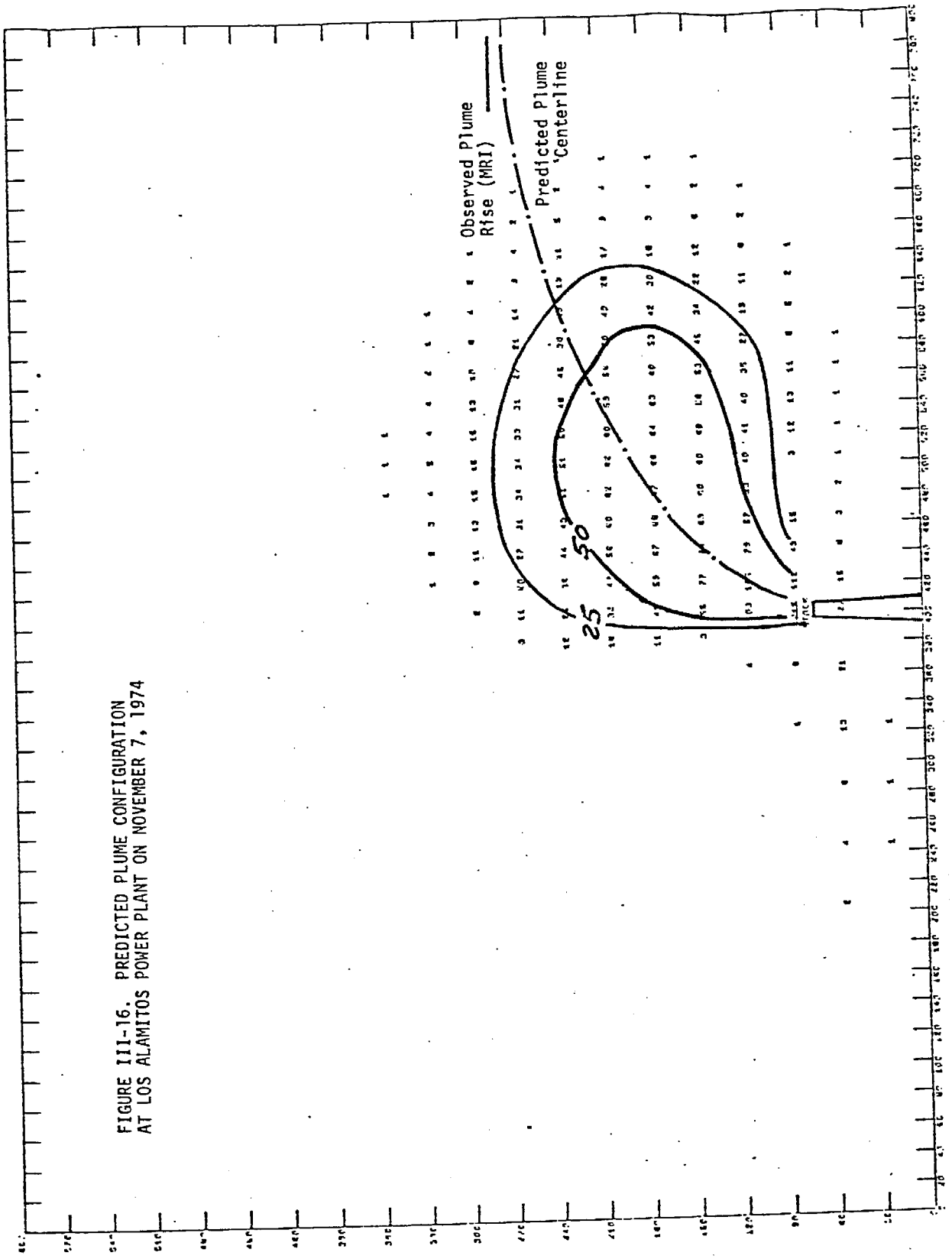

FIGURE III-16. PREDICTED PLUME CONFIGURATION
AT LOS ALAMITOS POWER PLANT ON NOVEMBER 7, 1974

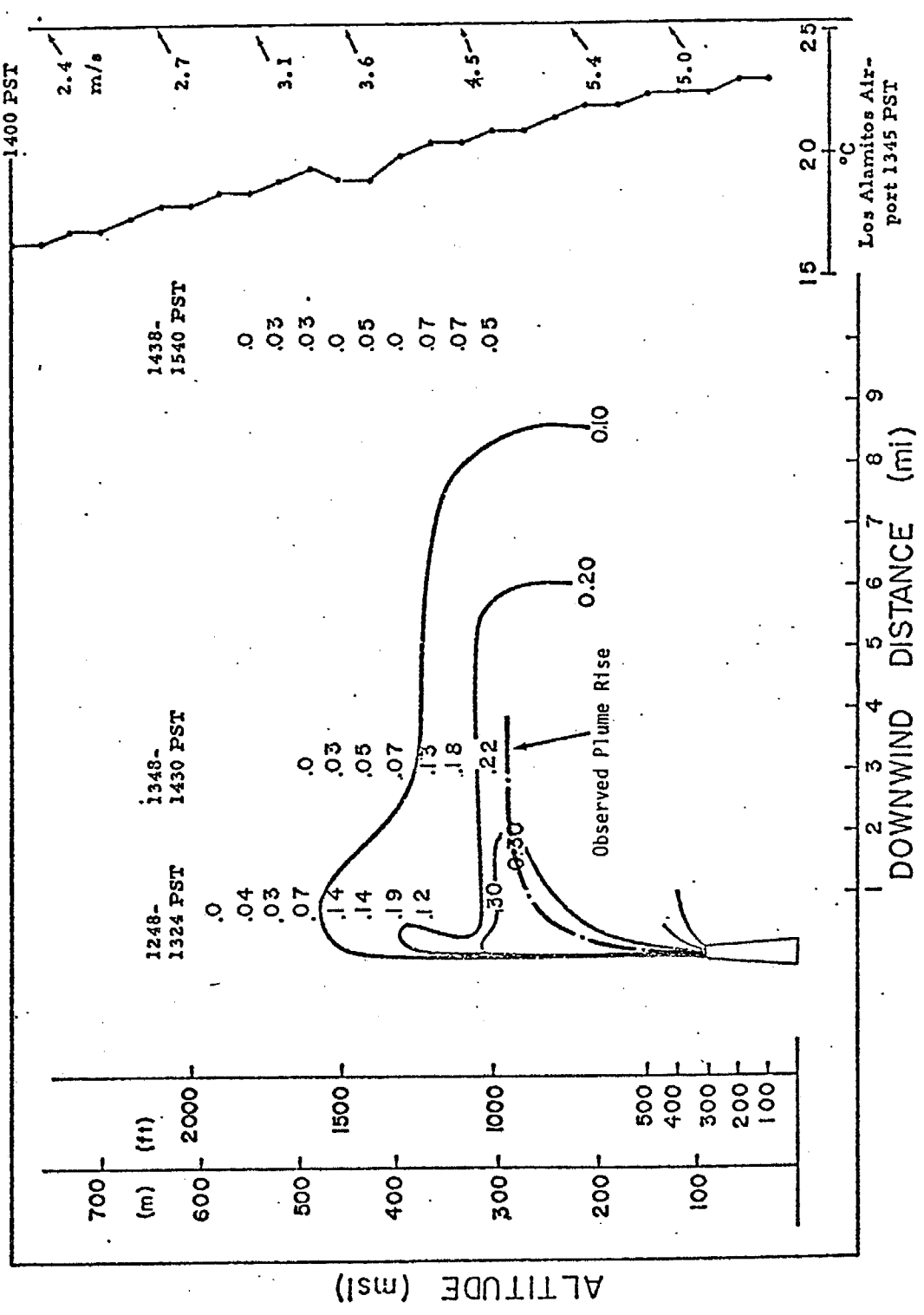

FIGURE III-17. OBSERVED PLUME PROFILE, LOS ALAMITOS POWER PLANT - 7 NOVEMBER 1974
(Source: Meteorology Research, Inc.)

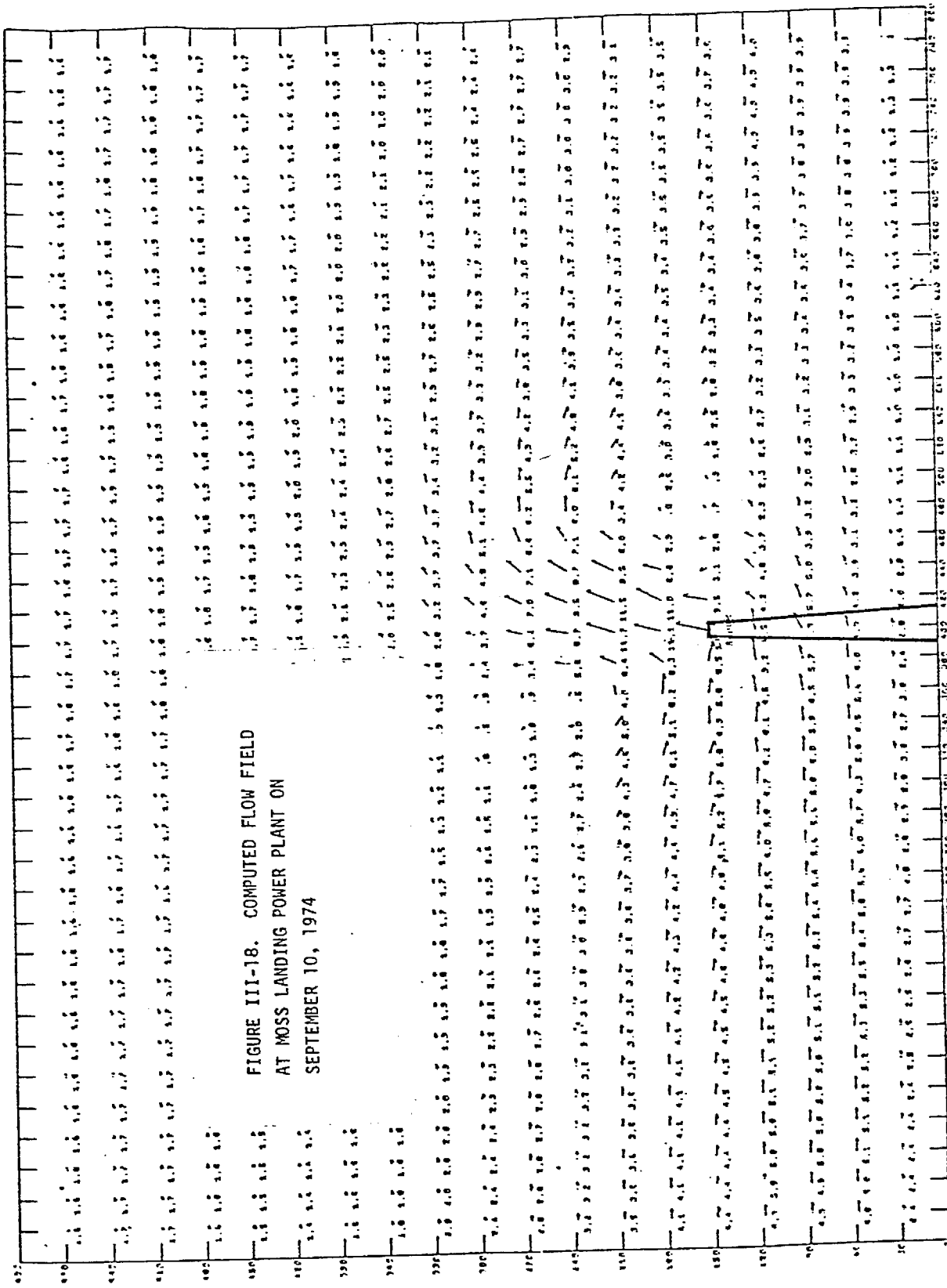

FIGURE III-18. COMPUTED FLOW FIELD
AT MOSS LANDING POWER PLANT ON
SEPTEMBER 10, 1974

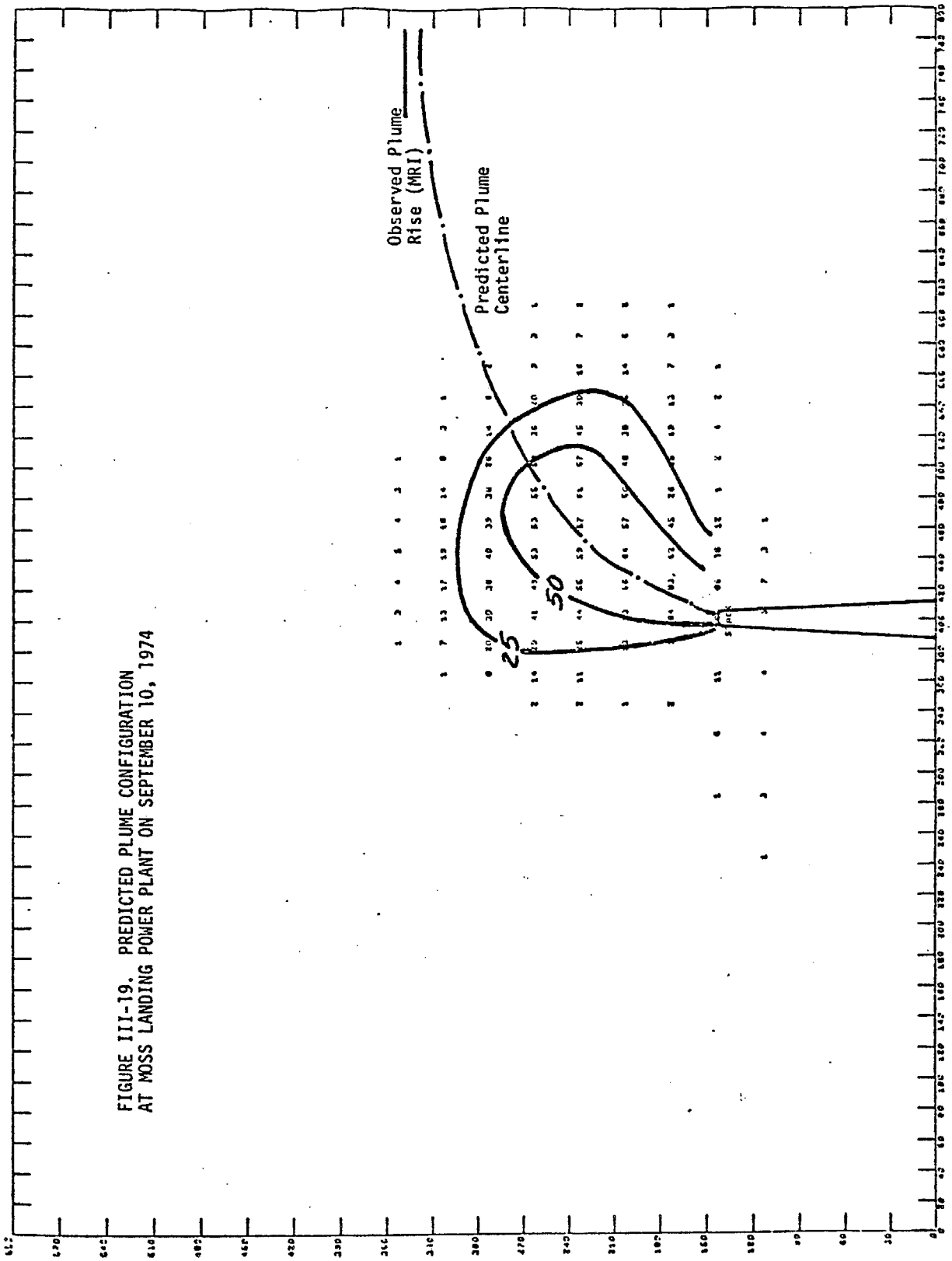

FIGURE III-19. PREDICTED PLUME CONFIGURATION
AT MOSS LANDING POWER PLANT ON SEPTEMBER 10, 1974

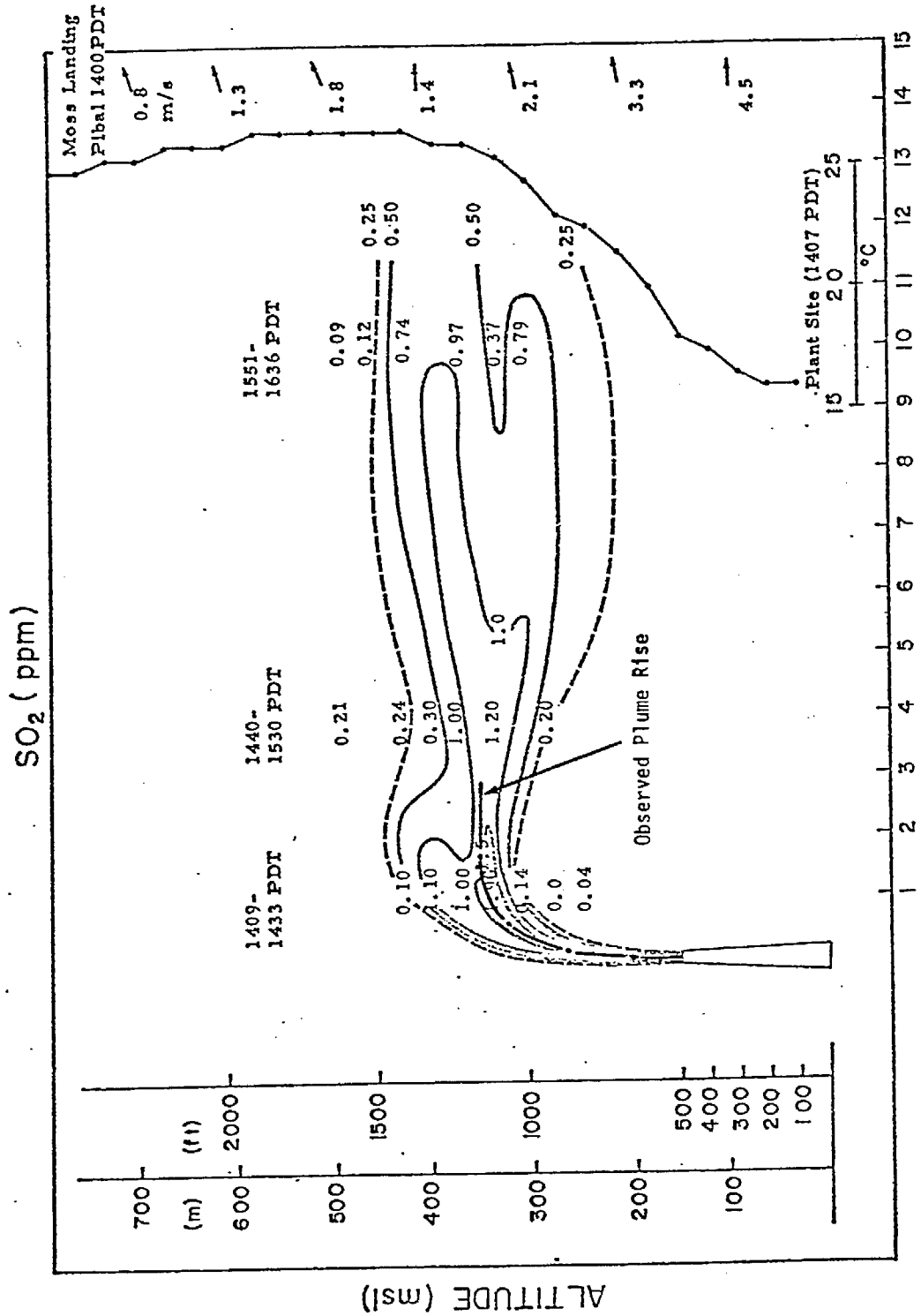

FIGURE III-20. OBSERVED PLUME PROFILE, MOSS LANDING POWER PLANT - 10 SEPTEMBER 1974
(Source: Meteorology Research, Inc.)

IV DEVELOPMENT OF THE PLUME DISPERSION MODEL

As envisioned in our general modeling approach, the plume dispersion model is designed to simulate the plume behavior from a few kilometers up to 100 kilometers from the stack. It is clear that beyond a few kilometers the hot plume has probably fully merged with the ambient atmosphere. Consequently, buoyancy and its attendant effects need no longer be considered. It is thus unnecessary to continue the dynamic calculations that were performed in the buoyant plume model.

The primary concern in the plume dispersion model is transport and diffusion of the pollutants from concentrated sources. Because of the relatively large space and time scales associated with the plume dispersion model, chemical reactions and other pollutant production and depletion processes should also become important. The problem at hand is therefore very similar to conventional urban air pollution modeling. In light of the recent proliferation of mesoscale airshed models, there is no lack of appropriate candidates for the plume dispersion model. A cursory review of several different modeling concepts pertinent to urban air pollution simulation can be found in Section A of this chapter. Based on the review of the various mesoscale airshed models, we adopted a grid model approach for the present project. The formulation of the plume dispersion model and the numerical technique selected for solving the model equations are discussed in Section B. Section C describes the data bases used in the simulations of plumes from the three power plants considered in this study (Moss Landing, Haynes, and Los Alamitos).

A. REVIEW OF MESOSCALE AIR POLLUTION MODELING

A variety of models are available for predicting air pollution concentrations from pollutant sources. They range in degree of complexity from

simple algebraic models to complex numerical models. The purpose of this section is to examine the limitations and capabilities of the various types of models, so that a logical decision can be made regarding the development of a mesoscale plume dispersion model. All air pollution models can be derived, in general, from the atmospheric diffusion equation:

$$\frac{\partial c_i}{\partial t} = - v \cdot \nabla c_i + \nabla \cdot (K \nabla c_i) + R_i + S_i \quad , \quad i = 1,2,\ldots,N \qquad \text{(IV-1)}$$

where

c_i = concentration of species i,
t = time
v = wind velocity vector,
K = mass diffusivity coefficient,
R_i = rate of production of species i due to chemical reaction,
S_i = rate of addition or depletion of species i due to sources and sinks.

Mesoscale models can generally be divided into two classes: 1) algebraic models, which are based on highly simplified solutions (in algebraic form) of the atmospheric diffusion equation, and 2) numerical models, which are based on the numerical solutions of the atmospheric diffusion equation. Some of the more well-known models in each of these classes are briefly discussed below.

1. Algebraic Models

a. The Gifford-Hanna Model

Based on a box-like and receptor-oriented approach, this model entails the use of the following algebraic formula (Gifford and Hanna, 1973; Turner, Zimmerman, and Busse, 1973):

$$c = \frac{1}{\bar{u}} \sum_i k_i \bar{q}_i + b \quad , \qquad \text{(IV-2)}$$

where

c = the concentration of the pollutant species at the receptor,

i = an index referring to a range of distances from the receptor,

$\bar{q}_i$ = the average area emission rate for this range of distance about the receptor,

$\bar{u}$ = mean wind speed,

b = background concentration of the pollutant considered beyond the last distance considered in the summation.

The coefficient, k_i, is determined from:

$$k_i = \int_{x_l}^{x_u} \frac{2}{\sqrt{2\pi}\,\sigma_z} \exp\left[-\frac{1}{2}\left(\frac{H}{\sigma_z}\right)^2\right] dx \quad , \qquad \text{(IV-3)}$$

where

x_l = the lower limit of distance of the i-th range,

x_u = the upper limit of distance of the i-th range,

σ_z = a dispersion parameter dependent upon distance and representative of mean stability conditions for the period of interest,

H = a single effective height of emission for the pollutant considered for area sources in the region under consideration.

In general, the value of b will be the concentration of the particular pollutant at the boundaries of the region considered, i.e., the boundary of the emission inventory. Note that the k's are dependent only upon the mean meteorological conditions and the height of emission; therefore, they are constant for a given distance range and are independent of receptor location. On the other hand, the $\bar{q}_i$'s are determined for different distance ranges about each receptor and, therefore, are dependent upon receptor location.

b. The Gaussian Model

The most commonly used technique for estimating atmospheric dispersion of gaseous pollutants is the so-called "Gaussian formula" (e.g., Turner, 1969). An assumption is made that the spread of the plume in the crosswind and vertical directions has a Gaussian distribution. Lin and Reid (1963) pointed out that the pollutant particles should have the same distribution as the wind direction fluctuations, since particle trajectories coincide with the instantaneous wind direction; the Gaussian is a fair approximation of these fluctuations in the atmospheric boundary layer. The pollutant concentration can be computed from the following formula:

$$c = \frac{Q_c}{2\pi\,\sigma_y\,\sigma_z\,U}\, e^{-\frac{1}{2}\left(\frac{y}{\sigma_y}\right)^2}\left[e^{-\frac{1}{2}\left(\frac{z-H}{\sigma_z}\right)^2} + e^{-\frac{1}{2}\left(\frac{z+H}{\sigma_z}\right)^2}\right] , \qquad \text{(IV-4)}$$

where

Q_c = rate of emission of the pollutant,
H = virtual stack height,
σ_y = standard deviation of the cross-wind pollutant distribution,
σ_z = standard deviation of the vertical pollutant distribution.

Generally, the dispersion coefficients in the Gaussian formula (σ_y and σ_z) are dependent upon the atmospheric stratification, surface roughness, vertical wind shear, and many other parameters that affect atmospheric structure. These coefficients can, however, be estimated from a knowledge of the Pasquill and Gifford stability category, which is a function of downwind distance from the source (Turner, 1967). Although the stability categories were developed for the description of dispersion from point sources, they can usually be used to describe area sources by specification of an appropriate fictitious upwind point source.

Deficiencies in the algebraic models are many and well known. Notably, these models generally have the following limitations:

> It is difficult to include chemical reactions.
> It is difficult to handle time-dependent problems.
> It is difficult to incorporate spatially varying parameters.

In view of these severe limitations, it is not surprising that the algebraic models, albeit simple, are not adequate for accurately simulating the sulfur dioxide concentration or predicting the rate of sulfate formation at large distances from the stack. They are therefore ruled out as possible candidates for the Plume Dispersion Model.

2. Numerical Models

A variety of numerical methods have been developed to solve partial differential equations. These methods have been applied to a form of the diffusion equation in some current models. For the purposes of this review, these models can be grouped into three general categories: the trajectory model, the particle-in-cell model, and the grid model. Examples of each will be outlined below and the shortcomings of each approach will be delineated.

a. Trajectory Models

A trajectory or Lagrangian model has frequently been adopted to describe numerically transport and photochemical transformations of pollutants introduced into the urban atmosphere. Conceptually, the approach is attractive because it obviates the need for air quality calculations in regions of lesser interest and it avoids the problems of "numerical" or "psuedo-diffusion" characteristic of Eulerian finite difference schemes. The essence of the trajectory model is the assumption that a hypothetical air parcel maintains its integrity while being advected across the region of interest by the mean

wind. Further, there is no exchange of mass, momentum, or energy between adjacent air parcels; these fluxes can exist only at the upper and lower horizontal boundaries of the parcel. The following principal assumptions characterize the trajectory model:

1) Horizontal turbulent diffusion across parcel boundaries is neglected.

2) The parcel is advected by a mean wind velocity that is assumed to be constant with height.

3) Vertical advective mass transport within the parcel is neglected (in most models).

4) Averaged velocities reported by meteorological measurement stations, used in determining parcel trajectories, are assumed to be representative of the actual wind velocities.

Many investigators have developed workable trajectory models, but few have included vertical advective mass transport or a chemical reaction mechanism. Most of the versions that incorporated chemical kinetics applied a linearized version of the kinetic mechanism of dubious "correctness". SAI has developed a trajectory model that includes both the vertical advection term and the fully nonlinear photochemical reaction equations.

Even the most sophisticated versions of the trajectory model have certain drawbacks. A list of the errors associated with the restrictive assumptions made in model formulation and characteristic of the model is presented below, in light of the special needs of the far-field problem.

> Liu and Seinfeld (1974, 1975) found that errors due to neglect of horizontal turbulent diffusion were generally small for the urban conditions they studied. Although the importance of diffusion increases with increasing horizontal diffusivity, concentration gradients, and wind shear, and with decreasing

wind speed, they found that for both typical and extreme conditions in the urban atmosphere the magnitude of the relative error was less than 10 percent. These errors may be greater in rough terrain areas in which horizontal diffusivity will be greater.

> Strictly speaking, a trajectory parcel receives no information about emission patterns adjacent to, but noncoincident with its path. Trajectories narrowly missing strong emission sources cannot account for the horizontal diffusive mass transport that will invariably occur. While not posing a major problem for Eulerian-based grid models (due to spatial averaging of source inhomogeneities and the explicit incorporation of horizontal diffusion) this is a major concern for the trajectory approach.

> Because vertical advection can be incorporated into the model, gross errors associated with its omission do not present insurmountable difficulties in the use of the models. However, problems are not completely avoided because in finite-differencing the advection term, numerical diffusion errors are introduced. But even these errors may be reduced through judicious selection of a numerical scheme.

> Another theoretical difficulty with the trajectory model lies in the method of obtaining the Lagrangian trajectory velocity. Dyer (1973) has shown that, depending upon the turbulence statistics, two different Lagrangian velocities can be obtained. One is temporally averaged; the other is spatially averaged. Meteorological data used for modeling are generally based upon hourly averages from many different stations. Construction of a wind field consequently requires the use of temporal wind averages to obtain velocities at grid node points. Thus, temporal and spatial averages are combined in an ambiguous fashion. How well these averages represent the actual wind velocities becomes a matter of concern.

> Neglect of wind shear is an inherent characteristic of the trajectory approach. To assess its impact upon model predictions,

Liu and Seinfeld (1974, 1975) compared analytic solutions of the diffusion equation to trajectory model predictions for the cases of: 1) a continuous line source, and 2) a time- and space-varying areal source. They found that under conditions likely to occur in the urban atmosphere, errors incurred due to the neglected wind shear can be quite substantial.

b. Particle-In-Cell Models

This subsection considers two models of this type: the original particle-in-cell model (Sklarew et al., 1971), and a modification of it (Egan and Mahoney, 1972). Both keep track of particles or pollutant masses as they are advected across a modeling region.

The particle-in-cell approach was first developed by Harlow and Welch (1965) for use in fluid mechanical problems. Since its initial development, the technique has been extended to include such variations as the marker-in-cell method as well as other codes. This technique has been modified by Sklarew et al. (1971) to model urban air pollution. In this technique, pollutant particles are generated in quantities proportional to a predetermined pollutant mass. Particles are tracked in space by determining the incremental change in their location due to advective and diffusive effects. Hotchkiss and Hurt (1972) developed a method very similar to Sklarew's except that the diffusive term was computed using a random number generator to simulate random particle motion. This variation produces better results in areas of high concentration gradients, such as around point sources.

More recently, this technique has been modified by Egan and Mahoney (1972). Unlike other models which compute only the average concentrations, the Egan and Mahoney approach follows air parcels as they move within a grid network and takes into account the zeroth, first, and second moments of the pollutant concentration. With this improvement, it is possible to maintain an extremely high resolution and to significantly reduce numerical diffusion caused by errors associated with finite difference approximations of the advective terms in the diffusion equation.

In general, particle-in-cell methods can provide an accurate description of advective transport if the number of particles per cell is sufficiently large. This approach, however, has the following shortcomings:

> It requires a large computer memory to store the particles.
> It requires a large amount of computing time to keep track of the particles.
> Diffusion is handled in a superficial way.
> It is difficult to extend this approach to include reactive species.

3. Grid Models

Of the three approaches, the grid model can be considered as the most direct one. In this approach the modeling region is first divided into an array of cells. The governing equation, Equation (IV-1), is discretized, but otherwise unaltered, using appropriate finite difference approximations. The set of finite difference equations are then solved numerically with relevant meteorological and emission input as well as compatible initial and boundary conditions, to produce predictions of pollutant concentrations. A typical model of this type is that developed by Systems Applications, Inc. (Reynolds et al., 1973).

The major deficiency in the grid approach is well known. Numerical errors, in a form which is equivalent to an artificial diffusion, will be generated in the discretization of the advection terms in the atmospheric diffusion equation. The net effect is to smooth out concentration variations. The magnitude of the error will depend primarily on the following (Liu and Seinfeld, 1974, 1975):

> The emission pattern
> The wind speed and the relative magnitude of physical diffusion

> The grid size
> The finite difference scheme selected
> The length of simulation time.

In view of these facts, it becomes clear that, although it is almost impossible to eliminate numerical diffusion in the grid model, it is likely that the errors can be reduced to an acceptable level for an application by selecting an adequate grid size and numerical scheme.

On the other hand, the grid possesses many distinct advantages. Among the most important ones are

> Chemical reactions can be properly incorporated.
> The model is very flexible in the sense that it can handle any time- and space-varying meteorological and emission input data.
> The model requires only a reasonable amount of memory and computing time.

A careful review of the various advantages and limitations of each of the modeling approaches as well as the specific needs pertinent to the present project suggests that the grid model seems to offer the best choice for the far-field problem. Therefore a grid modeling approach was selected for the task of simulating the transport and diffusion of plumes over long distances. This selection was made primarily because of the flexibility of a grid model, with which both variable meteorological conditions and multiple source situations can be handled easily. The latter consideration is decisive in view of the significant interactions of other point or areal sources with the plumes from the power plants of interest, particularly in Los Angeles.

B. FORMULATION OF THE PLUME DISPERSION MODEL

The Plume Dispersion Model developed under this project is similar in many aspects to the photochemical airshed model developed by Systems

Applications, Inc. (Reynolds et al., 1973; Roth et al., 1974; Reynolds et al., 1974). However, many modifications were made to accommodate the special nature of plumes from point sources. Two of the most important modifications are the inclusion of a diffusivity scheme for a better prescription of the plume dispersion, and the use of a numerical method for handling the sharp concentration gradients often encountered in simulations of point sources. These modifications are described in detail in the next two subsections.

The Plume Dispersion Model is based on the atmospheric diffusion equation of the following form:

$$\frac{\partial c_i}{\partial t} + u\frac{\partial c_i}{\partial x} + v\frac{\partial c_i}{\partial y} + w\frac{\partial c_i}{\partial z} = \frac{\partial}{\partial x}\left(K_H\frac{\partial c_i}{\partial x}\right) + \frac{\partial}{\partial y}\left(K_H\frac{\partial c_i}{\partial y}\right) + \frac{\partial}{\partial z}\left(K_Z\frac{\partial c_i}{\partial z}\right) + R_i + S_i$$

$$i = \begin{cases} 1 & SO_2 \\ 2 & \text{Sulfate} \end{cases} \qquad \text{(IV-5)}$$

where

t = time
c_i = pollutant concentration of species i
x,y,z = spatial coordinates
u,v,w = wind velocity components in the x-, y-, and z-directions, respectively
K_H = horizontal diffusivity
K_Z = vertical diffusivity
R_i = production or depletion of species i by chemical reactions
S_i = rate of emission of species i from sources.

The validity of this equation for modeling air pollution has been examined and established in several studies (Lamb, 1973; Lamb and Seinfeld, 1973; Liu and Seinfeld, 1975).

Although the model is capable of incorporating a complex kinetic mechanism for SO_2-sulfate conversion (at the expense of additional computa-

tion time), only a simple first-order overall reaction step was used in the present study,

$$SO_2 \xrightarrow{k} SO_3 \quad . \tag{IV-6}$$

If a more complex kinetic model were used, such as the one in the Reactive Plume Model, it would be necessary to compile a comprehensive emissions inventory for reactive hydrocarbons and oxides of nitrogen over the entire modeling region. The rate of conversion of SO_2 to sulfate apparently depends upon a large number of parameters. In the present study, based upon the results discussed in Chapter II, we assumed an overall rate of 3 percent per hour.

The modeling region chosen for the Los Alamitos-Haynes study was the 50 mile by 50 mile area shown in Figure IV-1; we covered this area with a 2 mile by 2 mile grid. For the Moss Landing study we used a 1 mile by 1 mile grid over the 25 mile by 25 mile area shown in Figure IV-2.

In both cases the source is located in a corner of the modeling region from which the sea-breezes prevailing during daytime tend to move the plume diagonally over the entire grid. This positioning allowed us to retain the emissions on the grid for the longest possible time so that the impact of the plumes would be examined to the fullest extent.

1. Prescription of Turbulent Diffusivities

Like many other related studies of the atmosphere, the most difficult and also the most crucial part in the simulation of pollutant dispersion is to seek a reasonable scheme to represent the turbulent processes. This is particularly true for simulating the dispersion of pollutants from localized point sources. Although theoretical studies based on higher closure schemes for hierarchies of turbulence moment equations have recently been carried out (Deardorff, 1970, 1972), they have been restricted to certain special cases. Furthermore, the computational effort required for this approach is beyond the limits of a practically oriented problem. Thus, an

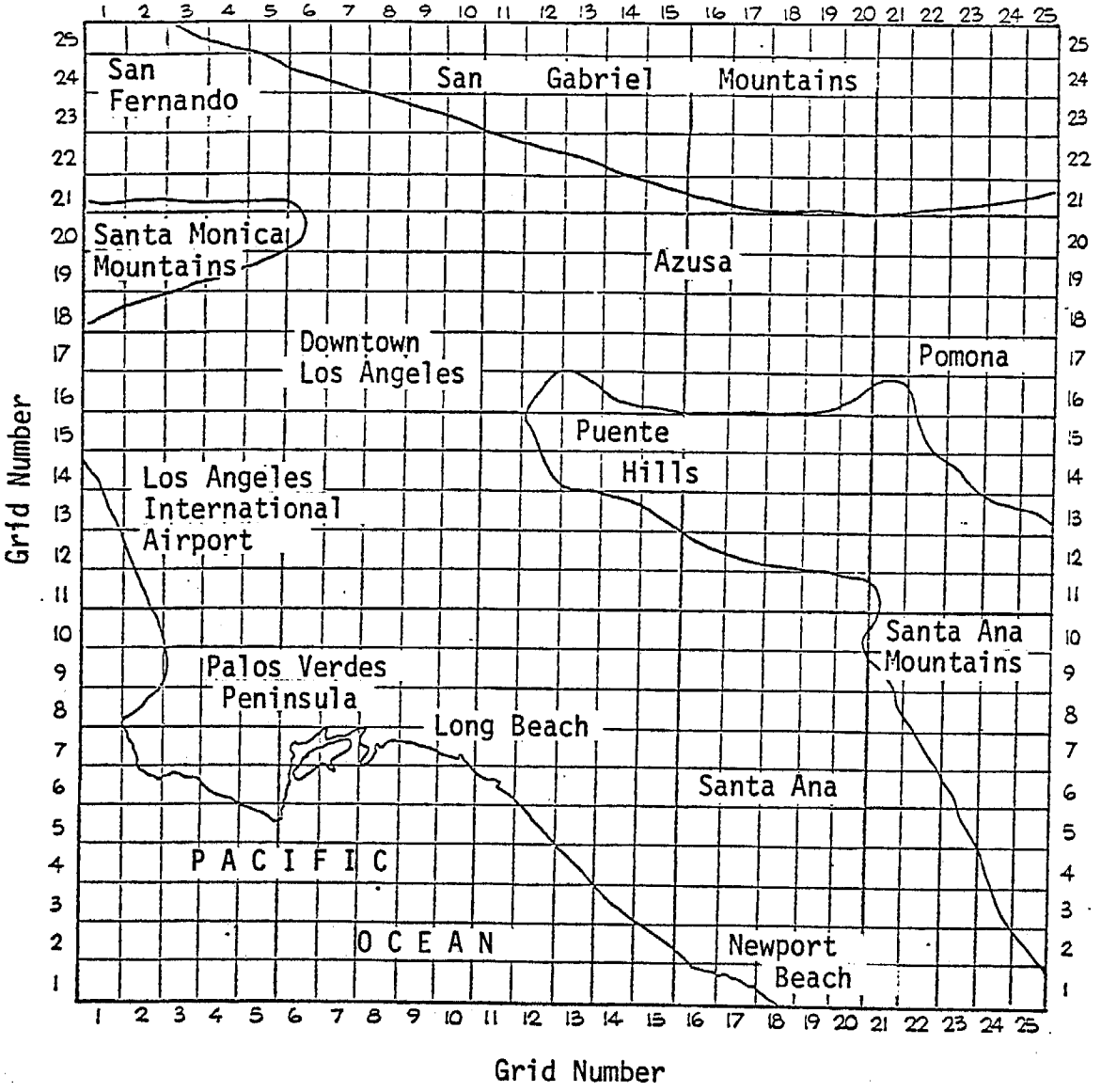

FIGURE IV-1. 50 MILE BY 50 MILE MODELING REGION OF LOS ANGELES BASIN USED FOR LOS ALAMITOS-HAYNES STUDY (Each grid square is 2 miles by 2 miles.)

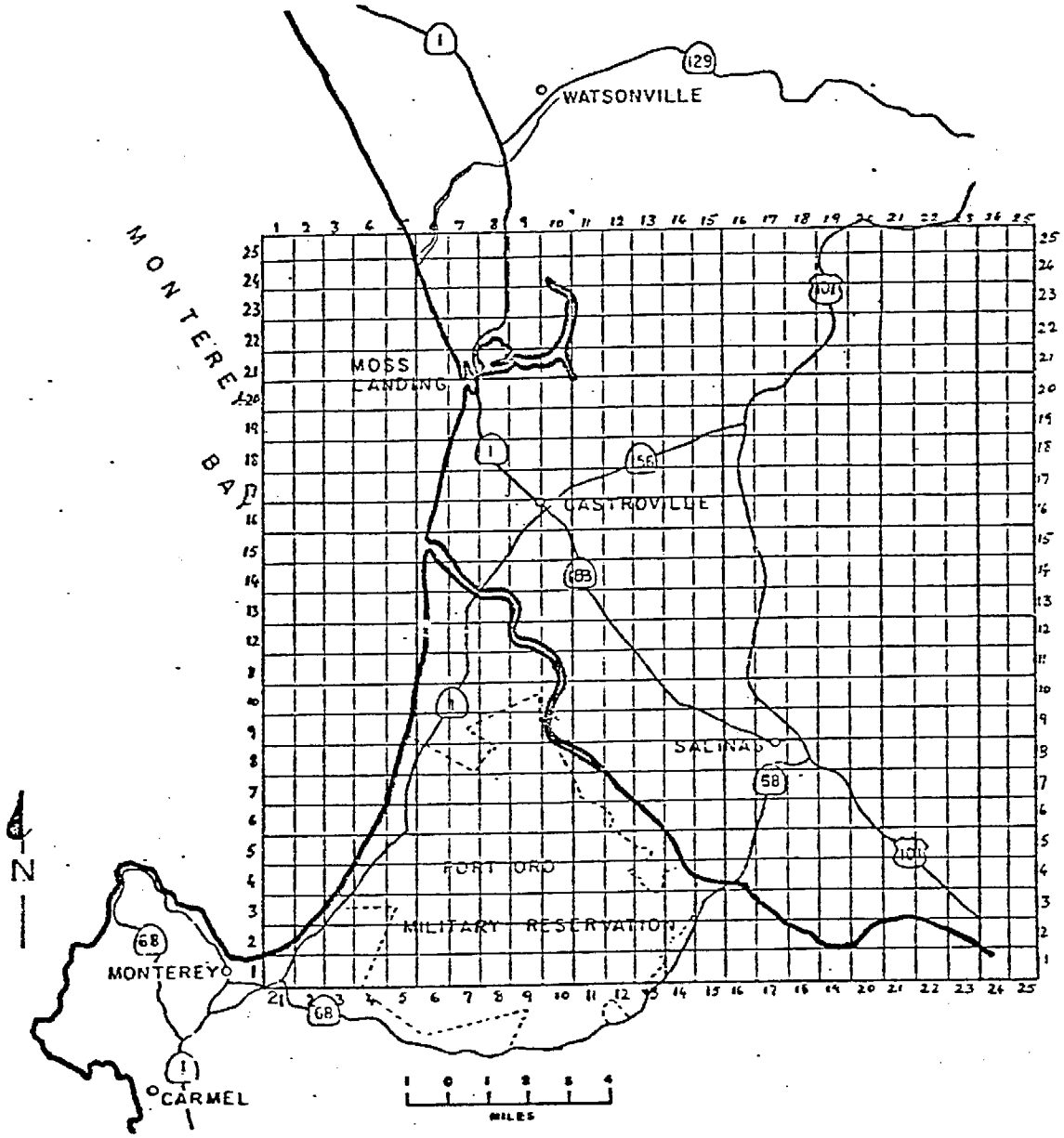

FIGURE IV-2. MOSS LANDING MODELING REGION

alternative based on the simple concept of turbulent eddy diffusivities--the K-theory--is usually adopted in most atmospheric dispersion models. Analogous to the molecular diffusion, the K-theory speculates that a pollutant flux in the direction of decreasing concentration is established as a result of turbulent fluctuations. The magnitude of this flux is proportional to the gradient of the average concentration:

$$\overline{u'c'} = - K_H \left(\frac{\partial \bar{c}}{\partial x}\right) \qquad \text{(IV-7)}$$

$$\overline{v'c'} = - K_H \left(\frac{\partial \bar{c}}{\partial y}\right) \qquad \text{(IV-8)}$$

$$\overline{w'c'} = - K_V \left(\frac{\partial \bar{c}}{\partial z}\right) \qquad \text{(IV-9)}$$

The limitations of models based on the K-theory or the gradient transport theory are numerous and well known. They can be generally grouped into length-scale and time-scale constraints and directional constraints. The length-scale and time-scale constraints are related to the spatial and temporal homogeneity of the mean field. Corrsin (1974) summarized the conditions necessary for satisfying such constraints:

> The transport mechanism length scale must be much smaller than the distance over which the curvature of the mean transported field gradient changes appreciably.
> The transport mechanism time scale must be much smaller than the time during which the mean transported field gradient changes appreciably.
> The transport mechanism length scale must be essentially constant over a distance of a length scale and over a distance for which the mean transported field changes appreciably.
> The transport mechanism velocity must be appreciably more uniform than the length scale.

Directional constraints arise when, for example, the Reynolds stress, a second-order tensor, is replaced by an inner product of a second rank tensor and a vector. The conditions for satisfying these constraints are more difficult to delineate. However, qualitative estimates for the validity of the urban airshed model based on the atmospheric diffusion equation have been obtained by Lamb and Seinfeld (1973). The result seems to indicate that the gradient-transport approach is plausible under a variety of conditions. Thus the remaining task is to find a means for prescribing the diffusivities.

Of the two diffusion components, the treatment of horizontal diffusivity is relatively simple. According to a sensitivity study by Liu et al. (1976), in meso-scale studies (with the modeling region of the order of several tens of kilometers) an order-of-magnitude change in the horizontal eddy diffusivity will affect the predicted surface concentrations by less than a few percent. Thus, a constant value of 50 $m^2 sec^{-1}$, compatible with the spatial scale of this project, has been used.

Based on a comprehensive review of the pertinent literature, an algorithm for prescribing the eddy diffusivity in the vertical direction has been used for the present project. In the surface layer, the following general formula is used:

$$K_V = \frac{k u_* z}{\phi\left(\frac{z}{L}\right)} \qquad (z_0 \leq z \leq |L|) \qquad \text{(IV-10)}$$

where

k = von Karman constant (= 0.35)

u_* = friction velocity

z = height

L = Monin-Obukhov length

z_0 = surface roughness.

This formula is the result of the similarity theory for the constant-flux surface layer (Businger et al., 1971). For the neutral case, the ϕ-function equals unity. For the stable and unstable cases, the ϕ-functions are greater and less than one, respectively. The following empirical expressions for the ϕ-function were proposed by Businger et al. (1971) based on observational data:

For the stable case ($L > 0$)

$$\phi_s\left(\frac{z}{L}\right) = 1 + 4.7\left(\frac{z}{L}\right) \tag{IV-11}$$

For the unstable case ($L < 0$)

$$\phi_u\left(\frac{z}{L}\right) = \left[1 - 15\left(\frac{z}{L}\right)\right]^{-\frac{1}{4}} \tag{IV-12}$$

The friction velocity is determined by the following equation,

$$u_* = \frac{ku_r}{f} \tag{IV-13}$$

where u_r denotes a reference wind speed measured at a reference height, z_r, and

$$f = \begin{cases} \ln\left(\frac{z_r}{z_0}\right) + 4.7\left(\frac{z_r - z_0}{L}\right) & \text{(IV-14)} \\ \ln\left[\frac{1 - \phi_u\left(\frac{z_r}{L}\right)}{1 + \phi_u\left(\frac{z_r}{L}\right)}\right] - \ln\left[\frac{1 - \phi_u\left(\frac{z_0}{L}\right)}{1 + \phi_u\left(\frac{z_0}{L}\right)}\right] & \text{(unstable)} \\ \quad + 2\tan^{-1}\left[\frac{1}{\phi_u\left(\frac{z_r}{L}\right)}\right] - 2\tan^{-1}\left[\frac{1}{\phi_u\left(\frac{z_0}{L}\right)}\right] & \text{(IV-15)} \end{cases}$$

Above the surface layer ($|L| \leq z \leq Z_i$), a second-order interpolation formula first proposed by O'Brien (1970) was adopted:

$$K_V(z) = K_{V,i} + \left(\frac{Z_i - z}{Z_i - |L|}\right)^2 \cdot \left\{ K_V(|L|) - K_{V,i} + (z - |L|) \cdot \left[K_V(|L|) + 2\left(\frac{K_V(|L|) - K_{V,i}}{Z_i - |L|}\right)\right]\right\} \qquad \text{(IV-16)}$$

where

$K_{V,i}$ = diffusivity at the elevated inversion,

$$K_V(|L|) = \left.\frac{d\, K_V(z)}{dz}\right|_{z = |L|} .$$

Z_i = inversion height

The implementation of this diffusivity scheme requires an estimate of the Monin-Obukhov length. The Monin-Obukhov length can in general be related to the Richardson number, which can be in turn be determined by experiments (McElroy, 1969). The estimate of this length is, however, accomplished in the present study via the following formula which relates the Monin-Obukhov length to the surface roughness, z_0, and the stability function, S,

$$L = \left\{ (a_1 S + a_2 S^3) \cdot z_0^{\,-(b_1 - b_2|S| + b_3 S^2)} \right\}^{-1} \qquad \text{(IV-17)}$$

where

$a_1 = 0.004349$

$a_2 = 0.003724$

$b_1 = 0.5034$

$b_2 = 0.2310$

$b_3 = 0.0325$

This formula is a result of the best fit of observational data reported by Golder (1972). The stability function, S, a digital version of the Pasquill stability category (Table IV-1), can be calculated as follows:

$$S = -\frac{1}{2}(3 - c_w + |c_e|)\cdot \text{Sign}(c_e) \qquad \text{(IV-18)}$$

where

$$\text{Sign}(c_e) = \begin{cases} 1 & c_e > 0 \\ 0 & c_e = 0 \\ -1 & c_e < 0 \end{cases}$$

and c_w and c_e are the wind speed class and exposure class, respectively,

$$c_w = \begin{cases} \frac{u_r}{2} & 0 \le u_r \le 8 \text{ m/sec} \\ 4 & u_r \ge 8 \text{ m/sec} \end{cases}$$

$$c_e = \begin{cases} 3 & \text{strong} \\ 2 & \text{moderate} \\ 1 & \text{slight} \end{cases} \Big\} \text{ daytime insolation}$$

$$\begin{cases} 0 & \text{heavy overcast} \end{cases} \text{ day or night}$$

$$\begin{cases} -1 & \ge \frac{4}{8} \text{ cloud cover} \\ -2 & \le \frac{3}{8} \text{ cloud cover} \end{cases} \Big\} \text{ nighttime cloudiness}$$

The prescription for the computation of the vertical eddy diffusivity is now completed. The primary inputs are the wind speed, the inversion height, the exposure class, and the surface roughness. The result of a sample calculation is included in Figure IV-3.

Table IV-1

PASQUILL CATEGORY AND STABILITY FUNCTION

Pasquill Category*	Stability Function
A	-3
B	-2
C	-1
D	0
E	1
F	2

2. Numerical Schemes for Solving the Model Equations

Numerical simulation of transport and diffusion of emissions from point sources is characterized by sharp concentration gradients. It is thus necessary to choose a numerical scheme that can handle the situation with reasonable accuracy. The SHASTA algorithm (Sharp and Smooth Transport Algorithm) was selected for this purpose.

To facilitate numerical computations, the following equation was derived from the model equation (Reynolds et al., 1974):

$$\frac{\partial}{\partial\tau}(\Delta Hc_i) + \frac{\partial}{\partial\xi}(u\Delta Hc_i) + \frac{\partial}{\partial\eta}(v\Delta Hc_i) + \frac{\partial}{\partial\rho}(Wc_i)$$

$$= \frac{\partial}{\partial\xi}\left(K_H\Delta H\,\frac{\partial c_i}{\partial\xi}\right) + \frac{\partial}{\partial\eta}\left(K_H\Delta H\,\frac{\partial c_i}{\partial\eta}\right) + \frac{\partial}{\partial\rho}\left(\frac{K_v}{\Delta H}\,\frac{\partial c_i}{\partial\rho}\right) \qquad \text{(IV-19)}$$

$$+ R_i\Delta H + S_i\Delta H.$$

*Turner (1969).

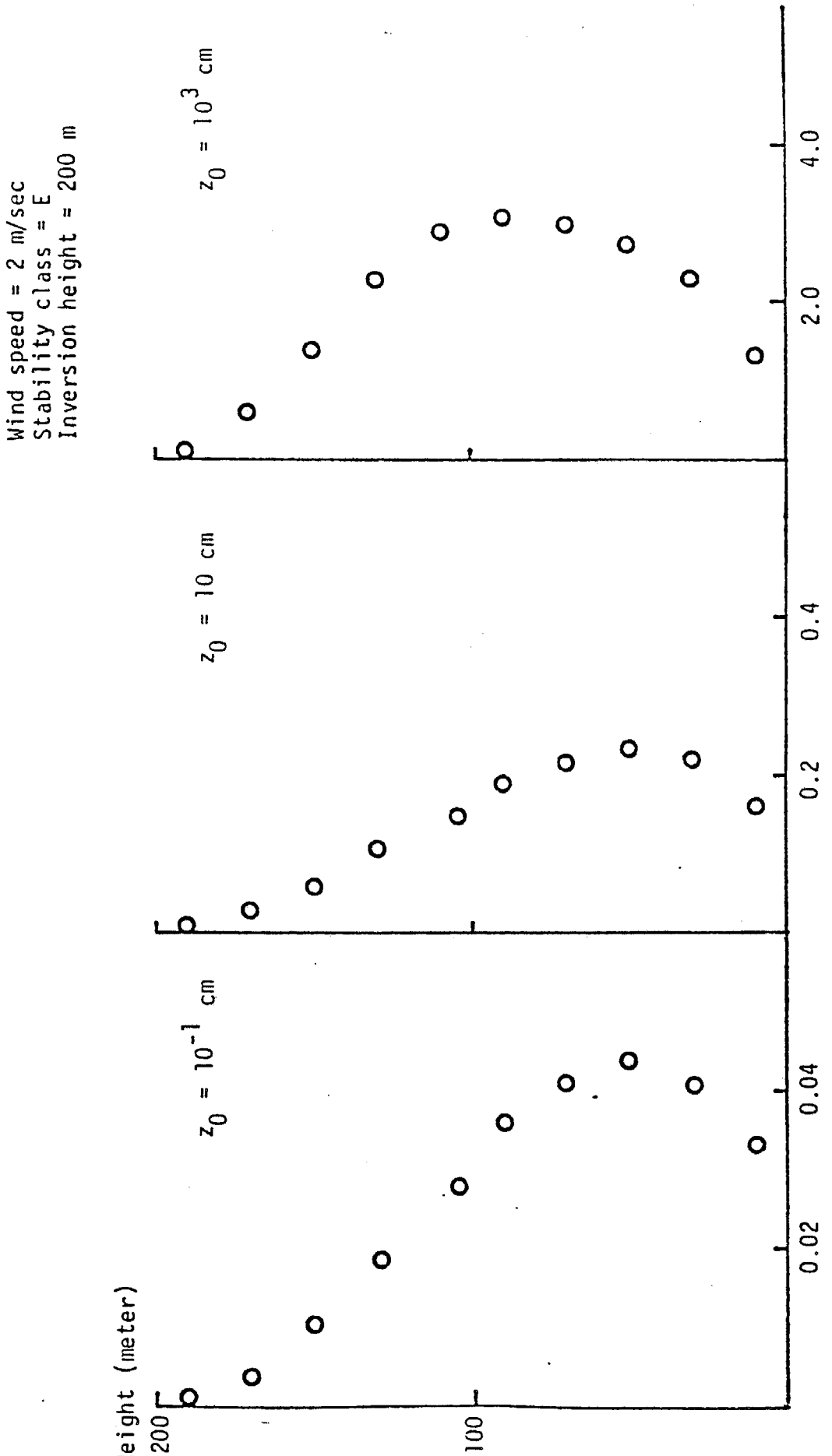

FIGURE IV-3. THE CALCULATED VERTICAL DIFFUSIVITY

as a result of the following coordinate transformations,

$$\tau = t$$
$$\xi = x$$
$$\eta = y$$
$$\rho = \frac{z - h(x,y)}{\Delta H}$$

where $\Delta H = H(x,y,t) - h(x,y)$ and $h(x,y)$ and $H(x,y,t)$ are the ground elevation and the base height of the temperature inversion. The method of fractional steps (Yanenko, 1971) was then applied to these model equations. It essentially involves the splitting of the original four-dimensional equation (Eq. IV-19) into three two-dimensional equations in (ξ,τ), (η,τ), and (ρ,τ):

$$\frac{\partial}{\partial\tau}(\Delta H c_i) + \frac{\partial}{\partial\xi}(u\Delta H c_i) = \frac{\partial}{\partial\xi}\left(K_H \Delta H \frac{\partial c_i}{\partial\xi}\right) \qquad \text{(IV-20)}$$

$$\frac{\partial}{\partial\tau}(\Delta H c_i) + \frac{\partial}{\partial\eta}(v\Delta H c_i) = \frac{\partial}{\partial\eta}\left(K_H \Delta H \frac{\partial c_i}{\partial\eta}\right) \qquad \text{(IV-21)}$$

$$\frac{\partial}{\partial\tau}(\Delta H c_i) + \frac{\partial}{\partial\rho}(w c_i) = \frac{\partial}{\partial\rho}\left(\frac{K_V}{\Delta H}\frac{\partial c_i}{\partial\rho}\right) + R_i \Delta H + S_i \Delta H \qquad \text{(IV-22)}$$

These reduced problems can be solved sequentially using a finite difference technique; after each cycle through the three equations, one obtains an approximate solution to the entire equation of continuity. The finite difference technique chosen for this project is the SHASTA scheme. This algorithm was first developed by Boris and Book (1973). It is an explicit Eulerian finite-difference scheme. Via a technique called "flux correction," this algorithm is able to strictly maintain the positivity of mass concentration so that it is ideally suited for handling steep concentration gradients. The potential of this algorithm for air pollution modeling has been demonstrated by a study carried out by Meyer and Durran (1976). Only a brief summary of the numerical method used in the present study is described here.

The SHASTA algorithm, as formulated for the solution of the pure advection equation of the form

$$\frac{\partial}{\partial \tau}(\Delta Hc_i) + \frac{\partial}{\partial \zeta}(u \Delta Hc_i) = 0 \qquad \text{(IV-23)}$$

may be written in terms of finite differences as follows:

let

$$\Delta Hc_i(n\Delta\tau, j\Delta\zeta) = r_j^n$$

and define

$$r_j^* = \frac{1}{2} Q_-^2 (r_{j-1}^n - r_j^n) + \frac{1}{2} Q_+^2 (r_{j+1}^n - r_j^n) + (Q_+ + Q_-) r_j^n \quad ,$$

where

$$Q_\pm = \frac{\frac{1}{2} \mp u_j \frac{\Delta t}{\Delta x}}{1 \pm (u_{j\pm1} - u_j) \frac{\Delta t}{\Delta x}} \quad .$$

Then

$$r_j^{n+1} = r_j^* - \frac{1}{8}(r_{j+1}^* - 2r_j^* + r_{j-1}^*) \quad . \qquad \text{(IV-24)}$$

Further details regarding the application of the SHASTA algorithm to the atmospheric diffusion equation can be found in Meyer and Durran (1976).

3. Treatment of Point Sources

A particular problem arises in the treatment of point sources in a mesoscale model because of the disparity in spatial resolution. The emissions are emanating from stacks whose sizes are of the order of a few meters, but the model has a spatial resolution of a few kilometers. Compounding the problem is the fact that a power plant plume is a collection of hot buoyant gases and the Plume Dispersion Model is not designed to simulate the dynamics of the hot buoyant gases as they rise through the surrounding air.

The optimal way to handle this problem would be to use a model like the Buoyant Plume Model described in Chapter II to follow the point-source plume until it grew wide enough to be properly represented by the mesoscale Plume Dispersion Model. Then the emissions could be introduced to the mesoscale model with minimal error. Unfortunately, because of the limited resources of the present project, the matching of these two models has not been attempted.

As an alternative, we chose, in the Plume Dispersion Model, to inject emissions into the vertical column of cells directly above each point source so that all the pollution was assigned to the cell located at the effective stack height of that source. The effective stack height is the sum of the physical stack height and the distance the plume rises above its point of emission. At this height the effects of plume buoyancy are negligible, and the Plume Dispersion Model is able to simulate the plume's behavior.

We calculated plume rise according to the formula given by Briggs (1971):

$$H = \frac{31.3(H_s)^{\frac{2}{3}}}{U}\left[\frac{\pi d^2 v}{4}(T_s - T_A)\right]^{\frac{1}{3}} , \qquad \text{(IV-25)}$$

where

d = stack diameter in feet
T_s = stack temperature in °C
T_A = ambient air temperature in °C
H_s = stack height in feet
U = horizontal wind in ft/min
ΔH = plume rise.
v = stack exit velocity in ft/min.

The effective stack height is $H_s + \Delta H$. If it is greater than the height of an inversion, there is a chance that the plume might penetrate that inversion and thereby leave the modeling region. Briggs (1969) gives the maximum height of an elevated inversion, h, that a buoyant plume can penetrate as:

$$h = 1.128\left[\frac{\pi d^2(T_s - T_A)v}{4U\Delta T}\right]^{\frac{1}{2}} + H_s \qquad \text{(IV-26)}$$

ΔT = the temperature difference between the top and bottom of the elevated inversion, which we took to be a constant 2°C.

Whenever the effective stack height was greater than the local mixing depth we calculated h. If h was also greater than the mixing depth, we assumed that the emissions penetrated the inversion and they were discarded. When h was less than the mixing depth, we assumed that the inversion was able to contain the plume and we therefore assigned the emissions to the topmost cell above the source.

C. DATA BASE FOR THE MODELING EXERCISE

The application of the Plume Dispersion Model requires a large data base. These data can generally be divided into three categories:

- Emissions data
- Meteorological data
- Air quality data.

Considerable effort was spent in this project on the collection and analysis of pertinent data available for Los Angeles and Moss Landing for use as inputs to the modeling exercise. This section is devoted to the discussion of this task.

1. Data Base for Los Angeles

a. Emissions Data

The Plume Dispersion Model requires an extensive inventory of SO_2 emissions. Power plants, petroleum refineries, chemical plants, and automobiles

are the major producers of SO_2 in the Los Angeles Basin. We treated emissions generated by other activities by lumping them together into a diffuse background source. The major activities associated with SO_2 generation are listed in Table IV-2.

Automotive Emissions. Automotive SO_2 emissions were calculated from traffic count data. The total SO_2 emitted by automobiles in any grid square was estimated by the total vehicle miles traveled in that square times an emissions factor of 0.23 grams of SO_2 per mile (U.S. Environmental Protection Agency, 1975). For the western 20 columns of the modeling region,

Table IV-2

EMISSIONS OF OXIDES OF SULFUR BY SOURCE*

Source	Percentage Contribution†
Gasoline Motor Vehicles	8.2
Other Transportation	4.1
Combustion of Fuels§	48.0
Petroleum Operations	15.1
Other Industrial Operations	8.2
Sulfur Recovery Operations	16.4

*Based on 1973 emissions in Los Angeles County.

†Total oxides of sulfur emitted are 365 tons per day

§Includes power plants, refineries, and other industrial and residential sources.

Roberts et al. (1971) figured the daily vehicle miles traveled in each square for the year 1967. Traffic data for the eastern 5 columns is given by Nordsieck (1974) for the year 1970. Unfortunately, this data is averaged over 2 mile by 2 mile squares that are offset from the grid used in this study by 1 mile in both the x and y coordinates. We interpolated this data onto our grid system. In so doing we inevitably smoothed the traffic count profiles, but we did attempt to avoid introducing freeway mileage into grid squares where no freeway exists.

This traffic data for 1967 and for 1970 must be converted into data for 1974. Table IV-3 gives traffic counts at several points in Los Angeles for 1967 and 1974. Because the average increase in vehicle miles traveled in this sample is approximately 3.2 percent per year, we assumed that the 1974 traffic was 22 percent greater than in 1967. For simplicity, we applied this correction factor uniformly over the entire modeling region.

Table IV-3

24-HOUR TRAFFIC COUNT
(To Nearest Hundred)

Location	Year 1967	1974
Alameda St.	4,800	4,800
Avalon Blvd. (North of Artesian Blvd.)	12,300	14,400
Carson St. (East of Normandie Ave.)	23,900	25,300
Crenshaw Blvd. (North of Palos Verdes Drive)	11,700	15,000
Lomita Blvd. (West of Figueroa St.)	12,800	17,900
Normandie Ave. (South of Sepulveda Blvd.)	8,900	10,900
Sepulveda Blvd. (East of Normandie Ave.)	26,200	32,000
Torrance Blvd. (West of Vermont Ave.)	14,100	17,700
Victoria St. (East of Wilmington Ave.)	1,300	4,200
Total	116,000	142,200

Source: Los Angeles County Road Department

This treatment implies that a larger percentage increase in traffic volume occurred in the eastern portion of the air basin, which is probably justifiable because of more new developments in this area.

Emissions from Power Plants. Table IV-4 contains a list of power plants in the Los Angeles Basin and their average 1974 SO_2 emissions. Except for Los Alamitos and Haynes, for which emissions data are available for each daytime hour of each test day, we used these yearly averaged emission rates in the Plume Dispersion Model. We corrected these rates to account for their daily temporal variations (except for the Haynes and Los Alamitos plants); the corrections were figured from data giving power plant emission fluctuations on a "typical" day (Roberts et al., 1973). Power plant emissions enter the Plume Dispersion Model as point sources.

Emissions from Chemical Plants and Refineries. Table IV-5 lists the major chemical plants and refineries in the Los Angeles Basin. These industries operate at an almost constant level all day; so it was not necessary to account for any temporal variations in their emission rates. In past modeling studies, refineries have often been treated as ground-level area sources; ground-level emissions are injected into the lowest vertical layer in the modeling region. In fact, most of the SO_2 from a typical refinery is emitted at very high temperature, from a few tall stacks. Under such conditions it is not good to automatically alot these emissions to ground-level vertical cells. Consequently we have introduced refinery and chemical plant emissions into the model as if they came from point sources (see Chapter IV Section B-3).

Emissions from Other Stationary Sources. Each year the Los Angeles Air Pollution Control District (LAAPCD) publishes a list of major polluters in Los Angeles County. According to the 1974 list, the plants listed in Tables IV-4 and IV-5 (except for SCE Huntington Beach and General Crude which are in Orange County) generate 82 percent of the total SO_2 emitted from stationary sources in Los Angeles. The remaining 18 percent is produced by numerous smaller sources scattered throughout the county. We incorporated these sources into the model as ground-based area source

Table IV-4

LOS ANGELES POWER PLANT DATA--1974

Plant	Location (square number)	Capacity* (megawatts)	SO_2 Emissions (lb-moles/hr)
Southern California Edison			
Los Alamitos	11,7	1950	87.5†
El Segundo	2,12	1020	33.9§
Redondo Beach	3,10	1530	6.9§
Huntington Beach	14,3	880	18.0**
Los Angeles Department of Water and Power			
Harbor	6,8	355	5.0§
Haynes	11,7	1580	53.1†
Scattergood	1,14	312	5.7§
Valley	3,24	512	3.8§
City of Pasadena	10,20	230	2.8§
City of Burbank	5,22	174	4.9§
City of Glendale	6,21	153	4.3§

*Roberts et al. (1971)

†Emissions on October 25, 1974.

§Data provided by Los Angeles County Air Pollution Control District

**Data provided by Orange County Air Pollution Control District

Table IV-5

MAJOR CHEMICAL PLANTS AND REFINERIES
IN THE LOS ANGELES BASIN

Source	Location (square number)	SO_2 Emissions (lb-moles/hr)
Atlantic Richfield Co., Carson	7,9	25.5†
Champlin Petroleum Co., Wilmington	7,8	1.2†
Collier Carbon and Chemical Co., Wilm.	7,8	0.8†
Douglas Oil Co., Paramount*	10,12	0.1†
General Crude Oil Co., Newport Beach	16,3	6.7§
Great Lakes Carbon Co., Wilm.	7,8	15.6†
Gulf Oil Co., Santa Fe Springs	12,12	9.3†
Mobil Oil Co., Torrance	4,10	16.0†
Morris P. Kirk and Son, Vernon	9,16	2.5†
Powerine Oil Co., Santa Fe Springs	12,13	2.7†
Shell Oil Co., Wilm.	7,10	9.6†
Standard Oil of Calif., El Segundo	2,12	16.1†
Stauffer Chemical Co., Dominguez	7,10	2.6†
Texaco Inc., Wilm.	7,8	5.3†
Union Oil Co., Wilm.	7,8	18.4†

*Included as an area source, not as a point source.

†Data provided by Los Angeles County Air Pollution Control District

§Data provided by Orange County Air Pollution Control District

emissions uniformly distributed over populated areas. Thus a grid square containing neither oceans nor mountains was assigned an area source emission rate of 5.68 kg of SO_2 per hour.

b. Meteorological Data

Air quality is a function of meteorological variables. The winds determine how pollution moves after it is emitted; the mixing depth determines the extent to which pollutants can be diluted by vertical diffusion.

Wind Data. Hourly averaged wind data for each of the test days was gathered by the 29 APCD stations listed in Table IV-6. We used a computer program to figure the wind vector in each grid cell from this data. The program calculates the interpolated wind vector at grid point j, $\hat{v}_j$, according to the formula (Liu et al., 1973),

$$\hat{v}_j = \frac{\sum_{r_{ij} < R} \left(\frac{\bar{v}_i}{r_{ij}} \right)}{\sum_{r_{ij} < R} \left(\frac{1}{r_{ij}} \right)} \qquad \text{(IV-27)}$$

where

$\bar{v}_i$ = measured wind vector at monitoring station i

v_{ij} = distance between grid point j and monitoring station i

R = radius of influence; in our study it was 16 miles.

Thus $\hat{v}_j$ is a weighted average of the velocity vectors at all wind stations within a given distance R of grid point j. If no station is within R miles, R is increased until some wind station comes within range. This formula was modified in the actual code so that calculated wind speed and direction was influenced by the presence of mountain barriers.

Table IV-6

APCD WIND STATIONS

Designation	Location/City
12W RB	Redondo Beach
14W VEN	Venice
75W CAP	Downtown Los Angeles
81W RVA	Pico Rivera
94W BKT	Brackett Field
95W KFI	KFI Transmitter
97W AZU	Azusa
100W BURK	Burbank
101W LONB	Long Beach
102W WEST	West Los Angeles
103W LACC	Los Angeles City College
106W WNT	Walnut
107W RESD	Reseda
108W LACA	La Cañada
109W POMA	Pomona
112W COMA	Compton Airport
113W MISH	Mission Hills
114W WHTR	Whittier
118W LENX	Lennox
119W ALH	Alhambra
120W DAHS	Dana High School
122W PASA	Pasadena
71W ANA	Anahiem
99W LAH	La Habra
LOSL	Los Alamitos
CAPS	San Juan Capistrano
COST	Costa Mesa
TORO	El Toro
GUNA	Laguna Beach

Mixing Depths. On each day of the measurement program, aircraft flown by Meteorological Research, Inc. measured vertical temperature profiles while flying in ascending and descending spiral patterns. They also released and tracked several pibal balloons. Inversion heights are usually determined from vertical temperature profiles. However, the pibal data frequently showed a pronounced decoupling of the winds aloft which, when compared with the spiral temperature measurements, appeared to occur at the same height as the bottom of the inversion layer. Encouraged by this observation we calculated mixing depths, when temperature profiles were unavailable, from pibal wind data if the winds showed a region of strong decoupling.

Unfortunately, since no measurements were taken before 11 a.m. on any of the days, we were forced to use typical Los Angeles values for the morning mixing depths. The data for one simulation is presented in Table IV-7. This data was used by a computer program to determine the mixing depth over each grid square during each hour of the simulation.

Surface Roughness. In the computation of turbulent diffusivities, a surface roughness characterizing the type of terrain for each grid square within the modeling region is also required. This input was obtained by examining the land-use pattern of each square according to the LARTS study. The results are shown in Figure IV-4.

c. Air Quality Data

The Plume Dispersion Model uses air quality data to determine its initial and boundary conditions. Such data also provide a yardstick with which model predictions can be compared. SO_2 concentrations were measured by the 26 stations listed in Table IV-8. The first 17 stations belong to the Los Angeles or Orange County APCD. The last 9, which also measured SO_4, were operated specially for this study by Rockwell International.

These data were processed by a computer program similar to that used on the wind data. The SO_2 concentration in each grid square was calculated

Table IV-7

MIXING DEPTHS FOR OCTOBER 11, 1974

Location	Time	Mixing Depth (feet)	Data Source
Los Angeles Airport	6:00	500	Typical Los Angeles Value
El Monte	6:00	500	" " " "
Los Alamitos Airport	14:18	3000	Spiral Temperature Profiles
Yorba Linda	17:01	3700	" " "
Fullerton Airport	17:17	3400	" " "
Los Alamitos Airport	18:02	3600	" " "
Riverside Airport	18:29	4300	" " "
Placentia	13:00	3000	Pibal
"	14:00	3100	"
"	15:00	2800	"
"	16:00	2800	"
"	17:00	3000	"
Los Alamitos	14:00	3000	"
"	15:00	2000	"
"	16:00	2000	"
"	17:00	2200	"
"	18:00	2200	"

Table IV-8

SO_2 SAMPLING STATIONS

Designation	Location/City	Designation	Location/City
1 CAP	Downtown Los Angeles	COST	Cost Mesa
60 AZU	Azusa	LAH	La Habra
69 BURK	Burbank	GUNA	Laguna Beach
71 WEST	West Los Angeles	LOSL	Los Alamitos
72 LONB	Long Beach	CT02	Anaheim
74 RESD	Reseda	CT03	Garden Grove
75 POMA	Pomona	CT04	Fullerton
76 LENX	Lennox	CT05	Whittier
78 RB	Redondo Beach	CT07	Orange
80 WHTR	Whittier	CT08	Fullerton
83 PASA	Pasadena	CT09	Anaheim
84 LYN	Lynwood	CT14	Featherly Park
ANA	Anaheim	CT16	Azusa

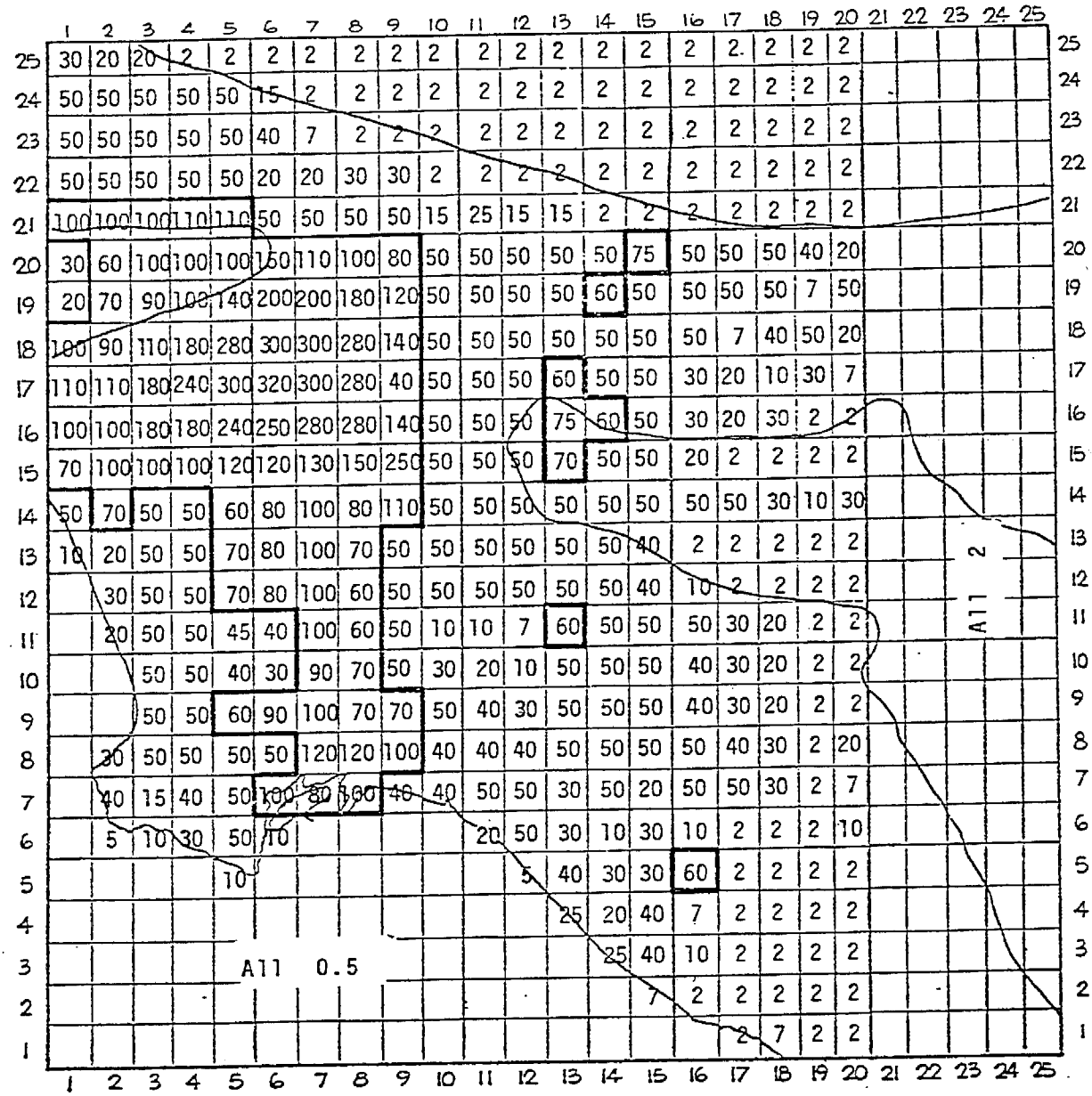

FIGURE IV-4. SURFACE ROUGHNESS IN CENTIMETERS BY GRID SQUARE FOR THE LOS ANGELES BASIN

according to the prescription

$$c_j = \frac{\sum_{r_{ij} < R} \frac{c_i}{r_{ij}^2}}{\sum_{r_{ij} < R} \frac{1}{r_{ij}^2}} \qquad \text{(IV-28)}$$

where

c_j = concentration at grid point j,

c_i = measured concentration at sampling station i,

r_{ij} = distance between grid point j and station i,

R = radius of influence, in our study it was 16 miles.

The set of concentrations calculated from the 6 a.m. data were used as initial conditions for each simulation. Those concentrations calculated at the edges of the modeling region were used to determine boundary conditions for each hour of the day.

2. Data Base for Moss Landing

The country around Moss Landing is mostly rural and is not industrialized; hence the only significant source of SO_2 is the power plant. The average SO_2 emissions from the plant on the study day were estimated to be 5000 lb/hr (Richards, 1976).

Meteorological and air qualtiy data for Moss Landing is scarce. Wind data were gathered at Monterey and Salinas at 900, 1200, 1500, and 1800 PST and at Fort Ord at 1800 PST. With the aid of wind streamline and isotach maps we estimated the wind speed and direction at nine points positioned symmetrically throughout the grid. We treated these points as hypothetical wind stations and used a computer program to interpolate the wind speed

and direction in each square exactly as was done for the Los Angeles Basin. Fortunately, the actual wind field seems to have been fairly constant over the modeling region so that the error generated by this process is not as critical as it could otherwise be.

Since we had measurements at only one site, we pretended that there was no horizontal variation in the mixing depths. Their vertical variation with time was suggested by only two data points, so the profile shown in Figure IV-5 was used.

Rockwell International set up ten stations to monitor ground-level SO_2 concentrations. Only two of these stations detected concentrations higher than the background concentration. The air quality measurements from these two stations were insufficient to characterize initial and boundary conditions for Moss Landing in the same fashion as was done for the Los Angeles Basin. Therefore, we set the initial concentration of SO_2 to 8 ppb at all points on the grid and used a constant boundary condition of 6 ppb. Finally a map (Figure IV-6) was prepared for the surface roughness over the modeling region.

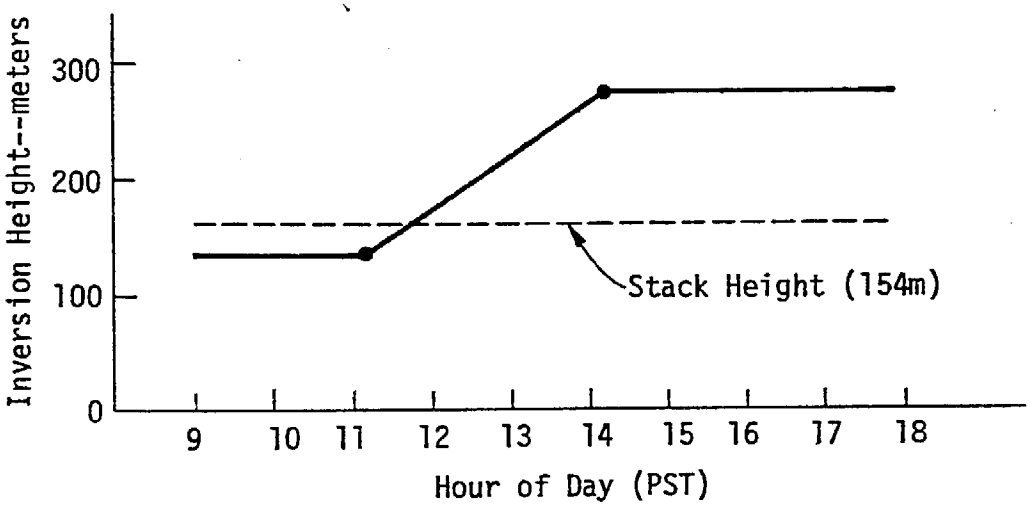

FIGURE IV-5. MIXING DEPTHS AT MOSS LANDING VERSUS TIME

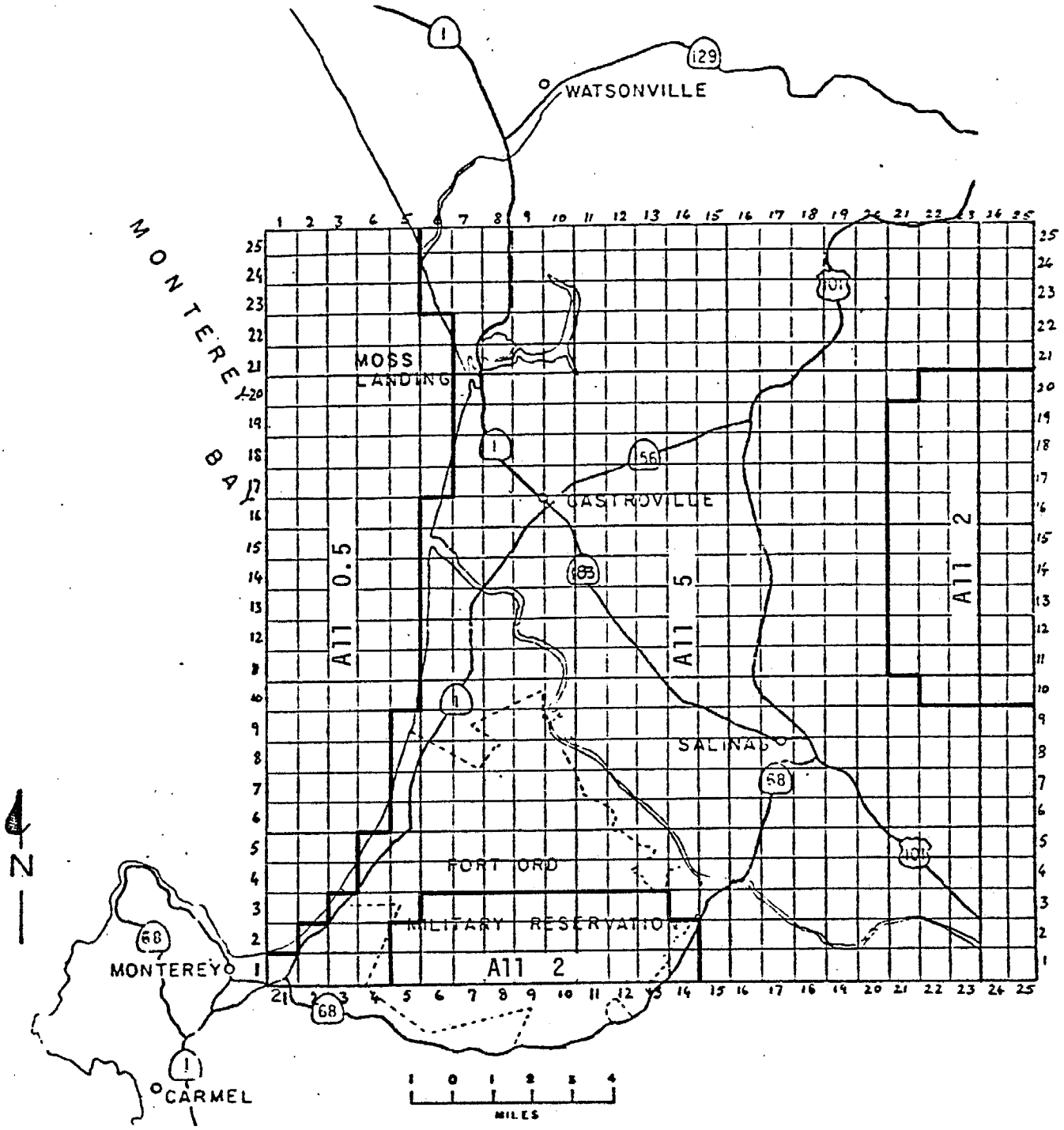

FIGURE IV-6. SURFACE ROUGHNESS IN CENTIMETERS FOR MOSS LANDING

D. APPLICATION OF THE MODEL

As the lengthy descriptions in the previous section may reveal, the application of the Plume Dispersion Model to any airshed requires a large data base. The collection, analysis, and reduction of the pertinent data is a very tedious task. However, to demonstrate the utility of the model, and to assess the impact of the emissions from the power plants of interest, we prepared data for the eight cases listed in Table IV-9 and exercised the Plume Dispersion Model with these data.

Table IV-9

SUMMARY OF PLUME DISPERSION MODEL SIMULATIONS

Location	Date	Emissions	
		All Sources	Power Plant of Interest
Los Angeles	October 1, 1974	✓	✓
Los Angeles	October 11, 1974	✓	✓
Los Angeles	October 25, 1974	✓	
Los Angeles	October 30, 1974	✓	✓
Moss Landing	September 11, 1974		✓

These runs produced predictions of hour-by-hour ground-level concentrations for SO_2 and sulfate ($SO_4^=$). Because of their volume, these concentrations are presented on maps along with the pertinent measurements in Appendix C. Only a general discussion concerning the analysis of these results is presented here.

From the sequence of maps showing predicted and measured SO_2 concentrations, it can be seen that while the Plume Dispersion Model is able to predict the general movement of the pollutant cloud over the air basin, it has only limited success in predicting the locations and magnitudes of the SO_2 concentration levels. This deficiency of the model may be attributed to deficiencies in a number of factors, notably

> The emissions inventory
> The meteorological parameters
> The air quality data.

Although every effort has been made to obtain the most accurate data possible, the data for most cases are still subject to large uncertainties. For example, the emissions inventory is assembled from different sources of information that are presumably applicable for certain periods of time. The predicted concentration levels are undoubtedly affected by the uncertainties in the emissions inventory.

In all simulations, and especially those for October 11, 25, and 30, we observe that the predicted concentrations during the first few hours of the simulations decrease from the initial values quite drastically, whereas the measured concentrations seem to remain constant or even increase. This suggests that excessive diffusion was predicted by the model. Such diffusion could only be caused by gross errors in the estimates of either the mixing depths or the concentrations aloft. Indeed, both of these estimates are based upon very limited information.

Similarly, the model predictions were also affected significantly by the uncertainties in air quality data. These data were used as initial and boundary conditions to characterize the pollutant concentrations of the air that was initially present in the air basin or flowed into the modeling region at a later time. In the absence of any real data, a constant value of 5 ppb for SO_2 was used for air coming from over the ocean. An analysis of the SO_2 concentrations measured near the coast suggests that this estimate may be too low. For example, there are no major SO_2 sources between the Pacific Ocean and Santa Ana Canyon, and the predicted SO_2 concentrations for the Santa Ana Canyon are significantly lower than the measurements.

The errors intrinsic to the Plume Dispersion Model should not be overlooked. Two major types of errors are known to exist: errors due to the treatment of point sources, and the numerical diffusion error. From a limited number of sensitivity runs, it was found that the predicted concentrations, particularly for grids near the stack, are critically dependent on when and how the emissions from large point sources are dumped in the mixing layer. The numerical error probably manifests itself to various degrees in all of the computations, but is particularly evident in the trough on the west side of the plume in the Moss Landing run, and the abnormally low concentration (2 ppb) between the hours of 1200 and 1300 on October 1, 1974 near Santa Monica in the Los Angeles run.

In spite of all the comments made above, the model predictions compare qualitatively with the measurements. Based upon an analysis of the predictions both for the cases where all emissions were included and the cases where only the emissions from the power plants were considered, the following general observations can be made:

- The plumes from the Los Alamitos and Haynes power plants tend to move with the on-shore breezes towards the northeastern portion of the air basin. Similarly, the plume from the Moss Landing power plant tends to move southeast into the Salinas Valley.
- The impact of these plumes on ground-level concentrations depends critically on when and where these plumes are entrained into the mixing layer as it rises due to surface heating during the day.
- Although sources of SO_2 in the western and southwestern portion of Los Angeles are generally responsible for the ground-level SO_2 concentrations, the emissions from the Los Alamitos and Haynes can make significant contributions in the vicinity of the plants.

V SUMMARY AND CONCLUSIONS

As a result of the increasing demand for energy and the dwindling supply of clean fuels, more high-sulfur fuel oil is being used by power plants in coastal California. In 1974 the California State Air Resources Board initiated a monitoring and analysis program to assess the impact of this fuel switch on air quality.

Three power plants in two locations, a rural area with low background pollutant concentrations (Moss Landing) and a polluted urban area (Los Alamitos and Haynes), were selected in this program. Many types of aerometric data were collected by five measurement teams during the period September to November 1974. This data base is probably the most comprehensive ever assembled for a power plant. In an effort to aid in the analysis of the field data collected in this program and to provide a tool for the assessment of power plant emissions on ambient air quality, three mathematical models were developed in the present study,

> Reactive Plume Model (RPM)
> Buoyant Plume Model (BPM)
> Plume Dispersion Model (PDM).

Because sulfate is a primary concern in the study of power plant plumes, the Reactive Plume Model was developed to study chemical reactions that lead to the formation of sulfate. RPM uses a Lagrangian approach to study the detailed chemical transformations that may take place in a plume. The model is based on equations describing the mass balance for the various pollutant species. The model uses a trajectory approach that can accommodate variations in wind speed, inversion height, and ambient pollutant concentrations. The spread of the plume is determined either by the classical Gaussian method or from observational data. Provision has been made

to allow for entrainment of background pollutants. A kinetic mechanism, which is a modified version of the Hecht-Seinfeld-Dodge mechanism, is included to describe gas-phase reactions between NO_x, SO_x, and hydrocarbons. This model has been validated using data collected at three power plants in California--the Moss Landing plant, the Los Alamitos plant, and the Haynes plant--for many days. The model predictions compare remarkably well with the observations. The model generally predicts a SO_2-sulfate conversion rate of 3 percent per hour.

The second model, the Buoyant Plume Model, is designed for the prediction of the rise of buoyant plumes and the eventual distribution of pollutants in the immediate vicinity of the stack. This model is based on the solution of the primitive equations with the Boussinesq approximation. A unique feature of this model is the inclusion of plume-generated turbulent diffusion. This is accomplished by parameterization of the turbulent diffusivity via the classical similarity theory for buoyant plumes. Provisions have also been made that can easily accommodate the variations in ambient eddy diffusivities encountered in a complex terrain. This model has been applied to data for the three power plants mentioned above. Comparisons with extensive airborne measurements show that the predicted plume rise and SO_2 distributions are all reasonable.

A few kilometers downwind of the stack, a plume will almost completely merge with the ambient atmosphere, and will reach its final height asymptotically. Beyond this point, the effect of buoyancy is no longer important. The third model, the Plume Dispersion Model, is thus designed to simulate the pollutant distributions at large distances. This model is based on the solution of the three-dimensional atmospheric diffusion equation. The spatial and temporal variations on a regional scale in wind speeds, wind directions, and turbulent diffusivities have been incorporated. Furthermore, this model also allows for interactions between the plume and other point or areal sources. Although the model is capable of including a complex kinetic mechanism (with the computation

time being the limiting factor), it currently uses a first-order reaction step to describe the conversion of SO_2 to sulfate. This model has also been applied to the three power plants mentioned above. The comparisons, in view of the uncertainties in the emissions rates, are reasonable.

APPENDIX A
A CRITICAL EXAMINATION OF THE GAUSSIAN DIFFUSION MODEL

APPENDIX A

A CRITICAL EXAMINATION OF THE GAUSSIAN DIFFUSION MODEL

It has become well-known that the commonly used Gaussian diffusion model has a tendency to predict pollutant concentrations greater than those observed whenever this model is applied to either a rough terrain or an urban complex (Start et al., 1974). The purpose of this appendix is to provide a theoretical explanation for the asymmetric prediction behavior of the Gaussian model. The first section of this appendix describes the conventional Gaussian model. In the second section, the similarity theory and its extension for prescribing turbulent diffusion in the mixing layer are delineated. Based on these theories, a method for calculating the vertical dispersion coefficient in the Gaussian model is derived in Section 3. This method provides the basis for assessing the predictive capability of the Gaussian model when the terrain of interest is not flat.

1. THE CONVENTIONAL GAUSSIAN MODEL

The conventional Gaussian model can be written as follows (Turner, 1969):

$$\chi(x,y,z,H) = \frac{Q}{2\pi\sigma_y\sigma_z u} \exp\left[-\frac{1}{2}\left(\frac{y}{\sigma_y}\right)^2\right] \cdot \left\{\exp\left[-\frac{1}{2}\left(\frac{z-H}{\sigma_z}\right)^2\right] + \exp\left[-\frac{1}{2}\left(\frac{z+H}{\sigma_z}\right)^2\right]\right\} \quad , \qquad \text{(A-1)}$$

where

χ = pollutant concentration
Q = emission rate
u = wind speed
σ_y = horizontal dispersion coefficient
σ_z = vertical dispersion coefficient.

In addition to a number of fundamental assumptions common to all simple diffusion models, the Gaussian model further assumes that the plume spread has a Guassian distribution in both the horizontal (cross-wind) and vertical directions. The standard deviations of pollutant concentration distributions in the horizontal and vertical are then represented by the so-called horizontal and vertical dispersion coefficients, σ_y and σ_z, respectively.

As noted by Turner (1969), the values for σ_y and σ_z vary with the average wind speed, the turbulent structure of the atmosphere (stability), the height above the surface, and surface roughness. The effects of these parameters, except for the last one, have been included in a scheme first proposed by Pasquill and Gifford and later modified by Turner (1969). The latter, which is now used commonly for estimating pollutant concentrations from point sources, requires first a specification of stability categories as follows:

Surface Wind Speed (at 10 m), m sec^{-1}	Day			Night	
	Incoming Solar Radiation			Thinly Overcast or ≥4/8 Low Cloud	≤3/8 Cloud
	Strong	Moderate	Slight		
< 2	A	A-B	B		
2-3	A-B	B	C	E	F
3-5	B	B-C	C	D	E
5-6	C	C-D	D	D	D
> 6	C	D	D	D	D

Note: The neutral class, D, should be assumed for overcast conditions during day or night.

Dispersion coefficients as a function of distance downwind of a point source can then be obtained from relationships in graphical form. (See, for example, the dashed lines in Figures A-1 and A-2.) These relationships were derived empirically from observational data, notably from the well-known Prairie experiment for which the underlying terrain was flat.

It is thus not difficult to understand why the Gaussian model cannot be expected to be valid for a complex terrain. From a theoretical point of view, the following two pehnomena will certainly affect its prediction:

> The dynamic interaction of the plume and major topographical features, e.g., the possible lifting or impingement of the plume as it approaches the slope of a nearby hill.
> The terrain-induced turbulence, i.e., the intensification of turbulent diffusion due to increases in the surface roughness over a complex terrain.

The first phenomenon can conceivably cause the uncorrected Gaussian model to either underpredict or overpredict, depending upon whether lifting or impingement occurs. Such an occurrence depends in general on whether the kinetic energy of the air stream approaching an obstacle is greater or smaller than the potential energy required to lift it over the obstacle. This potential energy, in turn, is dependent upon the atmospheric stability. Thus, conditions that are conducive to plume impingement are light winds and a stable atmosphere. The physical processes governing the occurrence of impingement are extremely complex, and have only very recently received the attention of air pollution researchers. Because most of the studies to date have been laboratory tests or scaling studies, it is difficult at this point to assess the impact of impingement on the Gaussian model predictions.

In contrast, the understanding of turbulent diffusion in the surface layer has been improved considerably through active research over the last decade. By combining these studies with the classical statistical theory for turbulent diffusion (Taylor, 1921), it is possible to examine the effects of terrain-induced turbulence on the predictions of the Gaussian model when

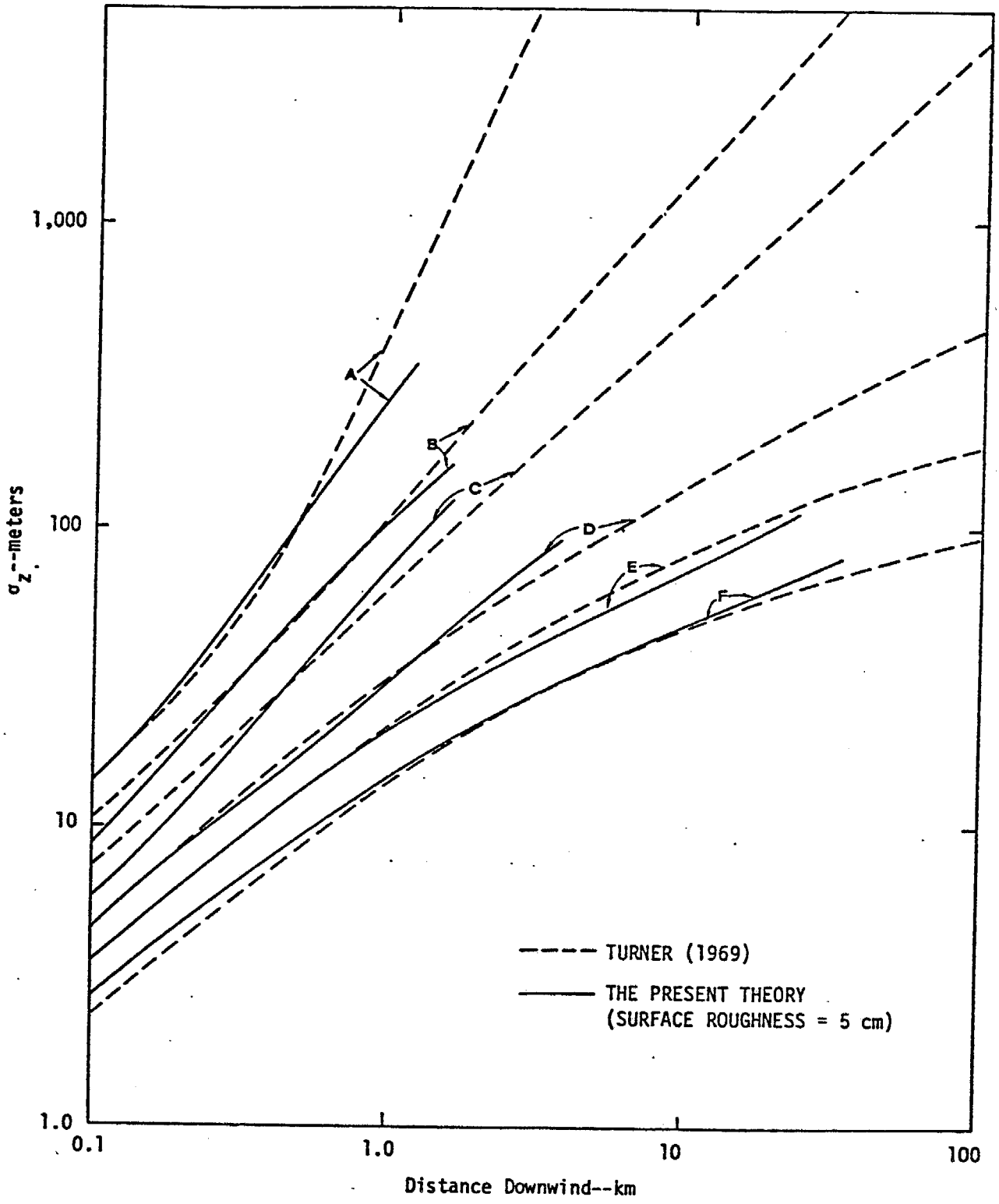

FIGURE A-1. VERTICAL DISPERSION COEFFICIENT AS A FUNCTION OF DOWNWIND DISTANCE FROM THE SOURCE FOR SMOOTH TERRAIN

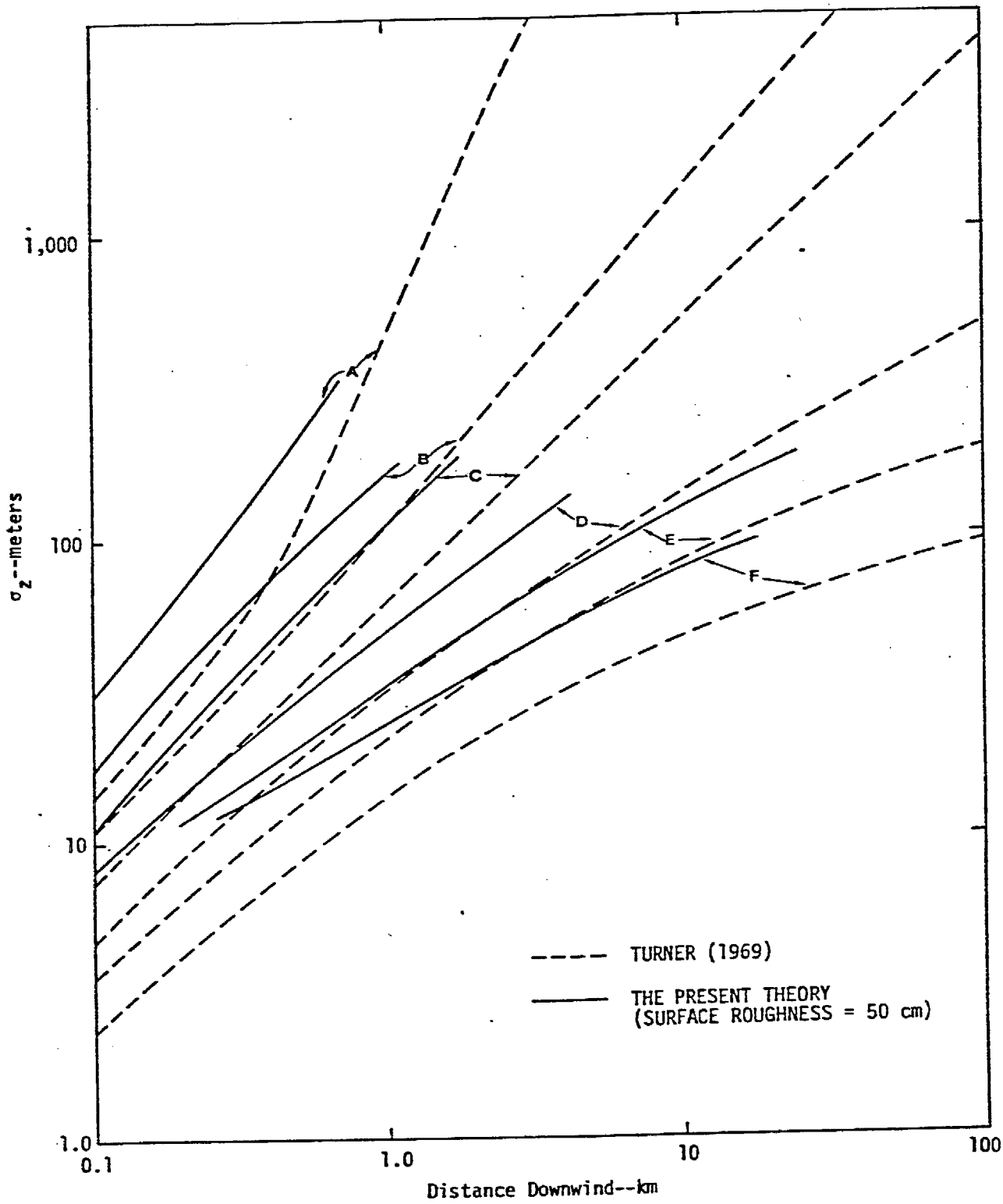

FIGURE A-2. VERTICAL DISPERSION COEFFICIENT AS A FUNCTION OF DOWNWIND DISTANCE FROM THE SOURCE FOR ROUGH TERRAIN

applied to complex terrain. A brief outline of the method used in this assessment is described in the following two sections; a detailed discussion of the methodology can be found elsewhere (Liu, 1976).

2. TURBULENT DIFFUSION IN THE MIXING LAYER

Based on a comprehensive review of the pertinent literature, we have developed an algorithm for prescribing the vertical eddy diffusivity in the surface layer. The following general formula is used:

$$K_i = \frac{ku_* z}{\phi_i\left(\frac{z}{L}\right)} \qquad (z_0 \leq z \leq |L|) \qquad \text{(A-2)}$$

where

K_i = turbulent diffusivity for momentum (i = M) or heat (i = H)
k = von Karman constant (= 0.35)
u_* = friction velocity
z = height
L = Monin-Obukhov length
z_0 = surface roughness.

This formula is the result of the similarity theory for the constant-flux surface layer (Businger et al., 1971). For neutral stability conditions, the ϕ-function approaches a constant value ($\phi_M = 1$, $\phi_H = 0.74$). For stable and unstable conditions, the ϕ-function is greater or less, respectively, than the corresponding constant value. The following empirical expressions for the ϕ-function were proposed by Businger et al.(1971) based on observational data:

For the stable case (L > 0)

$$\phi_M\left(\frac{z}{L}\right) = 1 + 4.7\left(\frac{z}{L}\right) \qquad \text{(A-3)}$$

$$\phi_H\left(\frac{z}{L}\right) = 0.74 + 4.7\left(\frac{z}{L}\right) \quad . \qquad \text{(A-4)}$$

For the unstable case ($L < 0$)

$$\phi_M\left(\frac{z}{L}\right) = \left[1 - 15\left(\frac{z}{L}\right)\right]^{-\frac{1}{4}} \tag{A-5}$$

$$\phi_H\left(\frac{z}{L}\right) = \left[1 - 9\left(\frac{z}{L}\right)\right]^{-\frac{1}{2}} . \tag{A-6}$$

The friction velocity is determined by the following equation:

$$u_* = \frac{ku_r}{f(z_r)} \tag{A-7}$$

where u_r denotes a reference wind speed measured at a reference height, z_r, and the function $f(z)$ is defined as follows:

for the stable case

$$f(z) = \ln\left(\frac{z}{z_0}\right) + 4.7\left(\frac{z - z_0}{L}\right) \tag{A-8}$$

for the unstable case

$$f(z) = \ln\left[\frac{1 - \phi_M\left(\frac{z}{L}\right)}{1 + \phi_M\left(\frac{z}{L}\right)}\right] - \ln\left[\frac{1 - \phi_M\left(\frac{z_0}{L}\right)}{1 + \phi_M\left(\frac{z_0}{L}\right)}\right] + 2\tan^{-1}\left[\frac{1}{\phi_M\left(\frac{z}{L}\right)}\right] - 2\tan^{-1}\left[\frac{1}{\phi_M\left(\frac{z_0}{L}\right)}\right] . \tag{A-9}$$

Above the surface layer ($|L| \leq z \leq Z_i$), a second-order interpolation formula first proposed by O'Brien (1970) is adopted to prescribe the vertical eddy diffusivity for the stable case.

$$K_i(z) = K_i(Z) + \left(\frac{Z - z}{Z - |L|}\right)^2 \cdot \left\{ K_i(|L|) - K_i(Z) + (z - |L|) \cdot \left[K_i'(|L|) + 2\left(\frac{K_i(|L|) - K_i(Z)}{Z - |L|}\right)\right]\right\} \qquad \text{(A-10)}$$

where

$K_i(Z)$ = diffusivity at the elevated inversion

$$K_i(|L|) = \left.\frac{d\, K_i(z)}{dz}\right|_{z = |L|}$$

Z = inversion height.

Above the surface layer the diffusion coefficients for mildly unstable cases (stability category A-B or lower) are assumed to be linearly proportional to the height and the constant is obtained by requiring the diffusivity profile to be continuous. For very unstable cases (stability category A-B or higher), the associated Monin-Obukhov lengths become very small. This corresponds to a case which is commonly referred to as "free convection." According to Monin (1959) and Priestley (1954),

$$\phi_H \propto \left(-\frac{Z}{L}\right)^{\frac{1}{3}} .$$

The proportionality constant is again determined by imposing the continuity conditions. The prescription of the diffusivity scheme is then complete if the relationship between surface roughness, stability, and the Monin-Obukhov length, as described in Chapter IV, is invoked.

3. ESTIMATION OF THE DISPERSION COEFFICIENT

Once a prescription of the turbulent diffusion coefficient is obtained, the classical statistical theory for turbulent diffusion first developed

by Taylor (1921) can be used to estimate the dispersion coefficient for the Gaussian model. According to Taylor, the variance, or the second moment, of particle distribution is given by

$$\overline{y^2}(t) = 2\,\overline{v'^2}\int_0^t\int_0^\tau R(\xi)\,d\xi\,d\tau \qquad \text{(A-11)}$$

where

$$R(\xi) = \frac{\overline{v'(t)\,v'(t-\xi)}}{\overline{v'^2}}$$

is the one-point Lagrangian velocity correlation coefficient. When t is large, R is expected to approach zero, such that in the limit,

$$\overline{y^2}(t) \approx 2Kt \qquad \text{(A-12)}$$

where

$$K = \overline{v'^2}\lim_{t\to\infty}\int_0^t R(\tau)\,d\tau \quad .$$

Thus we may write

$$\frac{\overline{dy^2}}{dt} = \frac{d\sigma_y^2}{dt} = 2\,K_y \qquad \text{(A-13)}$$

and analogously,

$$\frac{\overline{dz^2}}{dt} = \frac{d\sigma_z^2}{dt} = 2\,K_z \qquad \text{(A-14)}$$

where K_y and K_z are equivalent to the turbulent diffusion coefficients discussed above.

Because horizontal dispersion is generally less important than its vertical counterpart and there exists a close relationship between the two, only the latter will be dealt with here. The average downwind distance of the particle is determined by

$$\frac{dx}{dt} = u(z) = \frac{u_*}{k} f(z) \qquad \text{(A-15)}$$

while the average vertical travel is given by

$$\frac{dz}{dt} = \frac{k\ u_*}{\phi_H(z)} \qquad \text{(A-16)}$$

The above three equations can then be integrated to yield the vertical dispersion coefficient, σ_z, as a function of downwind distance.

These calculations have been made for all stability categories with the surface roughness set to 5 cm, a value chosen because it is believed to be representative of the Prairie experiment. The results are presented as solid lines in Figure A-1. It is interesting to note that they do indeed reproduce to a reasonable degree the empirical curves (dashed lines) suggested by Turner (1969).

The calculation has been repeated for the case where surface roughness is increased to 50 cm. The results, as shown in Figure A-2, indicate that the corresponding dispersion coefficients are significantly higher than those predicted by the conventional Gaussian model. Consequently the Gaussian model will overpredict the pollutant concentrations by a factor of more than two. It is most interesting to note that the curves for the higher surface roughness are generally equal to one class higher in the Turner counterparts of stability. As shown in Figure A-3, the same conclusion was reached by McElroy and Pooler (1968) based on field measurements.

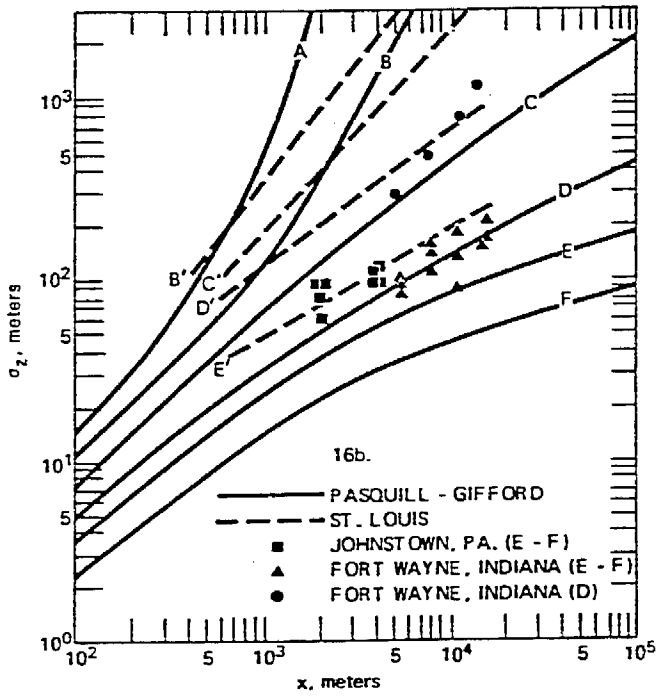

Source: McElroy and Pooler (1968)

FIGURE A-3. COMPARISON OF THE RESULTS OF THE ST. LOUIS AND OTHER URBAN TRACER EXPERIMENTS

APPENDIX B
DESCRIPTION OF THE FIELD MEASUREMENT PROGRAM

APPENDIX B
DESCRIPTION OF THE FIELD MEASUREMENT PROGRAM

Since the objective of this effort is to develop and validate power-plant emission impact models using data collected during the field study portion of this project, it is thus necessary to analyze and reduce the data collected during the measurement program in such a way that they can serve as an adequate data base for these plume models. However, the data requirements of the models developed under this project differ significantly, so the data base must be treated differently for each model. For this reason, we discuss only the general features of the measurement program and the associated data base in this appendix. More specific information about the data analyses and related model validation exercises is contained in the respective chapters.

1. DESIGN OF THE PROGRAM

In 1974, a program was initiated by the California Air Resources Board (ARB) to consider the effects of several fossil fuel power plants on air quality in California. ARB enlisted the services of five measurement organizations with the objective of compiling a relatively complete data base that would provide information about the chemistry, dispersion, and transport of pollutants from these plants. The program was carefully organized to stimulate close cooperation among the measurement groups, and thereby to provide for consistent and complementary sets of data.

The measurement program was to consist of nine days of sampling at plants selected to provide a variety of atmospheric conditions, background pollutant concentrations, and fuel types. Three days were allocated to the Moss Landing Power Station (Pacific Gas and Electric), which is located in a relatively "clean" rural environment and can burn either fuel oil or natural gas. The dates selected for Moss Landing were 10, 11, and 12

September 1974; fuel oil was burnt on the first two days and natural gas on the last. Measurements were also taken on three days (1, 11, and 17 October 1974) at the Haynes Station (Los Angeles Water and Power), which burns both fuel gas and oil, and on three days (25 and 30 October and 7 November 1974) at the Los Alamitos Station (Southern California Eidson Co.), which burns oil. Both Haynes and Los Alamitos are located in the "dirty" Los Angeles Basin. All three plants are located within a few miles of the Pacific Ocean and offer an interesting variety of climatological conditions representative of typical conditions in California.

The measurement program consisted of the following basic components:

- Definition of plant operating parameters and SO_2 emissions.
- SF_6 tracer releases into the plume at the plant stacks.
- SF_6 sampling (ground and airborne).
- SO_2 sampling (ground and airborne).
- Sulfate sampling (ground and airborne).
- Definition of meteorological conditions.
- NO, NO_x, O_3, and condensation nuclei (CN) sampling (airborne only).

Continuous SF_6 releases during seven-hour periods were made into the stack gases on most of the measurement days. Hourly SF_6 concentrations were obtained at eighteen ground-level stations for the Moss Landing tests and at nineteen stations in the Los Angeles Basin. Simultaneous measurements of SO_2 concentrations were collected at ten of the ground sites in each area. Instrumented aircraft and ground vehicles were operated in and around the plume during these experiments. The aircraft measured SO_2, SF_6, NO, NO_x, CN, and O_3 concentrations and the van measured SO_2 and NO_2 concentrations. Sulfate samples were collected by sequential filters on the ground and by a filter system in the aircraft. Pibal trajectories and airborne measurements of temperature and humidity were indicators of the meteorological conditions prevailing during the experiment.

2. MEASUREMENT TEAM AND TEAM MEMBER ROLES

The five organizations that participated in the measurement program were:

- Rockwell International/Air Monitoring Center
- Meteorology Research, Incorporated
- Environmental Measurements, Incorporated
- California Institute of Technology
- Air and Industrial Hygiene Laboratory

Each of these groups was responsible for one or more of the basic program components. The following sections describe the roles played by each of the members in the measurement project.

a. Rockwell International/Air Monitoring Center (AMC)

A ground network of ten sampling stations were set up for the power plant studies by AMC. Each station was equipped with a Rockwell Sequential Sampler, to obtain filter samples for sulfate analyses, and a Meloy SA 160-2 sulfur gas analyzer, to continuously monitor SO_2 (Richards, 1976). AMC was also responsible for estimating emission rates of the untested stacks at the participating power plants, and for analyzing all the ground-level data.

b. Meteorology Research, Inc. (MRI)

During the sampling program MRI was responsible for all airborne plume sampling, and for analysis of the aerometric data. MRI's Cessna 206 was equipped to obtain in-situ real time data on SO_2, NO, NO_x, CO, O_3, scattering coefficient, condensation nuclei, temperature, turbulence, humidity, and aircraft position, and to collect grab and filter samples for SF_6 and sulfate analyses. In addition, MRI collected all available meteorological information and released pilot balloons on a regular basis.

Among the instruments on board the aircraft were: MRI Integrating Nephelometer, Environment 1 Condensation Nuclei Monitor, REM 612 Ozone Monitor, Monitor Labs 8440 NO-NO_x Monitor, Andros Model 7000 CO Monitor,

Theta Sensor LS-400 SO_2 Monitor, MRI Airborne Instrument Package, and Metrodata #620 Data Loggers (Smith et al., 1975).

c. Environmental Measurements, Inc. (EMI)

During these power plant studies, EMI provided and operated an Air Quality Moving Laboratory (AQML), an instrumented van, equipped to measure overhead SO_2/NO_2, ground level SO_2/NO_x, and ground level SF_6. A Barringer Research COSPEC III correlation spectometer was used to determine the total overhead burden of SO_2 and NO_2. A Bendix Model 8300 Total Sulfur Monitor and a Meloy Model SA-185 Total Sulfur Monitor (for October measurements) were used to measure ground level SO_2 during the experiment. Ground level NO_x measurements were obtained using a Thermo Electron Oxides of Nitrogen Analyzer. SF_6 samples were collected in manually operated syringes (EMI, 1975).

The ARB designated six days as measurement days for EMI's AQML; 10 and 11 September 1974 at Moss Landing, and 11, 16, 17, 30, and 31 October 1974 in the Los Angeles Basin. Unfortunately, tracer and airborne measurements were not carried out on 16 and 31 October. Furthermore, EMI was not gathering data on 1 and 25 October 1974 and 7 November 1974 while the other members were participating. Therefore, these portions of the data base are not as complete as the remainder.

d. California Institute of Technology (Caltech)

The Caltech group was responsible for the release of SF_6 into the stacks at the power plant, for the establishment of ground-level SF_6 sampling systems, and analysis of all SF_6 samples (including airborne and mobile). SF_6 measurements were made using Development Sciences, Inc. automatic sequential sampling units, except for those made by MRI and EMI for which Caltech provided an automatically screw-driven 30-cc syringe sampler, and a manually operated syringe sampler, respectively. Samples were analyzed using four electron-capture gas chromatographs and a Spectra-Physics electronic digital integrator. The SF_6 stack injection system consisted of six large cylinders of SF_6, a Matheson Model 8H-590 pressure regulator and one F & P Co. Model B6-35-10/27 large volume flowmeter (Drivas and Shair, 1975).

e. Air and Industrial Hygiene Laboratory (AIHL)

AIHL was responsible for analyzing filter samples collected during the power plant studies for constituent sulfates (SO_4^{-2}). Gelman GA-1 membrane filter samples collected at the AMC ground-level stations and on board the MRI aircraft were analyzed by an AIHL microchemical method employing the addition of an excess barium dye (dinitrosulfanazo-III) complex (Wesolowski, 1974).

Further details about the monitoring procedures employed and the data collected by each group can be obtained from the references mentioned in each section or by directly contacting the authors of those references. As mentioned earlier, descriptions of the data analyses undertaken by SAI are presented in the sections on validation exercises in Chapters II, III, and IV.